SANDIA REPORT
SAND2003-2282
Unlimited Release
Printed July 2003

CPUF – A CHEMICAL-STRUCTURE-BASED POLYURETHANE FOAM DECOMPOSITION AND FOAM RESPONSE MODEL

Michael L. Hobbs, Kenneth L. Erickson, Tze Y. Chu, Theodore T. Borek, Kyle R. Thompson, Kevin J. Dowding, Dan Clayton, and Thomas H. Fletcher

Prepared by
Sandia National Laboratories
Albuquerque, New Mexico 87185 and Livermore, California 94550

Sandia is a multiprogram laboratory operated by Sandia Corporation,
a Lockheed Martin Company, for the United States Department of Energy's
National Nuclear Security Administration under Contract DE-AC04-94AL85000.

Issued by Sandia National Laboratories, operated for the United States Department of Energy by Sandia Corporation.

Available to DOE and DOE contractors from
U.S. Department of Energy
Office of Scientific and Technical Information
P.O. Box 62
Oak Ridge, TN 37831

Telephone: (865)576-8401
Facsimile: (865)576-5728
E-Mail: reports@adonis.osti.gov
Online ordering: http://www.doe.gov/bridge

Available to the public from
U.S. Department of Commerce
National Technical Information Service
5285 Port Royal Rd
Springfield, VA 22161

Telephone: (800)553-6847
Facsimile: (703)605-6900
E-Mail: orders@ntis.fedworld.gov
Online order: http://www.ntis.gov/help/ordermethods.asp?loc=7-4-0#online

SAND2003-2282
Unlimited Release
Printed July 2003

CPUF – A CHEMICAL-STRUCTURE-BASED POLYURETHANE FOAM DECOMPOSITION CHEMISTRY AND FOAM RESPONSE MODEL

Michael L. Hobbs, Kenneth L. Erickson, Tze Y. Chu,
Theodore T. Borek, Kyle R. Thompson, Kevin J. Dowding
Engineering Sciences Center
Sandia National Laboratories
P.O. Box 5800
Albuquerque, New Mexico 87185

Dan Clayton and Thomas H. Fletcher
Chemical Engineering Department
Brigham Young University
Provo, Utah 84602-4100

Abstract

A Chemical-structure-based PolyUrethane Foam (CPUF) decomposition model has been developed to predict the fire-induced response of rigid, closed-cell polyurethane foam-filled systems. The model, developed for the B-61 and W-80 fireset foam, is based on a cascade of bond-breaking reactions that produce CO_2. Percolation theory is used to dynamically quantify polymer fragment populations of the thermally degrading foam. The partition between condensed-phase polymer fragments and gas-phase polymer fragments (*i.e.* vapor-liquid split) was determined using a vapor-liquid equilibrium model. The CPUF decomposition model was implemented into the finite element (FE) heat conduction codes COYOTE and CALORE, which support chemical kinetics and enclosure radiation. Elements were removed from the computational domain when the calculated solid mass fractions within the individual finite element decrease below a set criterion. Element removal, referred to as "element death," creates a radiation enclosure (assumed to be non-participating) as well as a decomposition front, which separates the condensed-phase encapsulant from the gas-filled enclosure. All of the chemistry parameters as well as thermophysical properties for the CPUF model were obtained from small-scale laboratory experiments. The CPUF model was evaluated by comparing predictions to measurements. The validation experiments included several thermogravimetric experiments at pressures ranging from ambient pressure to 30 bars. Larger, component-scale experiments were also used to validate the foam response model. The effects of heat flux, bulk density, orientation, embedded components, confinement and pressure were measured and compared to model predictions. Uncertainties in the model results were evaluated using a mean value approach. The measured mass loss in the TGA experiments and the measured location of the decomposition front were within the 95% prediction limit determined using the CPUF model for all of the experiments where the decomposition

gases were vented sufficiently. The CPUF model results were not as good for the partially confined radiant heat experiments where the vent area was regulated to maintain pressure. Liquefaction and flow effects, which are not considered in the CPUF model, become important when the decomposition gases are confined.

Acknowledgements

The authors gratefully acknowledge the technical assistance provided by J. H. Bentz, J. G. Pantuso, W. Gill and L.L. Humphries (large-scale radiant heat experiments); T.A. Ulibarri and T. Neet (provided foam samples and synthesis details); R.S. Saunders (polymer structures and synthesis of model compounds for IR analysis); J. N. Castaneda, L. P. Jackson, and J. D. Kurtz (LPTGA experiments); G. H. Lemmon (uncertainty propagation for component-scale simulations); and L. M. Rawlings (image processing). Modeling discussions regarding percolation theory from D. M. Grant and R. J. Pugmire (University of Utah) are appreciated. R. J. Pugmire provided the NMR data in Fig. 3.3.C. D. G. Robinson gave insight into proper use of the mean value sensitivity analysis. M. S. Eldred helped set up the DAKOTA optimizer used to obtain the activation energies and the object function gradients used in the uncertainty analysis. L. A. Schoof helped set up the 2D and 3D mean value analysis using the EXODUS library. Comments from internal reviewers at Sandia National Laboratories, D. Dobranich, E. S. Hertel, L. M. G. Minier, M. R. Prairie, A. C. Ratzel, and A. C. Sun are also sincerely appreciated.

Table of Contents

List of Figures

List of Figures

List of Tables

List of Tables

Preface

In 1999, the report SAND99-2758 [1,2] was written to describe a model for decomposition of *unconfined* rigid polyurethane foam referred to as the PUF model. This model was composed of three basic components necessary to model decomposition of polymeric materials: 1) a bond-breaking mechanism, 2) a lattice statistics model, and 3) a vapor-liquid equilibrium model. Most of the PUF model components were taken from the open literature rather than from specific experiments on polyurethane foam. For example, the bond-breaking mechanism for the PUF model was based on a generalized *cellulose* decomposition mechanism. The kinetic coefficients for the PUF model were obtained by fitting results to low pressure thermogravimetric analysis (LPTGA) decomposition experiments. The overall root mean squared (RMS) error between predicted and measured mass loss for the LPTGA experiments was ~8%. A more accurate model based on experimental discovery was needed for high consequence nuclear safety calculations.

In the current report, a rigid polyurethane decomposition model referred to as the CPUF model for Chemical-structure-based decomposition of PolyUrethane Foam is described. Although the basic structure of the PUF model and the CPUF model are similar (*e.g.* both models consider bond breaking, lattice statistics, and vapor-liquid equilibrium), the CPUF model has numerous enhancements. For example, the bond-breaking mechanism for the CPUF model was based on a polymer fragmentation model using mass loss data [3-5] rather than using a modified cellulose decomposition mechanism as in the PUF model. The CPUF model also considers distributed activation energies that are dependent on the extent of thermal damage. Furthermore, the vapor-liquid equilibrium model considers non-ideal vapors. The RMS error for the CPUF predictions of mass loss in the LPTGA experiment is ~2% (compared to ~8% for the PUF model) for different heating conditions.

The CPUF model has been implemented into the thermal diffusion codes COYOTE [6] and CALORE [7], which solve the heat diffusion equation with a source term for chemistry. The complete foam response model includes the CPUF chemistry implemented into the finite element models (FEM) with appropriate thermophysical properties and is referred to as the *CPUF foam response model*. Species diffusion and fluid flow, features currently not available in the thermal diffusion codes, are needed to fully implement the effects of confinement using the CPUF model. The FEM code is not currently able to track the influx and efflux of polymer fragments and other solvents between discrete elements. The presence of these polymer fragments may be responsible for liquefaction that has been observed when decomposition gases are not sufficiently vented. Thus, the CPUF model has not been fully parameterized for highly confined decomposition. The CPUF model parameters in the current report are based on local concentrations and should only be used when the foam is sufficiently *vented*. Additional experiments and models are needed to better understand decomposition under these higher levels of confinement where small polymer fragments act as solvents that promote liquefaction.

Executive Summary

The purpose of Sandia's foam material response program is to develop a high fidelity computational tool for fire-induced response of foam filled systems, where encapsulated components are confined in an external metal enclosure (skin). Fire-induced response of the system includes the combined thermal, chemical, and mechanical response of the foam, components, and the enclosure. Direct mechanical interaction between the foam and the enclosure is probably not important because gas pressure will be the main driving force for enclosure deformation and failure. However, pressure-induced deformation of the foam can be important. Other physical processes, such as liquid production and flow at the heated interface, can also be important.

The RPU decomposition chemistry model (CPUF) was developed to predict mass loss in three-dimensional finite element models (FEM) [6] to simulate large unconfined foam-filled systems exposed to fire-like heat fluxes. The FEM model was successfully applied to unconfined experiments with large vent areas allowing gaseous products to leave the proximity of the decomposing foam to minimize secondary reactions with the decomposing polymer. Confinement of gaseous products via reduced vent area promotes secondary reactions associated with liquefaction mechanisms that are presently not well understood.

Mass loss from twenty-one ambient pressure thermogravimetric analysis (TGA) experiments, using ~5-mg samples in open pans ramped at 20°C/min, were used to determine the distribution of the individual activation energies associated with each step of the CPUF bond-breaking mechanism. Neither condensed-phase composition data nor gas-phase composition data were used in the evaluation of the CPUF chemistry parameters; and the CPUF chemistry model should only be used to predict mass loss. The experimental composition database was not available to extract activation energies to predict detailed evolution of the gas or condensed-phase composition.

The objective of the CPUF model, discussed in the current report, is to predict foam response for unconfined conditions with the hydrostatic pressure specified. To this end, the response model only requires an estimate of mass loss within individual elements. Calculating dynamic pressure response requires accurate predictions of species evolution, which is beyond the scope of the current report. The reason the CPUF chemistry mechanism has numerous steps is to show the methodology of implementing a detailed mechanism that considers lattice statistics and vapor-liquid equilibrium. However, the reader should keep in mind that mass loss data could be simulated with fewer reaction steps.

Activation energies were assumed to be normally distributed independent variables; and uncertainty was propagated into separate verification TGA simulations by using a mean value analysis. A separate Latin Hypercube Analysis (LHS) was performed to show the validity of the assumptions used in the mean value analysis. Verification TGA experiments were also conducted with nonisothermal TGA samples ramped 5-50°C/min at pressures between ambient and 0.36-MPa. Several isothermal experiments were also investigated with samples quickly ramped (20-50°C/min) to either 250, 270, or 300°C and held for a few hours. Dual isothermal experiments were conducted with samples ramped to 300°C and held for 2 hours and then ramped again to 400°C and held for an additional 4 hours. Predicted mass loss was within the scatter of the experimental data.

The shift of the *ambient pressure* TGA profiles toward higher temperatures *due to confinement* is *not related to pressure,* since the pressure in these TGA experiments was low. The shift *due to confinement* for these experiments is related to a delay in mass transport away from the decomposing foam surface. The decrease in mass transport at low pressure and increased levels of confinement may be related to a decrease in the concentration driving potential. Mass transport is not only inversely related to pressure, but is also proportional to the concentration

difference between the bulk concentration and the concentration near the surface of the decomposing foam. As the decomposition products are confined, the concentration driving potential is reduced, causing the mass loss profiles to shift to higher temperatures. Since confinement and pressure both cause delays in mass transport, the pressure effect can be thought of as a *de facto* confinement effect and the TGA profiles with increasing levels of confinement should be similar to TGA results at increasing levels of pressure.

Toluene diisocyanate (TDI) is one of the major decomposition products evolving from bond-scission at the urethane linkage [1,2]. As the vent area is decreased, the removal of TDI from the TGA cup is delayed. The confined TDI molecule can then undergo a retrograde reaction by reforming a urethane bond with the decomposing polymer [3-5]. The urethane bonds can also degrade by evolving CO_2 and converting the urethane linkages into amine linkages that can eventually break and evolve decomposition species such as toluene diamine (TDA). This alternative reaction pathway depends on the degree that the decomposition products are in contact with the decomposing polymer. The time-dependent change in the TDI gas-phase concentration within the enclosure must be modeled to resolve confinement effects.

The CPUF model with the parameters given in the current report is only valid for systems with sufficient venting. The CPUF model is also valid for systems at elevated pressures provided the system is continually purged to remove decomposition products from the vicinity of the decomposing foam. The effect of confining decomposition gases has been investigated for some of the TGA experiments and was the subject of a Sandia-funded PhD dissertation [8].

The decomposition model was implemented into COYOTE [6] making use of element death. Element death refers to the removal of finite elements creating a dynamic radiation enclosure. Elements were removed from the computational domain after meeting a criterion based on the calculated solid fraction within the finite elements using the CPUF model. A discretization

bias correction was used to obtain mesh independent solutions with large elements. Uncertainty was propagated into some of the numerical simulations to show the relative importance of model parameters. Model results were compared to TGA weight loss measurements and X-ray images of the various large-scale experiments. Although the shape of the front was difficult to determine near the wall in the X-rays, the calculated and measured shapes of the decomposition fronts for the unconfined experiments appear to agree very well. A few of the large-scale experiments were urn under significant confinement and the CPUF model is shown to predict regression rates that are significantly slower than observed in the X-rays. Better models and experiments are needed to help understand confined systems with significant liquefaction effects.

Component-scale experiments of cylinders of foam weighing up to 400-g were exposed to well-characterized fire-like heat fluxes to assess and validate the FEM with *parameters based only on the laboratory-scale data*. The effects of heat flux, bulk density, orientation, embedded components, confinement, and pressure were measured. The validation data included real time X-rays to track the progression of the decomposition front. The thickness and curvature of the decomposition fronts depended on various factors, including the degree that the decomposition gases were confined and the pressure of the enclosure. Higher boundary temperatures (higher fluxes) resulted in faster decomposition fronts and narrow reaction zones for the unconfined large-scale RPU experiments. The embedded components with high thermal capacitances (solid stainless steel cylinders) had little effect on the propagation of the decomposition fronts. However, the embedded components with low thermal capacitances (hollow aluminum cylinders) caused the foam near the surface of the components to heat; and the decomposition front moved rapidly around the component. Lower density foam resulted in faster front velocities because less material was available for decomposition.

Nomenclature

Acronyms

BYU	Brigham Young University
CPU	Central processing unit
CPUF	Chemical-structure-based polyurethane foam decomposition model
CSTR	Continuous stirred reactor
DAKOTA	Design analysis kit for optimization
DAE	Distributed activation energy
DEBDF	Backward differentiation code used to solve stiff differential equations
FEM	Finite element model (*e.g.* COYOTE or CALORE)
HMX	High melting point explosive (octahydro-1,3,5,7-tetranitro-1,3,5,7-tetrazocine)
HPTGA	High-pressure thermogravimetric analysis
IR	Infrared
LHS	Latin hypercube sampling
LPTGA	Low-pressure thermogravimetric analysis
MV	Mean value sensitivity/uncertainty analysis
NMR	Nuclear magnetic resonance
ODE	Ordinary differential equation
PUF	Polyurethane foam decomposition model
RMS	Root mean squared
RPU	Rigid polyurethane foam
SNL	Sandia National Laboratories
SPUF	Simple polyurethane foam response model
TGA	Thermogravimetric analysis

Chemistry

AA	Adipic acid
C	Unbreakable-bridge shown in Fig. 4.3.A
CO_2	Carbon dioxide
CPN	Cyclopentanone
DEG	Diethylene glycol
δ	Isocyanate-dangler
δ’	Aminourethane-dangler
δ”	Diamine-dangler
d	Adipate-dangler
P_f	Primary polymer fraction originating from the primary polymer bridge
P_f’	Semi-degraded polymer fraction originating from the semi-degraded polymer bridge
P_f”	Fully-degraded polymer fraction originating from the fully-degraded polymer bridge
H_2O	Two hydrogen atoms and one oxygen atom (does not refer to water)
Λ	Urethane-bridge
Λ’	Aminourethane-bridge
Λ”	Diamine-bridge
L	Adipate-bridge
TDA	Toluene diamine
TDI	Toluene diisocyanate
TMP	Trimethylol propane

Lattice Statistics Variables

A	Refers to all bridges, danglers, and gas populations except for CO_2 (Λ, Λ', Λ", L, C, δ, δ', δ", d, P_f, P_f', P_f", and CPN with $\Sigma_A A = 1$)
A_o	Initial value of bridges, danglers, or gas populations
a_n	Number of different ways to form a finite polymer fragment with n mers
B	Refers to all bridges (Λ, Λ', Λ", L, and C)
bridges	Sum of all the bridge populations (*bridges* = $\Sigma_B B = \Lambda + \Lambda' + \Lambda'' + L + C$)
D	Refers to all danglers (δ, δ', δ", d)
danglers	Sum of all the dangler populations (*danglers* = $\Sigma_D D = \delta + \delta' + \delta'' + d$)
DEG	Diethylene glycol mer
f_A	Mass fraction of A
f_{CO2}	Mass fraction of CO_2
f_n	Mass fraction of the n^{th} polymer fragment
f_f	Mass fraction of finite polymer fragments
F	Infinite sum of the finite polymer fragment populations
F_n	Probability that a mer is a given member of a finite polymer fragment consisting of n mers with s bridges
Γ	Standard gamma function
gases	Sum of the heavy gas populations (*gases* = $P_f + P_f' + P_f''$ + CPN)
K	Infinite sum of the finite polymer fragments populations on a site basis
L	Adipate-bridge population
L_o	Initial adipate-bridge population
m_A	Mass of A on a site basis
m_{CO2}	Mass of CO_2 on a site basis
m_f	Mass of all finite polymer fragments
m_n	Mass of a finite polymer fragment consisting of n mers with s bridges

m_t	Total mass on a site basis
$\bar{M}_B$	Average molecular weight of the bridges
$\bar{M}_D$	Average molecular weight of the danglers
M_A	Molecular weight of A
M_C	Molecular weight of the C bridge
M_{CO2}	Molecular weight of the CO_2 gas
M_{CPN}	Molecular weight of the CPN gas
M_δ	Molecular weight of the δ dangler
$M_{\delta'}$	Molecular weight of the δ' dangler
$M_{\delta''}$	Molecular weight of the δ" dangler
M_d	Molecular weight of the d dangler
M_Λ	Molecular weight of the Λ dangler
$M_{\Lambda'}$	Molecular weight of the Λ' dangler
$M_{\Lambda''}$	Molecular weight of the Λ" dangler
M_L	Molecular weight of the L dangler
M_m	Molecular weight of a mer
M_s	Molecular weight of a site
M_n	Molecular weight of the n^{th} polymer fragment
$M_{Pf'}$	Molecular weight of the semi-degraded bridge fragment
$M_{Pf''}$	Molecular weight of the fully-degraded bridge fragment
M_{Pf}	Molecular weight of the primary bridge fragment
n	Number of mers in a polymer fragment
$n - 1$	Number of bridges in a polymer fragment containing n mers
p	Population of intact bridges (p= Λ + Λ' + Λ" + L + C)
p_c	Critical bridge population, $p_c = 1/\sigma$, where an infinite network does not exist if $p \leq p_c$

Q_n	Probability that a given mer is a given member of a finite polymer fragment of n mers connected by s bridges on a site basis ($Q_n = F_n/n$)
$\sigma + 1$	Lattice coordination number
s	Number of bridges in a polymer fragment with n mers ($s = n - 1$)
TMP	Trimethylol propane mer
τ	Number of broken bridges on the perimeter of a polymer fragment containing n mers [$\tau = n(\sigma - 1) + 2$]

Miscellaneous Variables

A	Vapor pressure coefficient in Eq. (46) and Table 6.1
A_j	Pre exponential factor for the j^{th} reaction
bias	Discretization bias correction factor plotted in Fig. 8.9
B	Vapor pressure coefficient in Eq. (46) and Table 6.1
C	Vapor pressure coefficient in Eq. (46) and Table 6.1
C_p	Specific heat of the foam
D	Vapor pressure coefficient in Eq. (46) and Table 6.1
Δt	Time-step
Δt_{ave}	Average time-step
Δx	Average element dimension
E	Vapor pressure coefficient in Eq. (46) and Table 6.1
E_j	Activation energy for the j^{th} reaction
F	Total moles in the combined-phase sometimes referred to as the *feed*
Φ	Cumulative distribution function of a standardized normal random variable
Φ	Extent of the adipate bridge reaction ($\Phi = 1 - \frac{L}{L_o}$)
γ_i	Activity coefficient of the i^{th} species given by Eq. (42)
γ_i	Scaled sensitivity coefficient of the i^{th} species given by Eqs. (58) and (64)

Nomenclature

γ_i^2	Importance factor of the i^{th} species given by Eq. (66) and (73)
h_r	Reaction enthalpy of the foam
I_E	Interaction energy for the Regular Solution Model in Eq. (42)
I	Total number of species
J	Total number of reactions
k	Thermal conductivity of the foam (temperature dependency given in Table 7.2)
$k_{250°C}$	Measured conductivity at 250 °C
$k_{3500°C}^{\text{bias corrected}}$	Bias corrected extrapolated thermal conductivity at 3500 °C given by Eq. (67)
$k_{3500°C}^{\text{linear extrapolation}}$	Thermal conductivity linearly extrapolated to 3500 °C from experimental data
K_i	Ratio of mole fractions of two phases in equilibrium, equilibrium ratio, or *K-value*
k_j	Arrhenius reaction rate coefficient for the j^{th} reaction
$\overline{m}_i$	Mean value of the i^{th} CPUF model input parameter
$\overline{\mu}$	A vector representing the mean value of the CPUF model input parameters
μ_i	Mean value of the CPUF model input parameter
μ_{ij}	Concentration exponent matrix
μ_V	Mean decomposition front velocity
ν_{ij}	Stoichiometric coefficient matrix
N_i	i^{th} population variable
ν_{iL}	Pure species molal volume
P	Thermodynamic pressure
P_{c_i}	Critical pressure of the i^{th} species
P_i^*	Pure component vapor pressure of the i^{th} species at the system temperature, T, given by Eq. (46)
P_n^*	Pure component vapor pressure of the n^{th}-polymer fragment at the system temperature, T, given by Eq. (47)
P_{r_i}	Reduced pressure of the i^{th} species, $P_{r_i} = P / P_{c_i}$
q_j	Volumetric energy release for reaction j

Nomenclature

ρ	Foam density
ρ_o	Initial foam density
R	Gas constant
r_j	Rate expression for the j^{th} reaction
s_f^+	Solid fraction evaluated with the mean input parameters except for the ith parameter, which is set to the mean input parameter times 1.05
s_f^-	Solid fraction evaluated with the mean input parameters except for the ith parameter, which is set to the mean input parameter times 0.95
sf_i^{CPUF}	Solid fraction, initial solid mass divided by solid mass calculated with the CPUF model at various temperatures points i
sf_i^{HPTGA}	Solid fraction, initial solid mass divided by solid mass at measured in the HPTGA experiment at various temperatures points i
σ_i	Standard deviation of the i^{th} CPUF model input parameter
σ_E	Standard deviation of the activation energies
σ_V	Standard deviation of the decomposition front velocity
T	Temperature
T_o	Initial foam temperature
T_{c_i}	Critical temperature of the i^{th} species
T_{r_i}	Reduced temperature of the i^{th} species, $T_{r_i} = T \,/\, T_{c_i}$
V	Total moles in the vapor-phase given in Eq. (40)
V	Decomposition front velocity
ξ	Standardized normal random variable
x_i	Mole fraction in the liquid-phase
y_i	Mole fraction in the vapor-phase
z_i	Mole fraction in the combined-phase
$\overline{\zeta}$	A vector representing the mean value of all the CPUF input parameters
ζ_i	The i^{th} CPUF input parameter

ξ_i^+	1.05 times the i^{th} mean input parameter
ξ_i^-	0.95 times the i^{th} mean input parameter

CPUF – A CHEMICAL-STRUCTURE-BASED POLYURETHANE FOAM DECOMPOSITION AND FOAM RESPONSE MODEL

1. Introduction

This report describes the decomposition of rigid closed-cell polyurethane foam under a variety of conditions based on a model for using a kinetic bond-breaking scheme, lattice statistics, and vapor-liquid equilibrium. The Chemical-structure-based PolyUrethane Foam (CPUF) decomposition model simulates a cascade of bond-breaking reactions that produce CO_2. The bond-breaking scheme was implemented using percolation theory and a vapor-liquid equilibrium constraint to determine the vapor-liquid split based on individual vapor pressures of the polymer fragments. The progress of the cascading reaction scheme depends on whether or not the decomposition products remain in contact with the degrading foam. If the decomposition products are confined, decomposition pathways favor increased CO_2 yields and decreased toluene diisocyanate (TDI) yields. If the decomposition products are removed from the system via venting or via a carrier gas, CO_2 yields are lower and TDI yields are relatively high. This report describes the methods used to determine the various CPUF model parameters, several sensitivity and uncertainty analyses of the CPUF model, and a discretization bias correction needed for multidimensional problems. The report also includes some validation of the CPUF model by comparing predictions with several experiments at different scales from different laboratories.

2. Background

The Engineering Sciences Center's foam material response program began in 1995 with the goal to develop a high fidelity computational tool for fire-induced response of systems containing rigid, closed-cell polyurethane foam encapsulants. The foam was used to encapsulate components that were confined in an external metal enclosure (skin). Smoldering combustion may exist if the skin has multiple openings where air can be drawn into the system. Response of the system includes the combined thermal, chemical, and mechanical response of the foam, components, and the enclosure.

Rigid polyurethane foams are used as encapsulants to thermally isolate and mechanically support components within weapon systems. When exposed to abnormal thermal environments, such as fire, various encapsulated components are designed to fail sequentially. In high consequence nuclear hazards analysis, the thermal response of the encapsulated components may be highly dependent on the behavior of the foam. Modeling foam decomposition is a difficult problem not only because of the numerical challenges associated with steep reaction fronts but also because of the difficulty of describing important chemical and physical processes, such as fluid flow. In the current report, thermal transport and chemical decomposition are discussed in detail. The quantitative effects of mass transport, species diffusion, bubble mechanics, fluid flow, and gravitational effects are beyond the scope of this report. However, experiments are discussed that show the importance of these various phenomena.

Prior to 1995, simplifying assumptions regarding foam decomposition were made when predicting the thermal response of encapsulated components. For example, the decomposition of foam was ignored by assuming the foam was not present and adjusting surface emissivity to match thermocouple data, or by changing physical properties of the foam at prescribed tempera-

tures. Such simplifying approximations were necessary given the computational limitations of the day. With the advent of massively parallel computers, high-consequence predictions of foam decomposition can be made with a more fundamental foam decomposition model founded on experimental observations to determine accurate decomposition rates, decomposition species, and physical properties of the evolving solid residue.

Computational models used in hazards analysis at SNL are designed to accommodate mass loss associated with foam decomposition. For example, Fig. 2.1 shows a COYOTE [6] finite element calculation of a block of material containing inert components of various shapes exposed to a constant energy flux. In this calculation, the encapsulating material was assumed to

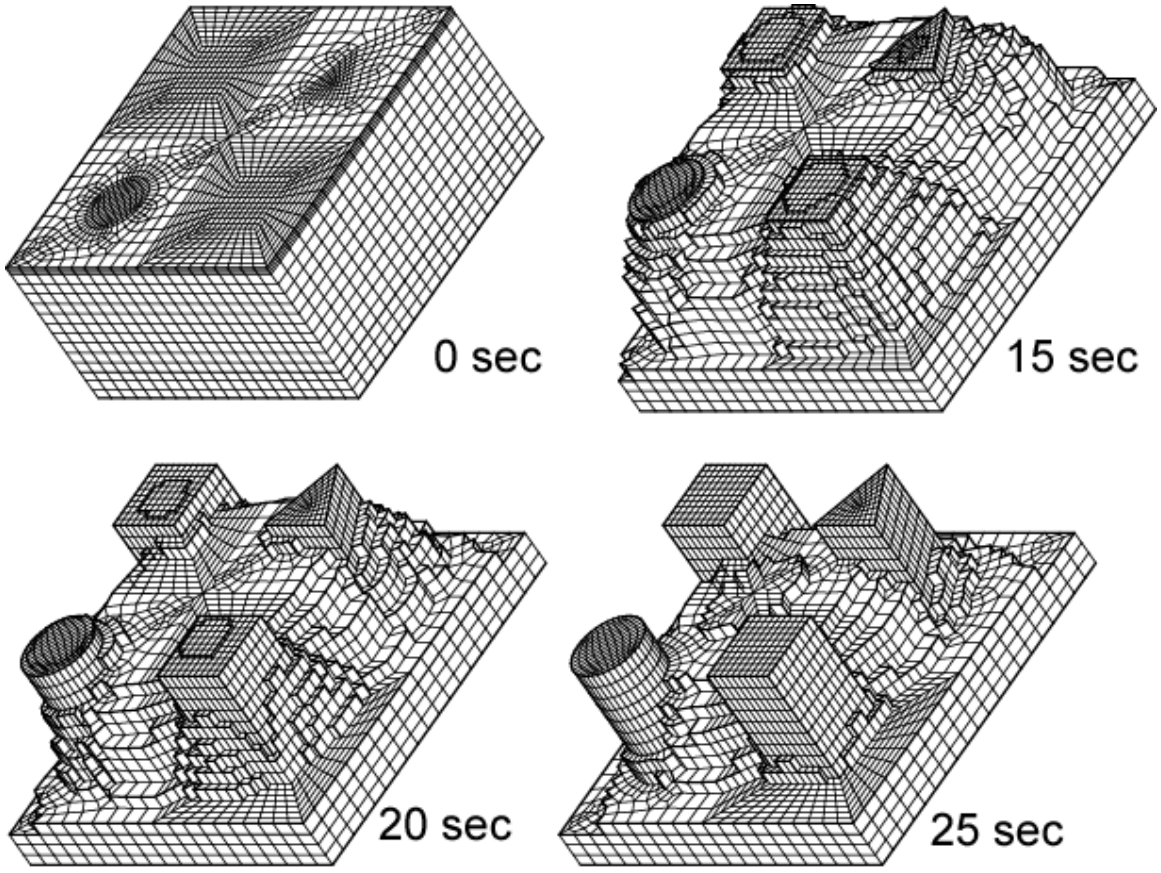

Fig. 2.1. Example calculation of inert components encapsulated in rigid polyurethane foam initially at 100°C exposed to a constant flux on the entire exposed surface. Elements were removed when element temperature exceeded 150°C. Although foam regression is shown as a function of time, a decomposition model was not used for this calculation. Figure used with permission from Gartling [6].

decompose by removing elements from the computational domain based on the element exceeding a specified temperature, without using a realistic decomposition mechanism. Actual tests of polyurethane foam exposed to abnormal thermal environments, such as fire, show the system response to be more complex.

Several groups studying the decomposition of large macromolecules have employed statistical network fragmentation models to describe decomposition chemistry. For example, Solomon and coworkers [9] have implemented a computationally intensive Monte Carlo technique to describe the breakup of coal. Grant et al. [10-12] have used pseudo lattice structures referred to as *Bethe lattices* (or *Cayley trees*) to obtain closed-form solutions of the network statistics as derived by Fisher and Essam [13]. These closed form solutions parallel the determination of molecular weight distributions during polymer synthesis leading to the critical condition required to form infinite polymer networks referred to as “gels” by Flory [14]. In the present report, Flory’s methods of building polymers are used to decompose polymers by assuming that closed rings or cycles cannot form and that bond reactivity depends on the extent of reaction or thermal degradation. Bond breaking is considered a random scission process that describes the extent of reaction. This method was used by Hobbs et al. [1,2] to describe decomposition of unconfined polyurethane foam. The method has also been used by Hobbs [15] to describe decomposition of the crystalline explosive, HMX (octahydro-1,3,5,7-tetranitro-1,3,5,7-tetrazocine) by assuming the energetic material is composed of an infinite network of sites connected by intermolecular attractions and chemical bonds.

The next section describes the chemical structure of the polyurethane foam, which is primarily taken from Hobbs et al. [1,2] since the same polyurethane foam was used in the previous study. Section 4 describes the chemical mechanism used to describe bond breaking. Section 5 presents the details of the lattice statistics using percolation theory as applied to bond

breaking. Section 6 describes the vapor-liquid equilibrium model used to determine the split between liquid species and gas species. Section 7 describes the methods used to determine the model parameters, which include thermophysical properties, lattice properties, and chemistry parameters. Section 8 presents data and predictions of small-scale thermogravimetric analysis (TGA) at various levels of pressure and confinement. Section 8 also describes several uncertainty quantification methods used to obtain mean responses with 95% prediction intervals. Section 9 presents mesh independent decomposition front velocities calculated with the CPUF foam response model. A subgrid model used to predict grid-size-independent decomposition velocities is also discussed in Section 9. Section 10 describes the component-scale radiant heat experiments. Decomposition front velocities determined using X-rays taken at regular intervals were used to determine front velocities for some of the radiant heat experiments. Section 11 presents CPUF simulations of 19 radiant heat experiments to show the effects of the 1) heat flux at two different densities, 2) orientation of the heated surface with respect to the gravity vector, 3) embedded components on the decomposition front for both high and low density foams, 4) confinement and backpressure. Predicted locations of the decomposition front are presented as solid fraction contours overlaying X-rays at selected times for the 19 RPU radiant heat experiments. Some general remarks close the report in a summary and conclusions section.

3. Chemical Structure of RPU Foam

Detailed information regarding the chemical structure of polyurethane foam is required to predict foam decomposition using lattice statistics. The structural units and resulting polymeric network of many synthesized macromolecules, such as polyurethane foam, can be inferred from the starting materials and the synthesis method used to make the macromolecule. Confirmation of the structure is often obtained using IR, solid-state NMR [16], and other analytical techniques.

The most common chemical structural units of the rigid polyurethane foam and the distribution of these structural units are shown in Figs. 3.1 and 3.2. These structural units were estimated using proprietary synthesis details by assuming equal reactivity of the hydroxyl groups. Various graphic representations of specific chemical structural units are also shown in Fig. 3.1. These structural units have been assembled to give a representative picture of the foam. The model foam shows the polyurethane structure as a large matrix (essentially infinite) of primary sites composed of trimethylol propane (TMP) and secondary sites composed of diethylene glycol (DEG) connected by primary bridges associated with toluene diisocyanate (TDI) and secondary bridges associated with adipic acid (AA), and small amounts of phthalic anhydride. The structural units depicted in Figs. 3.1 and 3.2 are only representative structures. Rather than relating specific structural units to the ingredients used in synthesizing the polymer (e.g. adipic acid, phthalic anhydride, etc.) it is probably more accurate to refer to these structural units as polymer fragments, which is discussed in more detail later in the report.

Figure 3.2 shows the three most common structural units divided into sites and bridges. The coordination number at each site used to determine the average coordination number of the lattice structure is also shown in Fig. 3.2. The average molecular weight of the sites and bridges

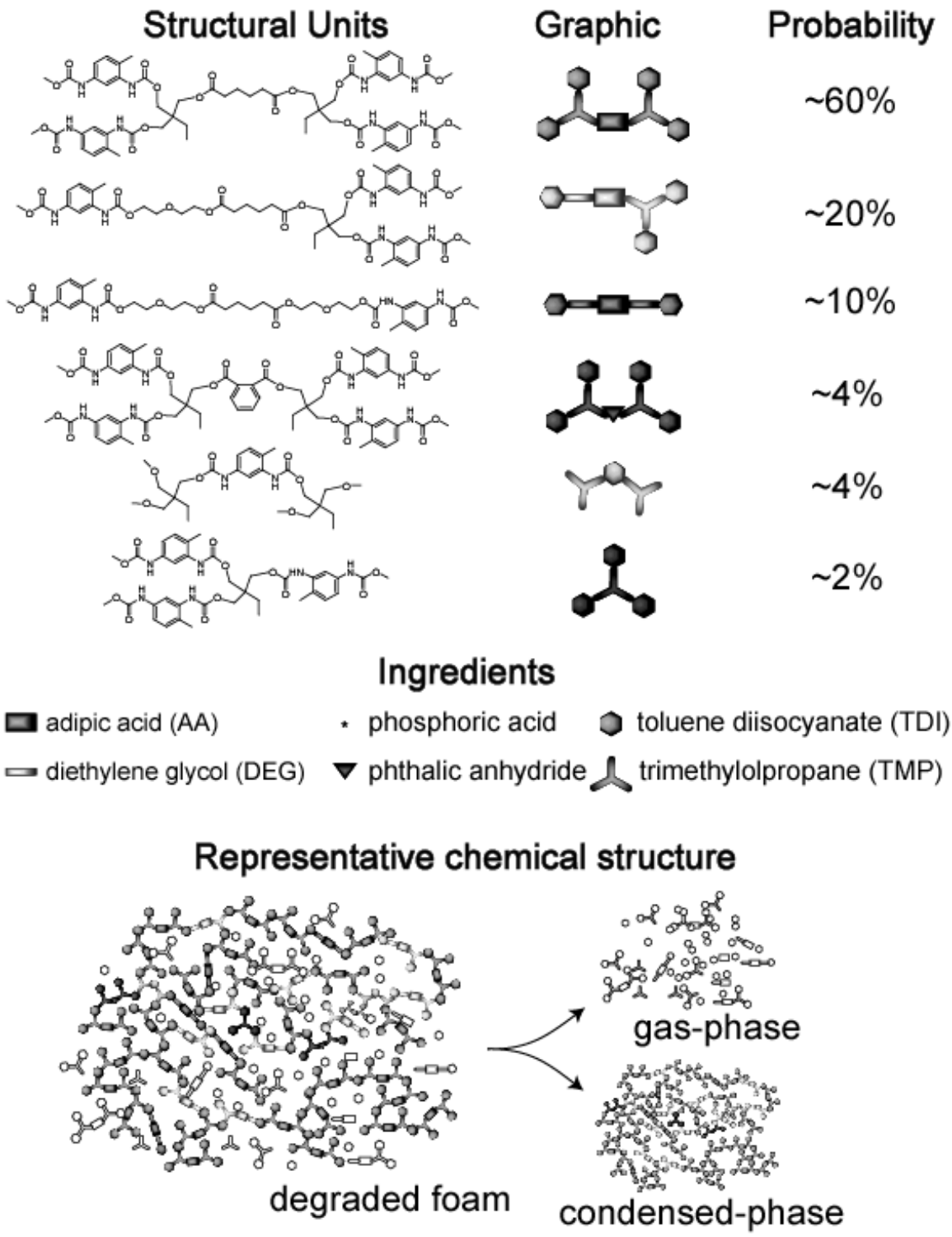

Fig. 3.1. Most common chemical structural units and hypothetical chemical structure of rigid polyurethane foam. The graphic symbols represent ingredients used to make the specific foam.

A) 60% most probable structural unit of a rigid polyurethane foam

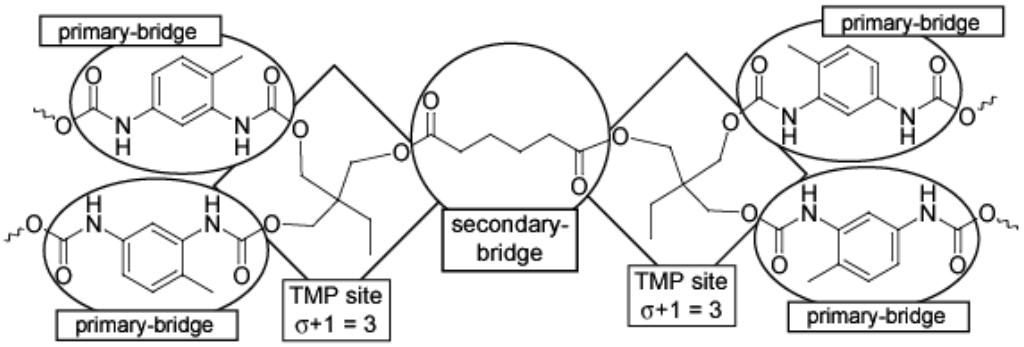

B) 20% most probable structural unit of a rigid polyurethane foam

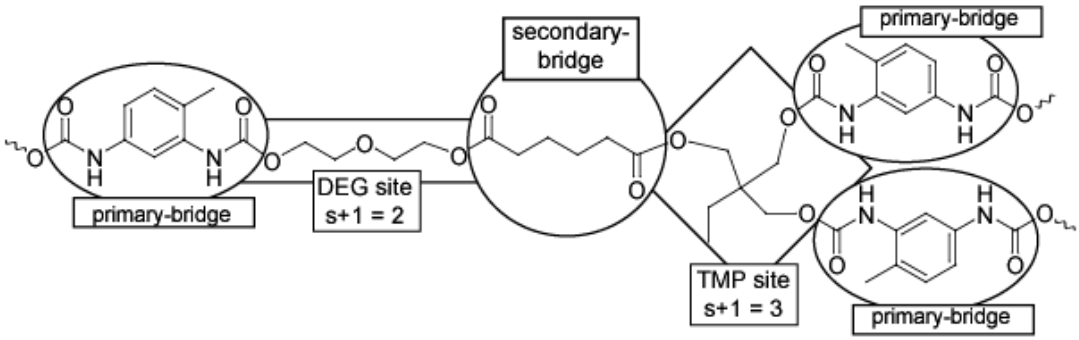

C) 10% most probable structural unit of a rigid polyurethane foam

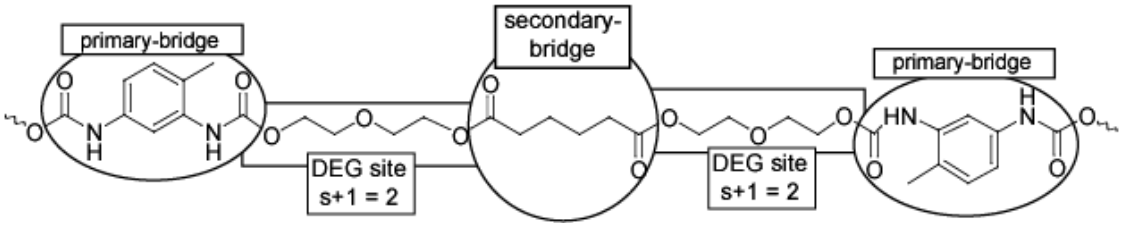

Fig. 3.2. Three most common structural units of a rigid polyurethane foam showing boundaries used to relate chemical structure to a Bethe lattice.

can also be determined from the chemical structure as discussed further in Section 7. In the present report, the site composition is determined from the average TMP-mer and DEG-mer composition. The bridges are composed of the primary (TDI) and secondary (AA) bridge structures.

Although the specification of the RPU foam into bridges and sites is somewhat arbitrary, the division between the sites and bridges is based on several experimental observations. For example, Fig. 3.3.A shows two bond types that likely break during thermal decomposition: 1) the ester bond of the carbamate group and 2) the ether bond of the ester group. Experimental evidence of bond type 1 breaking is shown in Fig. 3.3.B, where IR spectra of decomposition gases obtained using isothermal TGA-FTIR analysis shows a strong signal in the ~N=C=O stretch region of the IR spectra (wave number 2250) from evolving gases sampled at 350°C, 400°C, and 450°C [3-4]. Figure 3.3.B also shows the initial pristine foam with a modest signal in the ~N=C=O stretch region that is due to some unreacted isocyanide groups in the initial foam. Furthermore, solid-state NMR results, shown in Fig. 3.3.C, show the depletion of the carbonyls associated with the adipic acid and isocyanate structure. The NMR results are consistent with the bonds labeled 1 and 2 breaking. Although additional information regarding decomposition chemistry is evident in the NMR data, complete analysis was not available.

As bonds break at elevated temperatures, polymer fragments are generated. The fragments, with low molecular weights and corresponding high vapor pressures, evaporate to form gaseous polymer fragments as shown at the bottom of Fig. 3.1. Higher molecular weight fragments, with low vapor pressures, remain in the condensed phase.

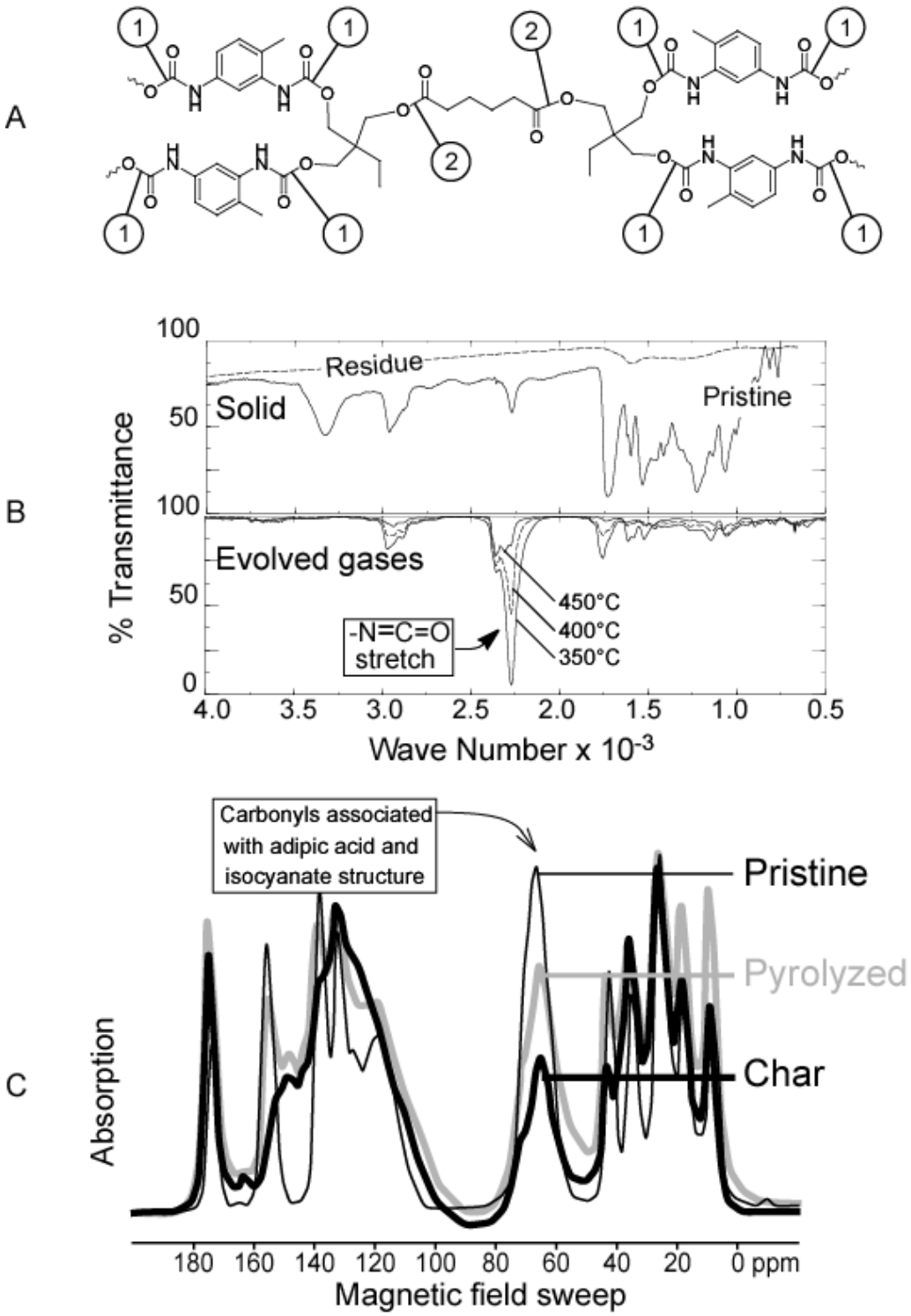

Fig. 3.3. A) Most probable chemical structure showing two possible weak bonds labeled 1 and 2. B) FTIR spectra showing evidence of urethane bond rupture. C) Solid-state NMR evidence showing change in carbonyls associated with adipic acid and isocyanate structures. Other information available in the NMR data has not been fully analyzed.

Chemical Structure of RPU Foam

4. Kinetic Mechanism

Figure 4.1 shows the decomposition behavior of a 4-mg sample of rigid polyurethane foam (RPU) heated at 20 °C/min in the HPTGA at ambient pressure. The initial decomposition between 250°C and 350°C was originally modeled by Hobbs et al. [1,2] as decomposition of a primary polymer forming various gases and a thermally stable secondary polymer. The secondary polymer was assumed to decompose at temperatures above 350°C at a different rate. This approach, which gave a percent RMS error between measured and predicted mass loss of about 8%, is probably adequate for unconfined decomposition where the reaction products are either vented or swept away by a purge gas. To get better agreement between measured and predicted mass loss for use in the foam response model, the CPUF bond breaking mechanism was formulated by assuming that the polymer was initially composed of primary and secondary bridges as well as primary and secondary sites. The primary bridges were allowed to degrade

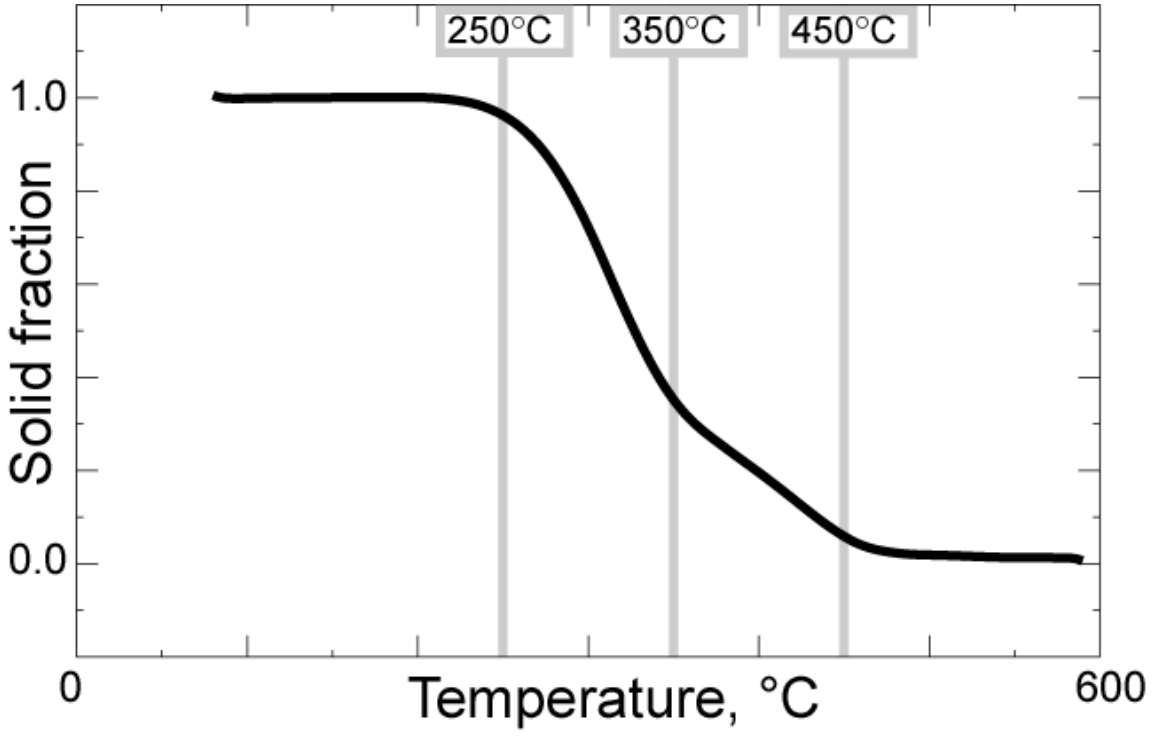

Fig. 4.1. HPTGA mass loss history for RPU foam at 1 bar ramped 20°C/min.

into other bride-types by evolution of CO_2. The CPUF mass loss mechanism gives a percent RMS error of about 2% between measured and calculated mass loss.

The CPUF bond-breaking mechanism is shown in Fig. 4.2 with the chemical symbols defined in the Nomenclature Section and further in Fig. 4.3. The CPUF mechanism describes various reactions associated with degradation of the primary bridges that were shown in Fig. 3.2 in ovals and the secondary bridges, which were shown in circles. The confinement affects, such as enhanced CO_2 generation, are primarily associated with alternate reaction pathways involving the primary bridge structure.

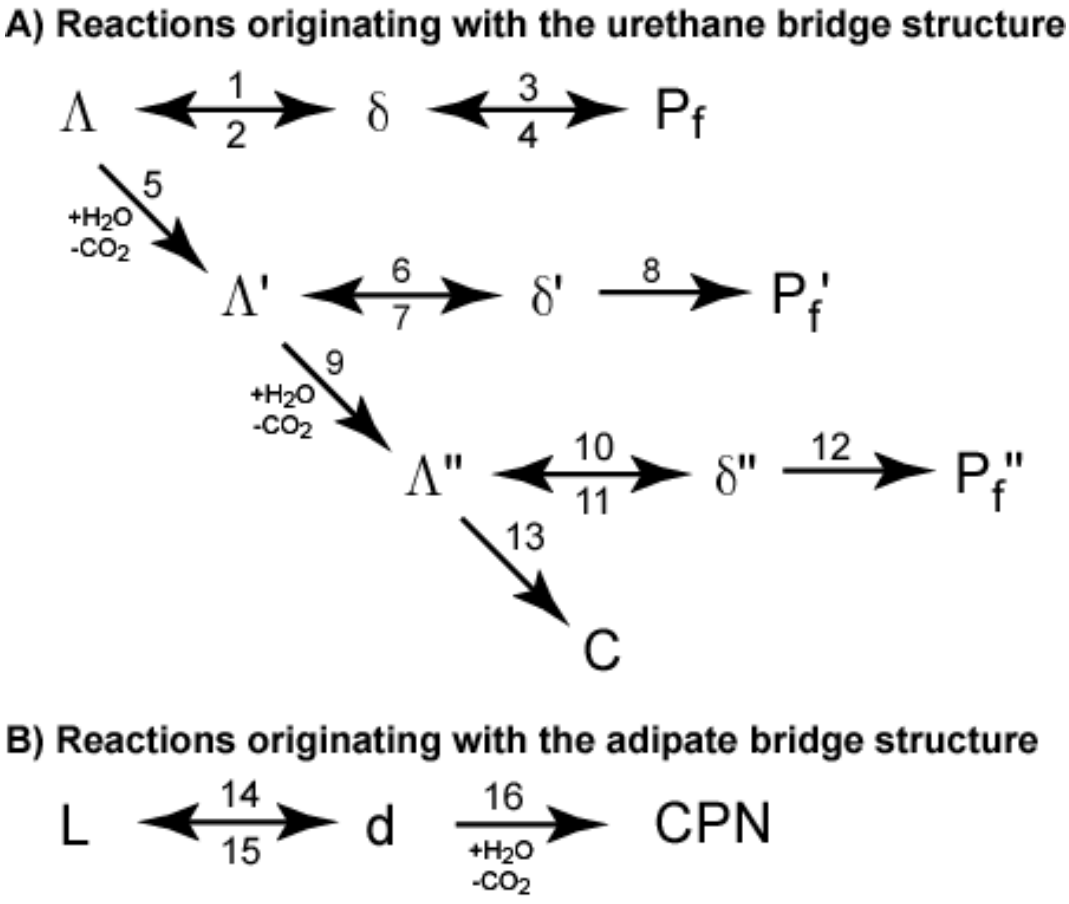

Fig. 4.2. Simplified CPUF reaction mechanism.

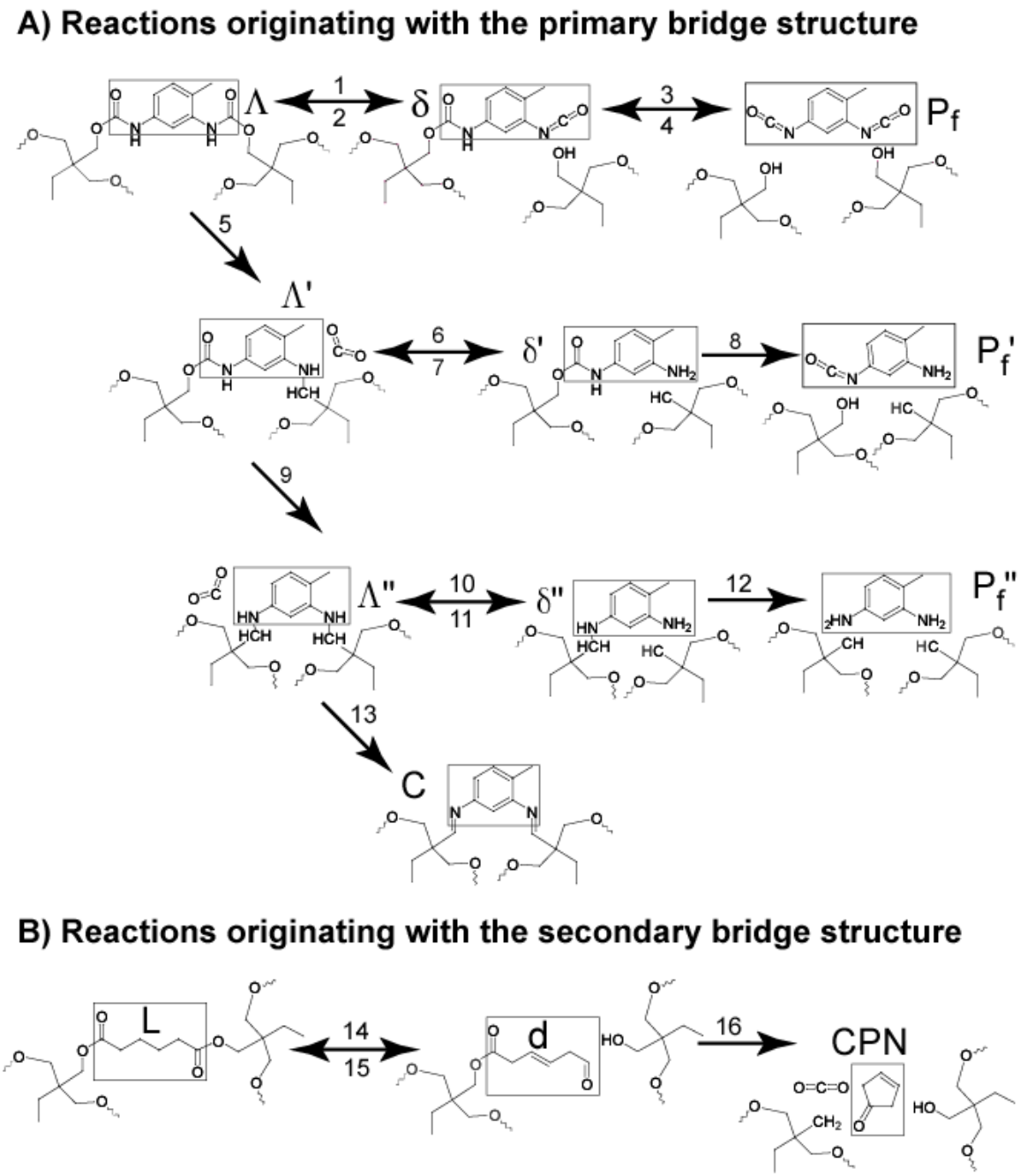

Fig. 4.3. Detailed PCUF reaction mechanism. Specific detail of the polymer structure is shown for illustration purposes only.

The CPUF mechanism consists of sixteen reactions and fifteen "species" that include five bridges (Λ, Λ', Λ", C, and L), four danglers (δ, δ', δ", d), and six polymer fragments (P_f, P_f', P_f", CPN, CO_2, H_2O). The term CPN denotes C_5 oxygen-containing fragments, such as cyclopentanone, that originate from bond scission at the adipate linkage. Quotation marks are used with "species" since bridges and danglers are not typically referred to as species. Rather, the bridges and danglers are population variables that can be used with the percolation lattice statistics discussed further in Section 5. Quotation marks are also used with the term "polymer fragments" since H_2O is not actually gaseous water. Rather, the H_2O in Fig. 4.2 accounts for a transfer of hydrogen and oxygen from the mer sites to the bridges. The single quotation mark (') is used to represent the conversion of one of the primary bridges into an semi-degraded bridge that has lost a CO_2. If the semi-degraded bridge loses another CO_2 molecule, the semi-degraded bridge becomes a fully-degraded bridge (Λ"). The double quotation mark (") represents the loss of CO_2 molecules. The fully-degraded bridge can become thermally stable by the formation of an unbreakable-bridge, C.

The reaction sequence begins when a weak bond – *e.g.* the ether bond of the carbamate group connecting one end of a primary bridge (Λ) to a trimethylol propane (TMP) mer – is broken to form a primary side-chain (δ) as indicated by reaction step 1 in Fig. 4.3. The primary side-chain, δ, may either reattach to the TMP mer (reversible reaction step 2) or evolve as primary polymer fragment, P_f, (reaction step 3). Reaction steps 1 and 3 were shown via sensitivity analysis by Hobbs et al. [1,2] to be dominant reaction steps for the PUF decomposition model. During confined decomposition, the primary polymer fragment, P_f, can reattach to the degrading foam as shown in Fig. 4.3 by the reversible reaction step 4. The kinetics for reaction step 4 were obtained by assuming the primary polymer fragment was in *local equilibrium* in a closed system since the

current FEM formulation does not consider species transport between integration points. A generalized mass balance constraint has been formulated by Clayton [8] to make reaction step 4 dependent on the TDI concentration in an open system. Clayton's formulation requires the TDI balance to be determined within the dynamically developing enclosure as well as within the decomposing polymer.

The dominant decomposition pathways associated with the primary-bridge structures change when foam is decomposed under significant confinement such as in hermetically sealed devices producing more CO_2. The lower molecular weight products result in higher pressurization rates that may lead to early breach of confinement. Decomposition under confinement may also lead to significant crosslinking (*e.g.* reaction 13) and higher yields of carbonaceous residues.

In Fig. 4.2, reactions 5 and 9 show an increase in H_2O and a decrease in CO_2. The CO_2 refers to an evolving CO_2 gas molecule; however, the H_2O does not refer to gaseous water. Rather, the H_2O is used to track mass continuity between mers, bridges, and gases. The two hydrogen atoms are reclassified from a site-basis to a bridge-basis to allow the eventual formation of a bridge or dangler without CO_2. Reclassification of hydrogen is not necessary for the formation of the primary polymer fragment since the hydrogen bonded to the nitrogen is originally classified as part of the site rather than the bridge. The $+H_2O$ in Fig. 4.2 refers to two hydrogen atoms and an oxygen atom transferred to the bridge. With the additional oxygen, the bridge can evolve a CO_2 molecule depicted as $-CO_2$ in Fig. 4.2. Material balances are enforced in the CPUF model by population balances that are discussed further in Section 5. Clayton [8] avoids the added complexity of transferring atoms between sites and bridges by letting broken bridges form two side chains. The side chains can be as large as the primary polymer fragment danglers or as small as an electron forming a radical.

Table 4.1. Mechanism, rate equations, and initial conditions for the CPUF model*

Rxn	*Mechanism*	*Species*	*Rate Equations*	*Initial Conditions*
(1)	$\Lambda \rightarrow \delta$	Λ	$d\Lambda/dt = -k_1\Lambda + k_2\delta - k_5\Lambda H_2O$	$\Lambda(0) = \Lambda_o = 0.78$
(2)	$\delta \rightarrow \Lambda$	Λ'	$d\Lambda'/dt = +k_5\Lambda H_2O - k_6\Lambda' + k_7\Lambda' - k_9\Lambda' H_2O$	$\Lambda'(0) = 0$
(3)	$\delta \rightarrow P_f$	Λ"	$d\Lambda''/dt = +k_9\Lambda' H_2O - k_{10}\Lambda'' + k_{11}\delta'' - k_{13}\Lambda''$	$\Lambda''(0) = 0$
(4)	$P_f \rightarrow \delta$	C	$dC/dt = +k_{13}\Lambda''$	$C(0) = 0$
(5)	$\Lambda + H_2O \rightarrow \Lambda' + CO_2$	L	$dL/dt = -k_{14}L + k_{15}d$	$L(0) = L_o = 0.22$
(6)	$\Lambda' \rightarrow \delta'$	δ	$d\delta/dt = +k_1\Lambda - k_2\delta - k_3\delta + k_4 P_f$	$\delta(0) = 0$
(7)	$\delta' \rightarrow \Lambda'$	δ'	$d\delta'/dt = +k_6\Lambda' - k_7\delta' - k_8\delta'$	$\delta'(0) = 0$
(8)	$\delta' \rightarrow P_f'$	δ"	$d\delta''/dt = +k_{10}\Lambda'' - k_{11}\delta'' - k_{12}\delta''$	$\delta''(0) = 0$
(9)	$\Lambda' + H_2O \rightarrow \Lambda'' + CO_2$	d	$dd/dt = +k_{14}L - k_{15}d - k_{16}dH_2O$	$d(0) = 0$
(10)	$\Lambda'' \rightarrow \delta''$	P_f	$dP_f/dt = +k_3\delta - k_4 P_f$	$P_f(0) = 0$
(11)	$\delta'' \rightarrow \Lambda''$	P_f'	$dP_f'/dt = +k_8\delta'$	$P_f'(0) = 0$
(12)	$\delta'' \rightarrow P_f''$	P_f''	$dP_f''/dt = +k_{12}\delta''$	$P_f''(0) = 0$
(13)	$\Lambda'' \rightarrow C$	CPN	$dCPN/dt = +k_{16}dH_2O$	$CPN(0) = 0$
(14)	$L \rightarrow d$	CO_2	$dCO_2/dt = +k_5\Lambda H_2O + k_9\Lambda' H_2O + k_{16}dH_2O$	$CO_2(0) = 0$
(15)	$d \rightarrow L$	H_2O	$dH_2O/dt = -k_5\Lambda H_2O - k_9\Lambda' H_2O - k_{16}dH_2O$	$H_2O(0) = 1$
(16)	$d + H_2O \rightarrow CPN + CO_2$			

*The concentration (μ_{ij}) and stoichiometric matrices (ν_{ij}) with the reactions loaded into 16 columns (J = 16) and the species loaded into 15 rows (I = 15) are written as:

$\mu_{ij} =$

	r_1	r_2	r_3	r_4	r_5	r_6	r_7	r_8	r_9	r_{10}	r_{11}	r_{12}	r_{13}	r_{14}	r_{15}	r_{16}
Λ	1	0	0	0	1	0	0	0	0	0	0	0	0	0	0	0
Λ'	0	0	0	0	0	1	0	0	1	0	0	0	0	0	0	0
Λ"	0	0	0	0	0	0	0	0	0	1	0	0	1	0	0	0
C	0	0	0	0	0	0	0	0	0	0	0	0	0	0	0	0
L	0	0	0	0	0	0	0	0	0	0	0	0	0	1	0	0
δ	0	1	1	0	0	0	0	0	0	0	0	0	0	0	0	0
δ'	0	0	0	0	0	0	1	1	0	0	0	0	0	0	0	0
δ"	0	0	0	0	0	0	0	0	0	0	1	1	0	0	0	0
d	0	0	0	0	0	0	0	0	0	0	0	0	0	0	1	1
P_f	0	0	0	1	0	0	0	0	0	0	0	0	0	0	0	0
P_f'	0	0	0	0	0	0	0	0	0	0	0	0	0	0	0	0
P_f"	0	0	0	0	0	0	0	0	0	0	0	0	0	0	0	0
CPN	0	0	0	0	0	0	0	0	0	0	0	0	0	0	0	0
CO_2	0	0	0	0	0	0	0	0	0	0	0	0	0	0	0	0
H_2O	0	0	0	0	1	0	0	0	1	0	0	0	0	0	0	1

$\upsilon_{ij} =$

	r_1	r_2	r_3	r_4	r_5	r_6	r_7	r_8	r_9	r_{10}	r_{11}	r_{12}	r_{13}	r_{14}	r_{15}	r_{16}
$d\Lambda/dt$	–1	1	0	0	–1	0	0	0	0	0	0	0	0	0	0	0
$d\Lambda'/dt$	0	0	0	0	1	–1	1	0	–1	0	0	0	0	0	0	0
$d\Lambda''/dt$	0	0	0	0	0	0	0	0	1	–1	1	0	–1	0	0	0
dC/dt	0	0	0	0	0	0	0	0	0	0	0	0	1	0	0	0
dL/dt	0	0	0	0	0	0	0	0	0	0	0	0	0	–1	1	0
$d\delta/dt$	1	–1	–1	1	0	0	0	0	0	0	0	0	0	0	0	0
$d\delta'/dt$	0	0	0	0	0	1	–1	–1	0	0	0	0	0	0	0	0
$d\delta''/dt$	0	0	0	0	0	0	0	0	0	1	–1	–1	0	0	0	0
dd/dt	0	0	0	0	0	0	0	0	0	0	0	0	0	1	–1	–1
dP_f/dt	0	0	1	–1	0	0	0	0	0	0	0	0	0	0	0	0
dP_f'/dt	0	0	0	0	0	0	0	1	0	0	0	0	0	0	0	0
dP_f''/dt	0	0	0	0	0	0	0	0	0	0	0	1	0	0	0	0
$dCPN/dt$	0	0	0	0	0	0	0	0	0	0	0	0	0	0	0	1
dCO_2/dt	0	0	0	0	1	0	0	0	1	0	0	0	0	0	0	1
dH_2O/dt	0	0	0	0	–1	0	0	0	–1	0	0	0	0	0	0	–1

Table 4.1 gives the mechanism, rate equations, and initial conditions for the CPUF model. The general reaction rate, r_j, for the CPUF model bond-breaking scheme is described by:

$$r_j = k_j(T)\prod_{i=1}^{I} N_i^{\mu_{ij}}, j = 1,...J, \quad (1)$$

where N_i represents either bridge populations Λ, Λ', Λ", C, L; dangler populations δ, δ', δ", d; polymer fragments P_f, P_f', P_f", CPN, CO_2, or the H_2O population used for continuity constraints. The H_2O population is used in the rate equations for reactions 5, 9, and 16 to stop these reactions when hydrogen becomes unavailable for reaction. The expressions for the kinetic coefficients, $k_j(T)$, are given in an Arrhenius form:

$$k_j(T) = A_j \exp(-E_j / RT), \tag{2}$$

where A_j (1/s), E_j (cal/mol or J/mol), and R (1.987 cal/mol-K or 8.314 J/mol-K) are the pre-exponential factors, activation energies, and the universal gas constant, respectively. In the current report, the activation energy, E_j, is assumed to be normally distributed as discussed further in Section 7.3. The rate of change of the population variables is given by:

$$dN_i / dt = \sum_{j=1}^{J} \upsilon_{ij} r_j \text{ , } i = 1, \ldots I, \tag{3}$$

where ν_{ij} are the stoichiometric coefficients of the j^{th} reaction as given in the footnote of Table 4.1. The kinetic mechanism requires the Arrhenius parameters, A_j and E_j, to be supplied for each reaction. The initial populations, which are related to the extent of curing, are also given in Table 4.1. The initial value problem described by Eq. (1)-(3) can be solved using a variable-order, backward-difference ordinary differential equation (ODE) solver package [17].

5. Lattice Statistics

Percolation theory has been used historically to describe fluid flow through a network of permeable and impermeable sites. To describe thermal decomposition, the permeable and impermeable sites are related to broken or unbroken bonds. Details of using percolation theory for foam decomposition has been documented in detail by Hobbs et al. [1,2] and only the specific details related to implementation of the CPUF model are given in this report. Reference [1] should be consulted for more detail on the general implementation of chemistry decomposition models using percolation theory.

Percolation theory using Bethe lattices was used to characterize the degraded foam structure with regard to the size and population of finite polymer fragments. Bethe lattices are "tree-like" structures, where sites continually branch to other sites. The sites do not contain "loop-backs" where one branch reconnects to the original site. "Loop-backs" occur when two sites are connected by more than one bridge.

The population variables determined from the kinetic mechanism can be used to determine the fraction of sites that are connected by bridges. For example, the fraction of intact bridges, *p*, can be determined as follows:

$$p = \Lambda + \Lambda' + \Lambda'' + C + L \tag{4}$$

The mass fraction of finite polymer fragments produced from the thermally degrading foam depends on the population of intact bridges, *p*, determined from the kinetic mechanism and the coordination number, $\sigma + 1$. The lattice statistics are independent of the type of bridges connecting sites provided the bridges are distinguished as either broken or intact. Thus, percolation theory

can be used with any kinetic mechanism provided the population of broken bridges (1 - *p*) or intact bridges (*p*) is determined [10]. As the number of broken bridges increases, the fraction of sites belonging to finite polymer fragments increases relative to the fraction of sites belonging to the infinite network. The infinite network no longer exists below a critical bridge population of $1/\sigma$ as shown by Fischer and Essam [13]. For a cluster to propagate indefinitely from a given intact bridge, the adjoining site must contain a least one other intact bridge. Since *p* is the probability that a bridge is intact and σ bridges radiate from the adjoining site, an infinite cluster exists only when $\sigma p_c > 1$ or $p_c > 1/\sigma$.

For Bethe lattices, the number of finite polymer fragments can be determined from the coordination number and the bridge population, *p*. The probability, F_n, that any given site is a given member of a finite polymer fragment of *n* sites with *s* bridges is

$$F_n = a_n p^s (1-p)^\tau , \tag{5}$$

where

$$s = n - 1 \tag{6}$$

and

$$\tau = n(\sigma - 1) + 2. \tag{7}$$

τ is the number of broken bridges on the perimeter of the polymer fragment with *s*-bridges connecting *n*-sites as shown for the dimer in Fig. 5.1. The number of different ways to form such fragments is represented by a_n [10]:

$$a_n = \frac{(\sigma+1)\Gamma(n\sigma+2)}{(n\sigma+1)\Gamma(n)\Gamma[n(\sigma-1)+3]} \tag{8}$$

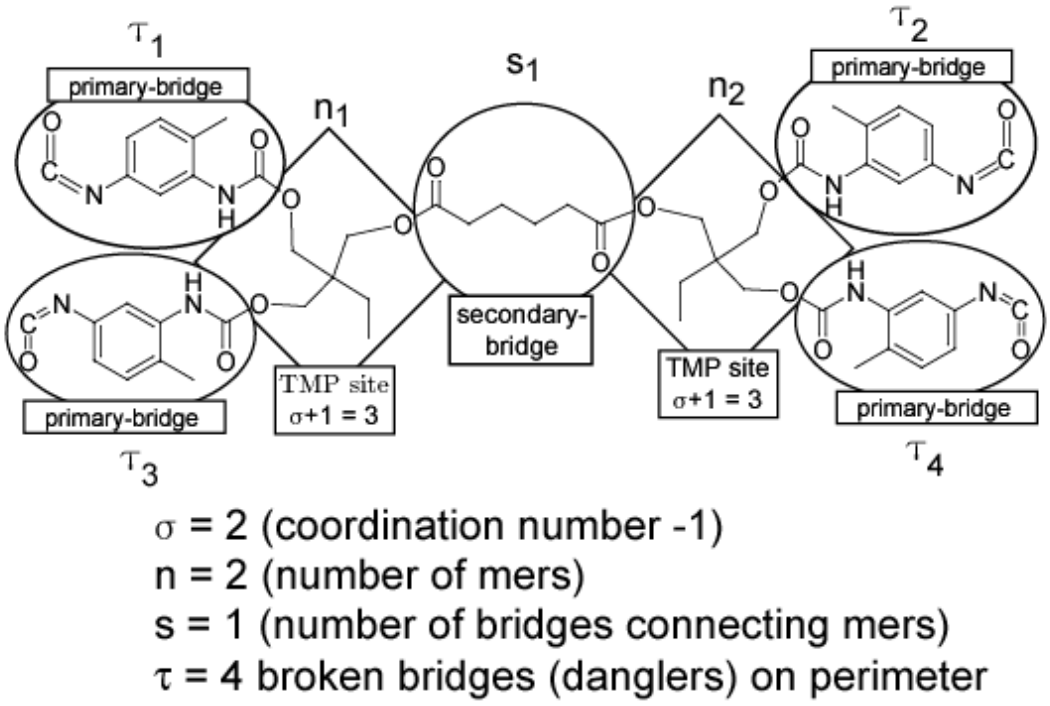

Fig. 5.1. Dimer showing s, n, s,, and t.

where Γ represents the standard gamma function. Equation (5) formally states that the probability that any given bridge belongs to an *n*-mer is the probability that the given bridge is intact or occupied (p^s) multiplied by the probability that the nearest neighbor bridges are broken or unoccupied $(1-p)^\tau$ with a_n accounting for the distinct number of configurations possible for the *n*-mer. Equations (5)-(8) are discussed more in Ref. [1].

The mass fraction and molecular weight of polymer fragments can be determined by relating the total mass and mass associated with the finite polymer fragments on a site basis. Up to this point, a site has been loosely defined as either the trimethylol propane (TMP) mer highlighted with a diamond shape in Fig. 5.1 or a diethylene glycol (DEG) mer enclosed within a long rectangle shape as shown in Fig. 3.2. Such definitions are convenient when discussing various structural components (*e.g.* TMP and DEG) connected by various bridge types (Λ, Λ', Λ", C and L). However, to determine the weight fraction of each polymer fragment, a more precise definition is

needed. An “extended” site is defined in this report to include not only the statistically averaged TMP and DEG mer units but also part of the bridge units. The total mass per “extended” site is:

$$m_t = M_m + \frac{(\sigma+1)}{2}\sum_A M_A A_o \,, \tag{9}$$

The symbol *A* in Eq. (9) is defined as *all* of the populations: Λ, Λ’, Λ”, C, L, δ, δ’, δ”, d, P_f, P_f’, P_f”, and CPN; where the sum over all population is unity ($\Sigma_A A$ = 1). M_m is the average molecular weight of the TMP and DEG units, M_A is the molecular weight of the population *A*, and σ+1 is the coordination number. The subscript *o* in Eq. (9) refers to the initial state of the various populations. Equation (9) was written for a closed system, such as a batch reactor, where influx and efflux of polymer fragments were not considered. A more general equation is necessary to allow influx and efflux of polymer fragments associated with confined decomposition [8]. In a finite element formulation, each element should be able to treat flow between elements with the exit stream composition the same composition as the mixture within the element, similar to a constant stirred reactor (CSTR) formulation. Since the general framework of the FEM does not allow influx or efflux of polymer fragments between elements, Eq. (9) is *sufficiently rigorous* to implement the CPUF kinetic mechanism into COYOTE or CALORE. However, a more general formulation is necessary to capture the effect of liquefaction induced by formation and flow of polymer fragments that act as solvating molecules. Such a model could be solved in a heat conduction code that incorporates flow effects at considers dynamic radiation enclosures. Currently there are no models that can accommodate all of the required, tightly coupled physical phenomenology.

The mass of the various populations on an “extended” site basis is given by

$$m_A = \tfrac{\sigma+1}{2}(M_A A). \tag{10}$$

The mass of the CO_2 is treated differently since the CO_2 gas is derived from the other populations. The CO_2 mass can be determined by an overall continuity balance as

$$m_{CO_2} = \frac{\sigma+1}{2}\left(\sum_A M_A A_o - \sum_A M_A A\right). \tag{11}$$

The mass fraction of various decomposition gases can be obtained directly from Eqs. (9), (10), and (11) as follows:

$$f_A = m_A / m_t \tag{12}$$

$$f_{CO_2} = m_{CO_2} / m_t . \tag{13}$$

Equation (12) is used to determine the mass fractions of the polymer fragments P_f, P_f', P_f'', and CPN. Each of these four decomposition products originates from the bridge populations. The CO_2 decomposition gas is a derived quantity based on overall continuity since mass for the CO_2 comes from the extended DEG or TMP sites as well as the bridges. Two other decomposition products can be identified: DEG and TMP, which are not determined from the bridge populations, yet evolve as monomers with a null dangler population. Although the DEG and TMP mass fractions cannot be determined explicitly using percolation theory, the monomer vapor pressure should be close to the vapor pressure of DEG and TMP as discussed further in Section 6.

The mass of finite polymer fragments which include monomers, dimers, trimers, etc. expressed on an extended site basis, m_n, can be determined from the mass of the finite fragment, M_n, multiplied by the n-site polymer fragment population on an extended site basis, Q_n:

$$m_n = M_n Q_n \tag{14}$$

where

$$M_n = nM_m + (n-1)\bar{M}_B + \left(\tfrac{\tau}{2}\right)\left(\tfrac{danglers}{danglers+gases}\right)\bar{M}_D \tag{15}$$

and

$$Q_n = F_n / n = \left[a_n p^{n-1}(1-p)^{\tau}\right] / n\,. \tag{16}$$

The mass fraction of the nth polymer fragments is then

$$f_n = m_n / m_t\,. \tag{17}$$

M_n is the molecular weight of the n^{th}-polymer fragment bin. The first term in Eq. (15) represents the number of mers in the n-mer multiplied by the mer molecular weight, M_m. The second term in Eq. (15) represents the number of bridges, n - 1, in the polymer fragment multiplied by the average molecular weight of the bridges, $\bar{M}_B$. The last term in Eq. (15) represents the weight of the side-chains, or "danglers." The fraction, $\frac{danglers}{danglers+gases}$, accounts for the danglers that have evolved as gases. For convenience, the sum of the bridges, danglers, and gas population variables are designated as $bridges$, $danglers$, and $gases$ as follows:

$bridges$ = Λ + Λ' + Λ" + C + L, (18)

$danglers$ = δ + δ' + δ" + d, (19)

and

$gases$ = P_f + P_f' + P_f" + CPN. (20)

Thus, the average bridge molecular weight, $\bar{M}_B$, and dangler molecular weight, $\bar{M}_D$, are

$$\bar{M}_B = \sum_B M_B B / bridges = \frac{M_\Lambda \Lambda}{bridges} + \frac{M_{\Lambda'} \Lambda'}{bridges} + \frac{M_{\Lambda''} \Lambda''}{bridges} + \frac{M_C C}{bridges} + \frac{M_L L}{bridges} \quad (21)$$

and

$$\bar{M}_D = \sum_D M_D D / danglers = \frac{M_\delta \delta}{danglers} + \frac{M_{\delta'} \delta'}{danglers} + \frac{M_{\delta''} \delta''}{danglers} + \frac{M_d d}{danglers}. \quad (22)$$

The summation indexes *B* and *D* in Eqs. (21) and (22) represent the bridge populations (Λ, Λ', Λ", C, and L) and dangler populations (δ, δ', δ", and D), respectively. The average molecular weight of the mer as well as the various bridges, danglers, and gases are defined as:

M_m = 128 g/mol (23)

$M_\Lambda = M_\delta = M_{Pf}$ = 174 g/mol (24)

$M_{\Lambda'} = M_{\delta'} = M_{Pf'}$ = 148 g/mol (25)

$$M_{\Lambda''} = M_{\delta''} = M_{Pf''} = 122 \text{ g/mol} \tag{26}$$

$$M_C = M_{\Lambda''} = 122 \text{ g/mol} \tag{27}$$

$$M_{CO2} = 44 \text{ g/mol} \tag{28}$$

$$M_{H2O} = 18 \text{ g/mol} \tag{29}$$

$$M_{CPN} = 84 \text{ g/mol} \tag{30}$$

$$M_L = M_d = 110 \text{ g/mol} \tag{31}$$

$$M_d + M_{H2O} = M_{CPN} + M_{CO2} \tag{32}$$

The molecular weight of the monomer unit, M_m, given in Eq. (23) is the average molecular weight of the TMP site and DEG site. The average is based on the three most common structural units of the polyurethane foam shown previously in Fig. 3.2, which makes up 90% of the foam structure. The 60% most probable structure is composed of only TMP sites with the same molecular weight as trimethylol propane – 134 g/mol. The 20% most probable structure is composed of an equal amount of TMP and DEG sites. The 10% most probable structure is composed of only DEG sites with the same molecular weight as diethylene glycol – 106 g/mol. The average monomer molecular weight given previously in Eq. (23) was calculated as follows:

$$M_m = \tfrac{0.6}{0.9}(134) + \tfrac{0.2}{0.9}\left(\tfrac{134+106}{2}\right) + \tfrac{0.1}{0.9}(106) = 128 \text{ g/mol}. \quad (33)$$

The fraction of all finite polymer fragments can be determined by summing all the polymer fragments as follows:

$$m_f = \sum_{n=1}^{\infty} m_n = \sum_{n=1}^{\infty} M_n Q_n \quad (34)$$

and

$$f_f = m_f / m_t . \quad (35)$$

An algebraic expression for the mass of the finite fragments can be obtained by letting

$$K = \sum_{n=1}^{\infty} Q_n = \left[1 - \frac{\sigma+1}{2} p^*\right]\left[\frac{p^*}{p}\right]^{(\sigma+1)/(\sigma-1)} \quad (36)$$

and

$$F = \sum_{n=1}^{\infty} n Q_n = \left[\frac{p^*}{p}\right]^{(\sigma+1)/(\sigma-1)}, \quad (37)$$

giving

$$m_f = F M_s + (F-K)\bar{M}_B + \left[\tfrac{F(\sigma-1)+2K}{2}\right]\left(\tfrac{danglers}{danglers+gases}\right)\bar{M}_D . \quad (38)$$

The derivation of Eq. (36) and (37) is given by Grant et al. [10]. In Eq. (36) and (37), p^* is the root of the following equation:

$$p^*(1-p^*)^{\sigma-1} - p(1-p)^{\sigma-1} = 0\,, \tag{39}$$

where p is obtained from Eq. (4). Two roots exist in the range $0 < p < 1$. The trivial root of Eq. (39), $p^* = p$, should be used when p is less than p_c. The other root that is bounded by $0 < p^* < p_c$ should be used when p is greater than p_c. For typical problems, the total fraction of material that belongs to the finite fragment bins, m_f/m_t, is not of interest. Rather, the individual fraction of monomers, dimers, and trimers are of most interest. The higher molecular weight fragments do not typically evolve into the gas-phase and do not affect the overall solid fraction.

The primary variables of interest for the network statistical model are molecular weight of the site and the various bridges, danglers, and gases [Eqs. (23)-(32)]; the mass fraction of the P_f, P_f', P_f'', CPN, and CO_2 [Eqs. (12) and (13)], the molecular weight of the n^{th}-polymer fragment [Eq. (15)] and the mass fraction of the n^{th}-polymer fragment [Eq. (17)]. A separate model is used to determine the amount of finite polymer fragments transported to the gas-phase.

6. Vapor-Liquid Equilibrium

The fraction of the polymer fragments that are gaseous (*e.g.* vapor-liquid split) can be determined by using a simple vapor-liquid equilibrium relationship using a combination of Dalton's law and Raoult's law. In the current report, a standard multicomponent isothermal flash calculation was used to determine the split between vapor and condensed phases following the procedure used by Fletcher et al. [12]. Details about the vapor-liquid model can be found in Ref. [1].

A standard *multicomponent isothermal flash calculation* based on the Rachford-Rice equation is used to determine the split between vapor and liquid *V*/*F* [18]:

$$0 = \sum_{i=1}^{n} \frac{z_i (K_i - 1)}{(K_i - 1)\frac{V}{F} + 1} \tag{40}$$

where the vapor-liquid equilibrium ratio or *K-value* is defined as,

$$K_i = \frac{y_i}{x_i} = \frac{\gamma_i P_i^*}{P}. \tag{41}$$

The activity coefficients, γ_i, are defined using three different solution models:

$$\gamma_i = \begin{cases} 1 & \text{, Raoult's Law solution} \\ \exp\left[\frac{0.4278}{T_{r_i}^{2.5} P_{c_i}}\left(P - P_i^*\right) + \frac{v_{iL}\left(P - P_i^*\right)}{RT}\right] & \text{, Ideal-solution} \\ \exp\left[\frac{z_i}{T_{r_i}}\left(\frac{I_E}{\ln(P+1)} \times \frac{P-1}{40}\right)\right] & \text{, Regular-solution.} \end{cases} \tag{42}$$

The second term in the ideal solution equation is the well-known *Poynting correction,* $\frac{v_{iL}\left(P-P_i^*\right)}{RT}$, for incompressible liquids. The Poynting correction is negligible compared to the gas correction at low to moderate pressures. The pure species molal volume, v_{iL}, was estimated by the method of Cavett using the following empirical equation [18]:

$$v_{iL} = \xi_i \left(5.7 + 3.0T_{r_i}\right), \tag{43}$$

where ξ_i is determined from the measured liquid molal volume at a known temperature.

The ratio, *V*/*F* in Eq. (40), is determined iteratively using the *zeroin* solver [19]. The parameters z_i, x_i, and y_i represent mole fractions in the combined-phases, condensed-phase, and vapor-phase, respectively. *V* and *F* represent the total moles in the vapor-phase and in the combined-phase, respectively. The nomenclature for the combined-phase is an "*F*" since the combined-phase is commonly referred to as the "feed." P_i^* represents the vapor pressure of the pure component at the system temperature, *T*. The mole fractions in the liquid (x_i) and vapor (y_i) phases can be determined as follows:

$$x_i = \frac{z_i}{(K_i - 1)\frac{V}{F} + 1} \tag{44}$$

$$y_i = K_i x_i = \frac{K_i z_i}{(K_i - 1)\frac{V}{F} + 1}. \tag{45}$$

Predicted activity coefficients for TDI using the three models described by Eq. (42) are plotted in Fig. 6.1. The *Raoult's Law solution model* describes an ideal solution with ideal gas be-

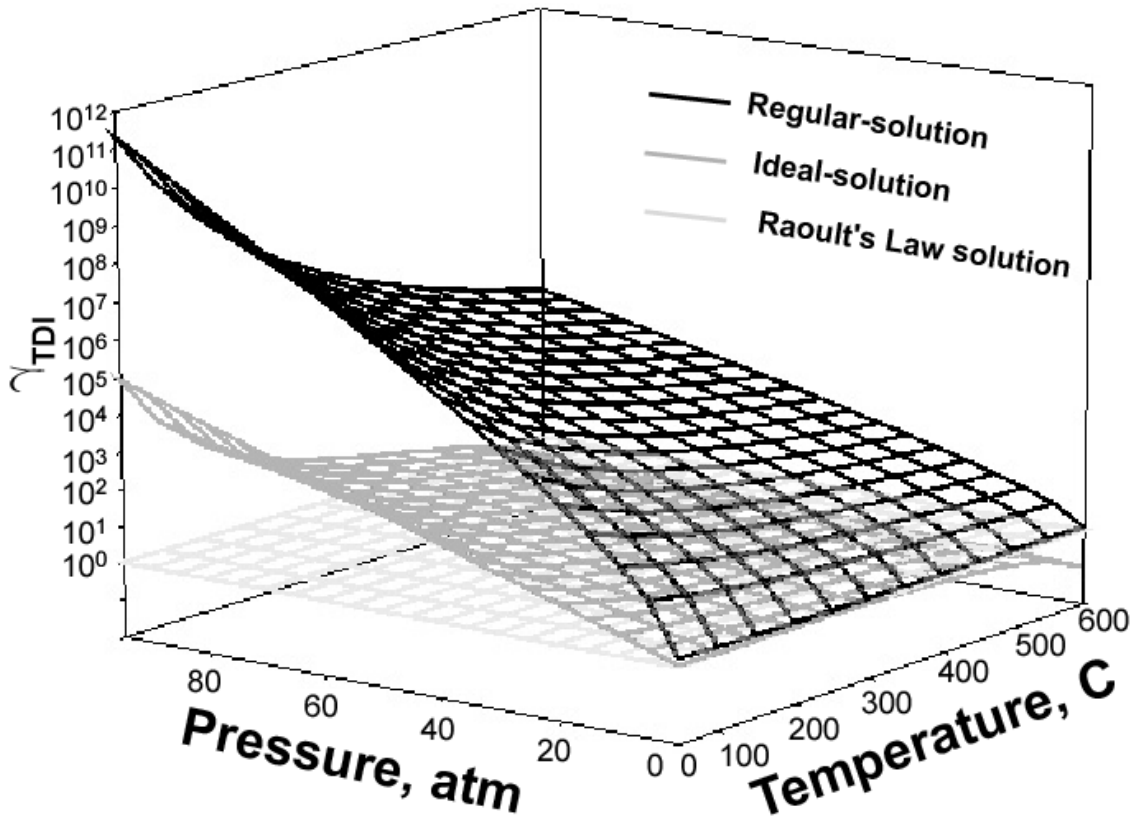

Fig. 6.1. Activity coefficient for TDI from Eq. (41).

havior; the *Ideal-solution model* describes an ideal solution with Redlich-Kwong gas behavior; and the *Regular-solution model* is an empirical model chosen to best match HPTGA data and is discussed further at the end of Section 7.1.

The following vapor pressure correlation was used for the polymer fragments CO_2, CPN, P_f, P_f', P_f", and the DEG-monomer and the TMP-monomer fraction [20]:

$$P_i^* = 9.87 \times 10^{-6} \exp\left(A + \tfrac{B}{T} + C \ln T + DT^E\right), \tag{46}$$

where the units on P_i^* and T, are in atmospheres and degrees Kelvin, respectively. The coefficients in Eq. (46) are given in Table 6.1 for CO_2, CPN, DEG, P_f, P_f" and TMP [20]. The coefficients for P_f' were estimated by taking the average vapor pressure of P_f and P_f" from 300 K to

1000 K. Furthermore, the vapor pressure of P_f and P_f" were assumed to be the same as toluene diisocyanate (TDI) and toluene diamine (TDA), respectively. Figure 6.2 shows the vapor pressures used for CO_2, CPN, P_f (TDI), P_f', and P_f" (TDA). The legend in Fig. 6.2 also gives the range of the data used to determine the coefficients in Eq. (46). The vapor pressure results seem to be good to about 800 K. This range is sufficient for the temperature range expected in most nuclear safety analyses. Critical properties for the major decomposition products are also given in Table 6.1.

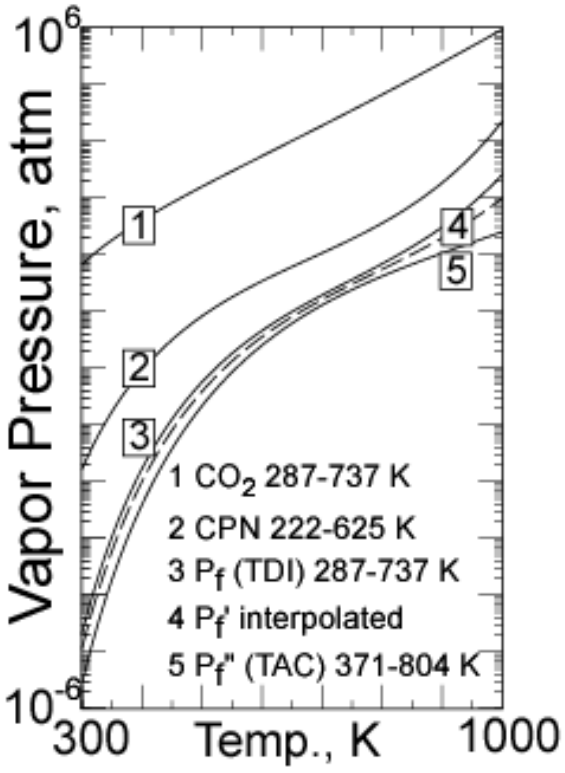

Fig. 6.2. Calculated (Eq. 45) vapor pressures.

Table 6.1. Vapor pressure coefficients used in Eq. (46) and critical properties,

$$P_i^* = 9.87 \times 10^{-6} \exp\left(A + \frac{B}{T} + C \ln T + D T^E\right)$$

Species	T_c, K	P_c, atm	A	B	C	D	E
CO_2	304	73	8.5530×10^{1}	-3.4813×10^{3}	-1.1336×10^{1}	2.1505×10^{-2}	1
CPN	625	45	5.6405×10^{1}	-6.4445×10^{3}	-4.8222×10^{0}	4.8774×10^{-18}	6
DEG	745	45	1.0523×10^{2}	-1.2565×10^{4}	-1.1121×10^{1}	3.0239×10^{-18}	6
P_f'	771	36	8.5908×10^{1}	-1.1069×10^{4}	-8.56708×10^{0}	2.7484×10^{-18}	6
P_f" (TDA)	804	43	7.5428×10^{1}	-1.1094×10^{4}	-6.9328×10^{0}	7.8095×10^{-19}	6
P_f (TDI)	737	30	9.9974×10^{1}	-1.1659×10^{4}	-1.0583×10^{1}	4.1543×10^{-18}	6
TMP	709	11	9.4806×10^{1}	-1.3703×10^{4}	-9.3429×10^{0}	3.0239×10^{-18}	6

The gases CO_2, CPN, P_f, P_f', and P_f", which originate from bridges, must be combined with other finite polymer fragments that contain sites (monomer, dimer, trimer, etc.) as well as the infinite polymer fragment to calculate the feed mole fractions, z_i. The vapor pressure for the dimer and higher molecular weight mer fragments were calculated from the following correlation proposed by Fletcher et al. [12] for organic molecules:

$$P_n^* = 87100 \exp\left(\frac{-299 M_n^{0.59}}{T}\right), \tag{47}$$

where P_n* is the vapor pressure of the pure n^{th}-polymer fragment in atmospheres, M_n is the molecular weight of the n^{th}-polymer fragment in g/mol as determined from Eq. (15), and T is the temperature in K. The functional form of Eq. (47) is similar to the Clausius-Clapeyron equation. The coefficients in Eq. (47) were obtained from coal tars with molecular weights ranging from 110 - 315 g/mol. The vapor pressure predicted with Eq. (47) increases with lower molecular weight species.

Fletcher et al. [12] have shown acceptable agreement with boiling point data for 111 organic compounds at pressures of 0.007, 0.08, 1, and 10-atm using the correlation given in Eq. (47). The 111 organic compounds, with molecular weights as high as 244, did not contain long chain alkanes or compounds with more than two oxygen atoms. Long chain hydrocarbons are not expected to occur in the polyurethane tar in significant quantities. However, some of the expected products measured by Erickson et al. [3-5], such as fragments containing trimethoxypropane, contain more than two oxygen atoms.

Figure 6.3 shows the vapor pressures for some typical monomers, dimers, and trimers calculated with Eqs. (46) and (47). The calculated monomer molecular weight is close to the molecular weight of the typical mers, DEG and TMP, which implies that the monomers typically do not have side-chains. The DEG and TMP vapor pressures were calculated using Eq. (46) with a valid temperature range of 262-744 K and 331-709 K, respectively. Because Eq. (46) is based on experimental vapor pressure data for TMP and DEG, the monomer vapor pressure is calculated by partitioning the monomer weight fraction into TMP and DEG bins by multiplying the calculated monomer weight fraction [Eq. (17)] by the initial weight fraction of TMP and DEG, which is 0.82 and 0.18, respectively.

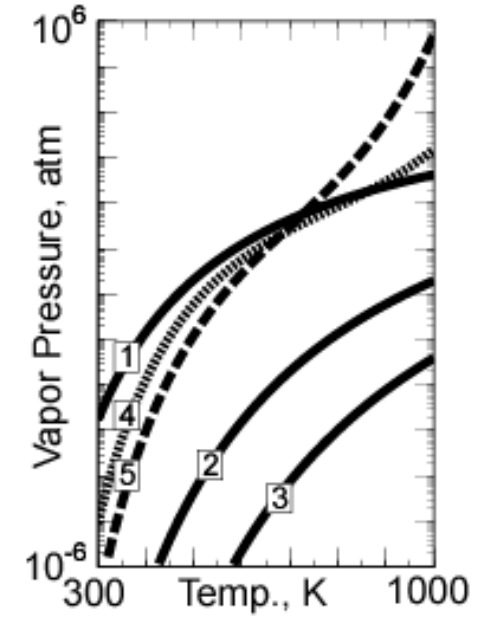

1 monomer	131 g/mol	Eq. (47)
2 dimer	428 g/mol	Eq. (47)
3 trimer	726 g/mol	Eq. (47)
4 DEG	106 g/mol	Eq. (46)
5 TMP	134 g/mol	Eq. (46)

Fig. 6.3. Vapor pressures for typical monomers, dimmers, and trimers.

7. CPUF Model Parameters

Table 7.1 gives the means (μ_i) and standard deviations (σ_i) of the CPUF input parameters, which include the initial density and temperature of the foam (ρ_o and T_o), the multiplying factors for temperature-dependent thermal conductivity and specific heat of the foam (k and C_p), the reaction enthalpy of the foam (h_r), the emissivity of the foam (ε), the interaction energy used in the regular solution vapor-liquid equilibrium model (I_E), the coordination number of the polymer lattice (σ+1), the initial lattice bridge population (Λ_o), 16 frequency factors (A_i), 16 activation energies (E_i), and the average standard deviation of the distributed activation energy model (σ_E). The input parameters are assumed to be normally distributed independent random variables.

7.1 Thermophysical Properties

All of the mean *thermophysical properties* in Table 7.1 are *based on measurements*. Densities were determined from the sample volume and mass. Initial temperatures were meas-

Table 7.1. Moments of various CPUF model parameters†

	Thermophysical							***Lattice***		***Chemistry***				
ξ_i	ρ_o	T_o	f_k‡	f_{cp}‡	h_r	ε	I_E	σ+1	Λ_o	A_i	E_1	E_2	E_3	E_4
μ_i	0.364	300	1	1	±20.6	0.8	40	2.8	0.78	3×10^{15}	50.2	50.6	49.4	50.4
σ_i	0.02	3	0.09	0.04	0.7	0.04	13	0	0.01	0	0.247	0.200	0.111	0.159
	Chemistry (continued)													
ξ_i	E_5	E_6	E_7	E_8	E_9	E_{10}	E_{11}	E_{12}	E_{13}	E_{14}	E_{15}	E_{16}	σ_E	
μ_i	50.0	49.5	50.4	49.3	51.6	49.8	50.2	50.1	50.2	51.1	49.6	49.7	3.52	
σ_i	0.149	0.233	0.079	0.104	0.179	0.125	0.132	0.251	0.130	0.219	0.165	0.080	0.017	

†Density (ρ_o) in g/cm^3, initial temperature (T_o) in K, reaction enthalpy (h_r) in cal/cm^3, frequency factors (A_j) in 1/s, activation energies (E_i) in Kcal/mol, and standard deviation of the activation energies (σ_E) in Kcal/mol.
‡k and C_p are given in Table 7.2. f_k and f_{cp} are scaling parameters used for uncertainty analysis.

ured using embedded thermocouples. The thermal conductivity and specific heat were measured at Purdue's Thermophysical Properties Laboratory [21, 22] between 23ºC and 250ºC using 1.3-cm wide by 0.3-cm thick samples. The thermal conductivity and specific heat for samples with densities of 0.078-g/cm^3, 0.150-g/cm^3, and 0.352-g/cm^3 are given in Table 7.2. The reaction enthalpy was measured with a differential scanning calorimeter using a nominally 5-mg sample ramped at 20ºC/min. The foam emissivity was *estimated* from measurements at Purdue.

The variability in the initial foam density may be caused by a skin effect. For example, the density of cast blocks of polyurethane foam varies considerably from near the surface to the interior of the foam. The skin effect is greatest when the density of the foam is high. Purdue measured from 1.4% to 23% difference in density between the machined samples used for the thermal conductivity measurements and the large blocks from which the samples were taken. The 1.4% difference was for the 0.078-g/cm^3 foam and the 23% difference was for the 0.150-g/cm^3 foam. Of course, these differences are based on significant skin effects that depend on the size of the bulk sample. The samples used in both the large and small-scale experiments were taken near the center of the foam block to avoid large edge effects. The density measured for the large-scale experiments was given in Table 7.1 (0.364 g/cc). The density used to determine the

Table 7.2. Thermal conductivity and specific heat for RPU foam at three densities

	***k*, cal/s-cm-K**			***C*$_p$, cal/g-K**		
T, ºC	**0.078 g/cm^3**	**0.150 g/cm^3**	**0.352 g/cm^3**	**0.078 g/cm^3**	**0.15 g/cm^3**	**0.352 g/cm^3**
23	5.7×10^{-5}	6.9×10^{-5}	1.4×10^{-4}	0.303	0.303	0.303
50	6.4×10^{-5}	7.6×10^{-5}	1.5×10^{-4}	0.324	0.324	0.324
100	7.4×10^{-5}	8.4×10^{-5}	1.6×10^{-4}	0.358	0.358	0.358
150	9.1×10^{-5}	9.8×10^{-5}	1.8×10^{-4}	0.440	0.440	0.440
200	9.8×10^{-5}	1.0×10^{-4}	2.0×10^{-4}	0.475	0.475	0.475
250	1.2×10^{-4}	1.2×10^{-4}	2.2×10^{-4}	0.526	0.526	0.526
3500*	9.1×10^{-4}	9.1×10^{-4}	1.3×10^{-3}	0.526	0.526	0.526

*Extrapolated thermal conductivity used in bias correction in Eq. (67) given as $k^{\text{linear extrapolation}}_{3500°\text{C}}$

thermal conductivity was given in Table 7.2 (0.352 g/cc). These two different values were used to determine the standard deviation of the foam density [3.3% of the mean value = (0.364-0.352)/0.364]. The standard deviation of density in the current report was taken to be twice this value or 6.6% of the mean density. A larger uncertainty is used in the current report because the foam used in the application will be cast in place and may have a significant skin effect.

The standard deviation of the initial foam temperature was based on the measured initial sample temperatures for both the small and large-scale experiments. For example, the mean initial temperature of the TGA experiments was 299 K with a standard deviation of 2.3 K. The mean initial temperature of the large-scale experiments was 294 K with a standard deviation of 4.0 K. For convenience, the nominal mean and standard deviation of the initial temperature was taken to be 300 K and 3 K, respectively.

The uncertainty in the thermal conductivity is based on multiple room temperature measurements using two different techniques – a laser flash diffusivity method and a heated probe method [21, 22]. The laser flash diffusivity method measures bulk conductivity and the heated probe method measures the conductivity parallel to the rise direction of the foam as well as orthogonal directions perpendicular to the rise direction of the foam. Three measurements were made at 23˚C for both the 0.078-g/cc samples and the 0.150-g/cc samples; and nine measurements were made at 23˚C for the 0.352-g/cc samples. The standard deviations for the 0.078-g/cc, 0.150-g/cc, and 0.352-g/cc samples were 9%, 4%, and 5% of the mean thermal conductivity value at 23˚C, respectively. The standard deviation was determined as a percent of the mean thermal conductivity to facilitate uncertainty analysis. The highest standard deviation (9% of the mean) was chosen to reflect the unknown variability at higher temperatures. Condensed-phase reactions and liquefaction are expected to cause the uncertainty in thermal conductivity to increase.

The specific heats of RPU samples preheated to 150 and 250˚ were measured with a differential scanning calorimeter with sapphire as the reference material. The samples were preheated to prevent contamination of the test cell with decomposition products. Variability in the conductivity is related to uncertainty caused by mass loss associated with decomposition. Polyurethane specific heat data was not available to estimate uncertainty. However, specific heat data for another foam was used to estimate variability. For this foam, the average standard deviation between ambient temperature and 200˚C was 3.7% of the mean specific heat value. The variability in the polyurethane specific heat (~4%) was assumed similar to the variability in this other foam.

Differential thermal analysis (DTA) was used to determine the energy changes for conditions similar to the TGA experiments run at 20ºC/min. The overall endothermic heat of reaction at these conditions was about 100 cal/g [23] or 36.4 cal/cc for foam with a density of 0.364. The heat of reaction shown in Table 7.1 is not the overall reaction enthalpy. The heat of reaction in Table 7.1 is the heat of reaction for the 16 individual reactions described by Eq. (1). If the reaction in Table 4.1 describes bond breaking, the reaction enthalpy is endothermic and the sign of the reaction enthalpy is negative. For example, reactions 1, 3, 6, 8, 10, 12, 14, and 16 in Table 4.1 are endothermic. If the reaction in Table 4.1 describes a bond that is being formed, the reaction enthalpy is exothermic and the sign of the reaction enthalpy is positive. For example, reactions 2, 4, 7, 11, and 15 in Table 4.1 are exothermic reactions. Reactions 5, 9, and 13 have a zero reaction enthalpy since no additional bridges are formed or broken.

The overall endothermic heat of reaction was used with the finite element code [6] to obtain the energy release for each reaction step j. The source term in the heat diffusion equation is used to account for the overall endothermic reaction enthalpy. The heat diffusion equation is

$$\rho C_p \frac{\partial T}{\partial t} = \frac{\partial}{\partial x}\left(k \frac{\partial T}{\partial x}\right) + \sum_{j=1}^{J} q_j r_j \,. \tag{48}$$

In Eq. (48), ρ, C_p, T, t, x, k, q, and r represent material density, specific heat, temperature, time, spatial coordinate, thermal conductivity, endothermic or exothermic energy release for reaction step *j*, and the reaction rate given previously in Eq. (1), respectively. Equation (48) was used iteratively with a 20ºC/min ramp to determine the individual heat of reaction values of ±20.6 cal/cc that gives an overall reaction enthalpy of –100 cal/g or –36.4 cal/cc. Figure 7.1.A shows the volumetric heat release, $\sum q_j r_j$, plotted as a function of time for the 20ºC/min TGA run. Figure 7.1.B shows the integrated volumetric heat release, which converges to a value of –36.3 cal/cc or –99.7 cal/g. Figure 7.1.C shows the volumetric heat release plotted as a function of time for heating rates ranging from 5 to 320ºC/min. Different values of the energy release at different heating rates reflect the effect of the heating rate on the reaction mechanism.

The uncertainty in the volumetric heat release is difficult to estimate because only one DTA experiment was performed at a heating rate of 20ºC/min. The density of the DTA sample was reported to be the same as the samples used in the TGA analysis [23]. The density of the DTA sample was assumed equal to 0.364 g/cc. However, the sample may have had a density of 0.352 g/cc, which is the density measured for the samples used to determine the thermal conductivity. The error associated with the assumed density is about 3.3% of the mean value. Thus, the standard deviation of the reaction enthalpy was taken to be 3.3% of the mean value, or 0.7 cal/cc (0.033×22.7 cal/cc).

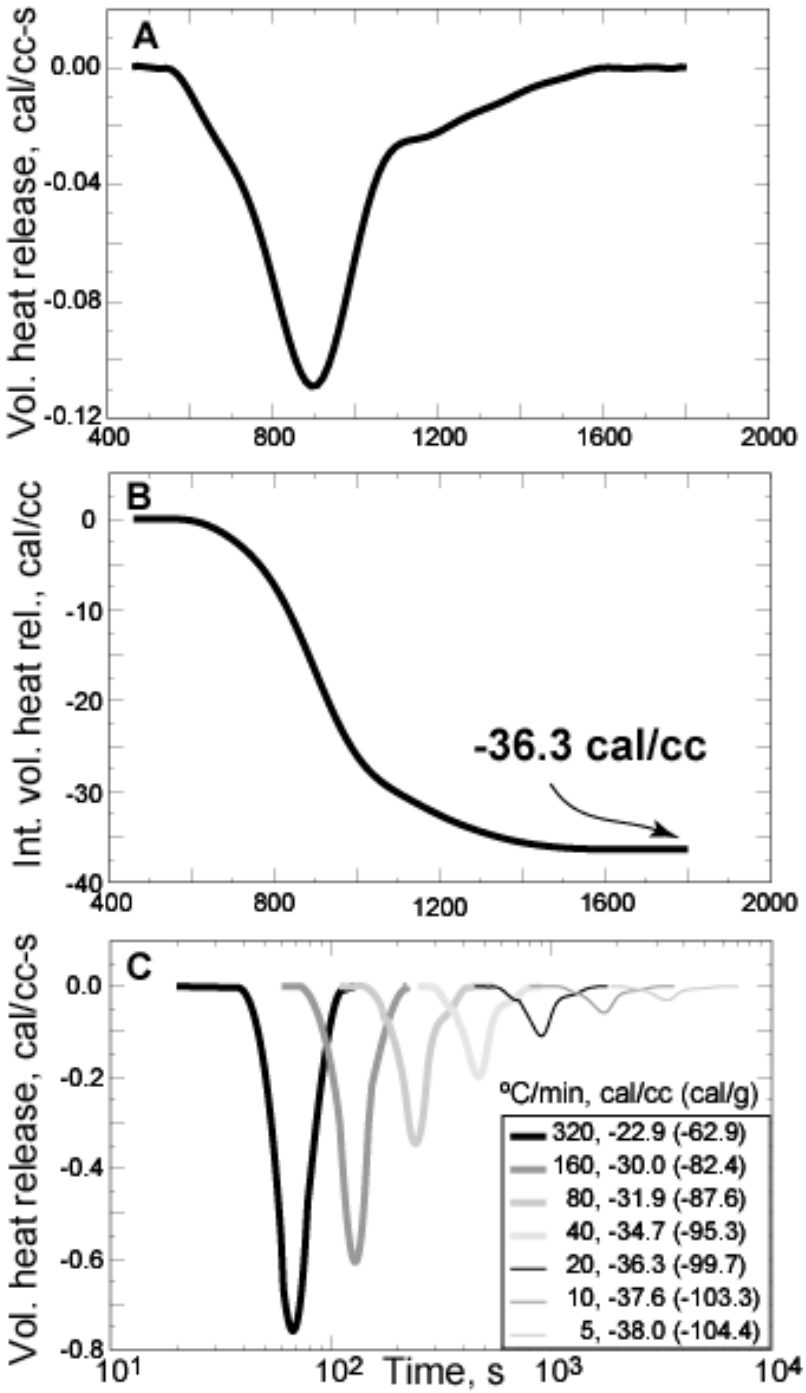

Fig. 7.1. A) Volumetric heat release for 0.364 g/cc sample heated at 20ºC/min, B) integrated volumetric heat release for 0.364 g/cc sample heated at 20ºC/min, and C) volumetric heat release for heating rates ranging from 5 to 320ºC/min.

The emissivity of the surface of the degraded foam surface was estimated since there were *no measurements of the foam emissivity*. The postmortem color of the decomposed foam was used to estimate the emissivity of the RPU foam. The postmortem color of the decomposed foam was similar to the color of the interior surface of the confining skin, which was painted black with Pyromark Paint 2500. The hemispherical emissivity of this paint was between 0.768 and 0.811 at temperatures between 460ºC and 1,014ºC [21]. The emissivity of the RPU foam was assumed to rapidly approach 0.8 with an estimated standard deviation of 0.04. The standard deviation of the foam emissivity was based on the range of the measured emissivity for the Pyromark Paint (0.04 = 0.81-0.77).

The final thermophysical property listed in Table 7.1 is the average interaction energy (I_E) for the regular solutions model, which is a vapor-liquid-equilibrium (VLE) fitting parameter obtained from the high pressure TGA data. The regular solution model is recommended for decomposition at elevated pressures provided the decomposition products are not kept in contact with the decomposing foam such as in the HPTGA experiments.

The form of the regular solutions model was given in Eq. (42) with the average interaction energy parameter (I_E) represented by the constant 40. Optimization techniques [24] were used to obtain the interaction energy parameter by minimizing the root mean squared (RMS) error between the calculated and measured mass loss for *each of the sixteen TGA experiments* listed in Table 7.3. During the optimization procedure, all of the other parameters were held at their mean values given previously in Table 7.1. The absolute RMS errors were calculated using the following equations:

$$\text{absolute RMS error} = \sqrt{\sum_{i=1}^{n}\left(sf_i^{TGA} - sf_i^{CPUF}\right)^2}\,. \tag{49}$$

The summation refers to the measured, sf_i^{TGA}, or calculated, sf_i^{CPUF}, solid fraction at selected temperatures during TGA experiments. The solid fraction refers to the mass of the sample divided by the initial mass (s_f = m/m_o) of the sample. Absolute error was used for the optimization routine rather than relative error since the solid fraction (s_f) approaches zero. Using relative error for the cost function would bias results near the end of the experiments. Table 7.3 gives the optimal values of the interaction energy for each of the sixteen TGA cases as well as the average and standard deviation of the interaction energy.

Table 7.3. High pressure TGA samples

Run	Sample	P, bar†	m_o, mg	Error	l_E
1	B050300	5	5.7	0.0144	43
2	B050500	5	5.9	0.0132	59
3	B050800	5	5.2	0.0193	21
4	B051500	5	5.1	0.0153	47
5	B051600	5	5.1	0.0099	73
6	B051700-1	10	5.9	0.0208	46
7	B051700-2	10	5.2	0.0256	54
8	B053000	10	6.2	0.0230	30
9	B060800	10	5.6	0.0201	37
10	B061500-1	10	5.6	0.0161	34
11	B061500-2	10	5.3	0.0163	36
12	B061600	30	5.1	0.0344	32
13	B062000-1	30	5.2	0.0336	38
14	B062000-2	30	5.5	0.0321	30
15	B062200-1	30	5.4	0.0288	27
16	B062200-2	30	5.3	0.0317	31
		Mean	**5.5**	**0.0222**	**40**
		St. Dev	**0.3**	**0.0080**	**13**

†Pressure in bars gauge

7.2 Lattice Properties

The lattice parameters in Table 7.1 were obtained by using the three most probable structures of the foam shown previously in Fig. 3.2. Table 7.4 shows a simplified representation of the three most common structural units of the RPU foam. The solid circles represent the TMP sites and the open circles represent the DEG sites. The primary bridges are represented as a solid black line; and the secondary bridges are represented as a white line. The number of bridge types in each structure is also indicated in Table 7.4. The uncertainty in the lattice coordination number for the CPUF model is small. The average coordination number was obtained from the three most probable chemical structures given in Table 7.4 as follows:

$$\sigma + 1 = \tfrac{0.6}{0.9}(3) + \tfrac{0.2}{0.9}(2.5) + \tfrac{0.1}{0.9}(2) = 2.8\,. \tag{50}$$

Table 7.4. Three most probable structures in RPU foam showing bridge and site populations

Probable Structure	Λ Bridges	L Bridges	TMP sites	DEG sites
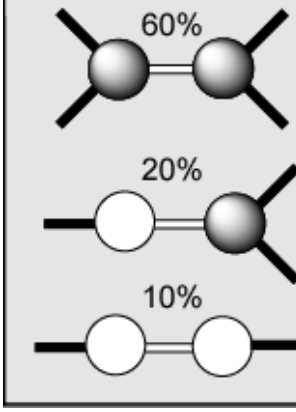 60%	4	1	2	0
20%	3	1	1	1
10%	2	1	0	2

The coordination number is also 2.8 if all of the five most probable structural units shown previously in Fig. 3.1 are used to determine the coordination number. Thus, the uncertainty in the lattice coordination number due to only using the three most probable structures is negligible.

The initial bridge population consists of only primary bridges (Λ) and secondary bridges (L). The initial primary bridge population, Λ_o, is based on the probability normalized bridge population from the three most common structural units as follows:

$$\Lambda_o = \frac{0.6}{0.9}\left(\frac{4}{5}\right) + \frac{0.2}{0.9}\left(\frac{3}{4}\right) + \frac{0.1}{0.9}\left(\frac{2}{3}\right) = 0.78 \tag{51}$$

and

$$\mathrm{L}_o = 1 - \Lambda_o = 0.22\,. \tag{52}$$

The remaining bridges and all of the dangler populations were initially set to zero. The initial bridge population, $\Lambda_o + L_o$, may be less than one and the dangler populations may be greater than

zero when the foam is not fully cured. Estimates of the extent of curing, which are related to aging studies, are beyond the scope of the current report. The primary bridge population can also be calculated using the five most probable structural units shown previously in Fig. 3.1. The primary bridge population is 0.79 when all five structural units are used to calculate the bridge population. Thus, the uncertainty in primary bridge population is taken to be 0.01. The uncertainty in the lattice parameters may even be higher since the chemical structures are only *estimates* of the actual chemical structure.

7.3 Chemistry Parameters

Three types of chemistry parameters are listed in Table 7.1 – the pre-exponential factors (A_i), the activation energies (E_i), and the standard deviation used with a distributed activation energy model (σ_E). Mass loss data from several TGA experiments were used to obtain these parameters. The mass-loss TGA data set is not sufficient to extract 16 sets of pre-exponential factors and activation energies in a meaningful way. Physical meaning should not be associated with the activation energies listed in Table 7.1. Quantitative species evolution data is needed to obtain meaningful kinetic parameters that would enable prediction of phase compositions. Predicting foam response in unconfined systems, which is detailed in the current work, does not require detailed composition data and only mass loss is used to predict unconfined foam response. However, predicting phase composition is necessary for predicting dynamic pressurization and foam response in confined systems.

The CPUF chemistry mechanism is a prototypical mechanism used for demonstration purposes only. See Clayton [8] for a more representative polymer decomposition chemistry model with the parameters obtained using a continuously stirred reactor (CSTR) approach. In the current report, the primary benefit of using a 16 step polymer fragmentation model was to show the methodology for incorporating complex chemistry into a lattice statistics model coupled to a

vapor liquid equilibrium model. Mass transport is also important for quantitative predictions of phase compositions, but is beyond the scope of the current work due to insufficient composition data to set chemistry parameters.

All of the pre-exponential factors, or frequency factors, were assumed constant at 3×10^{15} for all sixteen CPUF reaction steps. The value 3×10^{15} is consistent with the values used in the Chemical Percolation Devolatilization (CPD) model [10]. Volltrauer and Fontijn [25] also used a frequency factor of 3×10^{15} for their initial nitrocellulose decomposition reaction. The value 3×10^{15} may seem high when compared to the transition state theory value for a unimolecular reaction, which is 1×10^{13}. However, the CPUF bond-breaking mechanism is a global reaction set that cannot be described by unimolecular decomposition. Single values of pre-exponential factors speed global convergence in optimization routines because frequency factors and activation energies are highly correlated. Using frequency factors as fitting parameters will give better agreement with the data. However, only single values of frequency factors are used in the current report since the fit to the TGA mass loss curves were sufficiently accurate. Uncertainties in reaction rates are accounted for using only the activation energies because of the high degree of correlation between the pre-exponential factors and the activation energies.

The pre-exponential factors and activation energies are used with well-known Arrhenius rate expressions as described previously in Eq. (2). Up to this point in the report, the standard deviation used to distribute the activation energies has not been discussed. Distributing activation energies with respect to the extent of reaction is useful for approximating the effect of thermal damage on materials. Thermal damage includes mechanical damage such as cracks, fissures, density, and phase changes as well as chemical damage caused by thermal decomposition.

The CPUF model considers distributed activation energies for each of the 16 bond breaking reactions listed in Table 4.1. During foam decomposition, each of the activation energies is normally distributed based on the extent of the secondary bridge reaction, $1 - L / L_o$, as follows:

$$\Phi(\xi) = 1 - \frac{\mathrm{L}}{\mathrm{L_o}} = \int_{-\infty}^{\xi} \frac{1}{\sqrt{2\pi}} \exp(-\tfrac{1}{2} t^2) dt \,. \tag{53}$$

The cumulative distribution function of a standardized normal random variable, $\Phi(\xi)$ is shown in Fig. 7.2, where the total area under the standardized normal is equal to one. For negative values of ξ, the relationship, $\Phi(-\xi) = 1 - \Phi(\xi)$, is used. The distribution function initially starts at zero (all of the initial secondary bridges are intact) and ends at one (all of the secondary bridges are broken).

For convenience, a table lookup is used for the distribution function rather than evaluation of the indefinite integral in Eq. (53). Without any loss of accuracy, the following limits are used in the CPUF model for increased computational speed:

$$\xi = \begin{cases} -2 & \Phi < 0.0228 \\ +3.5 & \Phi > 0.9997 \end{cases} \tag{54}$$

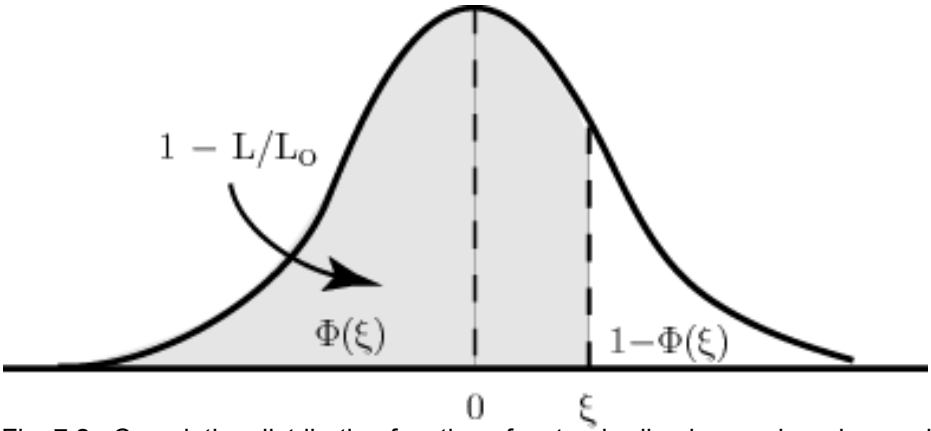

Fig. 7.2. Cumulative distribution function of a standardized normal random variable.

For all other values of Φ, ξ is linearly interpolated from tables [26].

The rate constants given previously in Eq. (2) for each reaction was modified to include the effect of the distributed activation energies as follows:

$$k_j(T) = A_j \exp\left[-\left(E_j + \xi\sigma_E\right)/RT\right]. \tag{55}$$

For the CPUF model, the standard deviation used with a distributed activation energy model (σ_E) is the same for all of the bond-breaking reactions. Distributing the activation energies tends to smooth the bond-breaking reaction rates and eliminates abrupt changes in calculated solid fractions, which is in agreement with experimental observations.

The mean and standard deviation of the chemistry parameters listed in Table 7.1 were obtained by using 21 different sets of thermogravimetric analysis (TGA) experiments, which are described in Table 7.5. Table 7.6 gives the chemistry parameters obtained from each individual

Table 7.5. Ambient pressure TGA samples

Run*	Sample	Ramp†	m_o, mg	Error‡	Error**
1	F_062199	20	4.50	0.0056	0.0117
2	Fm061499	20	5.14	0.0084	0.0143
3	Foam1112	20	6.16	0.0065	0.0168
4	Foam1114	20	6.08	0.0064	0.0197
5	Foam1117	20	4.48	0.0061	0.0102
6	Foam1118	20	4.51	0.0076	0.0100
7	Foam1119	20	4.47	0.0075	0.0118
8	Foam1202	20	5.24	0.0063	0.0120
9	Foam1204	20	4.69	0.0089	0.0108
10	Foam1205	20	4.56	0.0063	0.0129
11	fm102999	20	5.98	0.0077	0.0112
12	fm103099	20	6.14	0.0060	0.0259
13	fm110199	20	4.06	0.0066	0.0082
14	fm11019a	20	4.01	0.0061	0.0081
15	B051000-1	20	6.33	0.0060	0.0122
16	B051000-2	20	5.18	0.0057	0.0214
17	B051100-1	20	5.17	0.0070	0.0092
18	B051100-2	20	5.50	0.0076	0.0219
19	fm01280a	300	5.07	0.0060	0.0524
20	fm061599	300	5.94	0.0068	0.0484
21	foam0706	300	4.69	0.0042	0.0551
		Mean	**5.14**	**0.0066**	**0.0192**
		St. Dev.	**0.73**	**0.0011**	**0.0145**

*1-14 and 19-21 run at SNL; 15-18 run at BYU

†20 and 300 refer to 20ºC/min ramp or 300ºC isotherm

‡Error calculated with E_j from Table 7.6 (individual optimized values)

**Error calculated with E_j from Table 7.1 (mean values)

Table 7.6. Activation energies (E_i) and DAE model standard deviation (σ_E) calculated using 21 sets of data*

Run	E_1	E_2	E_3	E_4	E_5	E_6	E_7	E_8	E_9	E_{10}	E_{11}	E_{12}	E_{13}	E_{14}	E_{15}	E_{16}	σ_E
1	50.3	50.3	49.5	50.2	49.7	49.4	50.4	49.3	51.8	49.7	50.3	49.9	50.4	51.1	49.7	49.7	3.55
2	50.1	50.7	49.4	50.4	50.3	49.5	50.4	49.3	51.5	49.9	50.2	50.0	50.1	51.2	49.7	49.6	3.55
3	50.1	50.5	49.4	50.3	50.0	49.6	50.3	49.4	51.5	49.8	50.2	50.5	50.2	50.9	49.5	49.7	3.51
4	50.0	50.4	49.4	50.3	50.0	49.7	50.3	49.4	51.5	49.7	50.2	50.0	50.3	50.8	49.5	49.7	3.55
5	50.4	50.7	49.4	50.5	50.0	49.3	50.5	49.1	51.6	49.7	50.2	50.0	50.2	51.0	49.6	49.9	3.51
6	50.3	50.6	49.4	50.5	50.0	49.4	50.5	49.2	51.5	49.7	50.2	50.5	50.2	51.0	49.6	49.8	3.51
7	50.1	50.4	49.5	50.3	49.9	49.6	50.3	49.4	51.6	49.7	50.3	49.9	50.3	50.9	49.5	49.7	3.51
8	50.1	50.4	49.4	50.3	49.9	49.6	50.4	49.4	51.6	49.7	50.3	49.9	50.3	50.9	49.5	49.7	3.51
9	50.0	50.4	49.4	50.3	49.9	49.6	50.3	49.4	51.5	49.7	50.2	50.0	50.3	51.0	49.5	49.7	3.55
10	50.0	50.4	49.4	50.3	50.0	49.7	50.3	49.4	51.5	49.7	50.2	50.0	50.3	51.0	49.5	49.7	3.51
11	50.1	50.4	49.4	50.3	49.8	49.6	50.3	49.4	51.6	49.7	50.3	49.9	50.3	51.0	49.5	49.7	3.55
12	50.9	50.9	49.1	50.7	50.2	50.0	50.4	49.2	51.4	50.2	49.6	50.1	49.8	51.7	50.2	49.6	3.52
13	50.1	50.4	49.4	50.3	49.9	49.6	50.4	49.3	51.6	49.7	50.3	49.9	50.3	50.9	49.5	49.7	3.51
14	50.0	50.4	49.4	50.3	49.9	49.6	50.3	49.4	51.5	49.7	50.2	50.0	50.3	51.0	49.5	49.7	3.51
15	50.3	50.8	49.3	50.6	50.1	49.3	50.5	49.2	51.4	49.9	50.2	50.5	50.1	51.1	49.6	49.8	3.51
16	50.4	50.9	49.3	50.7	50.1	49.2	50.5	49.1	51.3	49.9	50.2	50.6	50.0	51.3	49.7	49.9	3.51
17	50.3	50.7	49.3	50.5	50.0	49.3	50.4	49.2	51.5	49.9	50.2	50.5	50.1	51.2	49.7	49.7	3.51
18	50.3	50.9	49.2	50.6	50.0	49.2	50.5	49.1	51.3	49.9	50.2	50.5	50.1	51.3	49.7	49.8	3.51
19	50.7	50.8	49.4	50.6	49.7	49.1	50.5	49.2	52.1	49.7	50.3	50.0	50.3	51.1	49.8	49.7	3.48
20	50.3	50.8	49.2	50.6	49.8	49.2	50.5	49.2	51.8	49.7	50.2	50.1	50.3	51.0	49.7	49.6	3.52
21	50.1	50.8	49.2	50.6	49.8	49.2	50.5	49.2	51.7	49.7	50.2	50.1	50.3	50.6	49.6	49.6	3.52
mean	50.2	50.6	49.4	50.4	50.0	49.5	50.4	49.3	51.6	49.8	50.2	50.1	50.2	51.1	49.6	49.7	3.52
st.dev.	0.247	0.200	0.111	0.159	0.149	0.233	0.079	0.104	0.179	0.125	0.132	0.251	0.130	0.219	0.165	0.080	0.017

* Units for Ei and σ_E are Kcal/mol

experiment listed in Table 7.5. Seventeen of the TGA experiments (1-14, 19-21) were run at SNL [3-5] and four of the TGA experiments (15-18) were run at BYU [8]. All of the experiments in Table 7.5 were run at ambient pressure; although, BYU's TGA apparatus (HPTGA) was designed for high pressure thermal decomposition experiments using a continuous purge of an inert gas. The initial weights of the 21 samples are also given in Table 7.5 with a mean and standard deviation of 5.14-mg and 0.73-mg, respectively. All 21 samples were ramped at 20ºC/min. For experiments 1-18, the samples were ramped at 20ºC/min until the sample temperature reached ~600ºC. For experiments 19-21, the samples were ramped at 20ºC/min until the sample temperature reached 300ºC (about 15 minutes), the samples were then held at 300ºC.

Optimization techniques [24] were used to obtain the chemistry parameters in Table 7.6 by minimizing the absolute root mean squared (RMS) error [see Eq. (49)] between the calculated and measured mass loss for *each of the twenty-one ambient pressure TGA experiments* listed in Table 7.6. The average RMS error for the twenty-one TGA experiments was 0.0066 as given in

Table 7.5 indicating an *exceptionally good match* between the CPUF model predictions and the ambient pressure TGA data. The average RMS error was only slightly higher (0.0145) when the mean activation energies were used. Table 7.6 gives the optimal values as well as the mean and standard deviation of the activation energies (E_i) and the distributed activation energy model parameter (σ_E) for each of the twenty-one ambient pressure TGA cases.

The standard deviation of the activation energies in Table 7.6 is consistent with error associated with cellulose pyrolysis. In a recent round-robin study of cellulose pyrolysis kinetics by thermogravimetric analysis [27], eight laboratories with access to five different thermogravimetric analyzers found a 17ºC scatter in the temperature measurements for a fixed value of weight loss. Initial comparisons of the TGA data from SNL and BYU also showed similar scatter, which could be accounted for using a mean value analysis with the standard deviation of the activation energies all set to 300 cal/mol [28]. Differences in the data were originally attributed to systematic errors such as the purge gas flow pattern since the HPTGA uses axial flow and the LPTGA uses cross flow. After considerable effort, the differences in the results were found to be related to the temperature measurement in the HPTGA rather than the flow pattern.

Helium was used as the purge gas for the HPTGA experiments to get consistent results between the two labs. Helium has a high thermal conductivity, which provides better heat transfer leading to a more accurate temperature measurement. Buoyancy corrections and associated noise were also minimized when a lighter gas, He, was used as the purge gas. The LPTGA apparatus does not have as much mass as the HPTGA apparatus and gives consistent results independent of the selection of purge gas. The error associated with using N_2-purge gas rather than He-purge gas in the HPTGA can be seen in Fig. 7.3, which shows a 16ºC shift in the TGA profile. In the legend of Fig. 7.3, B031599-1 designates a 5.30-mg sample run at BYU on March 15, 1999 with nitrogen purge gas. The B051000-2 legend entry designates a 5.18-mg sample run

at BYU on May 10, 2000 with helium purge gas. The initial HPTGA experiments that were completed with nitrogen purge gas were not considered further in this report.

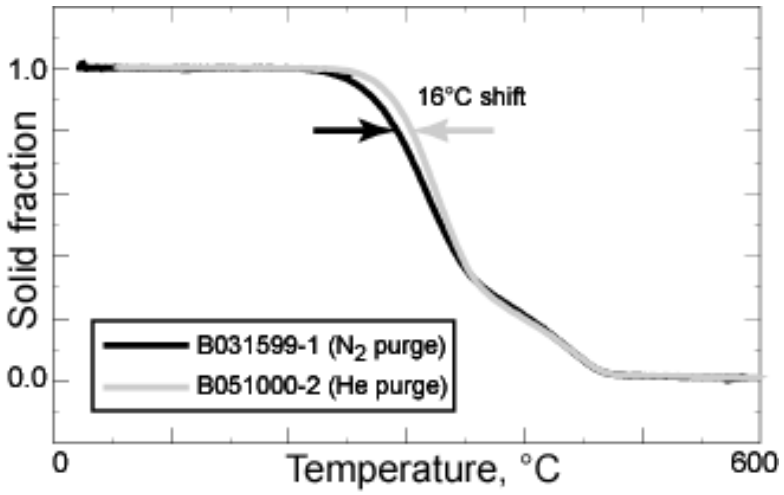

Fig. 7.3. RPU foam mass loss history at 1 bar and 20ºC/min.

8. Thermogravimetric Analysis (TGA) Experiments and Predictions

The TGA apparatus is composed of 1) a microbalance used to measure mass loss associated with thermal decomposition, 2) a thermocouple in close proximity to the sample to determine sample temperature, and 3) purge gas to sweep away decomposition gases from the surface of the sample. Sample sizes were chosen to minimize size effects and to maximize the signal to noise ratio. A high thermal conductivity purge gas was needed in the HPTGA to insure that the thermocouple temperature was sufficiently close to the sample temperature. Erickson et al. [3-5] and Clayton [8] give more information regarding the LPTGA and HPTGA experiments, respectively.

Sandia's LPTGA apparatus also included a Fourier Transform InfraRed (FTIR) spectroscope to analyze evolving gases. Alternative techniques using thermal desorption tubes connected to the exhaust from the LPTGA furnace were also used to analyze evolving gases. The product distributions obtained with unconfined samples were significantly different from the results obtained with the partially confined samples. The most notable difference was a large change in the composition of the evolved decomposition products. The unconfined samples evolved more TDI and much less CO_2 than the partially confined samples.

The TGA records the sample mass (m) versus temperature or time. Typically, the normalized sample mass (m/m_o) is plotted as a function of temperature if the sample is ramped at a constant heating rate. If the sample is held at a constant temperature, the normalized sample mass is plotted as a function of time. The TGA experiments discussed in the current report were performed using a variety of heating conditions that included nonisothermal "ramped" experiments as well as "isothermal" experiments. The temperatures of the samples in the ramped experiments were increased at constant heating rates (5ºC/min, 20ºC/min, and 50ºC/min) from ambient temperature to about 575ºC.

Two types of isothermal experiments were considered – “one-step isothermal” or “two-step isothermal” experiments. The “one-step isothermal” experiments considered samples heated from ambient temperature at a constant rate of 20ºC/min to a temperature of 300ºC; the sample temperature was then held at 300ºC for one hour or longer. The “two-step isothermal” experiments considered samples heated from ambient temperature at a constant heating rate of 40ºC/min to a temperature of 300ºC; the samples were then held at 300ºC for one hour or longer. Following this first constant temperature period, the “two-step isothermal” samples were then heated from 300ºC to 400ºC at a rate of 40ºC/min, the samples were then held at a second constant temperature period of one hour or more at 400ºC. The three nonisothermal ramped experiments in this report are referred to as 5, 20, and 50 representing temperature ramp rates of 5ºC/min, 20ºC/min, or 50ºC/min. The isothermal experiments are referred to as 250, 270, 300, and 300/400 representing a 250ºC one-step isothermal experiment, a 270ºC one-step isothermal experiment, 300ºC one-step isothermal experiment, and a 300ºC/400ºC dual isothermal experiment, respectively.

The mean value method [28,29] was used to calculated the mean and standard deviation of the normalized sample mass fraction (m/m_o), also known as the solid fraction (s_f), as a function of the heating conditions by assuming that the input parameters are independent random variables and that the response is linear. The mean solid fraction, μ_{sf}, and the standard deviation of the solid fraction, σ_{sf}, was determined using a simple Taylor series expansion of solid fraction, $s_f(\xi_i)$, about the mean of the individual random variables or input parameters, μ_i, by neglecting higher order terms as follows:

$$\mu_{s_f} = S_f(\xi)\big|_{\xi=\mu_i} \tag{56}$$

$$\sigma_{s_f}^2 = \sum_{i=1}^{n} \left[\sigma_i \frac{\partial s_f(\xi)}{\partial \xi_i} \Big|_{\xi=\mu_i} \right]^2 . \tag{57}$$

Equation (56) is a single-sample approximation of the mean solid fraction calculated as a function of temperature with the finite element model with all input parameters, ξ_i, equal to the mean values, μ_i. In Eq.(57), σ_{sf} is the standard deviation of the solid fraction; σ_i is the standard deviation of the i^{th}-input parameter (random variable); and μ_i is the mean value of the i^{th} input parameter.

The relative importance of each input variable to the uncertainty in the calculated solid fraction can be determined from the scaled sensitivity coefficients, γ_i, defined as:

$$\gamma_i = \frac{\sigma_i}{\sigma_{s_f}} \times \frac{\partial s_f(\xi)}{\partial \xi_i} , \tag{58}$$

where

$$-1 \le \gamma_i \le 1 \tag{59}$$

and

$$\sum_{i=1}^{n} \gamma_i^2 = 1 . \tag{60}$$

The input variables that contribute the most to the uncertainty in the calculated solid fraction also have the largest absolute sensitivity values. The sign of the scaled sensitivity coefficients indicate that an increase in the input parameter value causes an increase in the value of the response

function or solid fraction. Likewise, a negative sensitivity coefficient indicates that an increase in the input parameter value causes a decrease in the response function value. The square of the sensitivity coefficient is referred to as the importance factor, γ_i^2, which can be used to easily identify important input variables that contribute to the calculated uncertainty. The term "importance factor" is a misnomer. The importance factor only shows the relative importance of a parameter with respect to the uncertainty calculation. All model parameters are important and necessary to determine the foam response. The importance factors merely indicate which parameters contribute most to the response uncertainty. The importance factors are highly dependent on the estimates of the individual parameter uncertainty expressed in this report as a standard deviation.

Thermophysical properties are not needed to calculate the solid fraction when the temperature history of the sample is known. The primary variables that contribute to the standard deviation of the solid fraction for the ambient pressure TGA simulations are the activation energies (E_i) and the distributed activation energy parameter (σ_E). The interaction energy also contributes to the uncertainty for the pressurized TGA experiments. The derivatives in Eq. (57) were obtained using a central differencing technique with a finite difference step size of 0.01 times the mean input parameter. Thirty-five function evaluations were required to obtain the derivatives for the ambient pressure experiments: two for each of the 16 activation energies, two for the distributed activation energy parameter, and one evaluation using the mean input values.

A Monte Carlo technique was also used to calculate the mean solid fraction, μ_{sf}, and the standard deviation of the solid fraction, σ_{sf}, for the ambient pressure experiments ramped at 20ºC/min. The Monte Carlo method is a rigorous method to propagate parameter uncertainty into model results and was used to verify that the Mean Value method described by Eqs. (56)-(60) are acceptable. Traditional Monte Carlo methods use simple random samples to propagate uncer-

tainty into computational results. The number of samples required for adequate representation of the response function is on the order of 10,000 samples. A more efficient, *constrained sampling* technique was used in the present report: Latin Hypercube Sampling, (LHS). The LHS technique developed by McKay et al. [30] selects *n* different values for each of the 17 variables, ξ_i. In this report, the number of samples, *n*, was selected to be 250, which is more than adequate considering Hobbs and Romero [28] showed that LHS sample sizes of 25 and 50 give essentially the same result as a sample size of 300,000.

In the LHS method, the range of each input parameter is divided into *n* non-overlapping intervals based on equal probability. One random value from each interval is selected according to the probability density function in the interval. The *n* values thus obtained for ξ_1 are paired in a random manner with the *n* values obtained for ξ_2. These *n* pairs are then combined in a random manner with the *n* values of ξ_3 to form *n* triplets, and so on, until *n* sets of the 17 input variables are formed. The solid fraction history is then calculated *n* times with the *n* different sets of input parameters. The mean and standard deviation of the solid fraction history are then calculated from the *n* sets of responses. More information on the LHS technique can be found in [31].

8.1 Experimental Observations

Figure 8.1 shows the measured RPU TGA mass loss profiles at as a function of various pressures (0.1, 0.5, 1.0, and 3.0-Mpa), heating rates (5, 20, and 50ºC/min), and various levels of confinement for samples ramped at 20ºC/min (open pan, 1-mm orifice, 0.4-mm orifice, and 0.06-mm orifice). The sample masses used in the pressure and heating rate study (Figs 8.1.A and 8.1.B) were ~5-mg; and the sample masses used in the confined experiments (Fig 8.1.C) were ~2-mg samples. Sample sizes were chosen to minimize size effects and to improve the signal to noise ratios.

The effect of increasing pressure and confinement (retention of decomposition gases by using smaller vent areas) were similar – the dynamic mass loss (TGA profiles) shifted to higher temperatures. High pressures cause large polymer fragments with low partial pressure to remain in the condensed phase. At higher temperatures, these large polymer molecules break into smaller fragments with higher vapor pressures that can readily vaporize. The hydrostatic pressure also affects diffusion of the decomposition gases away from the thermally degrading foam because molecular diffusion is inversely proportional to pressure.

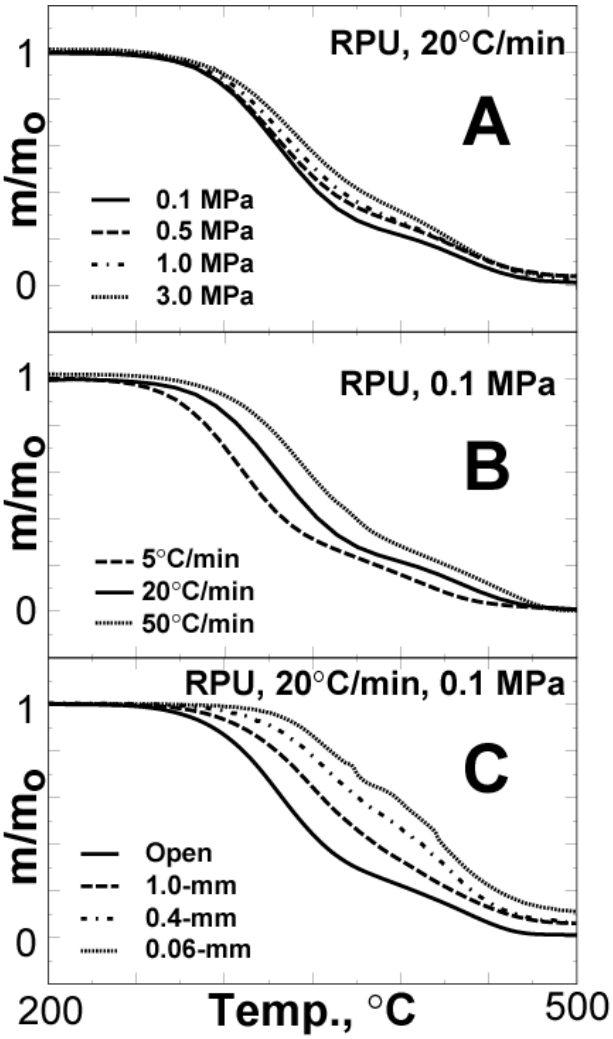

Fig. 8.1. Measured normalized TGA sample mass showing the effect of A) pressure, B) heating rate, and C) confinement.

The shift of the TGA profiles toward higher temperatures due to *confinement* is also related to reduced mass transport resulting in a shift in the decomposition mechanism for the RPU. As the vent area is decreased, the removal of toluene diisocyanate (TDI) from the TGA cup is delayed and the driving potential for mass transport (concentration difference between the bulk phase and the surface) is reduced. The confined TDI molecule may undergo a retrograde reaction by reforming a urethane bond with the decomposing polymer. The urethane bonds can also degrade by evolving CO_2 and converting the urethane linkages into amine linkages that can eventually break and evolve decomposition species such as toluene diamine (TDA). This alternative reaction pathway depends on the degree that the decomposition products are in contact with the decomposing polymer. The increased CO_2 production with confinement (as detected in the real time IR analysis of the TGA offgas) also causes the liquid polymeric material to bubble or even froth at moderate temperatures and pressures. Figure 8.1.C also shows up to 10% of a nonvolatile residue remaining after the experiment.

The following sections present predictions of the effects of pressurization and heating rates on TGA decomposition. The effects of confinement are not modeled. The effects of confinement shown in Fig. 8.1.C are beyond the current capability of the CPUF model as implemented into the finite element model due to an inadequate framework to solve the mass continuity equations for all of the predicted species.

8.2 LHS and Mean Value TGA Predictions (20ºC/min)

Figure 8.2 shows the CPUF predicted mass loss for a sample at ambient pressure heated at 20ºC/min from 25ºC to about 575ºC using the parameters in Table 7.1. In Fig. 8.2.A, the middle line marked with a "*" is the mean response. The lines on either side of the mean response bracket a 95% prediction interval. The 95% prediction interval (based on the CPUF

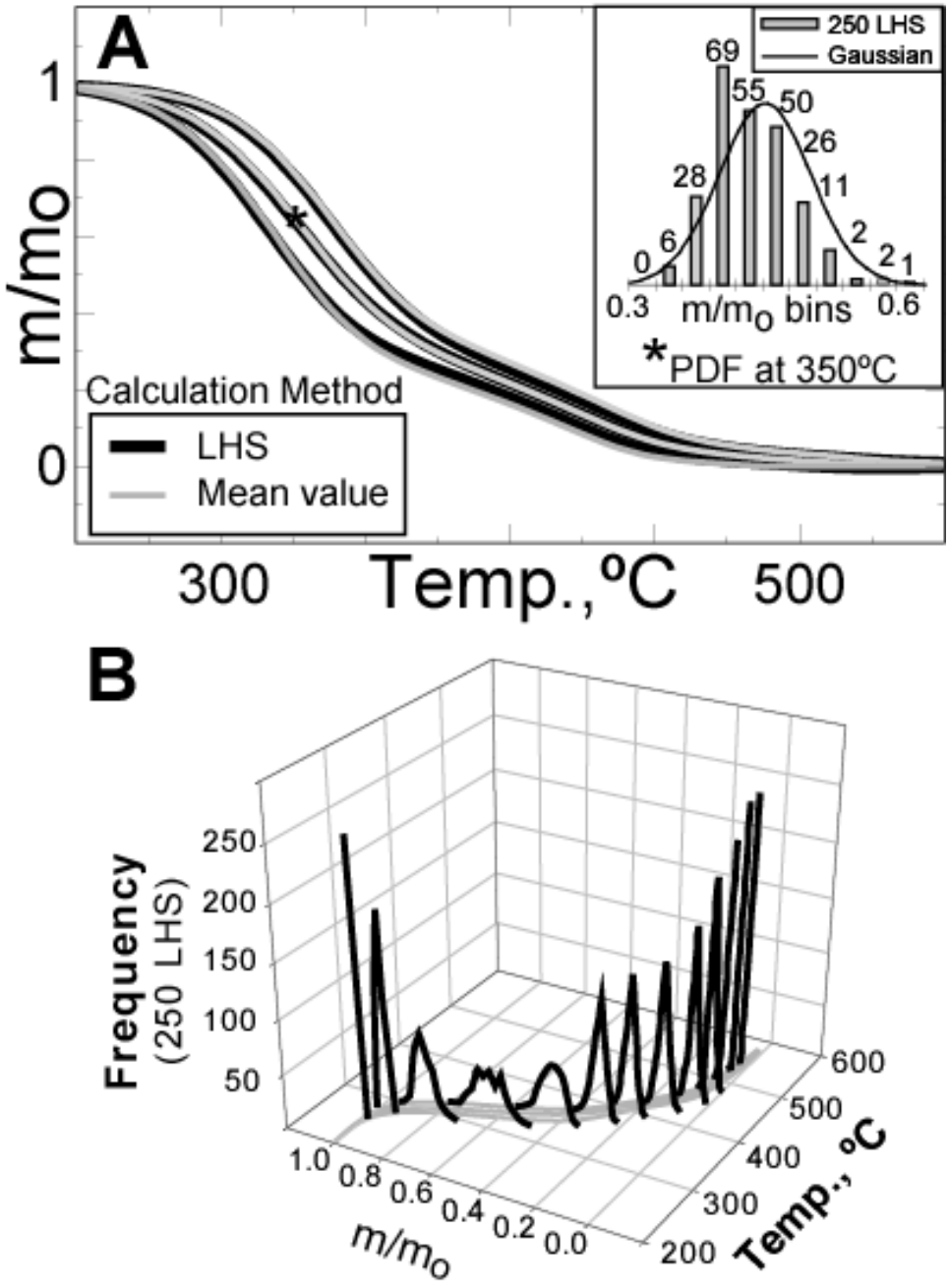

Fig. 8.2. Predicted mass loss for sample at ambient pressure heated at 20ºC/min from 25ºC. A) Mean and 95% prediction limits calculated with 250 LHS samples and mean value methods. The middle line with the * is the mean and the other two lines represent $\mu_{sf} \pm 2\sigma_{sf}$. The inset shows a histogram of the 250 LHS samples at 350ºC. In B) the LHS frequency is plotted for 13 temperatures: 248, 274, 300, 326, 350, 376, 399, 425, 451, 475, 501, 527, and 548ºC. The mean and 95% prediction limit is also plotted in gray.

model) is similar to a 95% confidence interval (based on data). The response is assumed to be normally distributed with the 95% prediction interval based on adding and subtracting $2\times\sigma_{sf}$ from the mean response, μ_{sf}. In this report, the term *prediction interval* will be used when the uncertainty is based on a *model prediction*. The term, *confidence interval* will be used when the response is based on *data*. The response uncertainty is based on the uncertainty in the 16 activation energies and the distributed activation energy model parameter given in Table 7.1.

Figure 8.2.A shows the predicted mean and 95% prediction interval for mass loss using both the LHS and mean value techniques. Both methods give essentially the same response indicating that CPUF chemistry parameters are relatively independent and that the uncertainty of the response is linear. This conclusion is complementary to the work of Hobbs and Romero [28] who also showed that the uncertainty associated with the propagation of a decomposition front in polyurethane foam was linear. Thus, only the mean value theory will be used for the remaining CPUF calculations in this report.

The inset in Figure 8.2.A shows a histogram of the 250 LHS samples at 350ºC. The inset also shows the continuous Gaussian or *normal* probability distribution function (PDF) as a solid line. The shape of the histogram is similar to the shape of the assumed PDF. In Fig 8.1.B, the LHS frequency is plotted for 13 temperatures: 248, 274, 300, 326, 350, 376, 399, 425, 451, 475, 501, 527, and 548ºC. The dispersion (as described by the standard deviation) is shown to be small before the onset of significant decomposition. The predicted dispersion is also small as the mass of the sample approaches zero.

Figure 8.3 shows the TGA mass loss profiles, major importance factors, and minor importance factors for a sample temperature ramped at 20ºC/min at 1-bar and 20-bars pressure. The 95% prediction limit for the CPUF model and the 95% confidence limit for the data are also shown

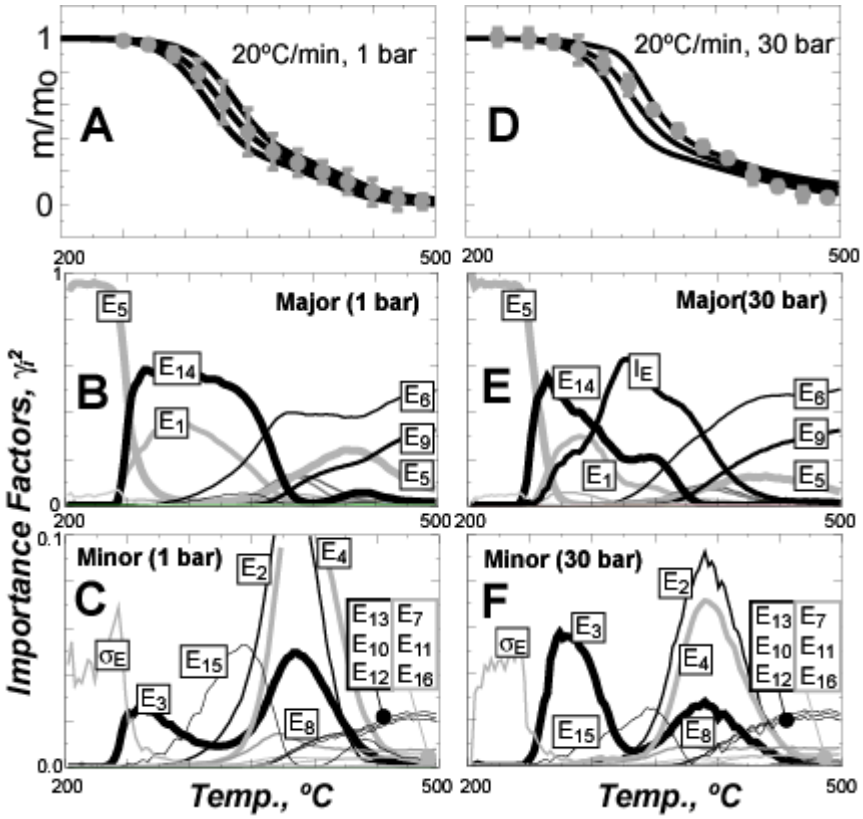

Fig. 8.3. TGA mass loss profiles, major importance factors, and minor importance factors predicted when the foam temperature was ramped at 20ºC/min at 1 bar (A -C) and 30 bar (D-F) pressure. The 95% confidence interval for the mass loss profiles is also given in A and D.

in Fig. 8.3. The most important chemistry parameters for the CPUF model are the activation energies for the initial bridge breaking reactions: E_1 for the primary bridges, E_6 for the semi-degraded primary bridges, and E_{14} for the secondary bridges. The reactions that form CO_2 (reactions 5 and 9) were also found to be important. At elevated pressures, the interaction energy parameter (I_E) becomes important.

8.3 Effect of VLE on HPTGA Predictions

In the current report, the activity coefficients are nearly the same at ambient pressure for the Raoult's law solution model, the Ideal-solution model, and the Regular-solution model as shown previously in Fig. 6.1. As pressure increases, the activity coefficients for these various models change considerably. Figure 8.4 shows the effect of the various activity coefficient mod-

els on the normalized mass loss predicted for a heating rate of 20°C/min and pressures of 5 bar, 10 bar, and 30 bar. Both the Raoult's Law Solution model and the Ideal Solution model predict an excessive shift in the TGA mass fraction (m/m_o) profiles to higher temperatures as the thermodynamic pressure is increased when compared to data. The shift in the TGA mass loss profile to higher temperatures due to increasing pressure is predicted best by the Regular solutions model. However, even this model, *which was fit to the data*, does not match the 30 bar data when the temperature exceeds about 340°C. Better activity coefficient models for both the condensed and gas phases are needed to obtain better agreement at elevated pressure.

The measured shift in the TGA profile with pressure may be caused by a shift in the chemical mechanism as well as a delay in gas evolution caused by the vapor liquid equilibrium (VLE) constraints. In the CPUF model, the VLE submodel is used to determine the split between the vapor and liquid as a function of pressure and does not affect the kinetic model. Conversely, confinement of the decomposition products can influence the kinetic model since reaction path-

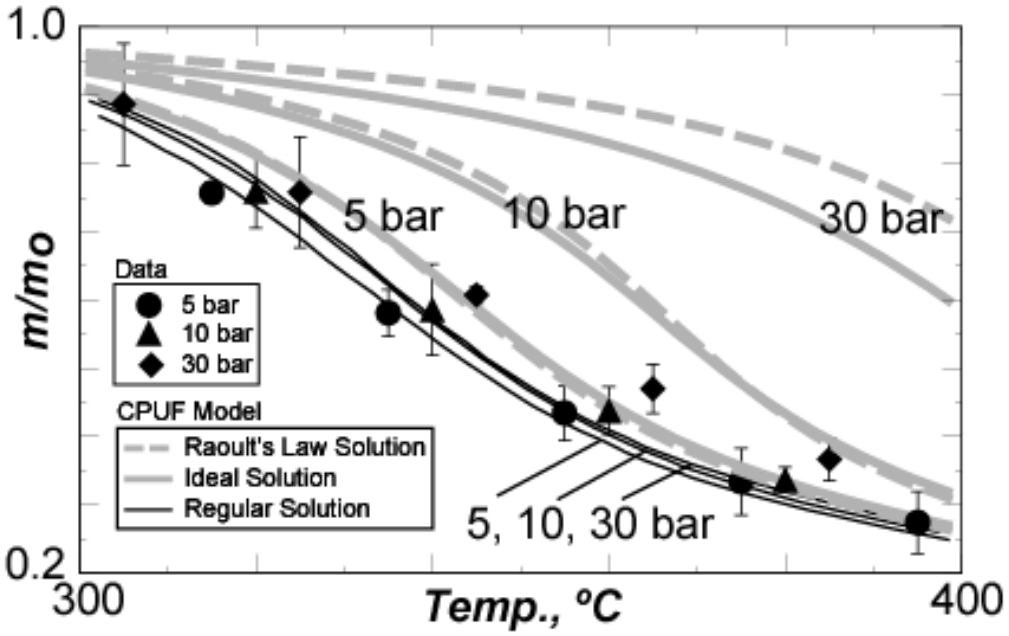

Fig. 8.4. Comparison between CPUF predictions using various vapor-liquid equilibrium models described by Eq. (42). The measured solid fractions are shown as symbols with the error bars depicting a 95% confidence interval. The sample temperature was ramped at 20ºC/min.

ways depend on the local gas concentration, particularly the TDI concentration. The shift in the TGA profile with pressure should be modeled with an accurate VLE model taking into consideration confinement effects that influence mechanism changes as discussed further by Clayton [8]. Limitations in the finite element model, such as the inability to track mass flux into and out of the dynamic radiation enclosure, prevented explicit modeling of confinement effects that change the dominant kinetic mechanism.

8.4 Ramped TGA (5ºC/min, 20ºC/min, 50ºC/min)

Figure 8.5 shows the predicted and measured mass loss for samples heated at various heating rates (5, 20, and 50ºC/min) and pressures (1, 5, 10, and 30 bars). The measured sample heating rates were used as the applied boundary conditions for the CPUF model. In Fig. 8.5; A, B, and C show the effect of heating rate and B, D, E, and F show the effect of pressure. All of the experiments were performed with "low-density" samples that were nominally 12 lb/ft^3 (0.19 g/cm^3), except for sample Foam0410 (Fig. 8.5.C, dashed gray line), which had a nominal density of 25 lb/ft^3 (0.4 g/cm^3). The middle black line is the mean prediction and the outer two black lines represent the 95% prediction interval. The symbols represent the mean measured solid fraction and the error bars represent the 95% confidence interval for the measurement. The symbols without error bars are larger than the 95% confidence interval. All predictions were done using the Regular Solution VLE model.

Only one experiment was performed at 5ºC/min (dashed gray line in A) and only two experiments were performed at 50ºC/min (gray lines in C). Confidence intervals were not calculated for the 5ºC/min and 50ºC/min experiments in A and C because of the limited number of experiments. The sample size, sample density, and heating rates for these three experiments were also outside of the parameter space used to obtain the activation energies for the CPUF model.

For example, the mean sample size in Table 7.5 is 5.14-mg with the 95% confidence interval between 3.7-mg and 6.6-mg. The sample sizes for the 5ºC/min and the 50ºC/min cases were 3.28-

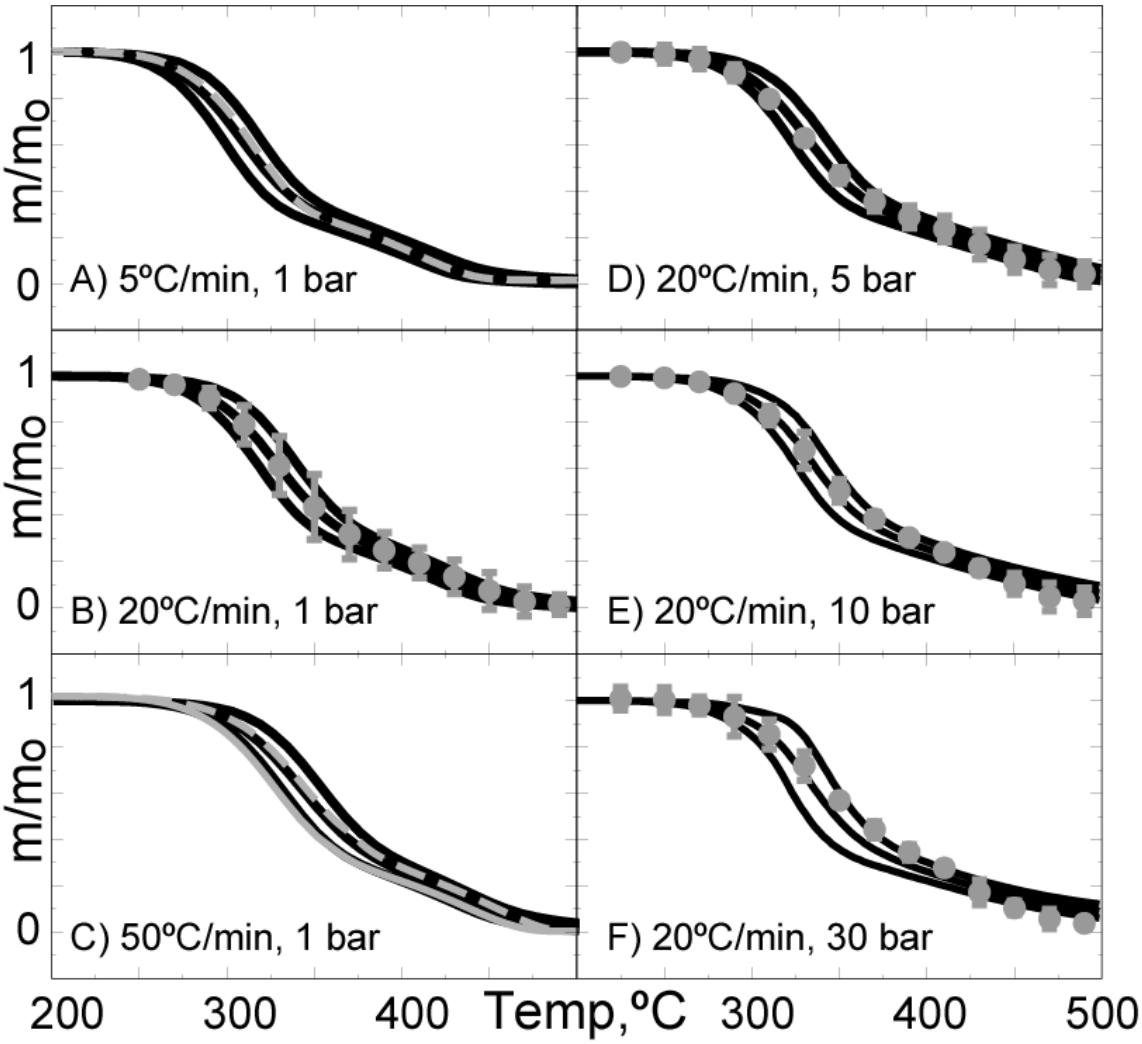

Fig. 8.5. Comparison between CPUF predicted (black lines) and measured (gray lines and symbols) solid mass fraction for various heating rates and pressures. The middle black lines represent the mean and the outer two black lines represent the 95% prediction interval. The gray lines in A and C represent single experiments and the symbols represent the mean measurement with error bars representing a 95% confidence interval.

mg (Foam0116, dash gray line in Fig 8.5.A), 1.86-mg (Foam0128, solid gray line in Fig 8.5.C), and 4.163-mg (Foam0410). Although the sample size for Foam0410 was close to the sample sizes used to determine CPUF activation energies, the density for Foam0410 was about twice as high at ~0.4 g/cm^3 (25 lb/ft^3). In the experiments, increasing sample size and density caused the TGA m/m_o profiles to shift toward higher temperatures. Erickson et al. [4] give more information regarding the effects of sample size and density on TGA profiles. Even though experimental conditions such as sample size and density were significantly different than the data used to obtain the CPUF kinetic parameters, the measured m/m_o TGA profiles were within the 95% prediction interval.

8.5 Predicted populations and compositions for 20ºC/min TGA

Figure 8.6 shows the predicted populations for a TGA sample heated with a 20°C/min temperature ramp. Populations are not pressure dependent since the VLE model, which is used to describe the split between the vapor and condensed phases, is not used to determine populations. Various scales are shown in Fig. 8.6 to show both major and minor population variables. As the bridges break to form danglers, the bridge populations (Λ, Λ', Λ", C, and L) decrease and the dangler populations increase (δ, δ', δ", d). As the dangler populations decrease the populations of P_f, P_f', P_f", and CPN increase. The population of H_2O starts at unity and decreases to zero. The CO_2 population increases as the primary bridge loses CO_2. The CO_2 population also increases, as the secondary bridges are broken.

Figure 8.7 shows the predicted bridge population ($P = \Lambda + \Lambda' + \Lambda'' + C + L$); the critical bridge population ($P_c = 1/\sigma$); the infinite polymer fragment (f_∞); the finite polymer fragment (f_f); the P_f, P_f', P_f", CPN, and CO_2; and the gas fractions at both 1 bar and 30 bar pressure. As the

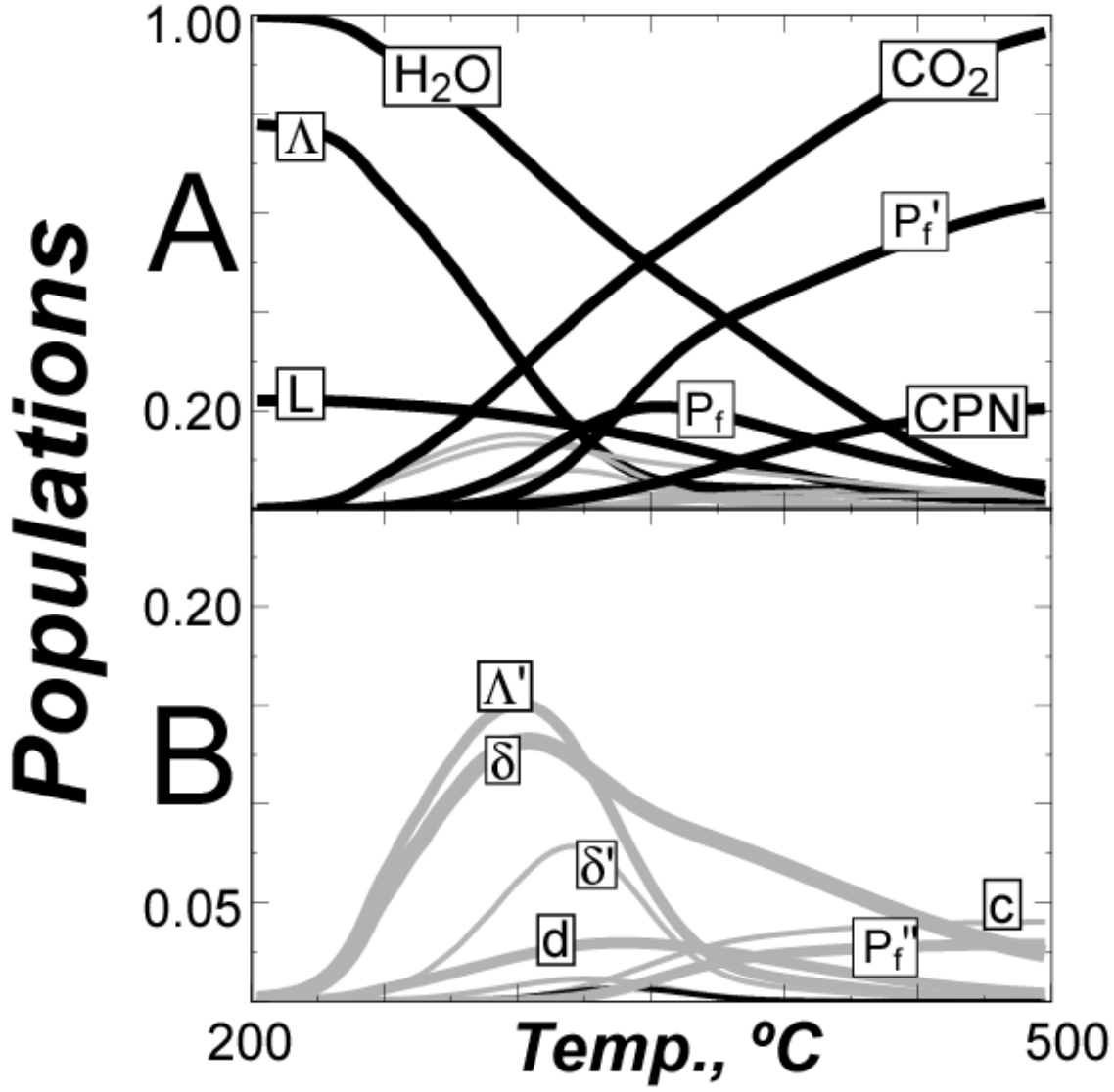

Fig. 8.6. Predicted CPUF populations for a temperature ramp of 20ºC/min. A and B show populations at different scales. Black and gray lines are used to differentiate major and minor populations.

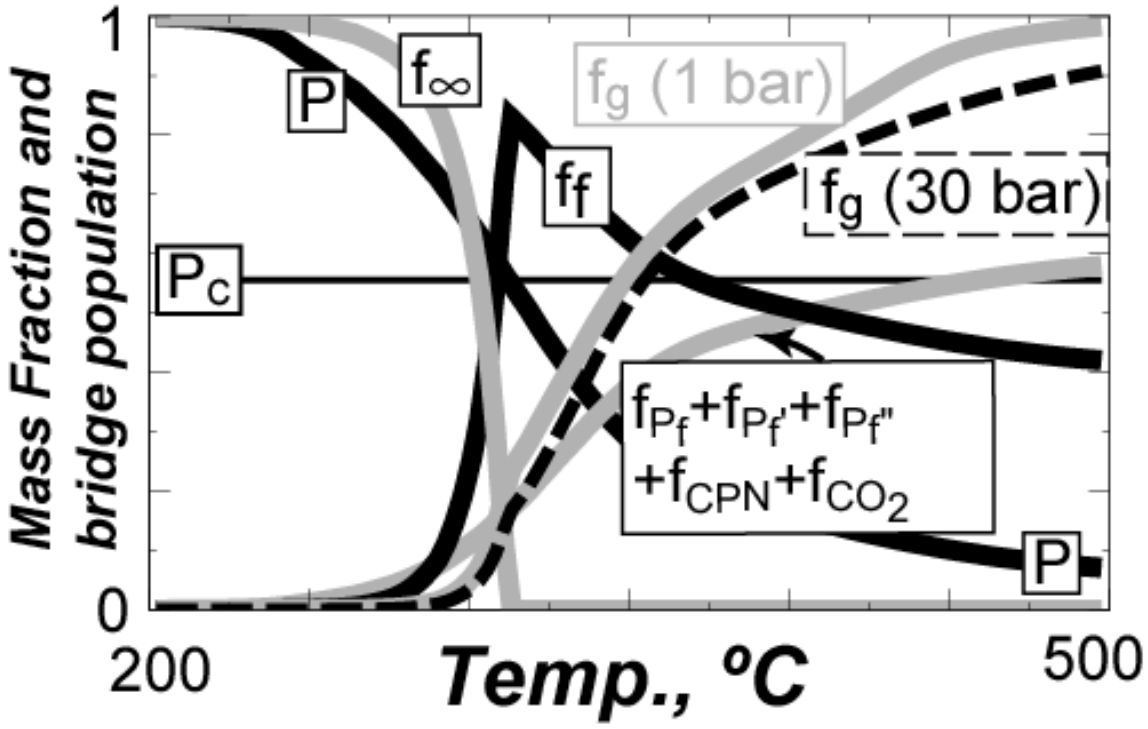

Fig. 8.7. Predicted bridge population (P); critical bridge population (P_c); infinite polymer fraction (f_∞); finite polymer fraction (f_f, see Eq. 35); P_f, P_f', P_f", CPN, and CO_2 fractions; and gas fraction at 1 bar and 30 bars. Foam temperature was ramped at 20°C/min.

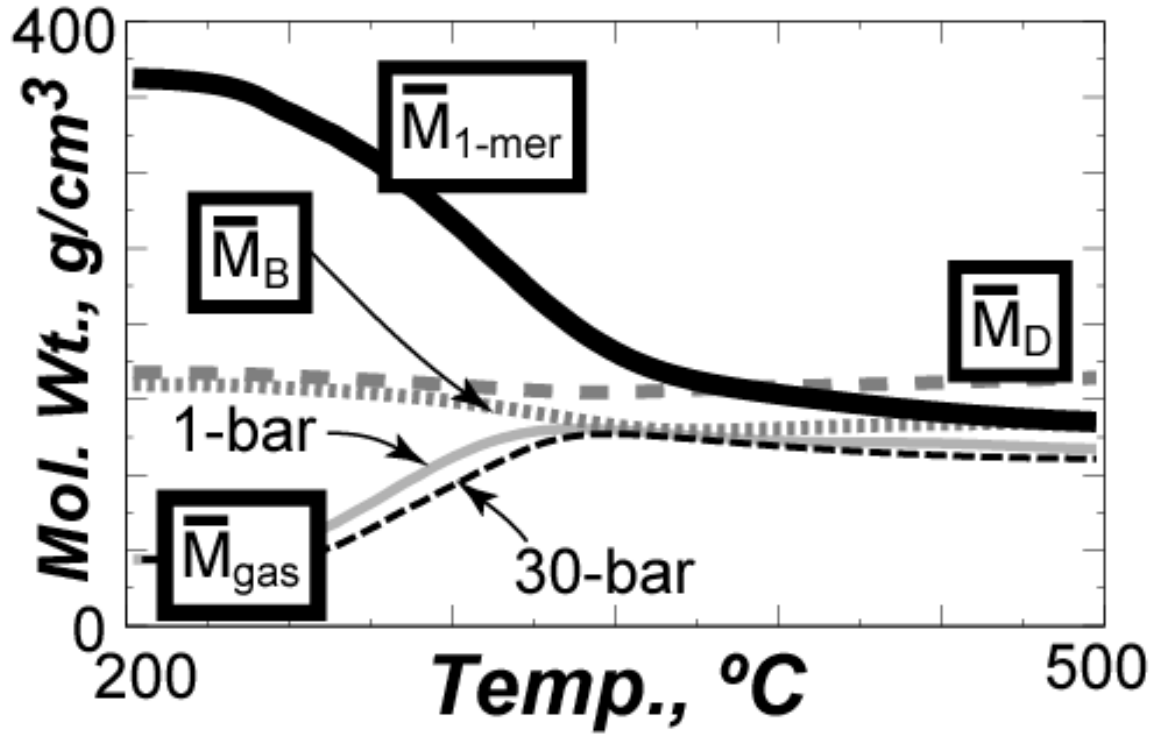

Fig. 8.8. Predicted average monomer (M_1-mer), dangler (M_D), bridge (M_{gas}) molecular weights. The gas molecular weight is given for both 1 bar and 30 bars pressure. The other molecular weights are not pressure dependent. Foam temperature was ramped at 20°C/min.

bridge population crosses the critical bridge population, the infinite polymer fragment goes to zero. All of the populations are the same as a function of pressure. In the CPUF model, pressure only affects the vapor-liquid split as determined with the VLE model. Thus, the predicted gas fraction at 1 bar is different than the predicted gas fraction at 30 bars pressure. With proper accounting for gases in contact with the decomposing foam, the affect of pressure on various populations can also be accounted for. The affect of confinement is discussed further by Clayton [8].

Figure 8.8 shows the average monomer, dangler, bridge, and gas molecular weights for the TGA sample ramped at 20°C/min at 1 bar and 30 bar pressure. Only the gas molecular weight is pressure dependent. The absolute values of the molecular weights are dependent on the predicted gas-phase composition. Since the kinetic parameters for the CPUF chemical mechanisms were obtained with only weight loss data, the gas composition is probably not representative of the actual gas-phase composition. More work is required to get quantitative phase compositions.

8.6 Isothermal TGA (250ºC, 270ºC, 300ºC, 300/400ºC)

The unconfined TGA samples (nominally 5-mg) were heated in open platinum pans. The TGA experiments were designed to examine decomposition mechanisms under conditions that minimize mass transfer and reversible and secondary reactions. Figure 8.9 shows a comparison between predicted and measure condensed mass fractions (foam mass measured by the TGA divided by the initial foam mass) for various isothermal TGA experiments. The 250°C samples were ramped from room temperature (27°C) to 250°C in about 14 minutes; the 270°C samples were ramped from room temperature to 270°C in about 14 minutes; the 300°C samples were ramped from room temperature to 300°C in about 16 minutes; and the dual isothermal samples were ramped from room temperature to 300°C in 8 minutes, held for 2 hours, ramped to 400°C in

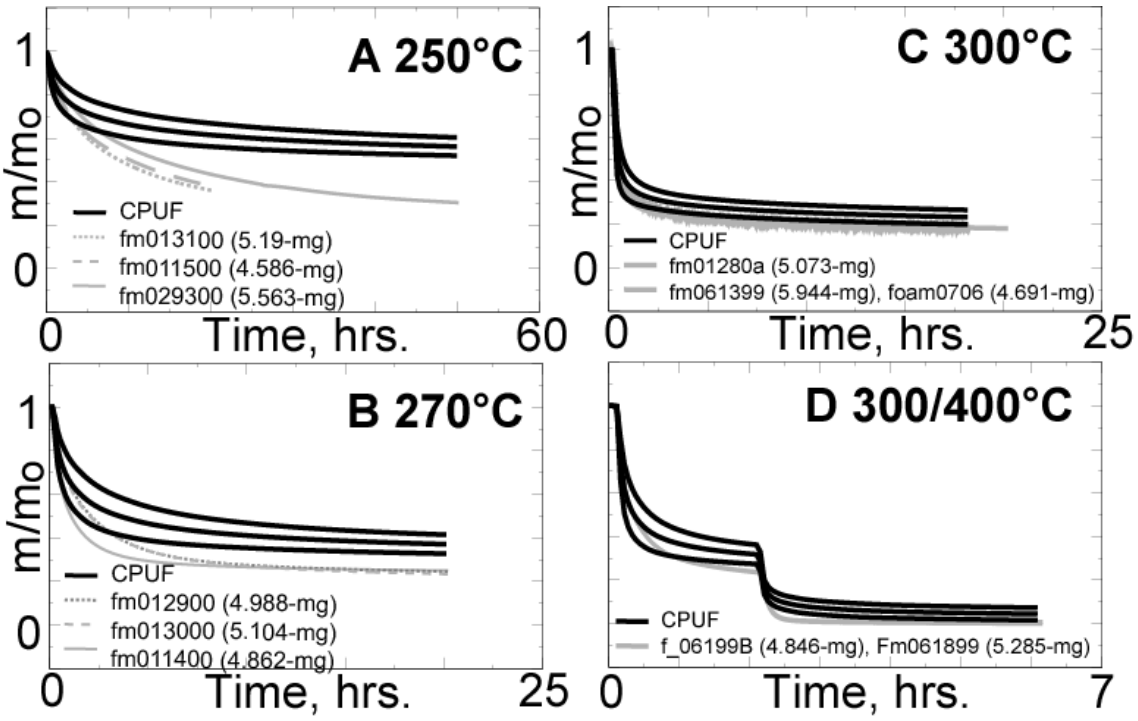

Fig. 8.9. Comparison between CPUF predicted (3 black lines) and measured (gray lines) solid mass fraction for various temperature histories at ambient pressure. The middle black lines represent the mean and the outer two black lines represent the 95% prediction interval. The legend gives the name of the experimental run as well as the initial mass of the sample (m_o). The sample temperatures were ramped at 20°C/min and held at A) 250°C for 50 hours, B) 270°C for 20 hours, and C) 300°C for 18-20 hours. In D, the sample temperatures were ramped at 40°C/min to 300°C and held for 2 hours, and then the temperatures were ramped at 40°C/min to 400°C and held for 4 hours.

about 4 minutes and held at 400°C temperature for 4 hours. The predicted mass loss for the 250°C isothermal TGA is in fair agreement for the first 5 hours of the experiment, thereafter the predicted mass loss is significantly less than the measured mass loss. The predicted mass loss for the higher temperature isothermal TGA is in better agreement with the measurements. If most of the primary bridges and none of the secondary bridges break at lower temperatures, asymptotic results would be in better agreement for these isothermal TGA experiments.

9. Mesh Independent Decomposition Front Velocities

This section describes the steady-state decomposition front velocity in a 1D strand of foam using an element death approach. The element death approach, discussed in this section, is used to model the component-scale radiant heat experiments discussed in Section 10. A good test of the CPUF model that includes the effect of spatially resolved temperatures is a 1D decomposition of a strand of foam. The decomposition of a strand of foam is modeled as a column of elements using the finite element code, COYOTE [6], by solving Eq. (48) with a radiation boundary condition at one end of the foam strand and an insulation (adiabatic) boundary condition around the other sides of the strand. The CPUF model has been implemented into COYOTE as an auxiliary-variable user subroutine. The thermophysical properties listed in Table 7.1 are implemented as material properties in COYOTE. In COYOTE, the solid fraction, m/m_o, is determined at each Gauss point and the average solid fraction can be determined for each element. When the solid fraction within an element drops below a specified element death criterion, the element is removed from the computational domain and the surface boundary condition is applied to the newly exposed element — the exposed face of the foam strand exchanges energy via radiative heat transport to a far-field reference radiation temperature.

9.1 Element Death Criterion

In COYOTE, elements were removed from the strand simulation when a specified criterion was reached. Removal of an element from the computational domain is referred to as “element death”. In this report, the solid fraction was used to control the elimination of elements during the computation. The solid fraction calculated within each element is checked every iteration to determine if the element should be removed from the computational domain. If the calculated

solid fraction within an element falls below a specified value, or “death criterion”, the element is removed from the computational domain. The death criterion is correlated to experimental data.

The 20°C/min ramped TGA experiments were used to determine the appropriate value to use for the death criterion. Figure 9.1 shows how the death criterion was selected based on experiment Foam1114 and the CPUF predictions. Figure 9.1 shows the predicted and calculated solid fraction when the sample is near the end of decomposition. At this point, a small amount of residue is left in the TGA pan, which does not decompose at high temperatures. For experiment Foam1114, the residual solid fraction was about 0.01. The intersection of the two tangent lines to the measured solid fraction for Foam1114 determines the temperature corresponding to a CPUF solid fraction (0.04) that is used as the element death criterion. Using the onset of complete decomposition gives a consistent method to determine the element death criterion using the TGA data. Other methods for determining the death criterion should be used when significant liquefac-

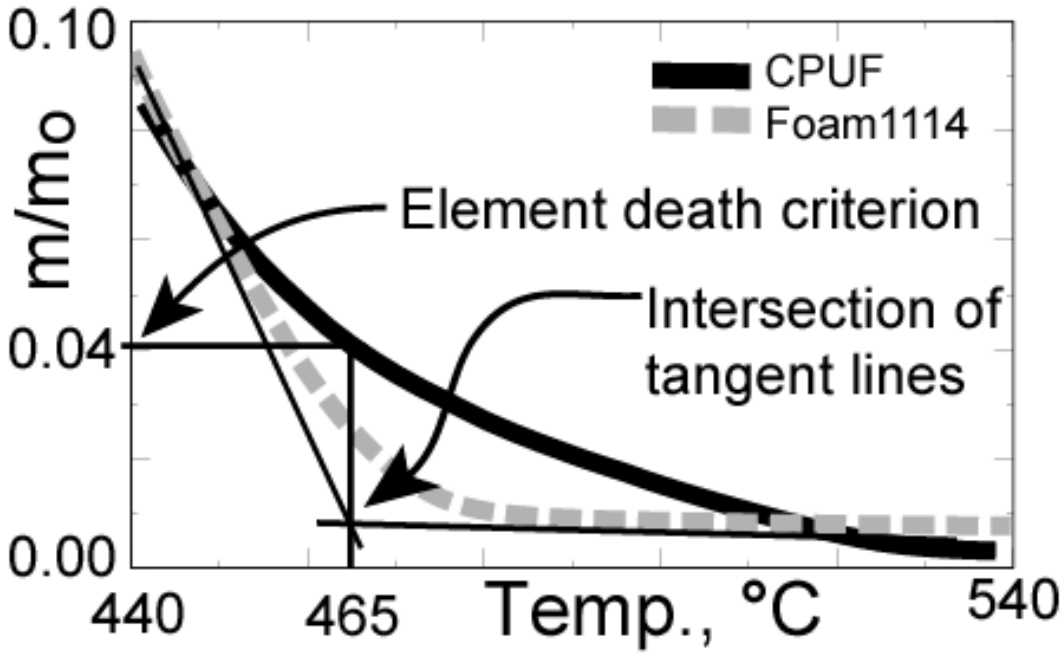

Fig. 9.1. TGA solid fraction contours near the end of decomposition. Tangent lines to the data intersect at 465°C corresponding to the CPUF solid fraction (0.04) used as the element death criterion.

tion occurs. For example, the effective viscosity of the degrading foam may also be used as a element death criterion when liquid formation is significant.

The mean element death criterion and associated uncertainty was determined for each of the 20°C/min LPTGA experiments that were obtained with a TA Instruments Model 2950. The intersection of the tangent lines near complete decomposition was obtained with TA Instrument's Universal Analysis 2000 software using the onset point analysis capability. Only the data taken at Sandia National Laboratories was used to determine the death criterion since the BYU data was not in a form compatible with the TA analysis software. The death criteria determined with the 20°C/min runs are given in Table 9.1. The mean and standard deviation of the death criterion are 0.036 and 0.007, respectively.

Table 9.1. Death criteria for various 20°C/min TGA runs*

Run	Sample	Death Temp., °C	S_f death criterion
1	F_062199	464.7	0.040
2	Fm061499	480.9	0.027
3	Foam1112	465.0	0.040
4	Foam1114	465.2	0.039
5	Foam1117	475.9	0.030
6	Foam1118	472.3	0.033
7	Foam1119	455.3	0.054
9	Foam1204	466.1	0.038
10	Foam1205	469.4	0.035
11	fm102999	476.3	0.030
12	fm103099	473.5	0.032
13	fm110199	468.5	0.036
14	fm11019a	469.7	0.035
	Mean	**469.4**	**0.036**
	St. Dev	**6.6**	**0.007**

*Run 8 removed since it is an outlier

9.2 1D Decomposition Front Velocity Calculations

The response variable for the 1-D analysis was chosen as the steady-state "burn velocity" of the foam, calculated as the derivative of the decomposition front location versus the elapsed time for element death. Figure 9.2 shows the front location calculated using various elements sizes ranging from 1-mm elements to 25-μm elements. The foam strands used for the

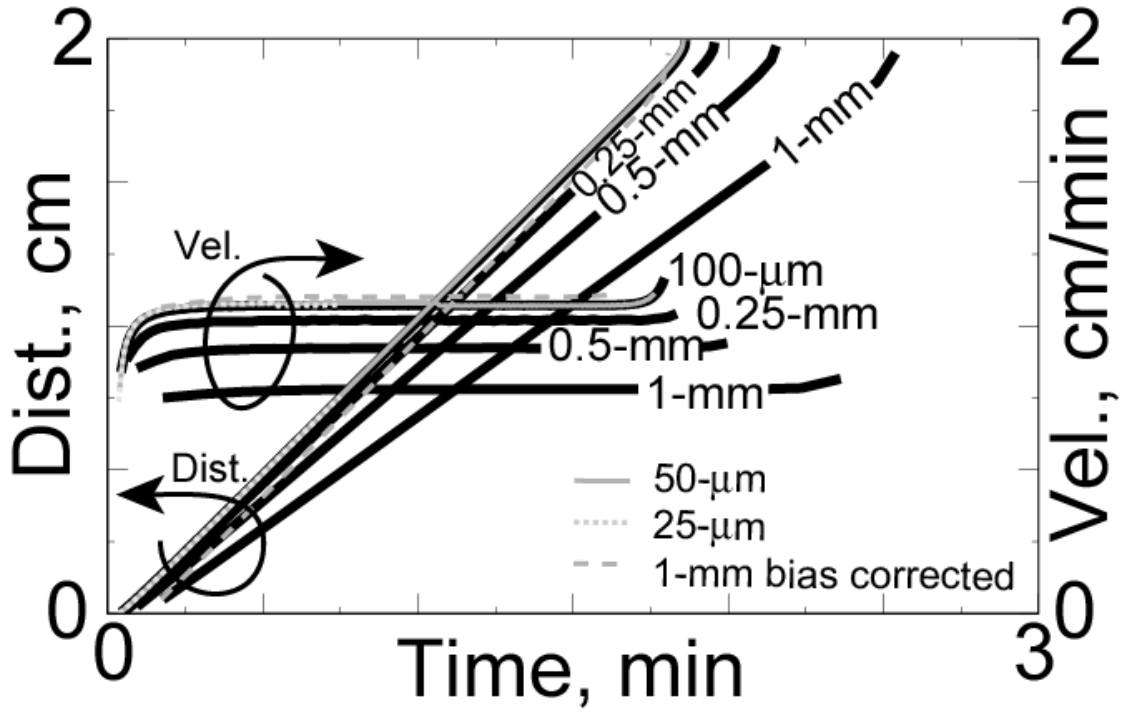

Table 9.2. Grid dependence of steady-state front velocities for 1000°C boundary temperature

Grid size	Vel., cm/min	Grid size	Vel., cm/min
1-mm	0.8	50-μm	1.1
0.5-mm	0.9	25-μm	1.1
0.25-mm	1.0	1-mm†	1.1
100-μm*	1.1		

*Grid independent velocity
†Bias corrected velocity

Fig 9.2. Front location and velocity calculated using various elements sizes ranging from 1-mm elements to 25-μm elements. The element size is indicated on the various curves except for the small elements (25-μm and 50-μm elements) that give essentially the same result. Table 9.2 is included in this figure to show that 100-μm elements are grid-independent and that a 1-mm element solution can be bias corrected to give the correct front velocity.

calculations in Figure 9.2 were exposed to a 1,000° C radiative temperature. The decomposition front location is taken as the centroid of the element associated with the radiation boundary. Elements are removed from the computational domain when the calculated solid fraction (m/m_o) dropped below the mean element death criterion, 0.036.

The front velocities shown in Fig. 9.2 start at zero and then increase rapidly to a steady-state velocity. The velocity increases near the end of the strand of foam due to the adiabatic boundary condition enforced at the end of the strand of foam. The steady-state front velocities plotted in Fig. 9.2 are also listed in Table 9.2. As the size of the element decreases, a grid independent velocity was determined. The velocity of the front became independent of the size of the element, or grid independent, when the size of the element was about 100-μm.

The velocities calculated in Fig. 9.2 were calculated using COYOTE's auto time-stepping scheme discussed by Gartling et al. [1] with an integration convergence tolerance of 10^{-4}. The solutions were also constrained to satisfy the following derivative smoothness criterion:

$$\Delta t \leq 0.003 \frac{\Delta x}{V}, \tag{61}$$

where Δt, Δx, and V represent the time-step, element size, and decomposition front velocity, respectively. Equation (61) was used to force the time-step to be small to avoid noisy velocities calculations as discussed by Hobbs and Romero [28]. The time-step constraint was determined by noting that the element size divided by the front velocity gives the time required for the front to traverse a single element. The constant 0.003 was determined by doing a time-step convergence study such as shown in Fig. 9.3 using the steady-state velocity calculation with 50-μm grids. In Fig. 9.3, a time-step of 8×10^{-4} was considered fully converged. The constant 0.003 was thus obtained by $\Delta t \times V/\Delta x = (8\times10^{-4})\times(1.09/60)/0.005 = 0.003$.

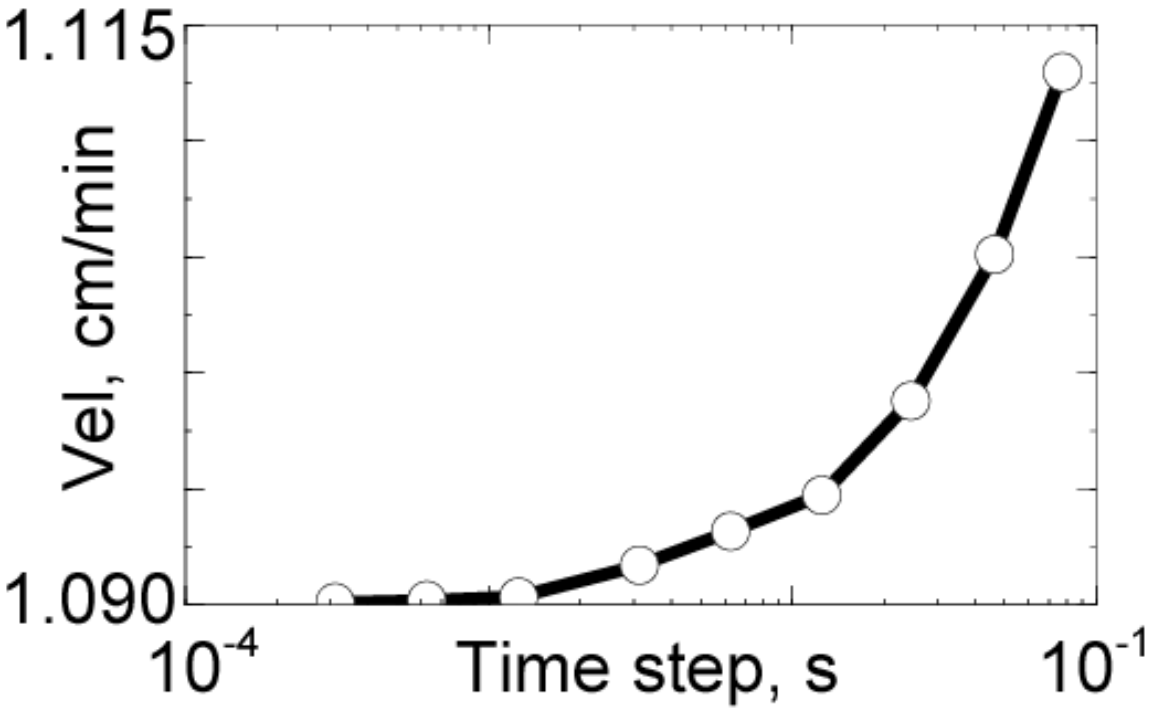

Fig. 9.3. Grid independent velocities calculated with various fixed time steps determined with a radiation boundary temperature of 1000°C.

The derivative smoothness criterion given in Eq. (61) ensures that the time-step is small enough so that the time of element death can be calculated precisely. Small perturbations in the time of element death lead to a noisy time-distance calculation, which can cause large fluctuations in the velocity time calculation. Although the derivative smoothness criterion gives smooth velocities, the excess amount of calculations is not necessary for accurate distance time simulations. The calculated velocity using the auto time-step function in COYOTE is essentially the same as the velocity calculated using the small time-step constraint given in Eq. (61) if the distance time curve is smoothed prior to determining the derivative.

Numerical noise is also related to the discrete removal of elements from the computational domain. Figure 9.4 shows the temperature gradient in element No. 20 for a 650°C radiation temperature using 0.6-mm elements. The first 20 elements are also shown in Fig. 9.4 cen-

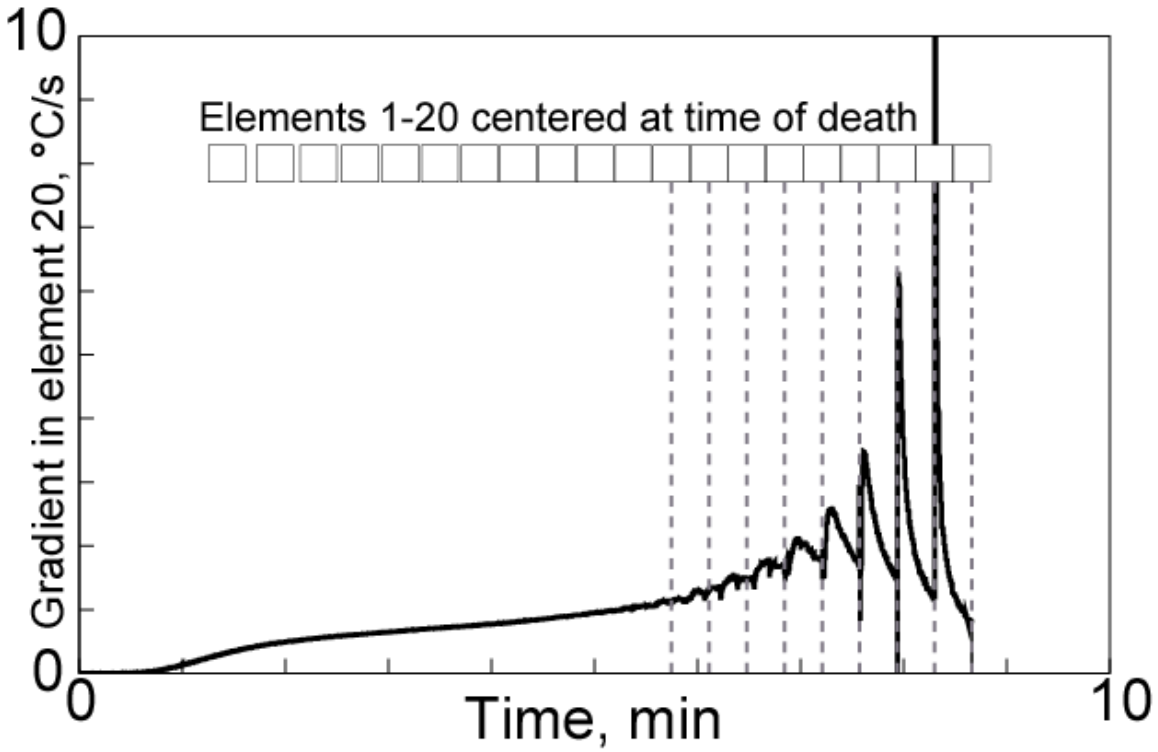

Fig. 9.4. Temperature gradient in element 20 for a strand of foam exposed to a 650°C radiation temperature.

tered about the time of "element death." The noise is associated with the death of neighboring elements and is related to the source of the velocity sensitivity to the computational time-step.

The next section of this report will focus on determination of the standard deviation of the decomposition front velocity and ranking the importance of the CPUF model parameters using the MV sensitivity analysis. Fully grid and time-step converged solutions using 100-μm elements and time-steps that satisfied Eq. (61) were used in the MV analysis.

9.3 Mean Value Analysis

A mean value analysis was performed to obtain the mean decomposition front velocity, μ_V, and the standard deviation of the decomposition front velocity, σ_V, by doing a simple Taylor series expansion of the decomposition front velocity, $V(\bar{\zeta})$, about the mean of the individual random variables or input parameters, ζ_i, neglecting higher order terms as follows:

$$\mu_V = V(\bar{\zeta})\Big|_{\bar{\zeta}=\bar{\mu}} \tag{62}$$

$$\sigma_V^2 = \sum_{i=1}^{n}\left[\sigma_i \frac{\partial V(\bar{\zeta})}{\partial \zeta_i}\Big|_{\bar{\zeta}=\bar{\mu}}\right]^2 . \tag{63}$$

Equations (62) and (63) are similar to the Equations (56) and (57) except that the response variable was chosen as the steady-state velocity of the decomposition front. The simple mean value approximation is adequate for the polyurethane decomposition model discussed in this report since the response surface is essentially linear and the higher order terms in the Taylor series are negligible. This conclusion is supported by the LHS calculation presented in Section 8.1.

Equation (62) is a single-sample approximation of the mean decomposition front velocity calculated with the finite element model with all input parameters equal to the mean values, $\bar{\mu}$. In Eq. (63), σ_V is the standard deviation of the decomposition front velocity (response variable) and σ_i is the standard deviation of the i^{th}-input parameter (random variable). The derivatives in Eq. (63) were obtained using a central differencing technique using a finite difference step size of 0.001 times the mean input parameter. For each temperature, 51 function evaluations (two for each random variable plus one evaluation at the mean input values) were required to obtain the derivatives for the 25 random variables.

The relative importance of each input variable to the uncertainty in the decomposition front velocity can be determined from the weighted sensitivity coefficients, γ_i, defined as:

$$\gamma_i = \frac{\sigma_i}{\sigma_V} \times \frac{\partial V(\bar{\zeta})}{\partial \zeta_i}, \tag{64}$$

where

$$-1 \le \gamma_i \le 1 \tag{65}$$

and

$$\sum_{i=1}^{n} \gamma_i^2 = 1. \tag{66}$$

The input variables that contribute the most to the uncertainty in the decomposition front velocity also have the largest absolute sensitivity values. The sign of the sensitivity coefficients indicate that an increase in the input parameter value causes an increase in the value of the response function or decomposition front velocity. Likewise, a negative sensitivity coefficient indicates that an increase in the input parameter value causes a decrease in the response function value. The square of the weighted sensitivity coefficient gives the importance factor, γ_i^2, which can be used to easily identify important input variables that contribute to response uncertainty.

Figure 9.5.A shows the mean velocity with error bars representing the 95% prediction interval calculated by adding and subtracting 1.96-σ from the mean velocity prediction. The results shown in Fig. 8.5 were calculated with the mean and standard deviation of the input

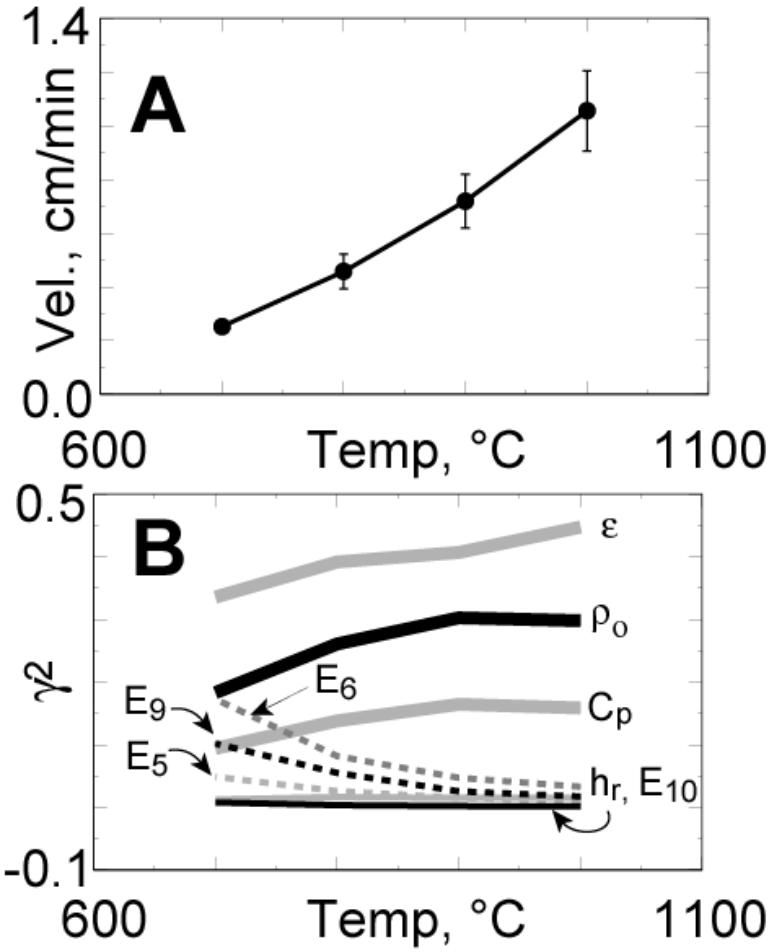

Fig. 9.5. A) Predicted decomposition front velocity as a function of radiation boundary temperature. Error bars represent the 95% prediction interval. B) Importance factors indicating CPUF parameters that contribute more than 1% to the variation in the decomposition front velocity.

parameters given in Table 7.1. The most important input parameters are shown in Fig. 9.5.B to be the emissivity of the foam followed by the foam density and specific heat. The reaction enthalpy and the activation energies associated with Reactions 5, 6, 9, and 10 are also shown to be important factors in Fig. 8.5.B. An increase in emissivity will cause the decomposition front velocity to increase, whereas an increase in density or specific heat will cause the decomposition front velocity to decrease.

9.4 Discretization Bias Correction

As shown in Section 9.2, the steady-state decomposition front velocity is strongly dependent on the size of the element, especially if the elements are larger than 100-μm. For elements that are 100-μm or less, the decomposition velocity is independent of the element size. Grid dependency is related to the discrete removal of elements and the inheritance of the radiation boundary condition on the newly exposed element. The application of the radiation boundary condition to newly exposed surfaces is a discrete rather than a continuous process. As the elements become smaller, the propagation of the front becomes more continuous.

Large elements contain more mass than small elements. Consequently, the lifetimes of larger elements are longer than the lifetimes of smaller elements with the same radiation boundary condition. Since element death is delayed when larger elements are used, the reapplication of the radiation boundary condition to the next element is also delayed, making the decomposition front move more slowly, since radiation to a surface is a more efficient means of heat transfer than conduction through an element. The size of the element has no effect on the front velocity when the element dimensions are 100-μm or less. Since 100-μm elements are impractical for realistic system-level models, a correction is needed to account for the bias associated with discretization.

In the current effort, the discretization bias correction is a subgrid model that increases the thermal conductivity near the decomposition front depending on the element size and heat flux driving the reaction front. Measured thermal conductivities are not changed in the subgrid model. However, the extrapolated thermal conductivity is used to obtain grid size independent decomposition front velocities. For example, Table 7.2 showed measured thermal conductivities up to 250°C. For the grid independent solutions with element sizes less than or equal to 100-μm, measured thermal conductivities are used when the temperature is 250°C or less. When tem-

perature exceeds 250°C, thermal conductivities were linearly extrapolated between the measured conductivity at 250°C, $k_{250°C}$, and the extrapolated conductivity at 3500°C, $k_{3500°C}^{\text{linear extrapolation}}$.

For larger element dimensions (>100-μm), the extrapolated conductivity at 3500 C can be multiplied by a bias correction to match the decomposition front velocities calculated using 100-μm elements with the following equation:

$$k_{3500°\text{C}}^{\text{bias corrected}} = bias \times k_{3500°\text{C}}^{\text{linear extrapolation}}. \tag{67}$$

The bias correction factor, *bias*, in Eq. (67) was determined using the DAKOTA optimization toolkit [24] by minimizing the difference between predicted front velocities using 100-μm elements and various larger element sizes over a wide range of far-field radiation boundary conditions. The results of the bias optimization are given in Fig. 9.6.

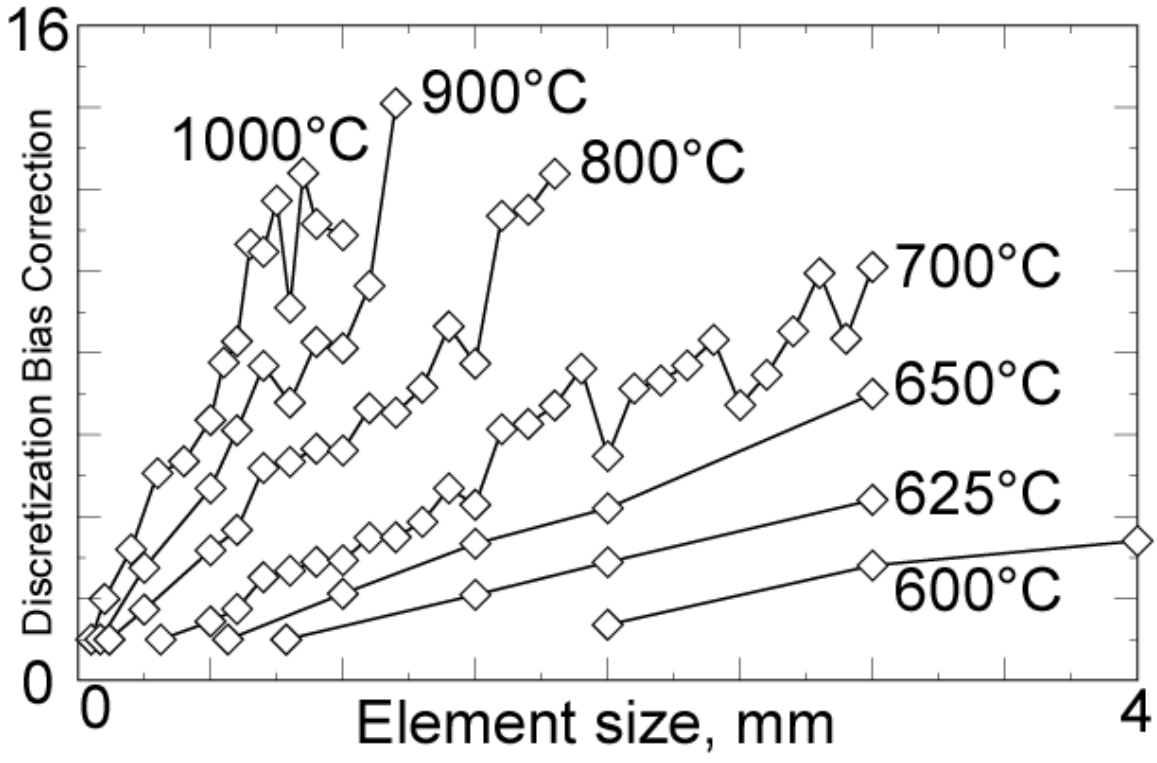

Fig. 9.6. Bias correction factor for various radiation boundary temperatures.

Figure 9.6 shows bias corrections for element sizes up to 4-mm. Discretization bias corrections were only obtained for elements sizes up to 1-mm elements when the radiation boundary temperature was set to 1,000°C. Above 1000° C, the bias corrected solutions for 1-mm elements using the DAKOTA optimizer were somewhat erratic. The erratic behavior may be related to the noisy temperature gradients as shown previously in Fig. 9.4. If the applied heat flux is less than the heat flux produced by a 1000°C far-field radiation boundary condition, a *larger* bias-corrected element dimension can be used. For calculations involving exposure to fire-like boundary conditions, a detailed bias correction was obtained for elements that are nominally 1-mm in dimension.

Figure 9.7.A shows that the bias correction factor for 1-mm elements varies linearly with the radiation boundary condition. To apply the bias correction in Fig. 9.7.A to general boundary conditions, the temperature gradient within the individual elements needs to be examined closely. As long as the temperature within individual elements is less than or equal to 250°C, then the measured thermal conductivity values should be used. If the element exceeds 250°C, the temperature gradient within the elements was used to determine the bias correction. Figure 9.7.B shows that the bias correction factor for 1-mm elements varies quadratically with the temperature gradient determined once the element reaches a temperature of 250°C as follows:

$$bias = 1.57 + 0.538\left(\tfrac{dT}{dt}\right) - 0.00812\left(\tfrac{dT}{dt}\right)^2 \tag{68}$$

For extreme conditions, the bias correction factor is determined from the following equation:

$$bias = \begin{cases} 10.48 & \tfrac{dT}{dt} \geq 33.1 \\ 1 & \tfrac{dT}{dt} \leq 1.55 \end{cases} \tag{69}$$

where 10.48 is the maximum bias correction and 1 signifies no bias correction.

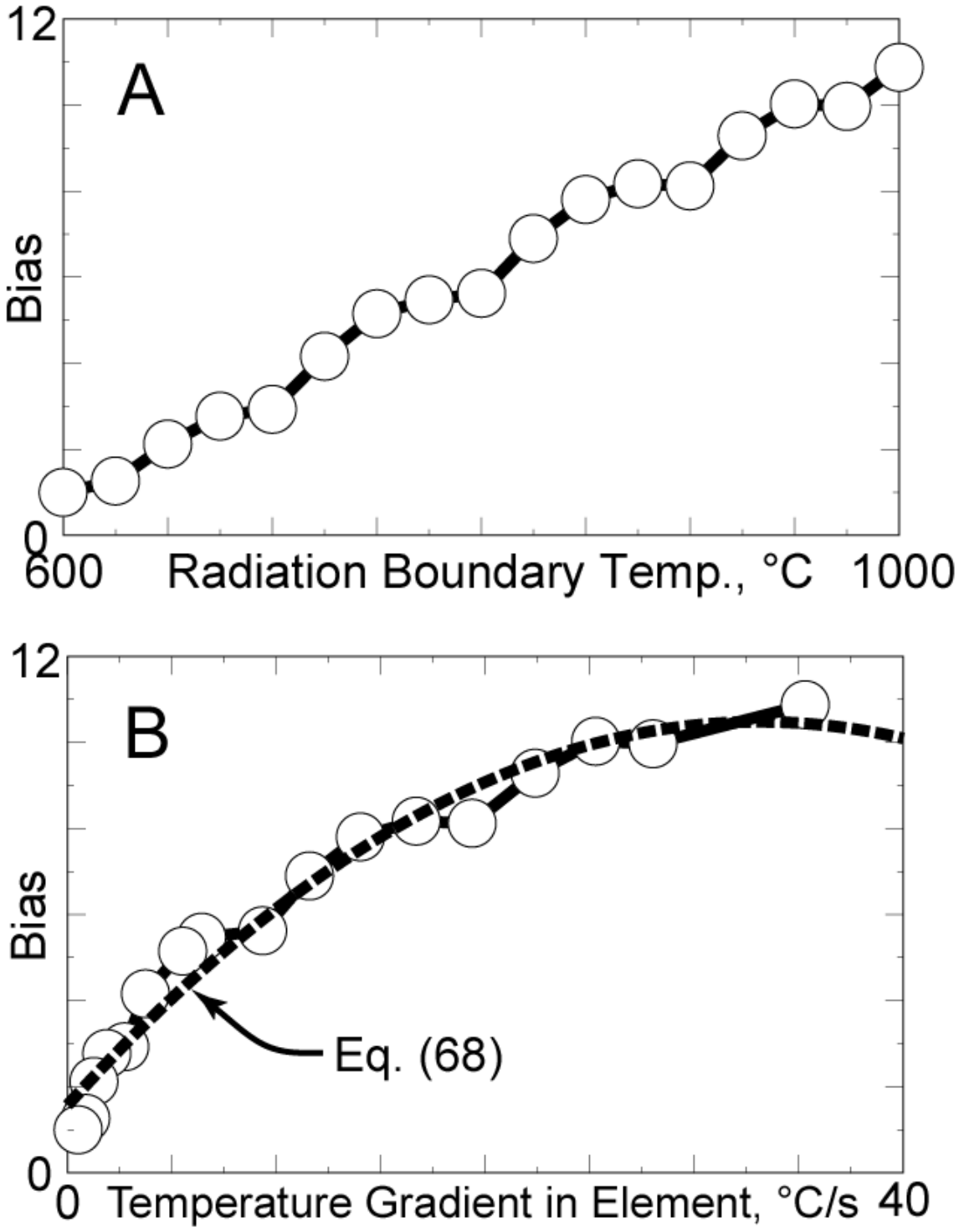

Fig. 9.7. Discretization bias correction for 1-mm elements. Bias correction plotted as a function of A) radiation boundary temperature and B) temperature gradient in element when temperature exceeds 250°C.

Using the 1-mm bias correction, the savings in terms of the number of elements for a mesh independent solution using 100-μm elements in 1-D, 2-D, and 3-D are 10:1, 100:1, and 1,000:1, respectively. Figure 9.8 graphically shows the saving for 3-D problems. The bias correction was implemented into COYOTE [1] with a user subroutine for the thermal conductivity. A more general bias correction based on both the element size and temperature gradient is possible. A generalized bias correction would require a characteristic dimension for each element used by the finite element code.

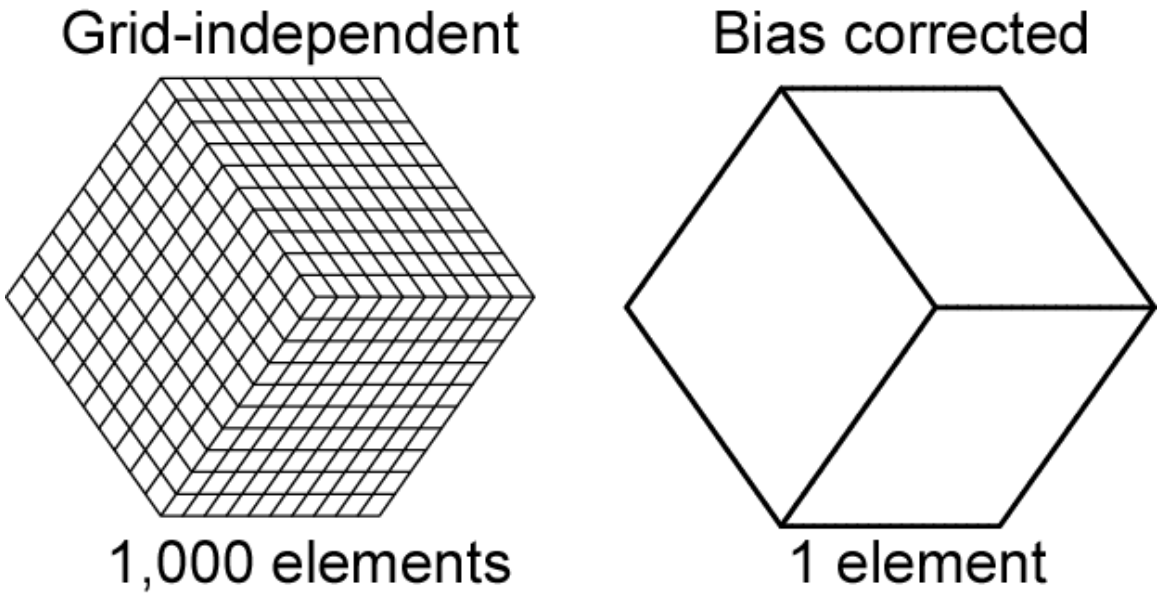

Fig. 9.8. Bias corrected mesh showing 1,000:1 savings over grid independent mesh.

Figure 9.9 shows a test problem run with both 50-μm elements and 1-mm elements. In Fig. 9.9, the two-dimensional axisymmetric geometry of the sample problem is shown with a 4-mm diameter by 6-mm long right circular cylinder of 304 stainless steel (SS) embedded in a 1-cm diameter by 1-cm long right circular cylinder of polyurethane foam. The face of the SS cylinder is located 4-mm from the heated end of the confinement. The temperature at the bottom of the confinement is ramped from 27°C to 1,000°C in 180 seconds. The temperature at the top corner of

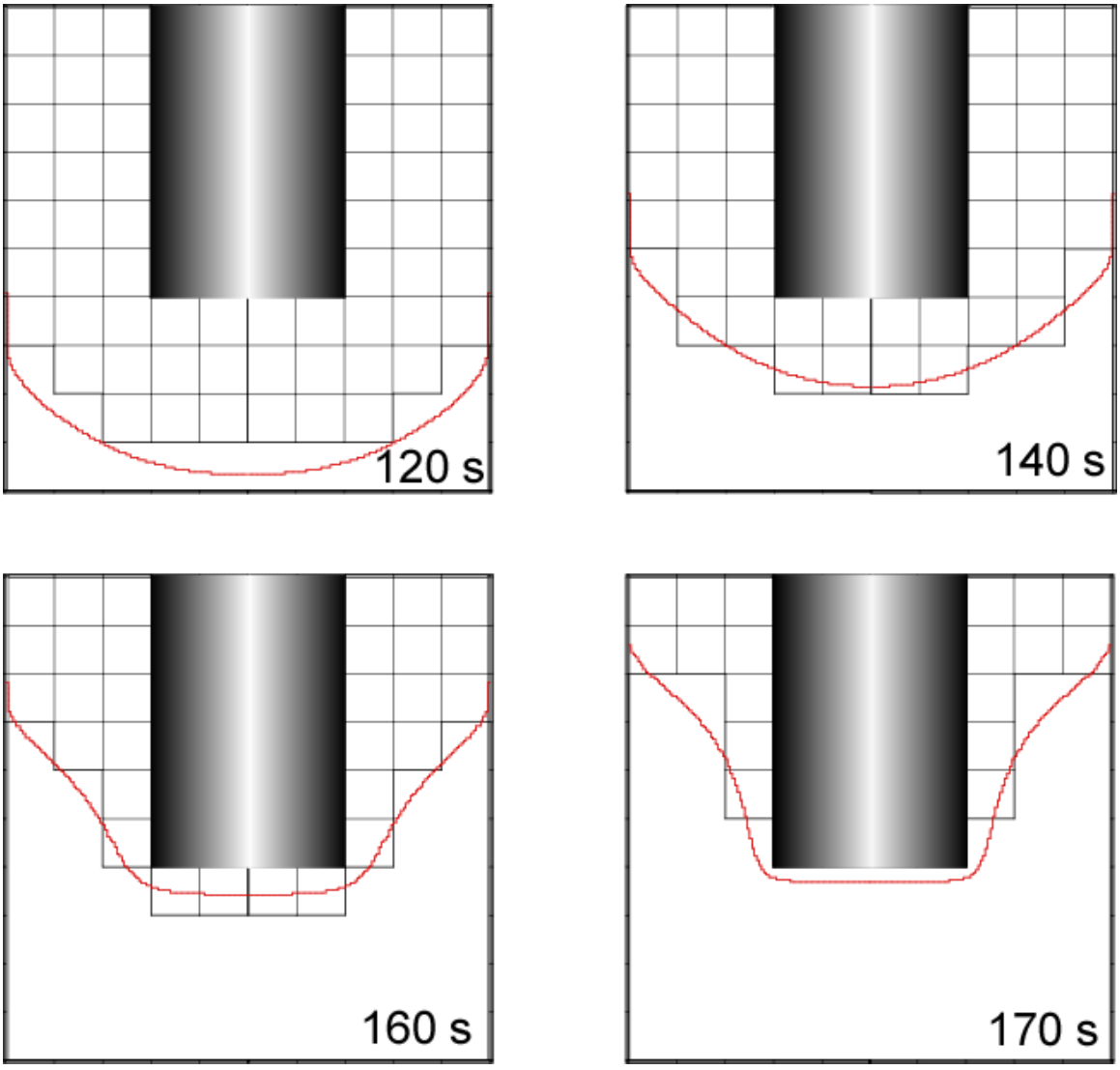

Fig. 9.9. Decomposition around an encapsulated component at various times using 1-mm elements and 50-μm elements. The 1-mm elements are shown as small squares. For the 50-μm element solution, the decomposition front is shown as a solid line.

the confinement is ramped from 27° to 500°C in 180 seconds. The spatial temperature distribution in the vertical walls of the confinement was varied linearly from the bottom plate temperature to the temperature of the top corner of the confinement.

The number of elements used for the 1-mm and 50-μm 2-D axisymmetric mesh were 38 and 15,020; respectively. In Fig. 9.9, only the 1-mm elements are shown in detail. For the 50-μm element solution, the edges of the internal surface elements of the foam are shown to indicate the location of the decomposition front. For the calculation in Fig. 8.11, the elements are removed from the computational domain when the solid fraction at the centroid of the element drops below 0.01. When an element was removed from the computational domain, the viewfactors within the enclosure were recomputed for the dynamic enclosure radiation calculation. The CPU times for the 1-mm mesh and 50-μm mesh were 10 minutes and 7 days, respectively. Even for 2-D problems, the CPU savings obtained by using the discretization bias correction is significant. Furthermore, the solution obtained using the discretization bias correction is nearly identical to the mesh independent solution.

The bias corrected solutions using the 1-mm elements result is a significant CPU savings compared to solutions obtained using true grid-independent solutions that require 100-μm element dimensions. Still, 1-mm elements may be too small for realistic 3-D problems unless massively parallel computational architectures are employed. Perhaps, the smaller elements only need to be used near the hot surfaces. As the foam burns away from the surface, the surface temperature of the decomposing front may only be 600°-800° C. For these elements, a bias corrected solution may allow use of in-depth elements with dimensions on the order of 3- to 4-mm as shown previously in Fig. 8.8. Another alternative method to obtain fast and accurate solutions may be to use the CPUF model to define decomposition front velocities for use with a level-set technique [32] to keep track of the decomposition front.

10 Radiant Heat Experiments

The radiant heat experiments provide a method to test the CPUF model for larger-scale systems of interest, where spatially resolved temperatures are important. The radiant heat experiment including geometry, test matrix, thermal and pressure boundary conditions are presented in this section. Specific data on the thermal boundary conditions for each of the radiant heat experiments are included in the Appendix. Section 11 presents the CPUF simulations of the radiant heat experiments.

10.1 Configuration

Pictures and schematics of the component-scale radiant heat experiments are shown in Figure 10.1, where the foam is shown as an 8.8-cm diameter, 14.6-cm high right circular cylinder. The foam was contained in a sample cup with a 6-mm stainless steel plate that was force-fit into a 7.3 to 16.4-cm long, thin wall (0.5-mm) stainless steel tube. Various orientations of the experiment are shown in Fig. 10.2. The 6-mm stainless steel plate was welded to the thin walled stainless steel tube. Both sides of the stainless steel plate and the inside of the stainless steel tube were painted with flat black Pyromark® 2500. Up to six 6-mm holes were drilled through the side of the stainless steel tube, near the cup plate, to vent decomposition gases into a flame guard. A flame guard was used to prevent fuel rich gases from oxidizing near the cup walls.

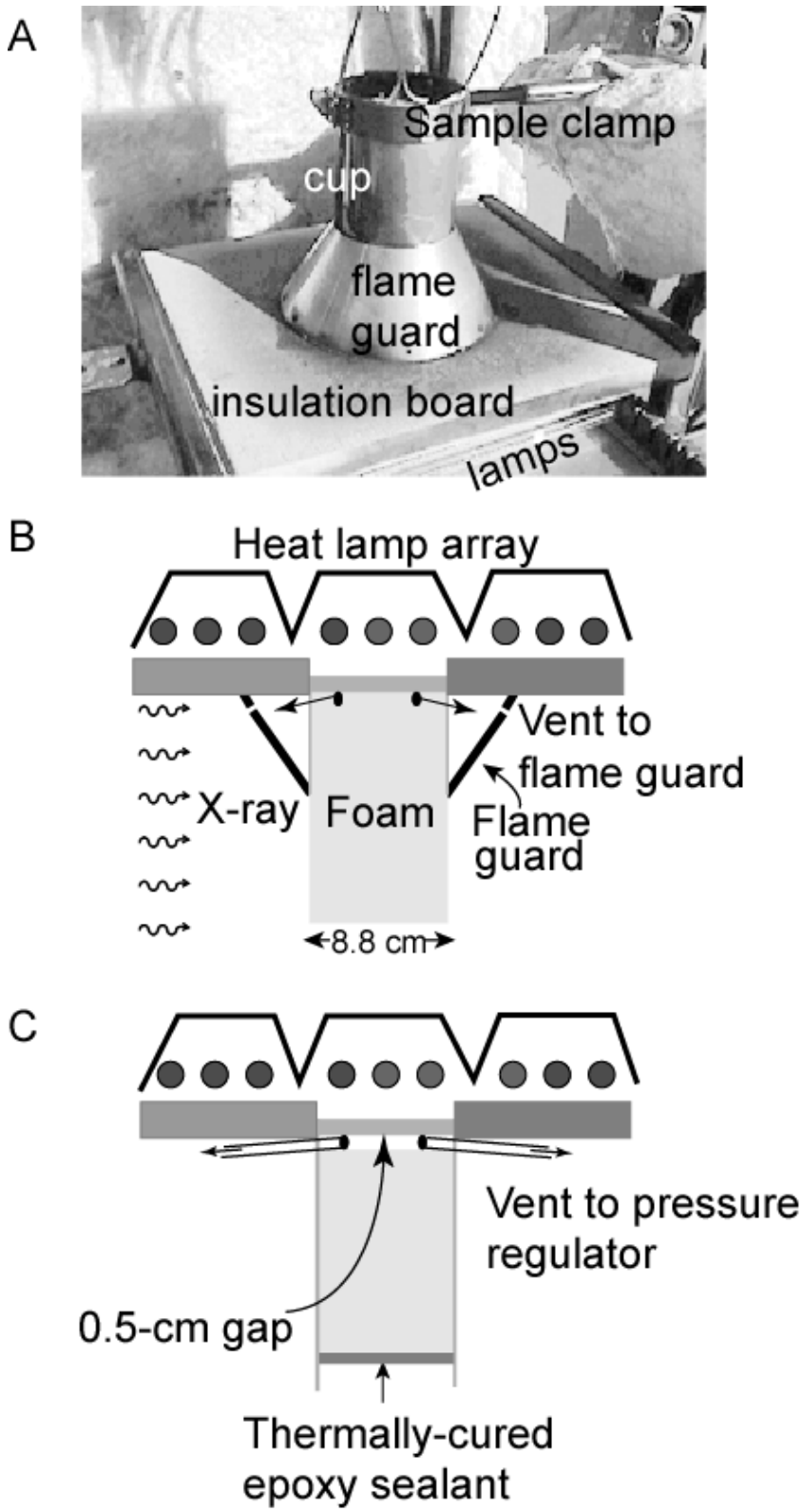

Fig. 10.1. A) Photograph of bottom heated radiant heat experiment, B) schematic of top heated unconfined radiant heat experiment, and C) schematic of partially confined top heated radiant heat experiment.

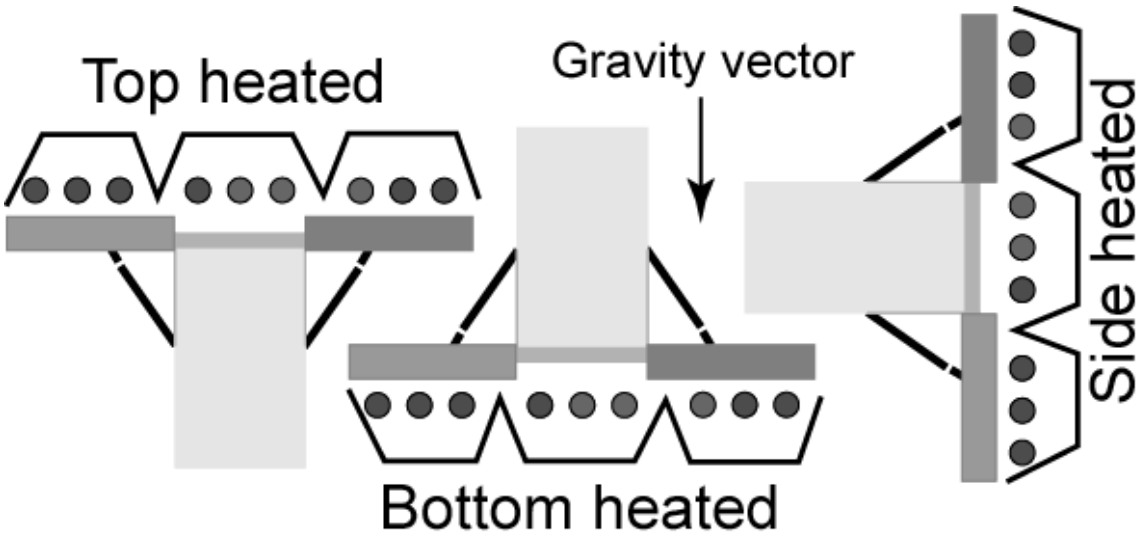

Figure 10.2. Three orientations for the radiant heat experiments.

Figure 10.1.C shows the partially confined component-scale radiant heat apparatus without the flame guard. The configuration for the partial confined radiant heat experiments are similar to the unconfined radiant heat experiments except that the outer cup was sealed at the top using a thermally cured epoxy sealant and the gases were vented to a pressure regulator. Four 5-mm ID stainless steel vent tubes (smaller vent area than the unconfined tests) were used for the partially confined experiments. The tubes were connected to a water-cooled (~5°C) condenser initially charged with nitrogen and regulated with a pressure control valve to the desired test pressures of 0.0, 0.1, and 0.3-MPa (0, 15, and 40-psig). In the partially confined experiments, the face of the foam cylinder was not flush with the heated plate. Rather, a 0.5-cm gap was left between the initial surface of the foam and the heated plate to prevent decomposition gases from clogging the vent holes. The gap was modeled as a radiation enclosure in the finite element analysis.

The cup was heated by an array of high intensity infrared radiant heat lamps as shown in Fig. 10.1. The relatively thick plate promotes uniform heating of the foam samples. The uninsulated thin stainless steel sidewall limits lateral conduction. As shown in Fig. 10.2, the experiments

were performed with the heated surface facing upward (top heated), downward (bottom heated), or sideward (perpendicular to the gravity vector). The experiments were fully instrumented with thermocouples, heat flux gauges, and an X-ray camera described previously [23].

Some of the experiments contained a simulated internal component that was positioned 2.1-cm from the heated foam surface. The internal component was 3.81-cm in diameter and 6.35-cm long. All surfaces were plated with black copper. Simulated embedded components were manufactured from 304 stainless steel or 6061-T6 aluminum. The stainless steel component was a solid cylinder, but the aluminum component was machined in the shape of a cup. The aluminum component was positioned within the foam cylinder so the solid end of the aluminum cup was close to the heated end of the foam. A 0.315-cm diameter stainless steel threaded rod prevented the component from shifting after the foam became soft due to thermal degradation. A foam plug was placed in the cavity after the component was in position.

A description of 19 large-scale experiments organized to emphasize various effects is given in Table 10.1. The quasi-steady incident heat flux, required to maintain the cup plate at various temperatures, is also given in Table 10.1 along with various notes regarding some of the experiments. The heat fluxes given in Table 10.1 are only approximate with more detail given in the next section. The temperature boundary conditions for each of the experiments are also given in the next section. The effects studied include the quasi-steady bottom plate temperature for both low density and high density foams, the orientation of the experiment with respect to the gravity vector, the presence of either a hollow aluminum component or a solid stainless steel component for both high and low density foam, and confinement with backpressures ranging from ambient conditions to 3.58-atm.

Table 10.1. Component-scale radiant heat experiments

Effect	Identifier[a]	*Description*[b]	Flux[c]	T_{plate}[d]	Notes
Bottom plate temperature (high density)	600-1	600-H.bot.no.u.0	6	h	
	750-2[e]	750.H.bot.no.u.0	11	h	Sampling (3.5 and 28-min)
	900-3	900.H.bot.no.u.0	19	c	Control oscillations
	900-14	900.H.bot.no.u.0	21	h	Test 900-3 repeat
Bottom plate temperature (low density)	ld600-6	600.L.bot.no.u.0	6	c	
	ld750-12	750.L.side.no.u.0	12	h	
	ld900-7	900.L.bot.no.u.0	22	c	Flame around base
Orientation	side-11	750.H.side.no.u.0	9	h	Shield obscured sample
	side-13	750.H.side.no.u.0	9	c	Test side-11 repeat
	top-10	750.H.top.no.u.0	12	h	
Component (high density)	al-4	750.H.bot.al.u.0	12	c	Late vent, al movement
	al-15	750.H.bot.al.u.0	14	h	Test ss-15 repeat
	ss-1000-19	1000.H.side.ss.u.0	31	c	
	ss-5	750.H.bot.ss.u.0	12	h	
Component (low density)	ldal-8	750.L.bot.al.u.0	11	h	
	ldss-9	750.L.bot.al.u.0	12	h	
Confinement	600-amb-p4	600.H.top.no.p.0	6	c	Cup thermocouple failed
	600-1.54-p2	600.H.top.no.p.1.	4	c	
	600-3.58-p3	600.H.top.no.p.3.	7	h	

[a]Identifiers give a brief description of the experiment followed by the run identification number. A more detailed explanation of the run is given in the description.
[b]Experiments described by six effects separated by periods. Effects refer to flux (cup plate temperatures of 600, 750, 900, or 1000°C), density (high, H, 0.364 g/cc; or low, L, 0.091 g/cc), orientation of heated surface (bot, top, side), embedded component (none, no; solid stainless steel, ss; or hollow aluminum, al), confinement (unconfined, u, partially confined, p), and gauge pressure (0: 0.0-MPa, 1: 0.07-MPa, 3: 0.28-MPa).
[c]Quasi-steady incident flux (W/cm2) measured after the plate reached a steady temperature.
[d]The heated plate had two thermocouples designated as either the “h” or “c” thermocouple. The “h” thermocouple read a slightly higher temperature than the “c” thermocouple. The “h” or “c” in this table refers to the thermocouple used as the plate boundary condition in the CPUF simulation.
[e]Experiment 750-2 is the base case.

10.2 Thermal Boundary Conditions

A heat flux gauge was mounted 6.35-cm from the centerline of the heated plate to the centerline of the gauge. The heat flux gauge was 2.22-cm closer to the lamps than the heated plate and is not an exact measurement of the incident heat flux on the heated plate. The heat flux measured for the 19 experiments listed in Table 10.1 are plotted in Fig. 10.3. The flux levels required to maintain the heated plate for the high-density experiments were similar to the flux

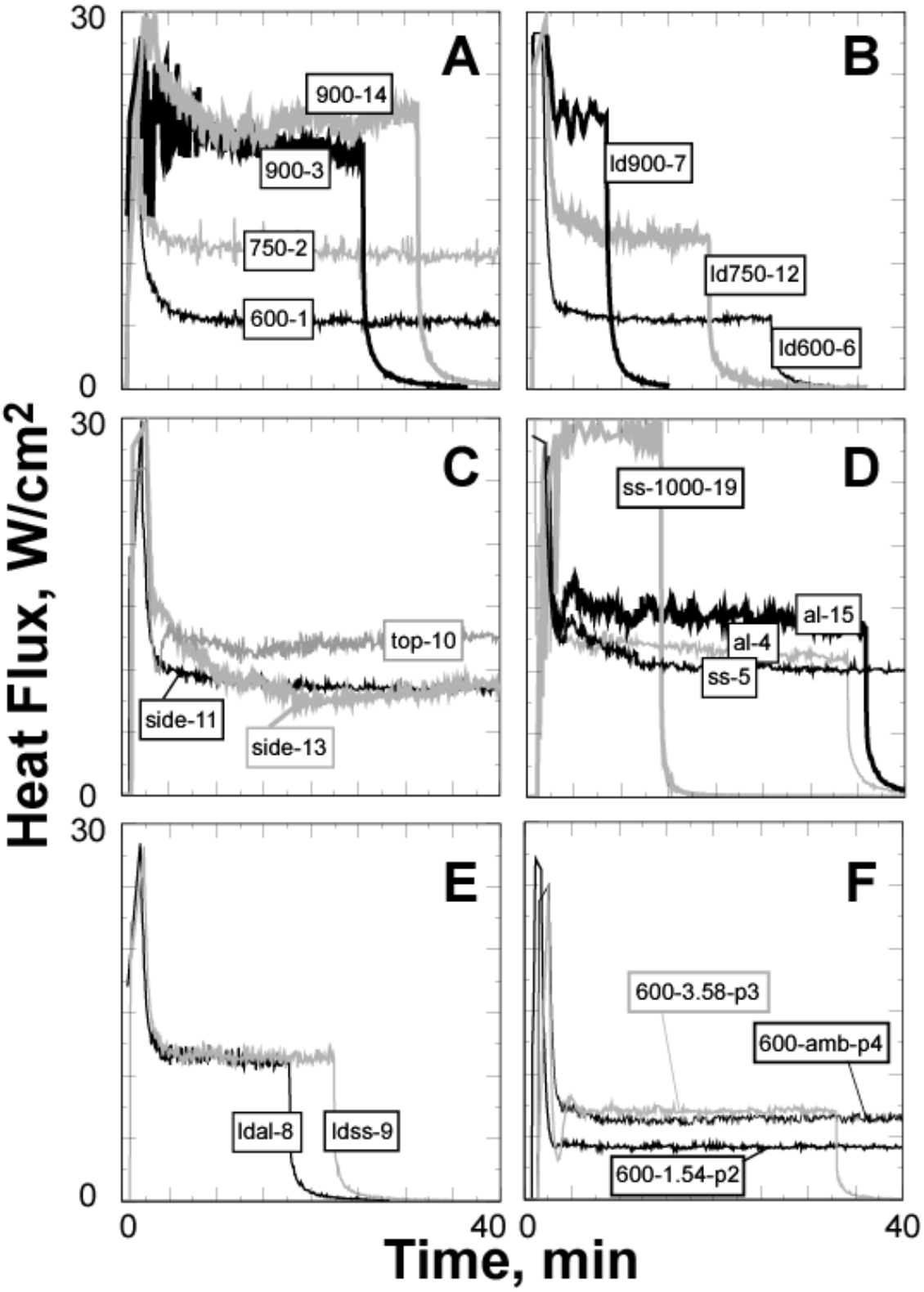

Fig. 10.3. Measured heat flux for the radiant heat experiments grouped by A) bottom plate temperature [high density], B) bottom plate temperature [low density], C) orientation, D) component [high density], E) component [low density], and F) confinement.

levels required to maintain the heated plate of the low density experiments at the same temperature. Some erratic behavior is apparent in the recorded heat fluxes shown in Fig. 10.3. For example, side-11 reached a steady heat flux level whereas the duplicate experiment side-13 was erratic.

The heat flux required to maintain the bottom plate temperatures at 750°C was also dependent of the orientation of the experiment as shown in Fig. 10.3.C. For example, the top heated experiment required a larger heat flux than the side heated experiments to maintain the heated plate temperature at 750°C. X-rays of the partially confined RPU experiments in Fig.10.3.F revealed liquid formation. For these experiments, the heat flux required to maintain the heated plate at 600°C was significantly different for these experiments exhibiting liquefaction effects.

A schematic of the confinement can for the radiant heat experiment is shown in Fig. 10.4. Thermocouples located within the heated plate are labeled “c” and “h” in Fig. 10.4. The “c” represents the cooler thermocouple because the “c” thermocouple is slightly farther away from the radiant heat source than the hotter thermocouple marked with an “h” in Fig. 10.4. The temperature of the bottom plate should be nearly uniform after the initial transient heating of the plate. The thermocouples labeled 1 through 5 on the outside of the confining can were also used as temperature boundary conditions for the CPUF simulations.

Figure 10.5 shows more detail of the bottom plate. Because of the close proximity of the “c” and “h” thermocouples, the temperature for these two thermocouples should be close. The bottom plate temperature was controlled in the CPUF model by either the “c” thermocouple or the “h” thermocouple. Table 10.1 indicates which thermocouple the CPUF model used for the bottom

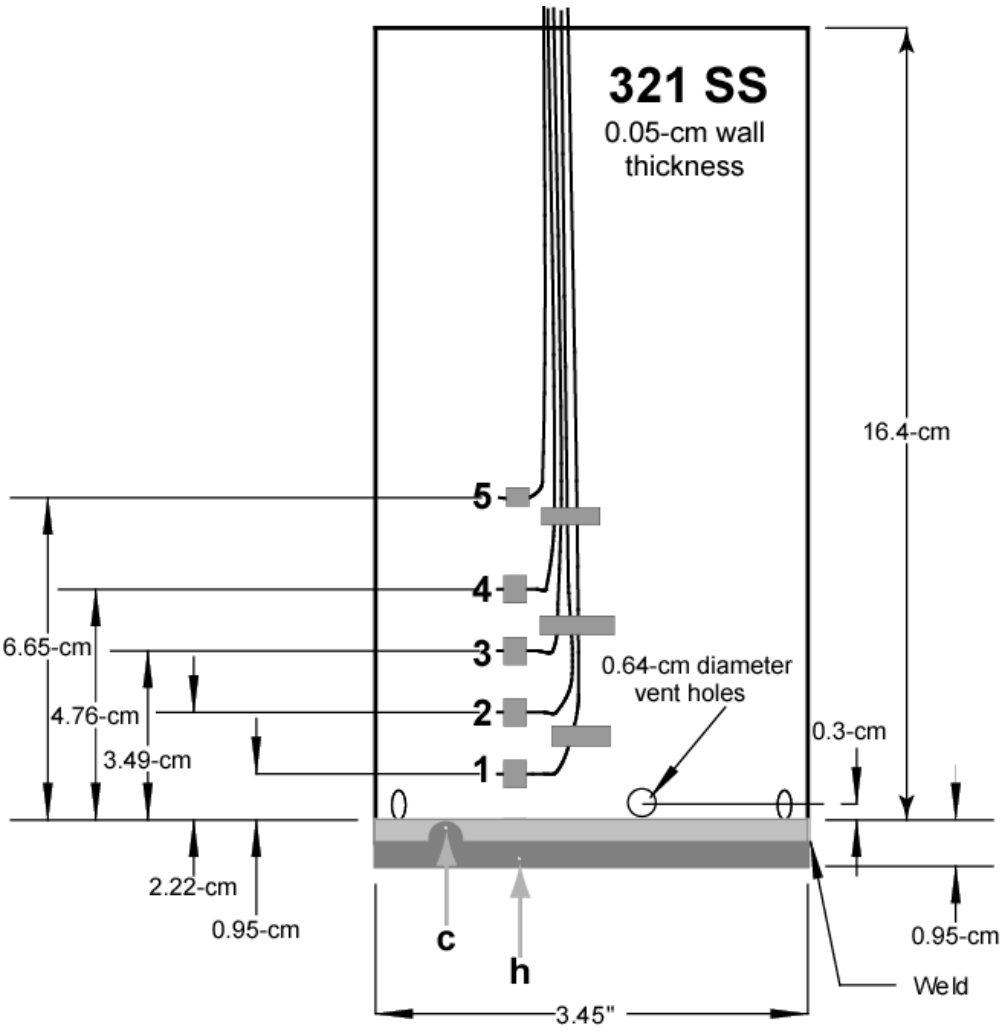

Fig. 10.4. Schematic of the confinement can for the radiant heat experiments.

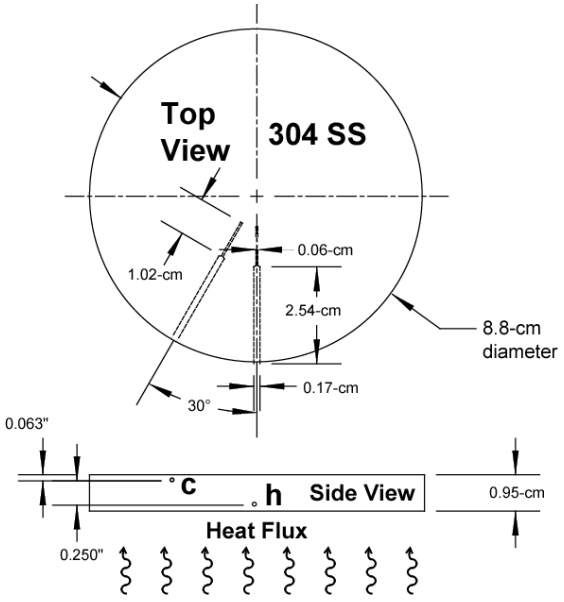

Fig. 10.5. Schematic of the heated plate.

plate temperature. The “c” thermocouple would have given the best estimate of the plate temperature since the “c” thermocouple is located closer to the foam surface. However, the original data set had the “c” and “h” thermocouple data mislabeled in some of the data files. Thus, 11 of the 19 CPUF simulations were run with the “c” thermocouple data for the bottom plate temperature and 8 of the 19 simulations were run with the “h” thermocouple data for the bottom plate temperature. This error in the bottom plate thermocouple resulted in temperature differences ranging from 2 to 18 degrees. Although boundary condition errors are not addressed in detail, other errors associated with the CPUF model parameters were investigated using a mean value approach [28]. *The error in the boundary condition is greater than the overall error due to parameter uncertainty* discussed later in Section 11. The uncertainty in the boundary condition is greater for the higher temperature boundary conditions due to higher temperature gradients within the heated plate.

Figure 10.6 through 10.9 show plots of the temperatures recorded for each of the 21 experiments listed in Table 10.1. The numbers and letters on the temperature profiles correspond to the thermocouples shown in Fig. 10.4 and 10.5, respectively. Temperatures used for boundary conditions in the radiant heat experiments are given in the Appendix. Figure 10.6, 10.7, 10.8, and 10.9 give the temperature boundary conditions for the experiments with the control thermocouple set to 600°C for the high/low density foam, 600°C for the partially confined experiments, 750°C for the high/low density foams with/without embedded components and various encapsulants polymers, and 900°C for the high and low density foams, respectively. The experiment with the stainless steel component and a bottom plate set temperature of 1,000°C is also shown in Fig. 10.9.

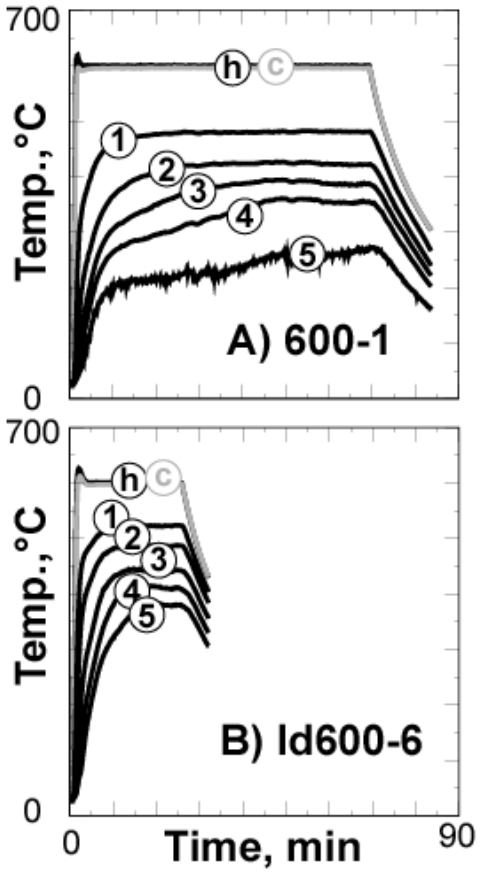

Fig. 10.6. Temperature boundary conditions for experiments A) 600-1 and B) ld600-6.

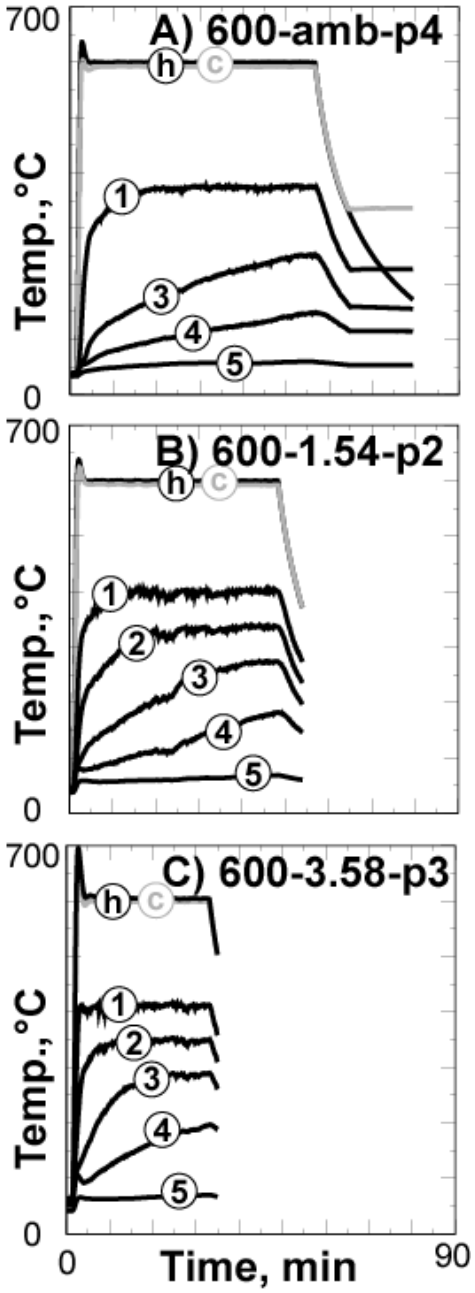

Fig. 10.7.Temperature boundary conditions for partially confined RPU experiments A) 600-amb-p4, B) 600-1.54-p2, and C) 600-3.58-p3.

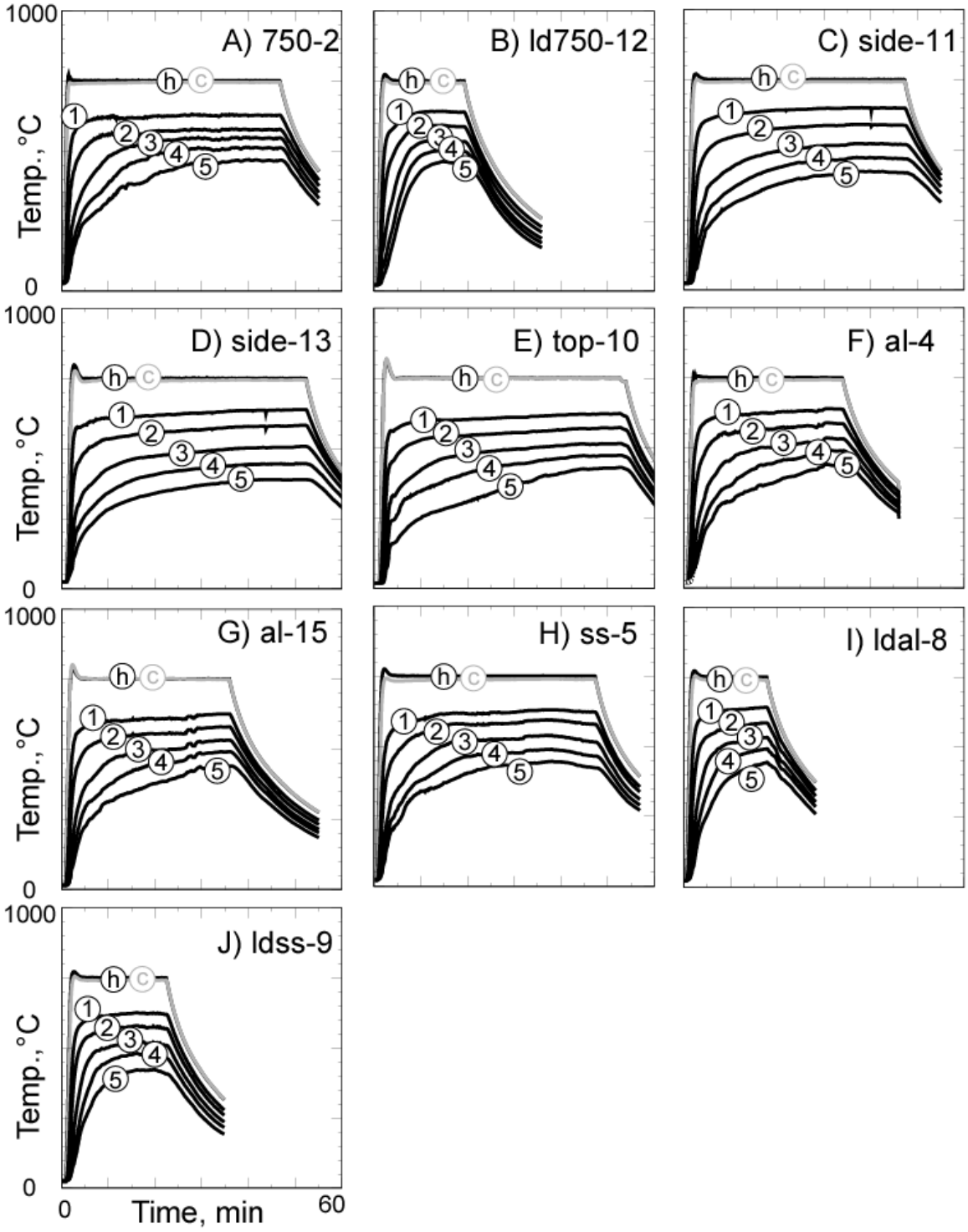

Fig. 10.8. Temperature boundary conditions for the 750°C radiant heat experiments.

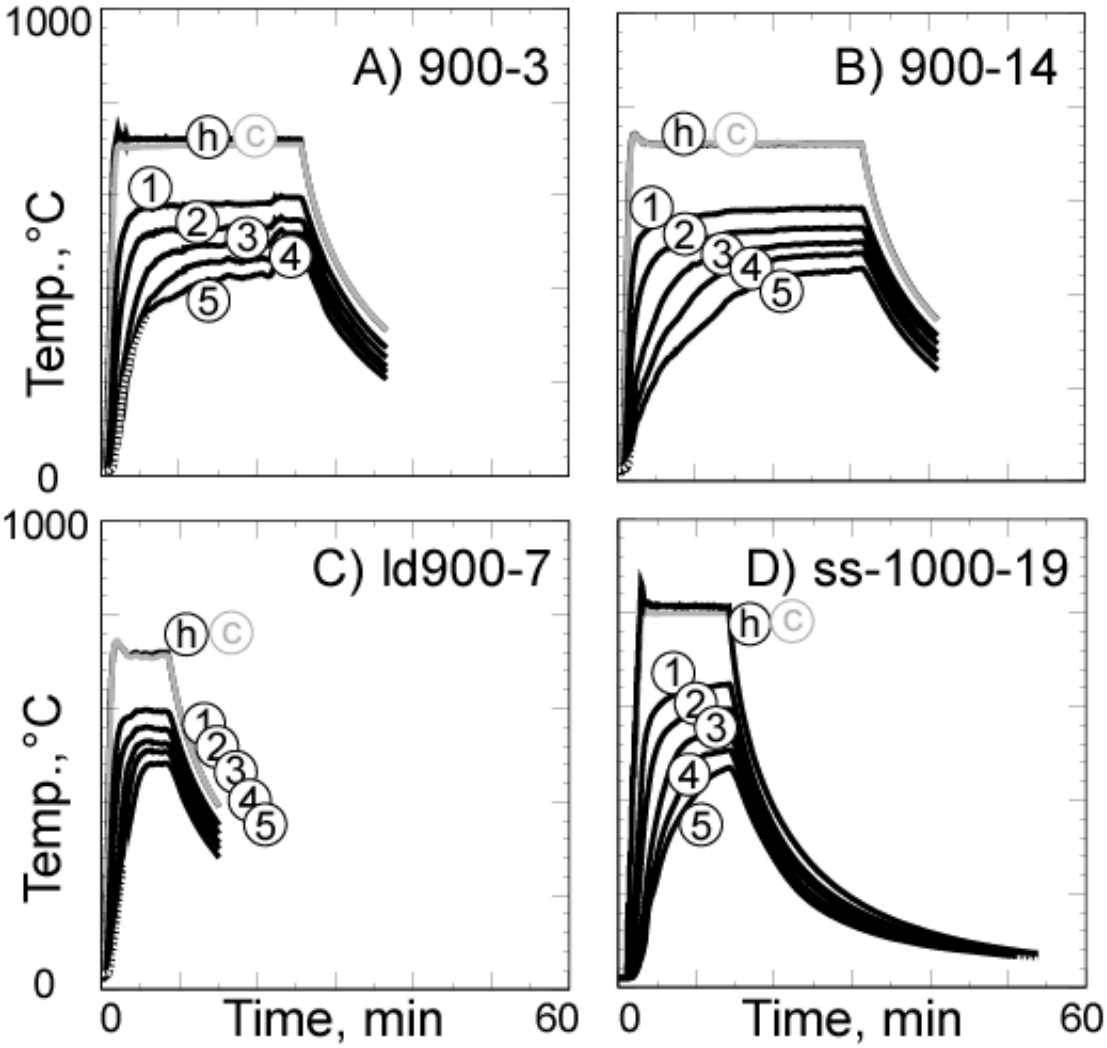

Fig. 10.9. Temperature boundary conditions for the radiant heat experiments at 900ºC and 1000ºC.

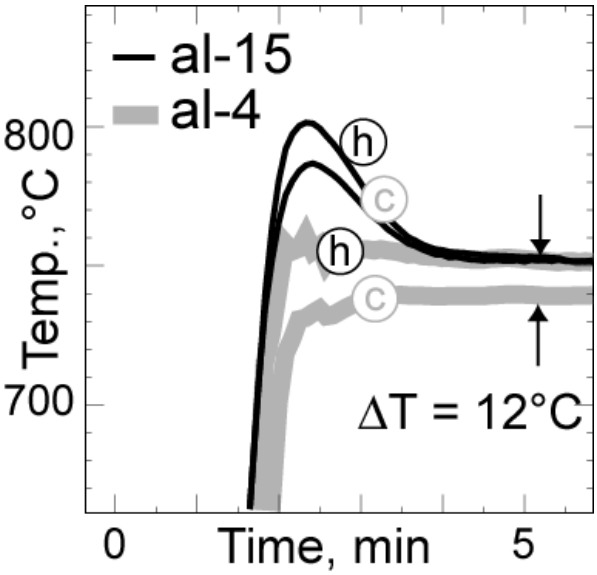

Fig. 10.10. Heated plate thermocouple readings for experiments al-15 and al-4.

The difference between the “h” and “c” bottom plate thermocouple reading is not obvious when the temperatures are plotted on the scales shown in Figs. 10.6 through 10.9. However, some differences are apparent. For example, Fig. 10.10 shows a zoomed in view of the “h” and “c” thermocouple temperature for experiments al-4 and al-15. The difference in the “h” and “c” temperature for experiments al-4 and al-15 at 5 minutes is 2°C and 12°C, respectively. It is difficult to speculate why the temperatures are so different for these replicate experiments. Contact resistance, thermocouple error, etc. are possible explanations. Rather than speculate further, the CPUF boundary conditions are considered only as an *estimate* of the actual boundary condition.

The pressure for the CPUF simulations was assumed constant with most of the experiments set to 1-atm. For the partially confined experiments; 600-amb-p4, 600-1.54-p2, and 600-3.58-p3; the pressure was set to 1-atm, 1.54-atm, and 3.58-atm, respectively. Figure 10.11 shows the measured pressure for these experiments. The errors associated with using a constant pressure are negligible since the mass loss shifts calculated with the CPUF model are negligible at these conditions. Future foam response models should calculate the dynamic pressuri-

zation using the predicted molecular weights of the decomposition gases taking into account gases that may enter or leave the enclosure due to confinement conditions.

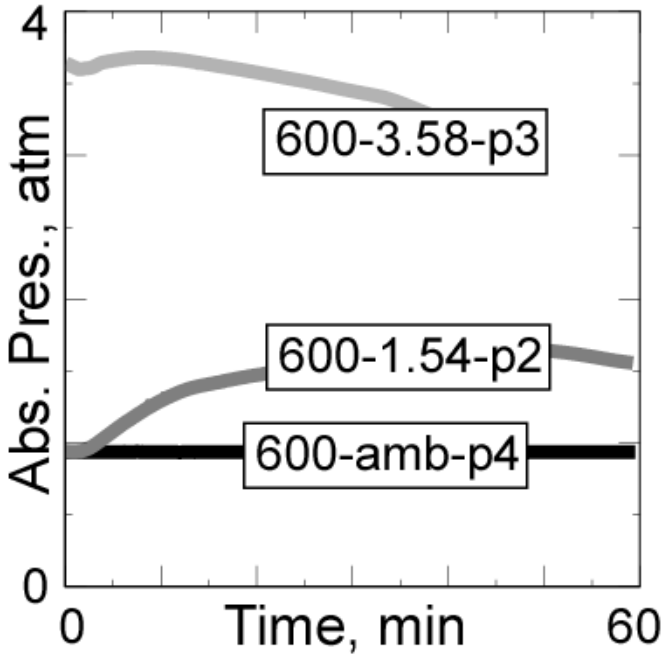

Fig. 10.11. Measured pressure for the partially-confined radiant heat experiments.

10.3 Experimental Observations

Figure 10.12 shows the effect of the boundary temperature and foam density on the centerline front locations as measured from the heated cup plate and velocities for experiments 600-1, 750-2, 900-14, ss-1000-19, ld750-12; Figure 10.13 shows the effect of pressurization and confinement on the centerline front locations for experiments 600-1, 600-amb-p4, 600-1.54-p2, 600-3.58-p3. Centerline front locations for the remaining experiments were not plotted since they are essentially the same as the representative experiments shown in Fig. 10.12 and Fig. 10.13. In these figures, the lines represent the *measured* front locations and velocities determined from a

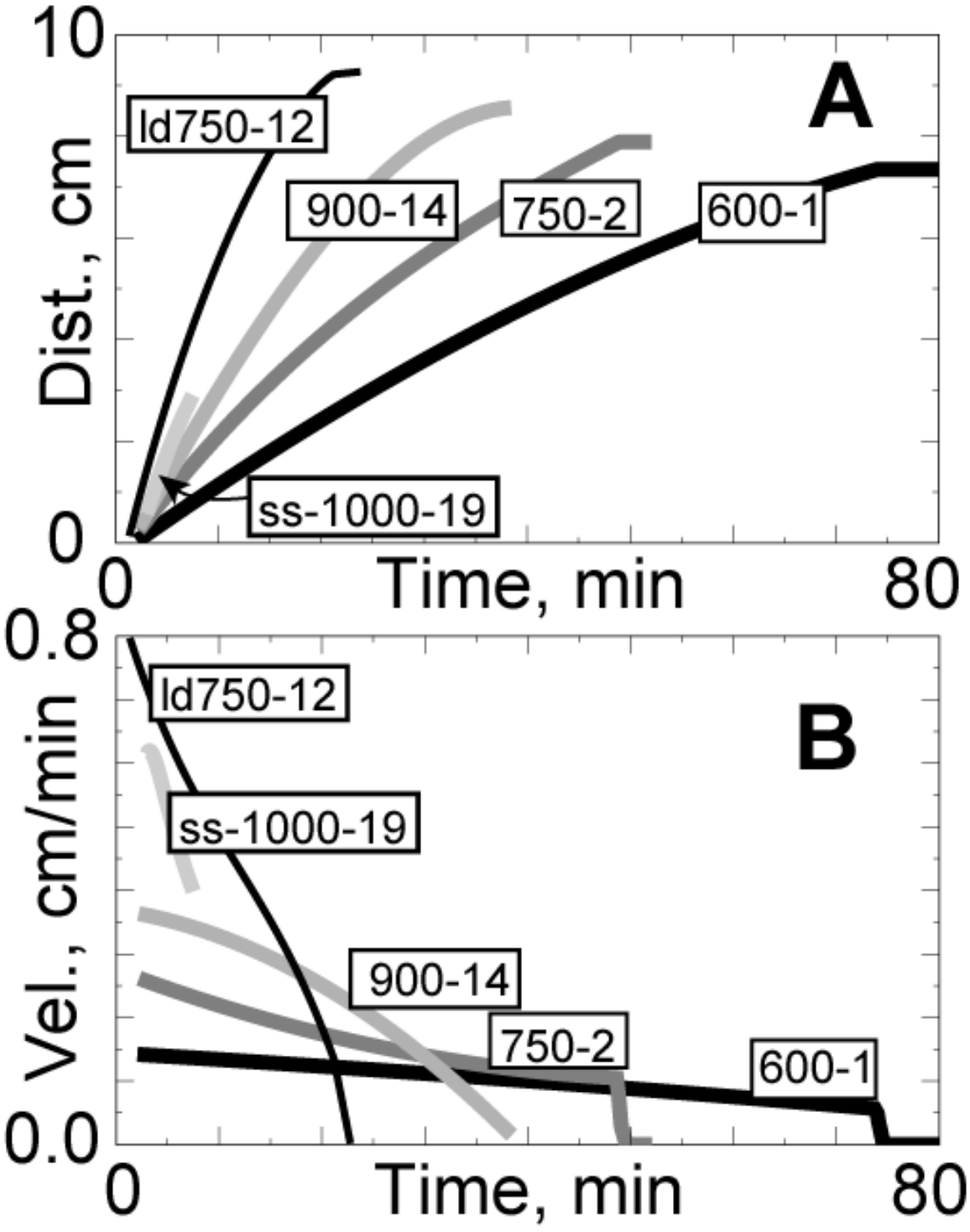

Fig. 10.12. A) Decomposition front locations measured from the heated plate and B) measured front velocities showing the effect of heated plate temperature (experiments 600-1, 750-2, 900-14, and ss-1000-19 and density (ld750-12).

series of X-ray images taken at various time intervals ranging from 5-60 seconds. The location of the decomposition front was determined using various image-processing software.

In Fig. 10.12, the front velocity is shown to increase with increasing plate temperatures for the high-density foam. The velocity of the low-density experiment ld750-12 was about 3 times faster than the velocity of the high-density experiment 750-2, even though the thermal conductivity for the higher density foam was greater than the thermal conductivity of the lower density foam. The primary reason for the faster decomposition velocity for the lower density foam was a lower volumetric energy sink for the low-density foam. In other words, fewer bonds needed to be

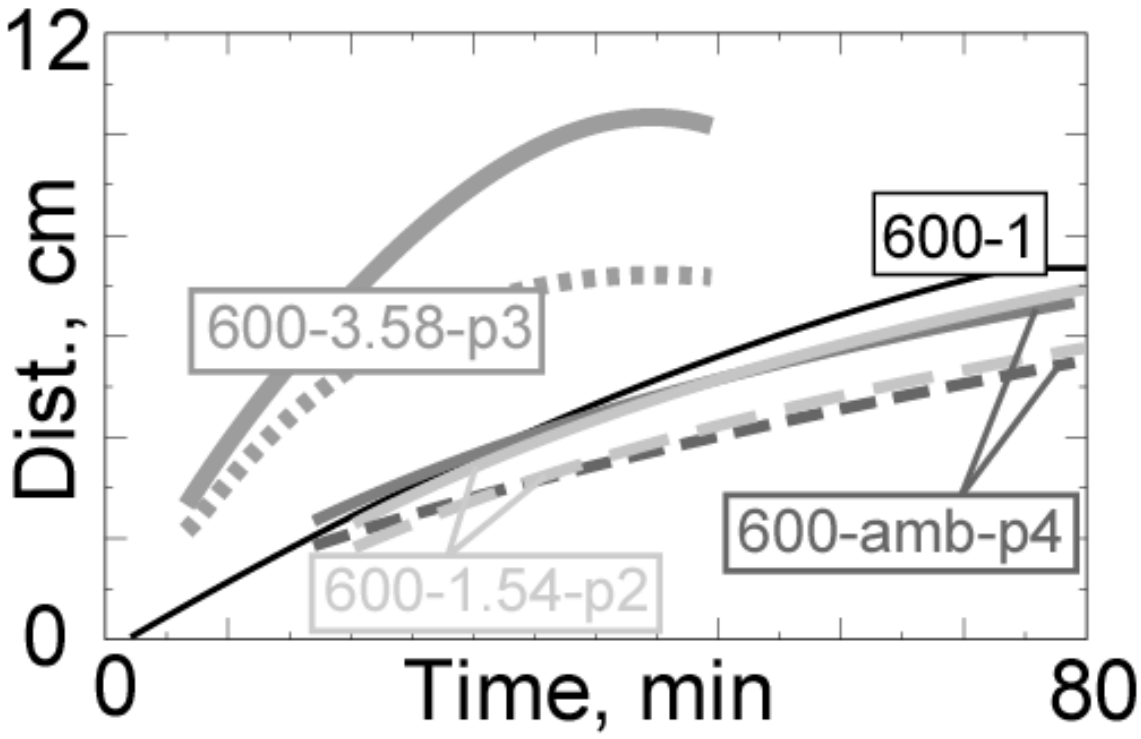

Fig. 10.13. Measured decomposition front locations showing the effect of confinement and pressure (600-1 is unconfined at ambient pressure, 600-amb-p4 is partially confined at ambient pressure, 600-1.54-p2 is partially confined at 0.16-MPa, and 600-3.58-p3 is partially confined at 0.36-MPa.

broken to decompose the same volume of material. Determination of the front velocities for the remaining lower density foam X-rays was not attempted due to difficulty in analyzing the low contrast X-ray film.

Figure 10.13 shows the centerline front locations for experiments 600-1 and 600-amb-p4, 600-1.54-p2, 600-3.58-p3 to illustrate the effect of confinement and pressure during decomposition of the RPU encapsulant in large-scale experiments. The front locations for the partially confined experiments 600-amb-p4, 600-1.54-p2, 600-3.58-p3 are shown with two lines – a solid line and a broken line – representing the interface between the *foam and bubbly liquid* and *bubbly liquid and gas*. In the TGA experiment, mass loss was delayed by increasing the level of confinement by using smaller and smaller orifices or by increasing the hydrostatic pressure as shown previously in Fig. 8.1. Delayed mass loss should cause the front velocities in the large-scale experiment to decrease as observed for the *partially confined*, large-scale experiment 600-amb-p4 at 0.09-MPa (ambient) and experiment 600-1.54-p2 at 0.16-MPa when compared to the *unconfined*, experiment 600-1. However, for the semi-confined large-scale experiment 600-3.58-p3 at 0.36-MPa, the velocity of the decomposition front increased.

The increased decomposition velocity at 0.36-MPa may be related to substantial liquid formation caused by partial confinement of the decomposition gases and increased pressure. The cellular structure, composed of struts and windows separating gas-filled bubbles, collapses when the polymer liquefies. The loss of the cellular structure causes the local density to increase as observed in the X-ray images. The collapse of the cellular structure at the heated surface is partially responsible for the observed increase in the decomposition front velocity. The decomposition front is also accelerated as the heat transfer rate is increased due to the higher thermal conductivity of the liquid front and convective heat transfer within the bubbly liquid.

Figure 10.14 gives an overlay of the X-ray images for the partially confined RPU experiments after 30 minutes to show the nonlinearity of the decomposition fronts with pressure. The X-ray movies of the 0.3-MPa experiment showed damage occurring within the closed-cell foam as cell windows opened (ruptured) and a liquid plume penetrated into the previously closed-cell foam. Predicting mechanical damage caused by decomposition chemistry and pressure loading is beyond the current capability of the FEM code.

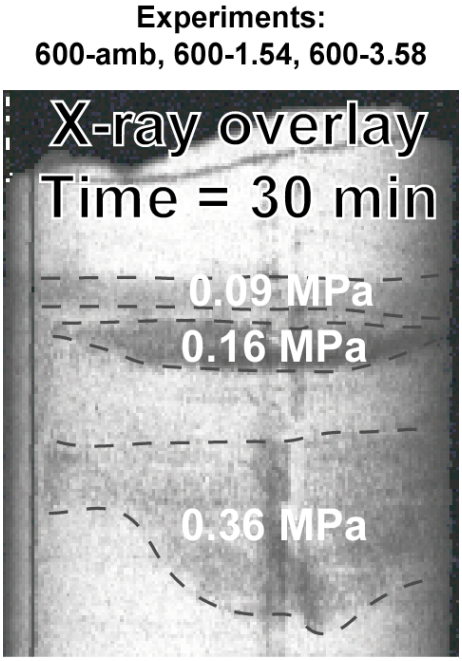

Fig. 10.14. Overlay of three X-ray images taken at 30 minutes for experiments 600-amb-p4, 600-1.54-p2, and 600-3.58-p3.

11 CPUF Simulations of the Radiant Heat Experiments

In Section 8, the CPUF chemistry model was evaluated with various TGA experiments. The 20ºC/min ambient pressure TGA experiments were used to determine the chemistry parameters. Separate TGA experiments at different heating conditions were used to show that the chemistry parameters were adequate. All of the TGA simulations were performed assuming spatially isothermal samples. To model the effect of decomposing foam within a weapon system with spatially resolved temperature distributions, the CPUF model was implemented into COYOTE using element death and a discretization bias correction model as discussed in Section 9. The primary objective of the simulations presented in Section 9 was to show that the discretization bias corrected solutions gave the same results as the fully mesh independent solutions. In Section 10, twenty-one radiant heat experiments were described in detail. All of the experiments were simulated with the CPUF model.

In this section, the COYOTE foam response model, including discretization bias correction, is evaluated by comparing model predictions with X-rays of the component-scale foam experiments. All of the CPUF model parameters and thermophysical properties were obtained with separate experiments and were given previously in Sections 7-9. The temperature boundary conditions were discussed in Section 10.2. *No **adjustable parameters*** are used in the simulations in this section.

11.1 Comparison of Solid Fraction Contours to X-ray Images

Figures 11.1-11.6 show a comparison between x-rays and the solid fraction contours calculated with the CPUF model for the 19 RPU experiments listed in Table 10.1. Since the radiant heat experiments are 2D axisymmetric, the contours are only plotted on one side of the X-ray.

For each experiment, three X-rays are shown at various times. The times are indicated on the X-rays. Arrows on the X-ray images show the approximate location of the decomposition front. The calculated solid fraction contours are shown on the X-rays as white lines

The solid fraction contours indicate of the location of the decomposition front calculated using the CPUF foam response model. The solid fraction is the mass of the foam in the element divided by the initial foam mass in the element at time zero. The low thermal conductivity of the RPU encapsulants causes the decomposition front to be narrow when exposed to high temperatures. In Figures 11.1-11.6, three white contour lines are plotted at values of 0.125, 0.5, and 0.875. The white contour line closest to the heated surface is the 0.125 contour line. The middle white contour line is the 0.5 contour line; and the white contour line farthest away from the heated surface is the 0.875 contour line. A black contour line is also shown in Figs. 11.1-11.6. The black contour line represents the 0.005 contour line. Since the death criterion for the CPUF model is 0.036, the black contour depicts the surface of the degrading foam that defines part of the dynamic radiation enclosure.

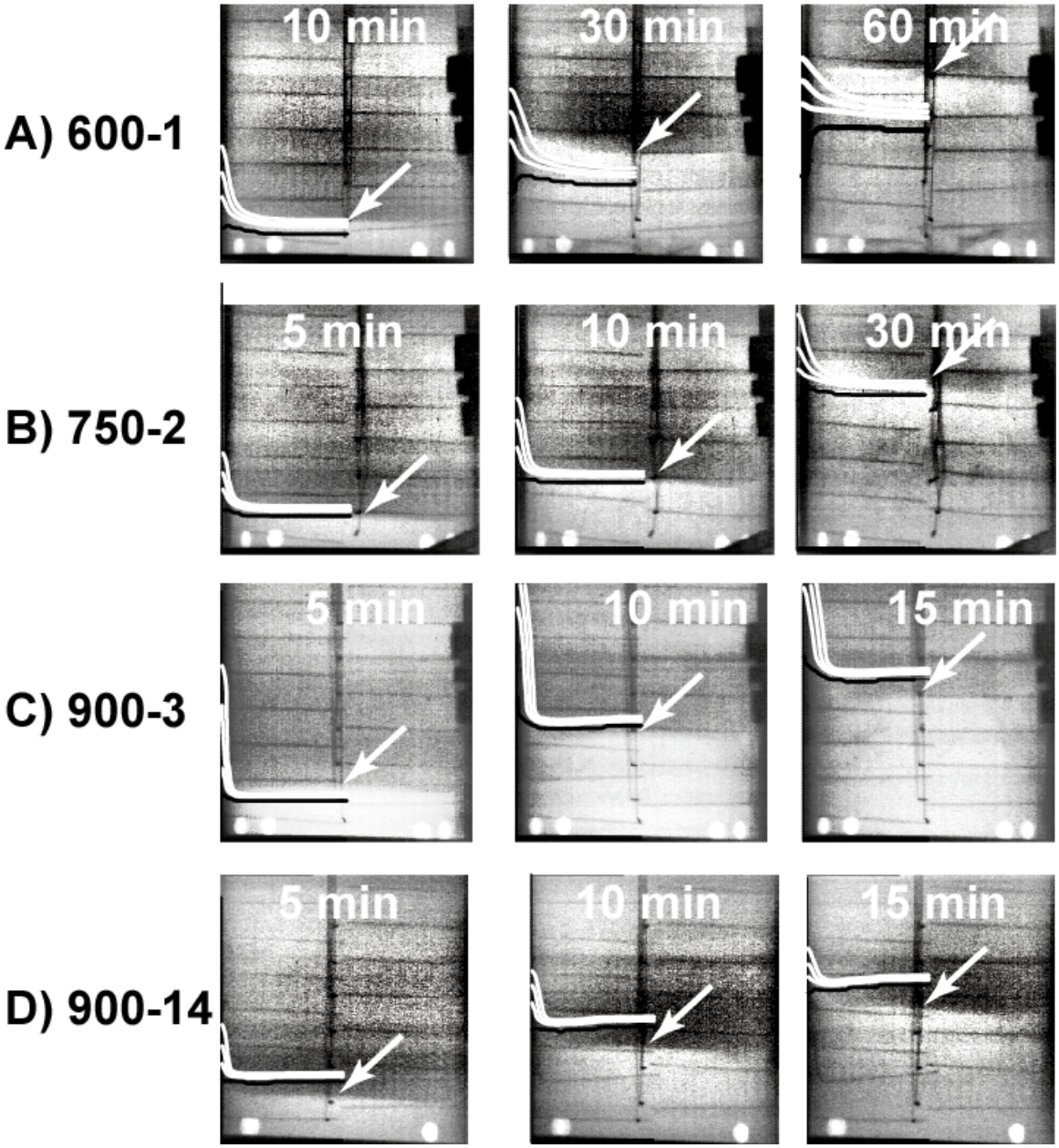

Fig. 11.1. Comparison between predicted solid fraction contour lines at 0.875 (white line farthest from the heated surface) 0.5 (middle white line), and 0.125 white line closest to the heated surface), and 0.005 (black line) to X-ray images for experiments A) 600-1, B) 700-2, C) 900-3, and D) 900-14. A white arrow on the X-ray shows the approximate location of the decomposition front.

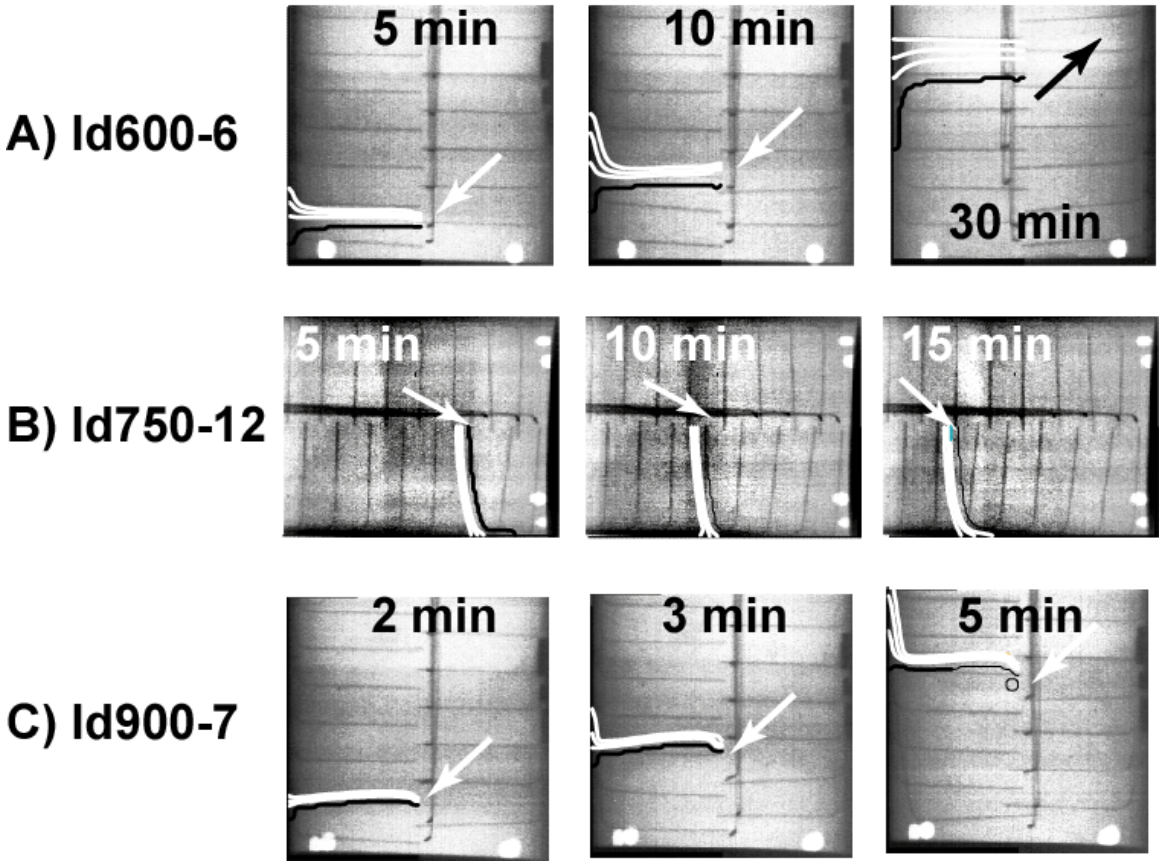

Fig. 11.2. Comparison between predicted solid fraction contour lines at 0.875 (white line farthest from the heated surface) 0.5 (middle white line), and 0.125 white line closest to the heated surface), and 0.005 (black line) to X-ray images for experiments A) ld600-6, B) ld750-12, and C) ld900-7. A white arrow on the X-ray shows the approximate location of the decomposition front.

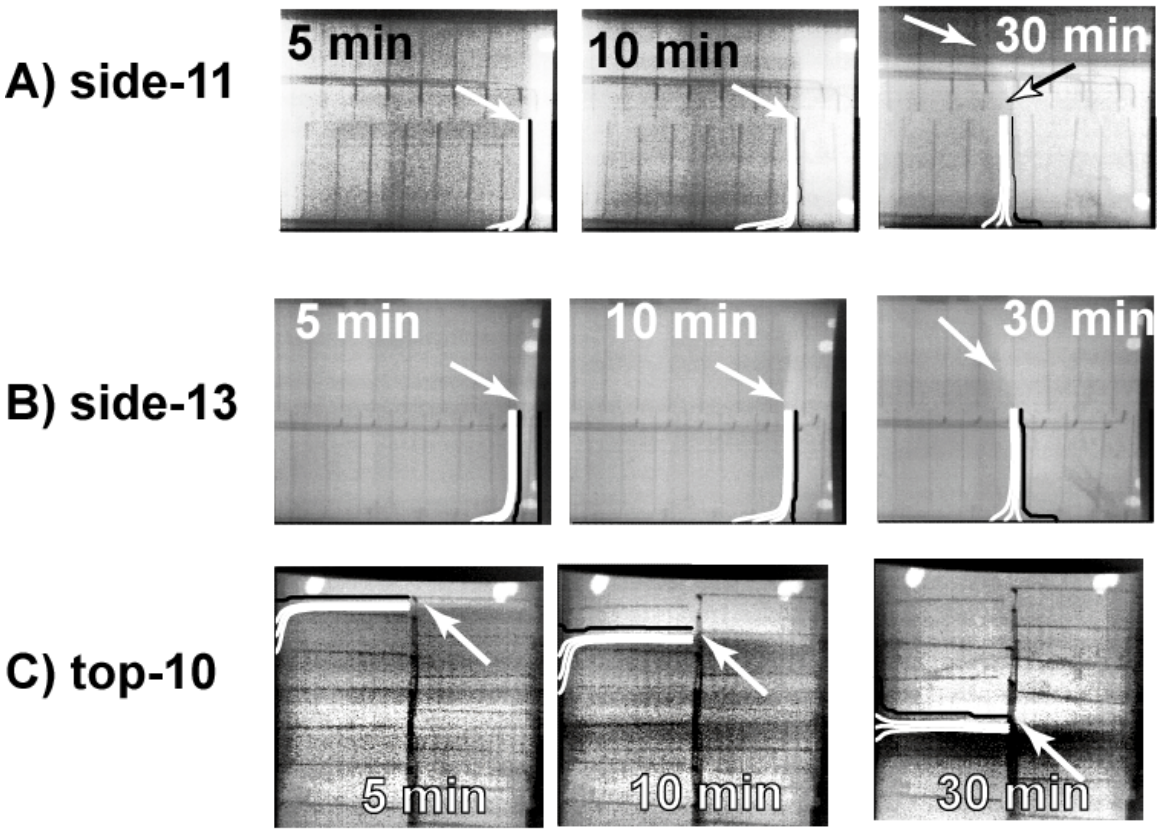

Fig. 11.3. Comparison between predicted solid fraction contour lines at 0.875 (white line farthest from the heated surface) 0.5 (middle white line), and 0.125 white line closest to the heated surface), and 0.005 (black line) to X-ray images for experiments A) side-11, B) side-13, and C) top-10. A white arrow on the X-ray shows the approximate location of the de-composition front.

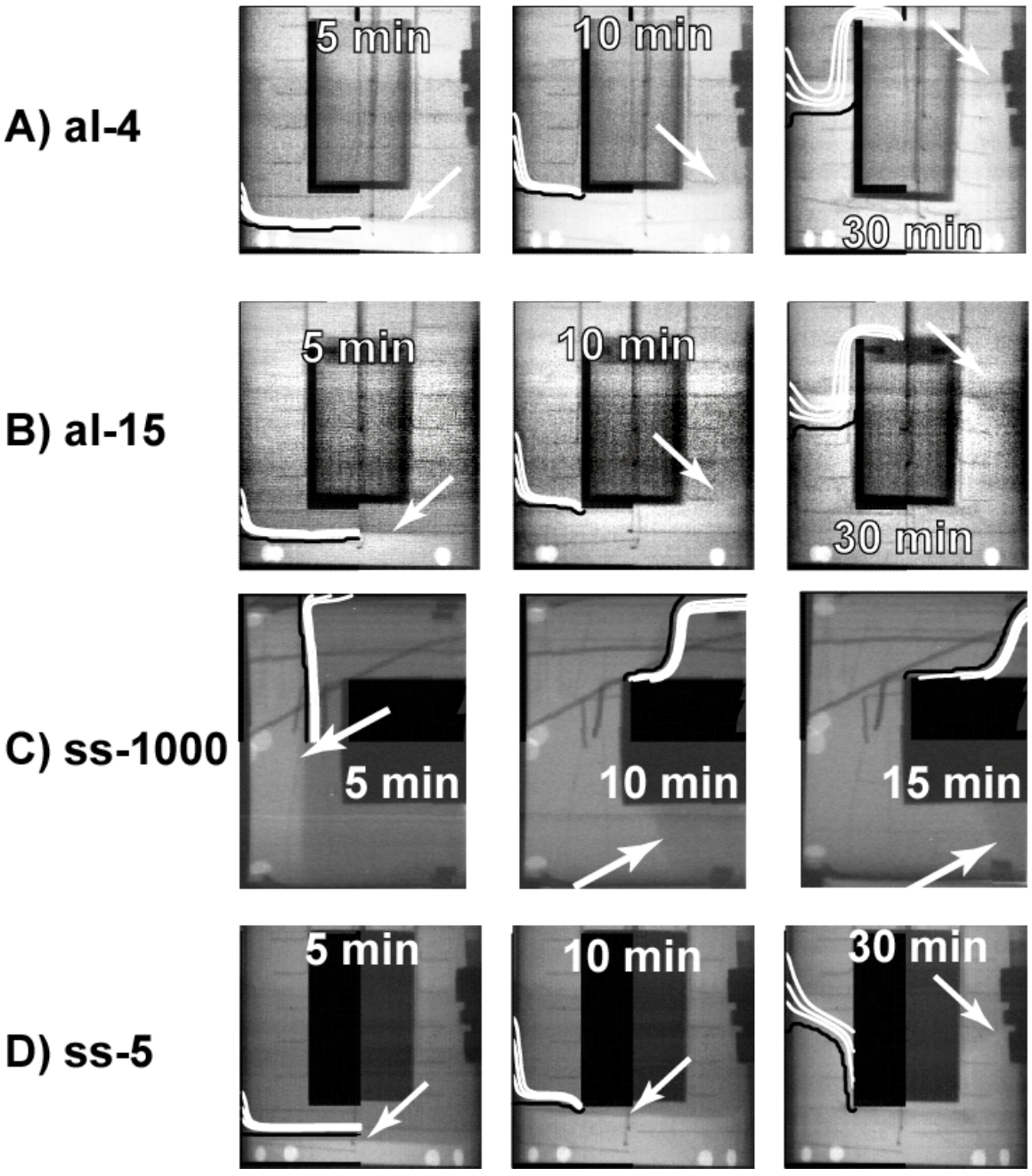

Fig. 11.4. Comparison between predicted solid fraction contour lines at 0.875 (white line farthest from the heated surface) 0.5 (middle white line), and 0.125 white line closest to the heated surface), and 0.005 (black line) to X-ray images for experiments A) al-4, B) al-15, C) ss-1000, and D) ss-5. A white arrow on the X-ray shows the approximate location of the decomposition front.

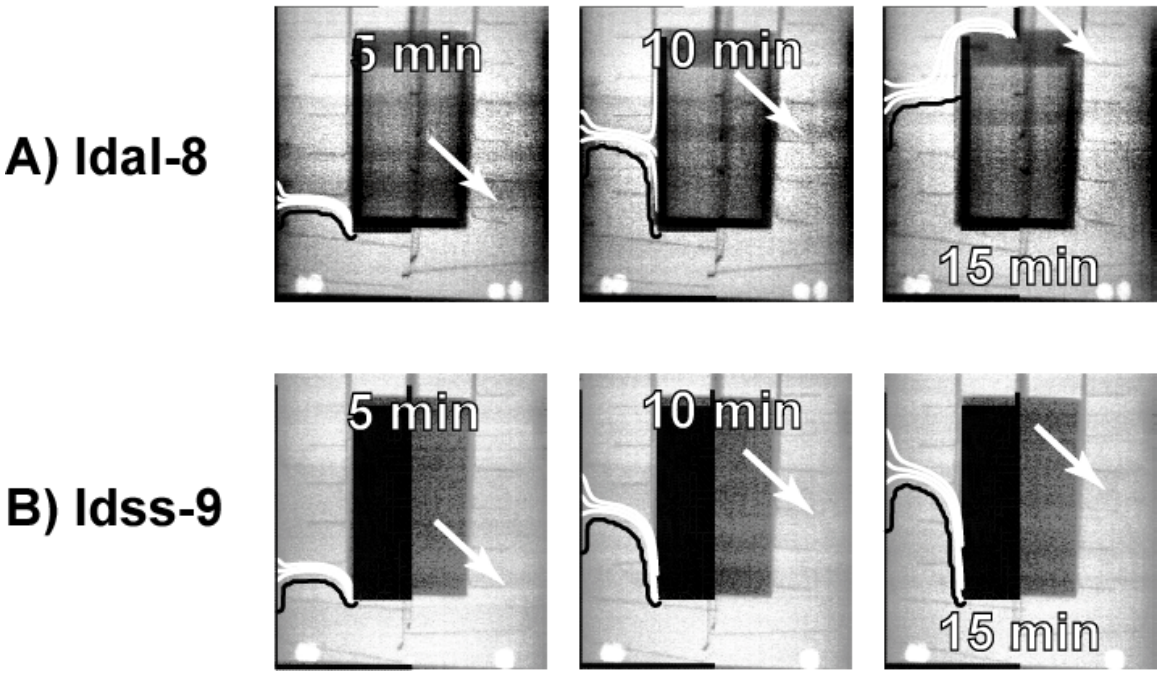

Fig. 11.5. Comparison between predicted solid fraction contour lines at 0.875 (white line farthest from the heated surface) 0.5 (middle white line), and 0.125 white line closest to the heated surface), and 0.005 (black line) to X-ray images for experiments A) ldal-8 and B) ldss-9. A white arrow on the X-ray shows the approximate location of the decomposition front.

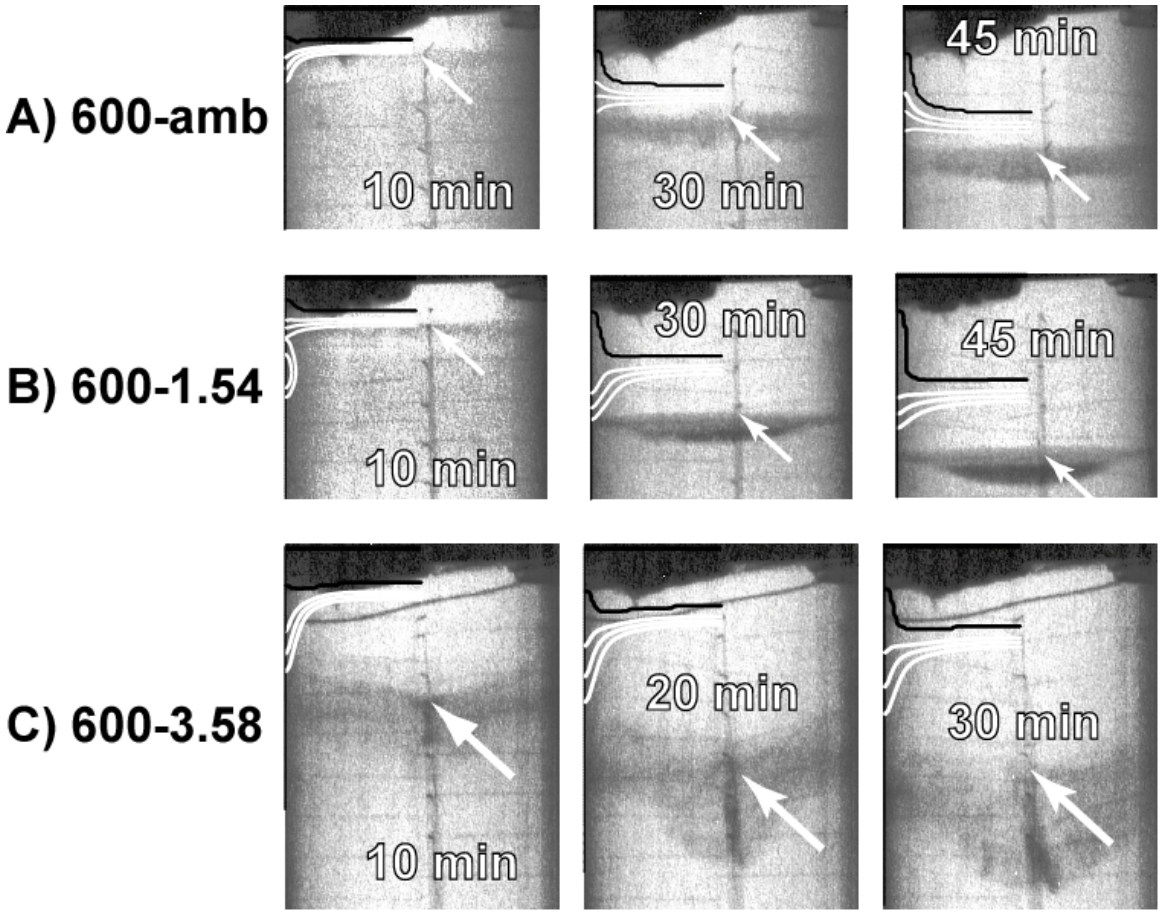

Fig. 11.6. Comparison between predicted solid fraction contour lines at 0.875 (white line farthest from the heated surface) 0.5 (middle white line), and 0.125 white line closest to the heated surface), and 0.005 (black line) to X-ray images for experiments A) 600-amb, B) 600-1.54, and C) 600-3.58. A white arrow on the X-ray shows the approximate location of the decomposition front.

In Fig. 11.1, the effect of the heated plate temperature for the experiments with the higher density foam is shown. Increasing temperatures causes the bond breaking rates to increase in an Arrhenius fashion. Consequently, the velocity of the decomposition front also increases with temperature resulting in the position of the front being located farther from the heated surface at equivalent times. A similar effect is shown in Fig. 11.2, which depicts the temperature effect for the low-density foam. However, the decomposition rate is significantly greater for the lower density foam, than for the higher density foam. For the lower density foam, the volumetric endothermic energy change is not as profound as for the higher density foam. The result is an increase in the decomposition front velocity for the lower density foam. Thermophysical properties of the foam also affect the velocity of the decomposition front.

Replicate experiments are shown in Fig. 11.1.C and 11.1.D for the high-density experiments with the plate temperature set to 900ºC. Experiment 900-3 was repeated due to an oscillation in the control thermocouple. The X-ray images show that the decomposition front for experiment 900-3 and 900-14 are at nearly the same location; however, the CPUF predicted front location for experiment 900-3 is in better agreement than the CPUF predicted front location for experiment 900-14. The bottom plate temperature measured with thermocouple “c” was used for the 900-3 boundary condition; and bottom plate temperature measured with thermocouple ‘h’ was used for the 900-14 boundary condition. The “c” thermocouple temperature is thought to be more representative of the actual boundary condition. Thus, the better agreement between the predicted and measured decomposition front locations for experiment 900-3 are likely due to a better representation of the thermal boundary condition.

An anomaly is shown in Fig. 11.2.C near the centerline of the CPUF contour lines. The shape of the predicted solid fraction contour has unnatural curvature near the centerline. In fact, the black contour forms a circle in the “5-min” plot shown in Fig. 11.2.C. The circle is actually an

element that has not satisfied the “death criterion.” This “ghost element” was not removed from the computational domain due to a numerical oscillation that caused local nodes within this element to have disparate temperatures. Some of the node temperatures were hot and some of the node temperatures were cold, which prevented the average solid fraction within the “zombie element” to drop below the specified “death criterion”. In the current context, a “zombie element” is referred to an element that should be dead (removed from the computational domain) but is not. This numerical instability did not occur in any of the other simulations. The combination of low-density and high thermal boundary temperature produced the highest RPU front velocities in agreement with the experimental data. A similar calculation using CALORE [7] for experiment LD900-7 did not have any numerical instabilities.

Figure 11.3 shows the effect of the heating orientation on the shape of the decomposition front. The RPU foam studied in this report does not exhibit strong liquefaction behavior when the foam is decomposed under ambient pressure with sufficient venting of the decomposition gases. Thus, orientation effects are shown to be negligible, although slight variations are shown in the X-rays in Fig. 11.3. Side-13 is a replicate of experiment Side-11. In experiment Side-11, the X-ray shield started to slowly creep into the line of site of the X-ray camera. One difference between experiment Side-11 and Side-13 was the steady-state temperature of the “c” thermocouple. The steady-state temperature of the “c” thermocouple for experiment Side-11 was about 4ºC colder than the steady-state temperature of the “c” thermocouple for experiment Side-13. The temperature differential of 4ºC caused the centerline front locations to differ by about 1-cm by the end of the experiment, giving an indication of the sensitivity of the radiant heat experiments to the boundary temperature. More discussion on the sensitivity of the CPUF model predictions to other model predictions is given in Section 11.2.

Figures 11.4 and 11.5 show the effect of components on the decomposition front for both the higher density foam and the lower density foam, respectively. The effect of two types of components were studied – 1) a hollow aluminum component and 2) a solid stainless-steel component. The hollow aluminum component has a lower thermal capacitance than the solid stainless-steel components. The components do not significantly influence the decomposition of the encapsulant until the component is exposed to the heated plate. The lower capacitance, hollow aluminum component heats more rapidly than the higher capacitance solid stainless steel component. The temperature of the hollow aluminum component rapidly reaches decomposition temperatures and decomposition of the encapsulant is accelerated near the surface of the component. Conversely, the temperature of the solid stainless steel component heats slowly. The calculated fronts shown as solid mass fraction contours in Fig 11.5 *agree very well* with the fronts shown in the X-ray images as density variations.

Figure 11.6 shows the effect of partial confinement at various levels of backpressure for a steady-state plate temperature of 600ºC. As shown previously in Fig. 10.1.C, the decomposition gases were vented to a backpressure regulator. The backpressure (shown in Fig. 10.11) was regulated to be nominally 0.9-atm, 1.54-atm, and 3.58-atm for Figure 11.6.A-11.6.C, respectively. The higher backpressures cause the CPUF predicted decomposition front velocities to slow. The delay in the predicted front velocity is a result of the pressure dependent vapor-liquid equilibrium model. As the backpressure is increased, the predicted V/L ratio decreases since the vapor-liquid equilibrium ratio or *K-value* is lowered with higher hydrodynamic pressure ($K_i \propto 1/P$).

The width of the reaction zone (decomposition front) for the *unconfined RPU* samples in Figs. 11.1 to 11.5 appeared in the X-ray images to be narrow with little or no liquid accumulation. In contrast, the reaction zones in the *partially confined RPU* samples shown in Fig 11.6 were broad with significant liquid accumulation even at ambient pressures. The front velocities de-

creased with moderate increases in absolute pressures from ambient (600-amb) to 0.16-Mpa (600-1.54), which was consistent with the high pressure TGA experiments. However, as the pressure was increased further in 600-3.58 (to 0.36-Mpa), the front velocity increased dramatically. The increased velocity of the *partially confined RPU at high pressure* was associated with liquefaction and enhanced heat transfer in the reaction zone. A subgrid model can account for enhanced thermophysical property enhancement associated with liquid formation and flow. Such a subgrid model is beyond the scope of the current CPUF foam response model.

The cellular structure, composed of struts and windows separating gas-filled bubbles, collapses when the polymer liquefies. The loss of the cellular structure causes the local density to increase as observed in the X-ray images (Fig 11.6). The collapse of the cellular structure at the heated surface is partially responsible for the observed increase in the decomposition front velocity. The decomposition front is also accelerated as the heat transfer rate is increased due to the higher thermal conductivity of the liquid front and convective heat transfer within the bubbly liquid. An X-ray movie of the 0.3-MPa experiment 600-3.58 showed damage occurring within the closed-cell foam as cell windows opened (ruptured) and a liquid plume penetrated into the previously closed-cell foam. Predicting mechanical damage caused by decomposition chemistry and pressure loading is beyond the current capability of the FEM code and is left as an unsolved research topic.

11.2 Uncertainty Analysis

Uncertainty in the heated plate temperature can lead to uncertainty in the predicted location of the decomposition front as discussed in the preceding section. There is also uncertainty associated with precise placement of the CPUF simulations on the X-ray image. The placement of the image depended on knowing the location of the initial foam interface. For example, in experiment ss-1000-19 a 3-mm gap was left between the face of the component and the foam. The

gap was caused by not fully seating the component before performing the experiment. Other sources of uncertainty include the presence or absence of a gap between the foam and the heated plate. The simulations were performed with a best estimate of the uncertainty in geometry and other model parameters.

To quantify some of the uncertainty in the foam response model, a mean value analysis was performed with the response variable chosen as the solid fraction for experiments 600-1, 750-2, and 900-14. For this analysis, recall from Section 8, the mean solid fraction and the standard deviation of the solid fraction can be calculated as follows.

$$\mu_{s_f} = S_f(\xi)\big|_{\xi=\mu_i} \tag{70}$$

$$\sigma^2_{s_f} = \sum_{i=1}^{n}\left[\sigma_i \frac{\partial s_f(\xi)}{\partial \xi_i}\Big|_{\xi=\mu_i}\right]^2 . \tag{71}$$

The mean solid fraction, μ_{sf}, and the standard deviation of the solid fraction, σ_{sf}, was calculated in every element of the 2D axisymmetric radiant heat mesh and at every time step. The partial derivatives in Eq. (71) were performed numerically by using a simple central difference scheme, which is expressed as follows:

$$\frac{\partial s_f(\xi)}{\partial \xi_i} \approx \frac{s_f^+ - s_f^-}{\xi_i^+ - \xi_i^-} \tag{72}$$

where s_f^+ represents the solid fraction evaluated with the mean CPUF parameters listed in Table 7.1 except for the ith variable evaluated at ξ_i^+, which is 1.05 times the mean value of the ith input parameter. Similarly, s_f^- represents the solid fraction evaluated with the mean CPUF parameters listed in Table 7.1 except for the ith input parameter evaluated at ξ_i^-, which is 0.95 times the mean value of the ith input parameter.

The number of simulations required to determine the sensitivity using central difference derivatives is 2n + 1 where n is the number of input parameters considered in the analysis. Only 24 of the 27 input parameters given in Table 7.1 were considered for the radiant heat experiment uncertainty analysis. The three parameters not considered in the uncertainty analysis were the interaction energy, I_E; the lattice coordination number, σ+1; and the pre-exponential factors, A_i. The standard deviations of the coordination number and pre-exponential factors were assumed to be zero and do not contribute to uncertainty. The interaction energy *only* has an influence on experiments performed at elevated pressure and would not contribute to the uncertainty of the response for experiments 600-1, 750-2, or 900-14. One parameter not listed in Table 7.1 that was also considered in the uncertainty analysis was the element death criterion with the mean and standard deviation listed in Table 9.1. With 25 variables of interest (24 from Table 7.1 and the death criterion from Table 9.1), 51 simulations were run for each of the three experiments for a total of 153 simulations. A FORTRAN code was written that evaluates the mean and standard deviation in both spatial and temporal space and is given in the appendix for experiment 750-2.

In addition to evaluating the uncertainty in the calculated solid fraction, the relative contribution to the uncertainty in the solid fraction from each on the input parameters can be evaluated using the following equation:

$$I_i = \gamma_i^2 = \left(\frac{\sigma_i}{\sigma_{s_f}} \times \frac{\partial s_f(\xi)}{\partial \xi_i} \Big|_{\xi=\mu_i} \right)^2 \tag{73}$$

where I_i, is the importance factor for parameter *i*. The variable γ_i is the scaled sensitivity coefficient for parameter *i*, which varies between –1 and +1 and indicates the relative sensitivity of solid fraction to uncertainty in the I^{th} input parameter. The importance factors are the squares of the scaled sensitivity coefficients and the sum of the importance factors equals unity. The impor-

tance factors provide a measure of which input parameters contribute the most to the total uncertainty in the calculated solid fractions.

Figure 11.8 shows X-rays of experiments 600-1, 750-2, and 900-14 at various times. The mean location of the 0.5 solid fraction contour is plotted on the X-rays using a solid white line. The mean solid fractions plus and minus two standard deviations are also plotted on the X-rays using solid black lines. The area between the black lines represents the 95% prediction interval for the location of the 0.5 solid fraction contour. Previously in Figs. 11.1 through 11.6, the 0.005, 0.125, 0.5, and 0.875 *mean solid fraction contours* were plotted. In Fig. 11.8, *only the 0.5 contours* are plotted with the uncertainty based only on model parameters. Uncertainty in the boundary temperatures is not included in the prediction intervals depicted in Fig. 11.8, which can be substantial as shown for the replicate experiments with the 900°C plate temperatures depicted previously in Fig. 11.C and 11.D. The boundary condition for the CPUF prediction of experiment 900-3 used the “c” thermocouple, which is probably a better representation of the actual plate temperature than the “h” thermocouple. A more representative boundary condition made the predicted front locations agree with the measured front location for the 900°C experiment. Even by considering uncertainty in 25 parameters, the 95% prediction interval did not cause the location of the burn front for the 900°C experiment to change substantially from the mean prediction. For experiment 900-14, the foam response is more sensitive to boundary conditions than to the uncertainty in the model parameters. Conversely, the foam response is more sensitive to the model parameters than to the uncertainty in using either the “h” or the “c” thermocouples for the lower temperature experiment 600-1,

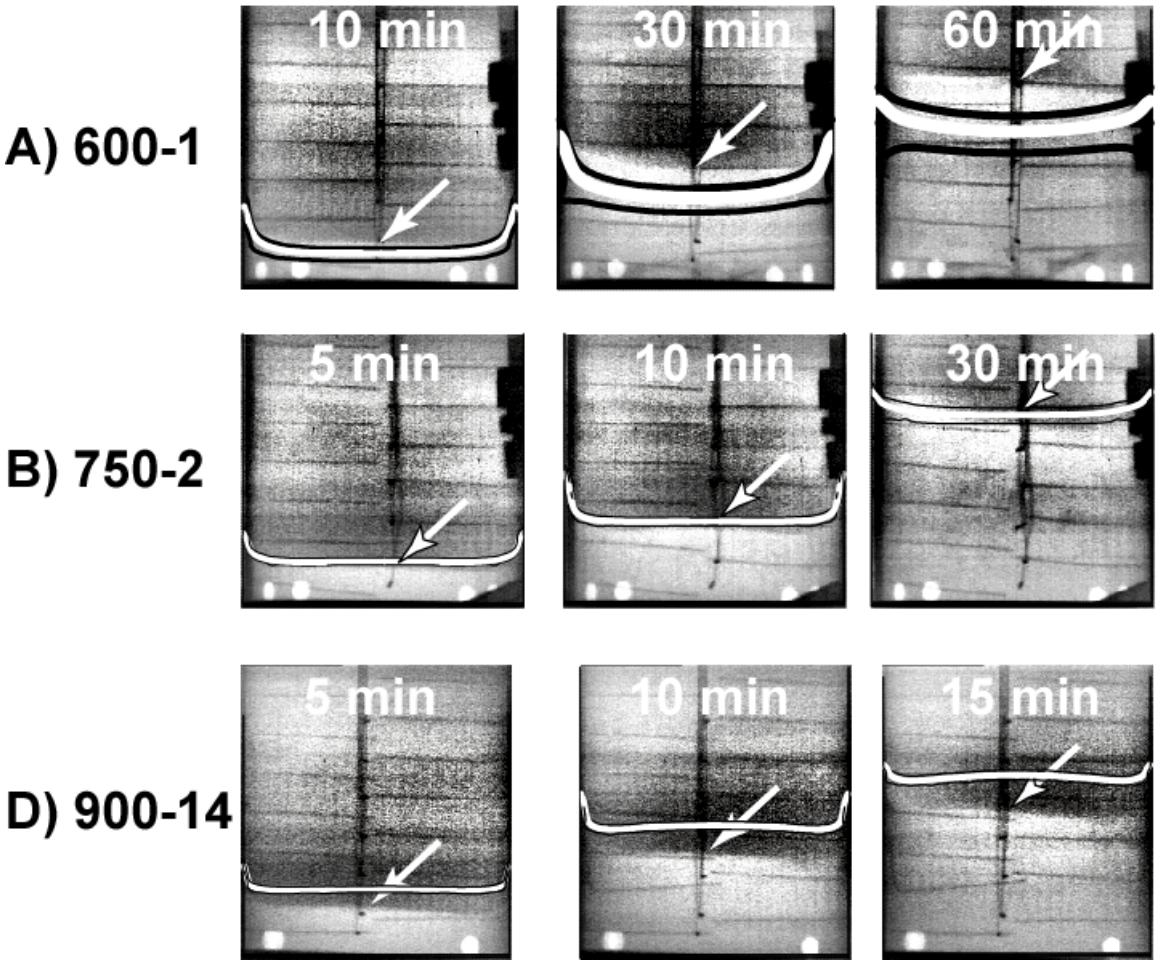

Fig. 11.7. X-ray overlay of the mean solid fraction contour line at 0.5 (solid white line) and the mean solid fraction contour line at 0.5 ±2 standard deviations (solid black lines) defining the 95% prediction interval.

In Fig. 11.7, the 95% prediction interval is larger for experiment 600-1 than it is for experiment 750-2 and 900-14. In fact, the 95% prediction interval or the 750-2 experiment is larger than the 95% prediction interval for experiment 900-14. The higher degree of uncertainty associated with the lower temperature experiments may be related to the thickness of the decomposition front. If the heated plate is kept at a lower temperature, the temperature gradient across the decomposition front is not as steep as the temperature gradient the decomposition front in the foam for higher plate temperatures. Lower temperature gradients result in thicker reaction fronts

and more material exposed to temperatures high enough for decomposition to be significant. Other factors that may cause greater uncertainty for low temperature decomposition is an increase in the potential for liquefaction. When decomposition occurs within the foam, decomposition products that do not readily escape the surface of the foam may act as solvents that induce liquefaction mechanisms that increase the apparent decomposition front velocity.

Figure 11.8 shows a plot of the 95% prediction interval for the location of the 0.5 solid fraction contour at the centerline of the radiant heat experiments. This prediction interval is centered about the mean location of the 0.5 solid fraction, which is represented by a black line in Fig. 11.8. The solid fraction contour locations were determined as the distance from the heated plate surface to the location along the foam centerline where the solid fraction contour was 0.5. The 95% prediction interval is greater for 600-1 than for 750-2. Likewise the prediction interval for 750-1 is greater than for 900-15. As noted earlier, even by considering uncertainty in 25 parameters, the 95% prediction interval did not cause the location of the burn front for the 900°C experiment to change substantially from the mean prediction. However, a change of the bottom heated plate temperature by 7°C (difference between the steady plate temperature as measured by the “c” and “h” thermocouples for experiment 900-3) was partially responsible for the predicted and measured decomposition front locations being in better agreement as shown previously in Fig. 11.1.C. The foam response is highly dependent on the boundary conditions.

The importance factors shown in Fig. 11.8 provide a measure of which input parameters contribute the most to the total uncertainty in the calculated solid fractions. In Fig. 11.8A, the most important parameters contributing to the uncertainty in the front location for experiment 600-1 are the heat of reaction, h_r, and the death criterion. The importance of a variable does not indicate importance in the model. Instead, importance refers to the contribution each input parameter has to the *uncertainty* of the calculated solid fraction or response. The chemistry parameters show minor contributions to the response uncertainty, implying that the uncertainty in chemistry parameters is not sufficient to contribute significantly to the response uncertainty.

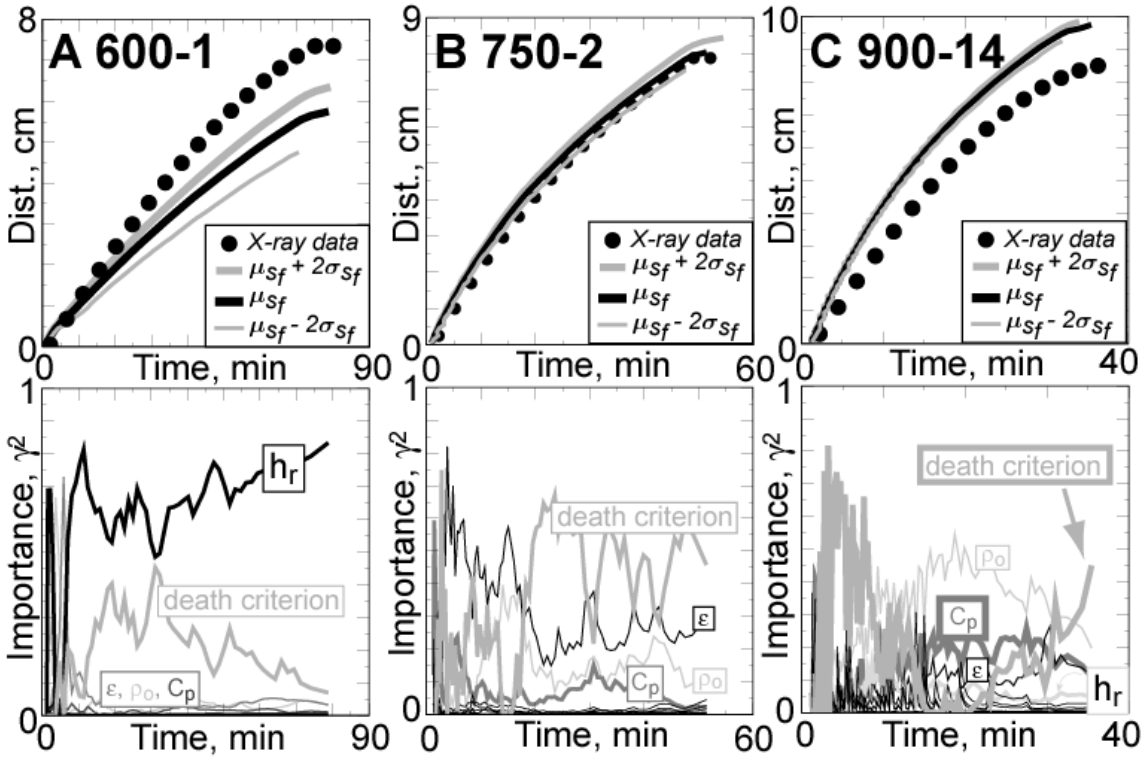

Fig. 11.8. Comparison of the measured centerline distance from the heated plate to the decomposition front determined from X-ray data (solid circles) to the calculated centerline distance from the heated plate to the location of the $\mu_{sf} \pm 2\sigma_{sf}$ centerline solid fraction (solid lines) for experiments A) 600-1, B) 750-2, and C) 900-14. The 0.5 solid fraction contour was used for μ_{sf}. The importance factors are given directly below the front location plots.

The heat of reaction is the primary input parameter that affects the uncertainty in the decomposition front for experiment 600-1. The influence of the heat of reaction does not significantly affect the predicted uncertainty in decomposition front location for experiments 750-2 and 900-14. The heat of reaction influences the velocity of the decomposition front when temperatures are lower due to a thicker reaction zone. More of the foam participates in the endothermic decomposition and influences the velocity of the decomposition front.

The importance of the thermophysical properties such as emissivity, density and specific heat have secondary influences on the uncertainty predictions for the 600ºC experiment. However, these parameters contribute more to the uncertainty as the boundary temperature is increased. Then again, the uncertainty in the foam response due to parameter uncertainty also decreases with increasing temperature. The only variable that seems to be a significant contributor to prediction uncertainty for all three experiments is the death criterion. Death is a primary effect parameter that may be used as with a subgrid-engineering model to correct the solution for phenomena that is not currently modeled such as liquefaction effects or fluid flow. Such a subgrid model may be necessary to model decomposition of encapsulants such as the removable epoxy foam (REF) that is known to have significant liquefaction.

11.3 Three-Dimensional Simulation of Experiment 750-2

To investigate the CPU requirements for large-scale, three-dimensional geometries, the initial decomposition of RPU with a 750ºC boundary temperature (experiment 750-2) applied for 5 minutes in both 3D and 2D were completed. The 3D and 2D models consisted of 277,652 and 1,760 elements, respectively. The time-resolved results for both models were consistent. The 3D model required 7 hours and 20 minutes of CPU time using 256 processors on JANUS (a massively parallel computer system at Sandia National Laboratories in Albuquerque); and the 2D model required 40 CPU minutes using one processor on a SUN Microsystems 400-MHz work-

station. Assuming the problem scales linearly, a complete simulation of the experiment (boundary temperature applied for 1 hour rather than 5 minutes) using the 3D mesh would have required 94 hours (~4 days) of CPU time using 256 processors. In contrast, the 2D model required 9 hours of CPU with 1 processor. Uncertainty quantification is currently prohibitive for 3D problems, unless a more simple foam response model is developed. This model should have a discretization bias correction for arbitrary element geometries and sizes. Such a model has been developed at Sandia and is referred to as the Simple PolyUrethane Foam (SPUF) response model [33].

Figure 11.9 shows the 2D and 3D mesh used to simulate experiment 750-2. For these simulations, only 4-cm of the foam cylinders were simulated. Figure 11.10 shows a comparison between the 2D and 3D model at various times. After 5 minutes, the decomposition front has moved approximately 1-cm.

Table 11.1 gives the CPU times for the 3D and 2D model. The viewfactor calculation dominates the simulation time in both 2D and 3D. Previous misconceptions that the viewfactor calculation in the 2D-axisymetric calculation would be about the same as a full 3D simulation are obviously not correct for foam decomposition problems since a uniform mesh is required to avoid discretization bias errors. A complete 2D simulation of the experiment (boundary temperature applied for 1 hour rather than 5 minutes) required 9 hours and 16 minutes of CPU time using 1 processor. Assuming the problem scales linearly, the required CPU time for the 3D calculation would be 256 processors is 94 hours.

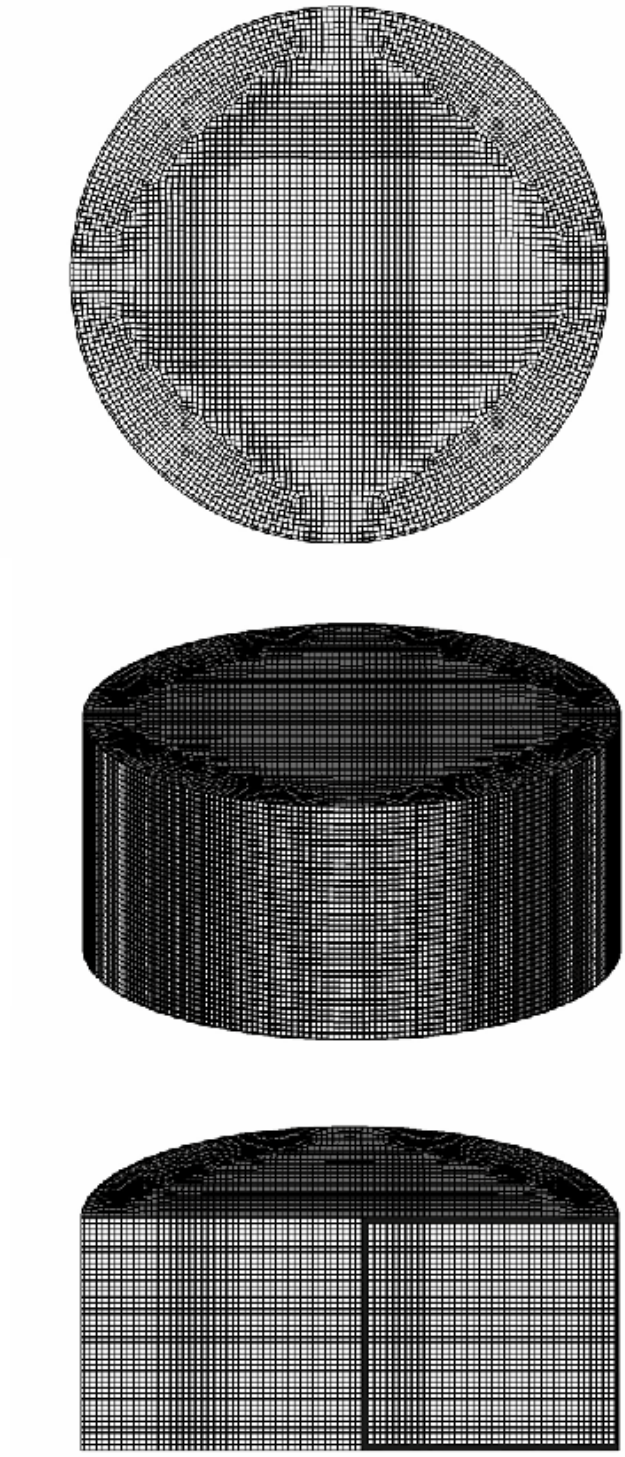

Fig. 11.9. Different views of the 3D mesh: end view, side view, and interior view. The interior view has the 2D-axisymetric mesh outlined.

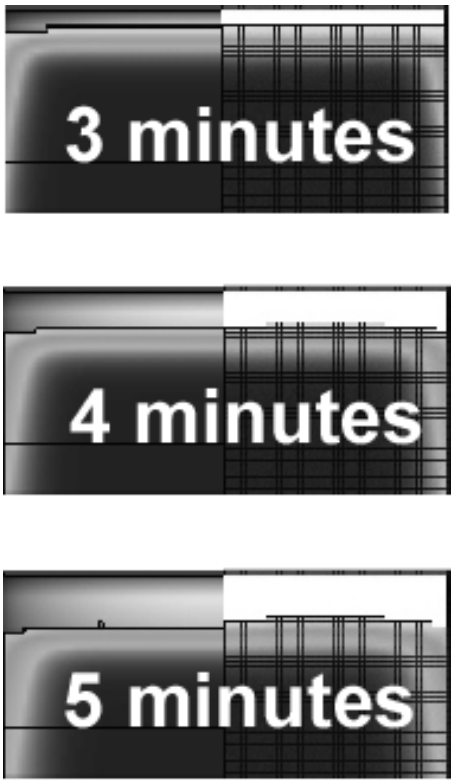

Fig. 11.10. Comparison between 3D (left side) and 2D (right side) calculation with top plate temperature held at 750ºC for 3, 4, and 5 minutes. The 3D enclosures show the temperature of the stainless steel skin in the background The 2D enclosure is shown in white.

Table 11.1. CPU times for 3D and 2D COYOTE calculation of reactive foam with dynamic enclosure.

	3D - 256 processors	**2D - 1 processor**
Viewfactors	4 hrs 39 min (63%)	24 min (55%)
Radiation	11 min (3%)	0.3 sec (0.0%)
Chemistry	2 hrs 19 min (32%)	19 min (44%)
Global Matrix	2 min (0.5%)	11 sec (0.4%)
Aztec Solver	2 min (0.5%)	9 sec (0.3%)
Time in Solution	7 hrs 20 min	43 min 25 sec

12 Summary and Conclusions

A detailed model based upon the chemical structure of rigid, closed-cell polyurethane foam has been presented. The chemical structure of the polymer was determined from the synthesis details by assuming equal reactivity of various functional groups. The chemical structure of the rigid polyurethane foam (RPU) was essentially an *infinite lattice* composed of trimethylolpropane and diethylene glycol sites connected by either primary or secondary bridges. The specific RPU discussed in this report will not be manufactured further due to carcinogens used in the formulation. However, the RPU foam is in existing systems, where the RPU decomposition model should be useful. The method of developing a detailed chemistry model and subsequent incorporation into an overall foam response model has been demonstrated.

A detailed bond breaking mechanism consisting of sixteen reactions was determined using various small-scale experiments. The reaction mechanism assumed that the weakest bonds in the polymer lattice would break at elevated temperatures. The progress of the bond populations, from an initial population of 1 to a final population of 0, was determined using Arrhenius kinetics. The activation energies for the 16 reactions were assumed to be distributed normally based on the extent of breaking the bonds associated with the adipate bridges.

Lattice statistics were used with the dynamic bond populations to determine the distribution of various polymer fragments of known molecular weights. Percolation theory was used as the lattice statistics model for computational efficiency. Percolation theory has been used extensively to model fluid permeation in porous materials where sites are either permeable or impermeable. When percolation theory is applied to polymer decomposition or synthesis, the bonds are specified as being either intact or broken. The primary assumption for using percolation theory is that the sites are only connected to each other by one bridge. Multiple bridges between two sites would create loops in the lattice structure that require either iterative solutions or Monte-

Carlo methods that are computationally inefficient. The assumption of no loop backs has been shown to give reasonable agreement with more intense Monte Carlo simulations [10].

Solution of the bond-breaking kinetic mechanism is performed using a stiff ODE solver package (DDEBDF, Ref. 20). After a given time step, the algebraic lattice statistics model is solved for the concentration of various chemical species such as carbon dioxide, various polymer fragments, monomers, dimers, etc. The lattice statistics model does not determine whether any of these chemical species are in the condensed-phase or in the gas-phase. Vapor-liquid equilibrium (VLE) is assumed to determine the amount of each species that resides in either the gas-phase or condensed-phase. Various activity coefficient models were investigated for the VLE model – 1) Raoult's law solution, 2) Ideal-solution, and 3) a Regular-solution. All three models were chosen to give the same solution at ambient pressures. However the Regular-solutions model performed best at elevated pressure since the high-pressure TGA data were used to obtain the "interaction energy" for the Regular-solutions model. A better liquid activity coefficient model is needed for more accurate solutions at elevated pressures.

The chemistry portion of the CPUF model is composed of the bond-breaking mechanism, lattice statistics, and VLE model. The chemistry portion of the CPUF model is sufficient to determine the mass loss associated with thermal degradation and the composition of the decomposition gases. However, to model the response of RPU foam in large-scale systems, thermophysical properties are needed to determine the energy transport within the foam. Reaction enthalpy is needed to account for energy changes associated with the bond-breaking mechanism. An element death criteria is needed to remove elements from the computational domain creating a dynamic radiation enclosure.

Elements are removed when the solid fraction within the element drops below a specified criterion. This criterion, known as the "death criterion", was specified in the CPUF model based

on experimental data. Various one-dimensional simulations based on element death were performed to determine the steady-state decomposition front velocity for a strand of foam insulated on three sides with one side exposed to a far-field radiation boundary condition. The steady-state front velocity was found to be highly dependent on the size of the element used in the simulations. By reducing the size of the element to 100-μm, a grid independent velocity was determined. Large-scale simulations are impractical using such small elements. A subgrid model for the CPUF foam response model was developed to correct the solution so that 1-mm elements can be used for large-scale calculations to give the same solution as a solution with a 100-μm sized grid. The methodology for bias correction could have been generalized for any size element, including mixed-element type such as hexahedral and tetrahedral elements [33].

All of the CPUF parameters were assumed normally distributed and were obtained from various small-scale experiments. Thermophysical parameters for the CPUF model included density, temperature, thermal conductivity, specific heat, reaction enthalpy, surface emissivity, and the interaction energy for the VLE model. The lattice statistics parameters for the model included the coordination number of the lattice and the initial bridge populations. The chemistry parameters included the frequency factor commonly referred to as the pre-exponential factor, the 16 activation energies and the standard deviation of the activation energy used to distribute the reaction rates. The thermal conductivity and specific heat were linear functions of temperature between 23ºC and 250ºC. For temperatures greater than 250ºC, thermal conductivity and specific heat were linearly extrapolated. Thermal conductivity and specific heat were measured for three densities of foam – 0.078-g/cm^3, 0.15-g/cm^3, and 0.352-g/cm^3

Mass loss predictions were compared to mass loss measurements made in both low pressure and high pressure TGA experiments with the sample temperature ramped at 5ºC/m, 20ºC/m, and 50ºC/m. The low-pressure TGA experiments were performed at various levels of

confinement (open pan, 1-mm orifice, 0.4-mm orifice, and 0.06-mm orifice). Predictions were not made for the partially confined TGA experiments. However predictions of pressure effects were made of pressurized TGA experiments where purge gas was used to sweep the decomposition from the TGA samples. The 20ºC/m experiments were performed at ambient pressure, 0.5-MPa, 1-MPa, and 3-MPa pressure. Predictions for the pressurized TGA experiments were made using various activity coefficient models with the best solutions predicted with the Regular-Solutions model. In the TGA experiments, mass loss was inhibited with increasing pressure (0.1-MPa, 0.5-MPa, 1.0-MPa, and 3.0-Mpa) and increasing levels of confinement (open pan, 1-mm orifice, 0.4-mm orifice, and 0.06-mm orifice). Most of the ramped TGA mass loss data were within the 95% prediction limit of the CPUF model determined using mean value analysis. Confirmatory calculations were performed with Latin Hypercube Sampling techniques to show that the mean value assumptions were valid.

Similar comparisons were made with isothermal experiments where small samples were ramped from ambient temperatures to 250ºC, 270ºC, and 300ºC and held for 50 hours, 20 hours, and 20 hours, respectively. Reasonable solutions were obtained for the 300ºC isothermal experiment for the duration of the experiment. For the lower temperature isothermal TGA experiments agreement was only good for the first 5 hours; after 5 hours, the predicted mass loss was greater than the measured mass loss. A dual isothermal experiment were also simulated where the sample temperature was ramped to 300ºC and held for 2 hours and then ramped to 400ºC and held for an additional 4 hours. The mass loss data for the dual isothermal simulations were within the 95% prediction limit of the CPUF model.

The activation energies that contribute to the uncertainty in the 20ºC/m TGA experiments were identified for the ambient pressure TGA experiments as well as the TGA experiment run at 30 bars. The parameters that contributed the most to the uncertainty in the mass loss predictions

were essentially the same for ambient pressure and 30-bar. However, at 30-bars, the interaction energy parameter in the VLE submodel also became significant. The interaction energy is not significant at ambient pressures. The parameters, which contributed the most to the uncertainty in the mass loss predictions, were the activation energy associated with breaking the initial urethane bridge structure and the activation energy associated with breaking the initial adipate bridge structure. Other significant contributions to response uncertainty were associated with the formation of the amino-urethane bridge and formation of the diamine bridge.

As the final test of the CPUF response model, 19 radiant heat experiments were simulated using a 2D axisymetric mesh. One of these experiments was simulated with a 3D mesh to get information regarding CPU requirements for large-scale, three-dimensional simulations. The 19 experiments included the effects of 1) the bottom plate temperature for high density RPU foams, 2) the bottom plate temperature for low density RPU foams, 3) the orientation of the heated plate in relationship to the gravity vector, 4) the influence of the embedded components in high density foam, 5) the influence of the embedded components in low density foam, 6) and the level of backpressure as well as the degree of confinement of the decomposition gases. The temperature boundary conditions for the heated plate and confinement walls were presented. The measured heat flux near the heated plate is also presented. A full mean value analysis was performed for the high-density foam in the radiant heat experiments for three experiments where the heated surface was maintained at 600ºC, 750ºC, and 900ºC. Uncertainties in boundary temperatures were shown to contribute more to the uncertainty of the decomposition front location than uncertainty in the CPUF parameters. The model parameters, which contributed most to uncertainty for the lower temperature radiant heat experiments, were the heat of reaction and the element death criterion. With higher boundary temperatures, the thermophysical properties of the foam contributed more to the uncertainty in the predicted decomposition front location. The de-

gree of uncertainty due to model parameters is related to the thickness of the reaction fronts, which in turn are related to the thermal boundary conditions.

The radiant heat experiments were analyzed using an X-ray camera with shots taken for most of the experiments every 30 seconds (for experiment ss-1000-19, the X-ray pictures were taken every 18 seconds). For the 21 radiant heat experiments, selected X-rays were compared to CPUF predictions. The X-rays show density variations that correspond to different densities within the experiment. In the X-ray pictures, the decomposition front appeared darker than the surrounding foam or enclosure. In the CPUF predictions, the decomposition front can be highlighted by plotting the solid fraction contours. Solid fraction contours were overlaid onto the X-rays for comparison with the decomposition front measured with the X-ray camera. Agreement between most of the CPUF predictions are within expected uncertainty due to model parameters and boundary conditions.

The front velocities for the partially confined radiant heat experiments at relatively low pressures, 600-amb-p4 and 600-1.54-p2, increased slightly in comparison to the ambient pressure unconfined experiment 600-1. However, at 0.36-Mpa backpressure, the decomposition front velocity for experiment 600-3.58-p3 was shown to increase, rather than decrease. The enhanced decomposition at 0.36-Mpa may be due to liquefaction resulting in collapse of the foam structure and increased heat transfer. Liquefaction of the RPU foam was also observed in the X-ray movies for all of the semi-confined decomposition experiments, even at low pressures.

Higher boundary temperatures (higher fluxes) resulted in faster decomposition fronts and narrow reaction zones for the unconfined radiant heat experiments using RPU encapsulants. Orientation did not seem to have a large effect on the unconfined RPU experiments. Flow effects were observed when the RPU foam was partially confined. The high thermal capacitance components had little effect on the propagation of the decomposition fronts. However, the low ther-

mal capacitance components caused the foam near the surface of the component to preheat significantly and caused the decomposition front to move rapidly around the component. Lower density foam resulted in faster decomposition front velocities due to less material available for decomposition.

In summary, various unconfined experiments were modeled using a foam decomposition mechanism, lattice statistics model, and a vapor-liquid equilibrium model. The dynamic radiation enclosure was simulated by removing elements from the computational domain after meeting an element death criterion based on the foam chemistry (calculated solid fraction within the finite elements). Uncertainty was propagated into some of the numerical simulations to show the relative importance of model parameters. Model results were compared to TGA weight loss measurements and X-rays images of the various large-scale experiments. Although the shape of the front was difficult to determine near the wall in the X-rays and the location of the front was difficult to see in the low-density experiments, the calculated and measured shapes of the decomposition fronts for the unconfined experiments appear to *agree very well*.

Appendix

The appendix contains the FORTRAN data statements used to specify the boundary conditions for each of the radiant heat experiments. The appendix also contains the FORTRAN code used to determine the mean value uncertainty analysis of experiment 750-2.

Boundary Conditions:

600-1

```
C z distance from bottom plate TC to CUP TC's
      data z/ 0.0, 0.48, 1.11, 2.38, 3.65, 4.92, 6.83,16.51/
C ts time in s
      data ts/ 0.0, 39.8, 89.8, 119.8, 179.8, 314.8, 459.8, 599.8,
     & 879.8, 1501.8, 2901.8, 4156.8, 4281.8, 4436.8, 4661.8, 5016.8/
C t0 thermocouple 0 (bottom plate thermocouple)
      data t0/ 294.0, 295.4, 854.5, 889.1, 873.8, 873.2, 873.5,
     & 873.5, 879.8, 873.8, 873.2, 873.8, 800.3, 733.3, 659.0, 576.8/
C t1 thermocouple 1
      data t1/ 300.0, 296.2, 525.3, 662.3, 736.1, 775.1, 791.1,
     & 797.6, 801.6, 804.6, 804.6, 805.2, 763.0, 707.8, 641.7, 558.4/
C t2 thermocouple 2
      data t2/ 300.0, 297.2, 399.9, 521.1, 616.1, 679.2, 716.7,
     & 733.3, 744.5, 751.8, 754.6, 754.2, 727.4, 680.4, 620.5, 539.3/
C t3 thermocouple 3
      data t3/ 300.0, 298.7, 316.2, 385.0, 474.3, 554.8, 608.8,
     & 637.4, 666.0, 690.7, 699.5, 695.3, 680.3, 641.4, 588.2, 512.8/
C t4 thermocouple 4
      data t4/ 300.0, 300.0, 306.5, 338.6, 407.1, 492.1, 550.0,
     & 577.9, 602.4, 638.4, 667.2, 660.0, 647.0, 613.6, 565.7, 494.9/
C t5 thermocouple 5
      data t5/ 300.0, 301.2, 306.9, 322.9, 371.0, 455.0, 510.7,
     & 536.0, 556.8, 579.1, 632.7, 626.9, 616.8, 587.7, 540.9, 475.2/
C t6 thermocouple 6
      data t6/ 300.0, 303.4, 309.1, 314.4, 339.3, 409.9, 457.2,
     & 470.5, 486.5, 493.2, 530.2, 544.2, 539.4, 521.2, 481.5, 434.2/
C t7 thermocouple 7 (Assumed temperature at the top of the cup)
      data t7/ 300., 300., 300., 300., 300., 300., 300., 300., 300.,
     & 300., 300., 300., 300., 300., 300., 300./
```

750-2

```
C z distance from bottom plate TC to CUP TC's
      data z/ 0.0, 0.48, 1.11, 2.38, 3.65, 4.92, 6.83,16.51/
C ts time in s
      data ts/ 0., 34.8, 39.8, 64.8, 89.8, 139.8, 199.8, 254.8,
     & 334.8, 499.8, 879.8, 1079.8, 1499.8, 2419.8, 2794.8,
     & 2909.8, 3044.8, 3306.8/
C t0 thermocouple 0 (bottom plate thermocouple)
      data t0/ 300.0, 300.5, 402.2, 937.7, 1045.4, 1024.5, 1024.7,
```

```
     & 1023.8, 1023.9, 1023.1, 1023.5, 1023.5, 1023.3, 1023.4, 1024.0,
     & 912.2, 816.7, 700.4/
C t1 thermocouple 1
      data t1/ 300.0, 300.6, 301.3, 507.2, 703.5, 822.2, 856.2,
     & 870.2, 879.2, 891.5, 891.8, 894.6, 898.6, 899.2, 900.9,
     & 849.6, 777.0, 669.0/
C t2 thermocouple 2
      data t2/ 300.0, 301.2, 301.3, 382.2, 541.8, 678.3, 739.2,
     & 768.3, 794.0, 824.5, 835.0, 838.0, 845.3, 847.4, 850.0,
     & 812.3, 750.9, 648.3/
C t3 thermocouple 3
      data t3/ 300.0, 302.6, 302.7, 313.0, 383.2, 509.6, 580.9,
     & 619.5, 661.5, 721.6, 790.0, 795.1, 813.2, 817.9, 819.2,
     & 784.7, 722.9, 624.4/
C t4 thermocouple 4
      data t4/ 300.0, 304.1, 304.2, 307.4, 340.3, 437.3, 500.2,
     & 542.1, 582.3, 624.2, 727.9, 741.4, 772.9, 783.4, 783.8,
     & 756.0, 696.7, 604.0/
C t5 thermocouple 5
      data t5/ 300.0, 305.9, 306.1, 309.6, 333.3, 407.3, 462.2,
     & 504.8, 530.2, 566.0, 655.4, 664.2, 714.2, 740.3, 739.1,
     & 720.0, 666.3, 579.9/
C t6 thermocouple 6
      data t6/ 300.0, 309.0, 310.3, 318.1, 329.4, 376.5, 404.3,
     & 466.2, 457.9, 471.6, 534.8, 534.2, 571.3, 640.0, 644.1,
     & 636.6, 595.6, 527.4/
C t7 thermocouple 7 (Assumed temperature at the top of the cup)
      data t7/ 300., 300., 300., 300., 300., 300., 300., 300., 300.,
     & 300., 300., 300., 300., 300., 300., 300.,300.,300./
```

900-3

```
C z distance from bottom plate TC to CUP TC's
      data z/ 0.0, 0.48, 1.11, 2.38, 3.65, 4.92, 6.83,16.51/
C ts time in s
      data ts/ 0.0, 34.8, 59.8, 104.8, 134.8, 184.8, 259.8,
     & 394.8, 514.8, 789.8, 1229.8, 1284.8, 1384.8, 1539.8,
     & 1639.8, 1764.8, 1934.8, 2194.8/
C t0 thermocouple 0 (bottom plate thermocouple)
      data t0/ 282.9, 286.2, 514.2, 1076.7, 1155.6, 1150.9,
     & 1151.7, 1154.3, 1155.3, 1156.3, 1156.7, 1157.5,
     & 1159.4, 1156.1, 999.4, 878.0, 770.2, 662.9/
C t1 thermocouple 1
      data t1/ 283.2, 283.4, 352.1, 704.9, 853.1, 933.9,
     & 975.5, 988.4, 995.1, 1000.2, 1002.6, 1002.8,
     & 1021.9, 1016.4, 918.3, 815.5, 718.0, 616.1/
C t2 thermocouple 2
      data t2/ 283.4, 283.4, 304.1, 516.8, 660.8, 785.7,
     & 881.1, 919.0, 931.0, 936.4, 938.3, 937.2, 965.5,
     & 956.0, 876.0, 778.8, 688.3, 590.5/
C t3 thermocouple 3
      data t3/ 283.8, 283.8, 286.0, 358.3, 459.0, 596.6,
     & 726.2, 835.7, 867.0, 889.8, 894.7, 891.2, 930.7,
     & 919.9, 848.7, 747.1, 660.7, 566.2/
C t4 thermocouple 4
      data t4/ 284.1, 284.1, 284.8, 321.9, 385.5, 522.0,
     & 644.3, 752.0, 795.1, 842.4, 856.7, 851.4, 900.4,
```

```
     & 889.3, 826.9, 724.5, 641.9, 550.9/
C t5 thermocouple 5
      data t5/ 284.4, 284.5, 285.2, 310.3, 371.2, 494.4,
     & 624.9, 723.3, 744.0, 790.7, 814.7, 806.9, 857.9,
     & 846.5, 794.2, 696.4, 618.5, 532.8/
C t6 thermocouple 6
      data t6/ 285.0, 285.4, 288.2, 296.8, 376.8, 529.3,
     & 619.6, 702.7, 700.7, 721.4, 758.6, 722.5, 744.1,
     & 743.4, 709.5, 630.7, 565.2, 495.4/
C t7 thermocouple 7 (Assumed temperature at the top of the cup)
      data t7/ 300., 300., 300., 300., 300., 300., 300., 300., 300.,
     & 300., 300., 300., 300., 300., 300., 300.,300.,300./
```

900-14

```
C z distance from bottom plate TC to CUP TC's
      data z/ 0.0, 0.48, 1.11, 2.38, 3.65, 4.92, 6.83,16.51/
C ts time in s
      data ts/ 0., 34.8, 39.8, 94.8, 104.8, 134.8, 149.8, 199.8,
     & 269.8,359.8, 429.8, 639.8, 894.8, 1354.8, 1879.8, 1959.8,
     & 2069.8, 2194.8, 2464.8/
C t0 thermocouple 0 (bottom plate thermocouple)
      data t0/ 296.3, 296.4, 314.3, 1112.4, 1163.4, 1201.0,
     & 1197.5, 1175.8, 1174.1, 1173.1, 1173.4, 1173.0, 1173.7,
     & 1173.3, 1173.7, 1045.0, 925.0, 832.6, 704.4/
C t1 thermocouple 1
      data t1/ 297.1, 297.2, 298.0, 685.3, 752.9, 872.9, 900.8,
     & 933.4, 953.4, 967.5, 970.3, 982.6, 995.9, 1001.8, 1003.0,
     & 934.7, 847.9, 772.7, 661.8/
C t2 thermocouple 2
      data t2/ 297.8, 297.9, 298.1, 508.2, 569.3, 691.5, 728.9,
     & 804.1, 856.4, 889.9, 897.6, 919.2, 937.6, 948.1, 950.8,
     & 895.3, 816.1, 745.2, 640.2/
C t3 thermocouple 3
      data t3/ 299.0, 299.1, 299.4, 367.1, 423.9, 515.9, 551.5,
     & 620.0, 685.8, 762.7, 799.5, 857.6, 889.0, 905.1, 912.9,
     & 864.5, 788.2, 718.0, 615.9/
C t4 thermocouple 4
      data t4/ 300.1, 300.2, 300.6, 339.0, 386.7, 451.5, 477.7,
     & 531.4, 590.4, 660.9, 693.5, 786.4, 844.9, 872.6, 883.8,
     & 839.2, 764.9, 696.7, 595.9/
C t5 thermocouple 5
      data t5/ 301.4, 301.5, 301.7, 330.7, 362.9, 411.4, 433.1,
     & 477.1, 526.6, 587.2, 610.0, 683.1, 768.1, 824.8, 841.6,
     & 802.6, 732.1, 668.2, 569.9/
C t6 thermocouple 6
      data t6/ 303.8, 303.8, 304.9, 321.9, 327.3, 349.2, 363.3,
     & 399.9, 437.3, 474.6, 487.3, 528.9, 571.2, 651.3, 693.7,
     & 664.4, 615.6, 570.9, 492.7/
C t7 thermocouple 7 (Assumed temperature at the top of the cup)
      data t7/ 300., 300., 300., 300., 300., 300., 300., 300., 300.,
     & 300., 300., 300., 300., 300., 300., 300.,300.,300.,300./
```

Id600-6

```
C z distance from bottom plate TC to CUP TC's
      data z/ 0.0, 0.48, 1.11, 2.38, 3.65, 4.92, 6.83,16.51/
C ts time in s
```

```
      data ts/ 0.0, 34.8, 44.8, 94.8, 114.8, 134.8, 164.8, 209.8,
     & 294.8, 429.8, 639.8, 864.8, 1174.8, 1554.8, 1724.8, 1924.8/
C t0 thermocouple 0 (bottom plate thermocouple)
      data t0/ 297.8, 298.1, 336.9, 813.1, 872.4, 884.7, 881.2, 871.9,
     & 869.0, 869.8, 869.7, 870.4, 870.3, 869.7, 780.2, 703.5/
C t1 thermocouple 1
      data t1/ 299.7, 299.8, 304.8, 546.0, 633.0, 682.7, 722.7, 744.7,
     & 761.2, 782.2, 793.5, 796.0, 796.0, 795.7, 741.0, 676.5/
C t2 thermocouple 2
      data t2/ 300.8, 300.9, 301.9, 437.5, 516.2, 571.8, 627.9, 665.9,
     & 698.8, 736.9, 755.8, 760.0, 759.8, 759.3, 716.2, 656.7/
C t3 thermocouple 3
      data t3/ 303.0, 303.2, 303.3, 339.3, 385.0, 433.8, 490.7, 543.9,
     & 596.8, 666.9, 706.5, 717.0, 716.5, 714.4, 683.0, 628.6/
C t4 thermocouple 4
      data t4/ 305.0, 305.3, 305.4, 318.7, 337.4, 363.3, 404.1, 459.5,
     & 522.2, 597.2, 661.4, 682.4, 686.6, 680.9, 654.3, 603.2/
C t5 thermocouple 5
      data t5/ 307.2, 307.4, 307.5, 316.9, 331.9, 345.0, 361.8, 410.6,
     & 475.2, 547.8, 601.2, 636.8, 654.5, 651.6, 626.9, 579.1/
C t6 thermocouple 6
      data t6/ 310.4, 310.7, 311.1, 317.1, 321.6, 328.8, 340.0, 360.4,
     & 363.7, 380.5, 401.3, 429.0, 478.6, 518.9, 537.2, 550.5/
C t7 thermocouple 7 (Assumed temperature at the top of the cup)
      data t7/ 300., 300., 300., 300., 300., 300., 300., 300., 300.,
     & 300., 300., 300., 300., 300., 300., 300./
```

Id750-12

```
C z distance from bottom plate TC to CUP TC's
      data z/ 0.0, 0.48, 1.11, 2.38, 3.65, 4.92, 6.83,16.51/
C ts time in s
      data ts/ 0.0, 4.8, 39.8, 89.8, 99.8, 114.8, 139.8, 199.8, 279.8,
     & 319.8, 374.8, 389.8, 554.8, 659.8, 814.8, 1154.8, 1284.8,
     & 1454.8, 1684.8, 2154.8/
C t0 thermocouple 0 (bottom plate thermocouple)
      data t0/ 300.0, 294.5, 296.4, 919.7, 984.7, 1032.7, 1046.8,
     & 1030.4, 1024.4, 1024.5, 1024.6, 1024.3, 1024.1, 1024.1,
     & 1023.9, 1023.8, 879.7, 765.6, 660.3, 532.5/
C t1 thermocouple 1
      data t1/ 300.0, 294.9, 295.1, 518.3, 606.3, 706.3, 786.2, 841.9,
     & 864.5, 875.4, 886.6, 890.2, 909.3, 913.6, 915.0, 912.5, 825.9,
     & 722.4, 622.0, 502.6/
C t2 thermocouple 2
      data t2/ 300.0, 294.9, 295.1, 400.7, 470.9, 555.6, 636.2, 727.5,
     & 779.8, 799.1, 819.2, 824.9, 856.4, 862.8, 865.1, 860.2, 792.6,
     & 696.3, 598.1, 483.8/
C t3 thermocouple 3
      data t3/ 300.0, 295.4, 295.5, 322.4, 408.4, 422.4, 465.8, 562.2,
     & 654.4, 693.1, 729.4, 740.0, 797.2, 808.0, 813.8, 807.4, 758.0,
     & 669.7, 571.9, 461.4/
C t4 thermocouple 4
      data t4/ 300.0, 295.5, 295.6, 306.1, 351.7, 359.3, 378.7, 457.8,
     & 550.9, 597.9, 645.2, 659.3, 745.2, 764.3, 774.2, 771.2, 733.8,
     & 651.6, 554.1, 445.5/
C t5 thermocouple 5
      data t5/ 300.0, 295.9, 296.0, 302.7, 309.9, 322.3, 341.1, 399.5,
```

```
     & 485.6, 531.0, 579.5, 593.1, 684.8, 714.1, 731.0, 731.1, 703.2,
     & 627.5, 532.7, 428.8/
C t6 thermocouple 6
      data t6/ 300.0, 296.7, 297.0, 306.1, 308.0, 311.4, 319.5, 348.7,
     & 405.7, 436.4, 468.8, 478.0, 535.4, 554.9, 582.6, 601.1, 595.5,
     & 543.6, 473.6, 392.8/
C t7 thermocouple 7 (Assumed temperature at the top of the cup)
      data t7/ 300., 300., 300., 300., 300., 300., 300., 300., 300.,
     & 300., 300., 300., 300., 300., 300., 300.,300.,300.,300.,300./
```

ld900-7

```
C z distance from bottom plate TC to CUP TC's
      data z/ 0.0, 0.48, 1.11, 2.38, 3.65, 4.92, 6.83,16.51/
C ts time in s
      data ts/ 0.0, 24.8, 64.8, 84.8, 99.8, 114.8, 134.8, 164.8,
     & 204.8, 244.8, 289.8, 394.8, 519.8, 629.8, 734.8, 904.8/
C t0 thermocouple 0 (bottom plate thermocouple)
      data t0/ 300.1, 314.6, 916.9, 1133.9, 1189.9, 1203.7, 1198.0,
     & 1184.0, 1162.8, 1162.1, 1161.6, 1157.2, 1154.6, 981.4,
     & 874.8, 761.3/
C t1 thermocouple 1
      data t1/ 302.3, 303.0, 555.1, 763.0, 857.8, 916.3, 961.2,
     & 988.1, 999.3, 1008.2, 1016.3, 1015.7, 1010.4, 895.2,
     & 809.4, 711.4/
C t2 thermocouple 2
      data t2/ 304.0, 304.2, 429.7, 622.2, 698.6, 773.4, 849.6,
     & 907.3, 939.2, 956.0, 968.8, 969.4, 962.2, 859.9,
     & 780.3, 688.1/
C t3 thermocouple 3
      data t3/ 306.9, 307.1, 331.5, 477.5, 518.7, 568.9, 638.1,
     & 765.5, 866.9, 904.1, 927.1, 930.8, 925.0, 828.4, 752.0,
     & 663.7/
C t4 thermocouple 4
      data t4/ 309.3, 309.4, 319.6, 409.8, 442.6, 483.9, 544.0,
     & 644.6, 773.8, 853.1, 892.7, 906.6, 903.0, 809.6, 734.2,
     & 647.8/
C t5 thermocouple 5
      data t5/ 311.6, 311.6, 317.8, 368.0, 398.2, 439.0, 500.6,
     & 580.5, 690.9, 765.6, 833.4, 873.4, 873.2, 783.9, 710.1,
     & 624.9/
C t6 thermocouple 6
      data t6/ 314.4, 315.0, 317.3, 331.4, 366.2, 409.6, 454.3,
     & 514.6, 617.9, 669.7, 695.9, 726.7, 732.3, 668.1, 611.0,
     & 543.5/
C t7 thermocouple 7 (assumed temperature at the top of the cup)
      data t7/ 300., 300., 300., 300., 300., 300., 300., 300., 300.,
     & 300., 300., 300., 300., 300., 300., 300./
```

side-11

```
C z distance from bottom plate TC to CUP TC's
      data z/ 0.0, 0.48, 1.11, 2.38, 3.65, 4.92, 6.83,16.51/
C ts time in s
      data ts/ 0.0  , 4.8  , 49.8 , 54.8 , 119.8, 159.8, 184.8,
     & 234.8, 299.8, 479.8, 764.8, 1064.8, 1394.8, 2034.8, 2119.8,
     & 2824.8, 2894.8, 3029.8, 3164.8, 3304.8/
C t0 thermocouple 0 (bottom plate thermocouple)
```

```
      data t0/ 296.0, 295.8, 295.9, 346.6, 1012.7, 1044.1, 1037.4,
     & 1029.0, 1025.0, 1024.5, 1024.0, 1023.3, 1024.1, 1024.1,
     & 1024.2, 1024.8, 951.9, 837.3, 760.5, 700.0/
C t1 thermocouple 1
      data t1/ 296.0, 295.9, 295.9, 296.5, 652.5, 798.5, 836.9,
     & 866.1, 878.5, 895.0, 903.7, 912.0, 916.3, 921.3, 922.5,
     & 921.8, 890.5, 805.4, 739.7, 682.6/
C t2 thermocouple 2
      data t2/ 296.0, 296.1, 296.1, 295.9, 481.4, 633.4, 688.4,
     & 734.5, 767.7, 806.3, 828.0, 844.3, 853.2, 860.3, 862.9,
     & 860.9, 843.0, 775.6, 717.9, 664.6/
C t3 thermocouple 3
      data t3/ 296.0, 296.4, 296.4, 296.4, 350.3, 464.1, 520.9,
     & 571.4, 634.3, 684.5, 733.6, 760.5, 776.0, 789.3, 793.0,
     & 792.0, 785.6, 739.0, 690.4, 641.4/
C t4 thermocouple 4
      data t4/ 296.0, 296.7, 296.7, 296.7, 316.7, 380.7, 430.4,
     & 488.3, 545.3, 605.2, 659.6, 698.0, 722.5, 738.4, 742.7,
     & 741.0, 737.4, 704.5, 662.8, 617.5/
C t5 thermocouple 5
      data t5/ 296.0, 297.1, 297.1, 297.1, 309.5, 348.6, 375.9,
     & 436.0, 493.7, 551.8, 597.6, 636.9, 663.2, 685.5, 691.7,
     & 691.3, 688.2, 663.1, 627.0, 585.8/
C t6 thermocouple 6
      data t6/ 296.0, 297.8, 297.8, 298.0, 306.4, 323.6, 334.9,
     & 363.9, 407.1, 460.3, 490.8, 516.5, 536.0, 555.8, 562.1,
     & 573.8, 574.2, 559.7, 539.9, 509.5/
C t7 thermocouple 7 (Assumed temperature at the top of the cup)
      data t7/ 300., 300., 300., 300., 300., 300., 300., 300., 300.,
     & 300., 300., 300., 300., 300., 300., 300.,300.,300., 300., 300./
```

side-13

```
C z distance from bottom plate TC to CUP TC's
      data z/ 0.0, 0.48, 1.11, 2.38, 3.65, 4.92, 6.83,16.51/
C ts time in s
      data ts/ 0.0  , 4.8  , 69.8 , 94.8 , 114.8, 134.8, 169.8,
     & 279.8, 479.8, 594.8, 869.8, 1599.8, 2329.8, 3144.8, 3299.8,
     & 3579.8, 3914.8/
C t0 thermocouple 0 (bottom plate thermocouple)
      data t0/ 297.6, 297.6, 301.2, 537.7, 815.3, 992.2, 1050.5,
     & 1011.2, 1017.1, 1021.0, 1015.5, 1017.2, 1018.7, 1017.1,
     & 859.9, 706.4, 599.8/
C t1 thermocouple 1
      data t1/ 297.6, 297.8, 307.5, 423.4, 589.7, 741.7, 832.0,
     & 856.4, 878.1, 881.5, 883.4, 898.3, 909.1, 912.2, 808.6,
     & 678.4, 573.1/
C t2 thermocouple 2
      data t2/ 297.6, 297.9, 303.4, 366.2, 465.3, 586.3, 681.5,
     & 753.7, 795.9, 807.2, 819.0, 838.1, 851.5, 855.8, 778.6,
     & 661.7, 558.4/
C t3 thermocouple 3
      data t3/ 297.6, 298.1, 302.2, 337.7, 380.1, 432.3, 525.7,
     & 616.3, 674.5, 700.9, 732.2, 758.2, 774.8, 780.9, 736.9,
     & 638.6, 539.6/
C t4 thermocouple 4
      data t4/ 297.6, 298.2, 301.1, 325.3, 349.0, 371.8, 448.1,
```

```
     & 525.2, 588.5, 615.0, 655.2, 696.6, 715.5, 719.5, 690.9,
     & 606.9, 516.2/
C t5 thermocouple 5
      data t5/ 297.6, 298.4, 300.4, 315.7, 330.1, 343.3, 392.7,
     & 467.9, 530.2, 555.7, 589.1, 632.5, 657.6, 662.8, 642.9,
     & 569.1, 488.6/
C t6 thermocouple 6
      data t6/ 297.6, 298.9, 299.4, 306.3, 316.0, 325.8, 343.7,
     & 397.9, 453.6, 467.5, 487.7, 512.4, 539.8, 554.4, 543.9,
     & 494.9, 437.8/
C t7 thermocouple 7 (Assumed temperature at the top of the cup)
      data t7/ 300., 300., 300., 300., 300., 300., 300., 300., 300.,
     & 300., 300., 300., 300., 300., 300., 300.,300./
```

top-10

```
C z distance from bottom plate TC to CUP TC's
      data z/ 0.0, 0.48, 1.11, 2.38, 3.65, 4.92, 6.83,16.51/
C ts time in s
      data ts/ 0.0  , 4.8  , 64.8 , 74.8 , 79.8 , 84.8 ,
     & 139.8, 159.8, 199.8, 259.8, 359.8, 504.8, 734.8,
     & 1264.8, 1744.8, 1854.8, 2099.8, 2654.8, 3164.8,
     & 3234.8, 3349.8, 3499.8, 3699.8, 3964.8/
C t0 thermocouple 0 (bottom plate thermocouple)
      data t0/ 290.0, 291.1, 291.3, 353.3, 412.3, 482.4,
     & 1066.0, 1085.3, 1056.7, 1022.4, 1024.0, 1023.3,
     & 1025.4, 1023.3, 1024.4, 1024.4, 1022.7, 1024.3,
     & 1021.3, 1010.2, 888.9, 784.7, 690.8, 603.2/
C t1 thermocouple 1
      data t1/ 290.0, 291.2, 291.2, 294.0, 300.7, 312.0,
     & 696.6, 777.5, 830.7, 838.0, 854.5, 865.9, 874.1,
     & 877.6, 883.4, 883.7, 887.4, 894.9, 896.9, 887.4,
     & 814.0, 727.3, 642.2, 561.9/
C t2 thermocouple 2
      data t2/ 290.0, 291.2, 291.2, 291.6, 293.1, 296.3,
     & 534.4, 614.7, 712.9, 733.4, 768.6, 792.0, 810.9,
     & 820.9, 827.9, 829.0, 833.1, 843.8, 847.1, 839.0,
     & 779.1, 700.3, 619.2, 541.9/
C t3 thermocouple 3
      data t3/ 290.0, 291.2, 291.2, 291.2, 291.3, 291.6,
     & 381.3, 445.2, 573.3, 602.6, 641.4, 675.4, 717.5,
     & 755.4, 768.1, 770.6, 776.5, 789.0, 790.6, 783.4,
     & 735.6, 665.4, 588.9, 514.9/
C t4 thermocouple 4
      data t4/ 290.0, 291.1, 291.1, 291.2, 291.2, 291.3,
     & 334.1, 373.8, 499.4, 518.8, 575.1, 606.3, 637.4,
     & 690.5, 713.5, 718.4, 728.0, 745.9, 748.5, 742.7,
     & 704.9, 641.4, 568.0, 496.1/
C t5 thermocouple 5
      data t5/ 290.0, 291.0, 291.0, 291.0, 291.2, 291.3,
     & 312.3, 344.4, 418.1, 435.6, 468.9, 507.6, 542.8,
     & 590.3, 638.2, 650.1, 666.8, 698.9, 705.1, 699.1,
     & 668.2, 610.8, 541.0, 473.8/
C t6 thermocouple 6
      data t6/ 290.0, 290.8, 290.8, 290.9, 291.1, 291.3,
     & 298.5, 306.5, 336.3, 357.5, 381.9, 410.2, 436.8,
     & 459.9, 485.5, 494.4, 513.4, 559.9, 572.8, 573.5,
```

```
     & 562.7, 526.2, 474.1, 423.9/
C t7 thermocouple 7 (Assumed temperature at the top of the cup)
      data t7/ 300., 300., 300., 300., 300., 300., 300., 300., 300.,
     & 300., 300., 300., 300., 300., 300., 300.,300.,300., 300., 300.,
     & 300., 300., 300., 300. /
```

al-4

```
C z distance from bottom plate TC to CUP TC's
      data z/ 0.0, 0.48, 1.11, 2.38, 3.65, 4.92, 6.83,16.51/
C ts time in s
      data ts/ 0.0, 49.6, 114.6, 129.6, 154.6, 189.6, 269.6, 379.6,
     & 389.6, 504.6, 664.6, 1074.6, 2029.6, 2209.6, 2479.6, 2759.6/
C t0 thermocouple 0 (bottom plate thermocouple)
      data t0/ 292.7, 293.4, 945.8, 996.9, 1005.0, 1011.6, 1012.2,
     & 1012.6, 1012.8, 1013.7, 1014.2, 1015.1, 1015.4, 868.3,
     & 735.9, 650.9/
C t1 thermocouple 1
      data t1/ 292.7, 292.9, 646.5, 720.8, 784.7, 829.4, 862.7,
     & 879.2, 880.7, 891.2, 892.6, 897.5, 911.2, 819.1, 701.9,
     & 617.1/
C t2 thermocouple 2
      data t2/ 292.6, 292.7, 483.6, 558.9, 636.6, 692.1, 753.4,
     & 799.1, 801.6, 824.6, 829.8, 839.6, 859.4, 791.3, 681.5,
     & 599.0/
C t3 thermocouple 3
      data t3/ 292.6, 292.6, 345.0, 390.0, 466.6, 516.1, 595.2,
     & 669.6, 672.4, 716.5, 745.7, 774.8, 805.1, 758.6, 655.1,
     & 576.8/
C t4 thermocouple 4
      data t4/ 292.5, 292.6, 315.8, 336.5, 383.3, 431.8, 517.9,
     & 583.8, 587.2, 626.6, 657.3, 715.6, 762.7, 728.5, 633.2,
     & 560.8/
C t5 thermocouple 5
      data t5/ 292.3, 292.4, 310.8, 332.3, 368.3, 389.7, 474.6,
     & 526.5, 534.4, 575.3, 597.2, 642.9, 713.4, 690.6, 606.7,
     & 541.6/
C t6 thermocouple 6
      data t6/ 292.2, 293.0, 302.2, 306.9, 319.8, 338.1, 390.0,
     & 436.7, 440.5, 468.1, 488.3, 519.7, 592.4, 595.4, 540.7,
     & 494.7/
C t7 thermocouple 7 (Assumed temperature at the top of the cup)
      data t7/ 300., 300., 300., 300., 300., 300., 300., 300., 300.,
     & 300., 300., 300., 300., 300., 300., 300./
```

al-15

```
C z distance from bottom plate TC to CUP TC's
      data z/ 0.0, 0.48, 1.11, 2.38, 3.65, 4.92, 6.83,16.51/
C ts time in s
      data ts/ 0, 39.8, 49.8, 54.8, 104.8, 119.8, 144.8, 204.8, 279.8,
     & 334.8, 509.8, 619.8, 904.8, 1319.8, 1609.8, 1779.8, 2154.8,
     & 2264.8, 2399.8, 2589.8, 2919.8, 3304.8/
C t0 thermocouple 0 (bottom plate thermocouple)
      data t0/ 300.0, 288.9, 317.3, 369.3, 980.5, 1038.8, 1059.9,
     & 1034.4, 1025.1, 1024.7, 1024.9, 1024.7, 1024.5, 1023.9, 1024.1,
     & 1024.0, 1023.7, 908.6, 814.7, 727.8, 628.3, 548.0/
C t1 thermocouple 1
```

```
      data t1/ 300.0, 288.4, 289.0, 293.7, 594.8, 689.6, 769.0,
     & 831.7, 850.0, 856.8, 870.0, 872.7, 877.7, 881.7, 886.7,
     & 895.2, 899.4, 838.9, 766.6, 690.7, 594.1, 520.2/
C t2 thermocouple 2
      data t2/ 300.0, 288.1, 288.2, 289.0, 453.3, 531.8, 622.7,
     & 715.0, 760.8, 778.6, 806.9, 813.3, 823.6, 828.7, 837.7,
     & 849.0, 853.3, 807.0, 742.6, 671.1, 575.6, 505.0/
C t3 thermocouple 3
      data t3/ 300.0, 287.8, 287.8, 287.9, 329.5, 381.2, 447.3,
     & 559.8, 626.4, 653.5, 706.8, 733.0, 758.9, 770.9, 785.4,
     & 801.6, 805.7, 772.3, 714.5, 646.7, 555.3, 487.8/
C t4 thermocouple 4
      data t4/ 300.0, 287.4, 287.5, 287.6, 309.2, 335.5, 380.8,
     & 476.8, 550.8, 580.4, 622.2, 648.5, 693.8, 722.4, 740.4,
     & 760.6, 764.4, 741.8, 690.9, 626.3, 541.7, 475.5/
C t5 thermocouple 5
      data t5/ 300.0, 286.9, 286.9, 287.0, 311.0, 327.0, 358.6,
     & 429.3, 489.9, 513.1, 567.7, 588.6, 620.2, 658.0, 689.5,
     & 710.7, 713.5, 700.6, 658.0, 597.3, 521.6, 458.0/
C t6 thermocouple 6
      data t6/ 300.0, 285.7, 287.0, 287.8, 300.9, 306.6, 323.6,
     & 354.9, 398.2, 416.2, 451.4, 472.4, 497.5, 515.9, 539.5,
     & 559.6, 602.3, 605.0, 577.9, 537.7, 479.6, 425.2/
C t7 thermocouple 7 (Assumed temperature at the top of the cup)
      data t7/ 300., 300., 300., 300., 300., 300., 300., 300., 300.,
     & 300., 300., 300., 300., 300., 300., 300., 300., 300., 300.,
     & 300., 300., 300./
```

ss-1000-19

```
      data z/ 0.15875, 0.79375, 2.06375, 3.33375, 4.60375, 6.50875/
C ts time in s
      data ts/ 0., 2.8, 17.8, 32.8, 47.8, 62.8, 77.8, 92.8, 107.8,
     & 122.8, 137.8, 152.8, 167.8, 182.8, 197.8, 212.8, 227.8, 242.8,
     & 257.8, 272.8, 287.8, 302.8, 317.8, 332.8, 347.8, 362.8, 377.8,
     & 392.8, 407.8, 422.8, 437.8, 452.8, 467.8, 482.8, 497.8, 512.8,
     & 527.8, 542.8, 557.8, 572.8, 587.8, 602.8, 617.8, 632.8, 647.8,
     & 662.8, 677.8, 692.8, 707.8, 722.8, 737.8, 752.8, 767.8, 782.8,
     & 797.8, 812.8, 827.8, 842.8, 857.8, 872.8, 887.8, 902.8, 917.8,
     & 932.8, 947.8, 962.8, 977.8, 992.8, 1007.8, 1022.8, 1037.8,
     & 1052.8/
C t1 thermocouple 1
      data t1/ 297.7, 297.7, 297.7, 297.7, 297.7, 297.7, 304.2, 348.2,
     & 409.4, 503.0, 578.4, 658.1, 745.7, 845.3, 906.3, 943.0, 965.2,
     & 982.6, 997.3, 1005.8, 1013.5, 1020.1, 1026.1, 1031.2, 1036.0,
     & 1040.5, 1044.1, 1046.9, 1050.2, 1053.1, 1054.7, 1057.7, 1060.7,
     & 1062.0, 1063.2, 1064.7, 1066.7, 1067.7, 1068.7, 1069.5, 1070.5,
     & 1071.1, 1072.0, 1072.7, 1073.3, 1074.6, 1075.2, 1075.5, 1076.0,
     & 1076.4, 1077.4, 1078.9, 1079.3, 1080.5, 1081.2, 1081.6, 1081.9,
     & 1083.2, 1083.2, 1067.2, 1043.7, 1018.6, 995.0, 970.4, 946.8,
     & 925.7, 904.9, 884.9, 867.6, 850.7, 834.7, 819.7/
C t2 thermocouple 2
      data t2/ 297.5, 297.5, 297.5, 297.6, 297.6, 297.6, 298.2, 314.2,
     & 344.4, 394.9, 446.5, 501.8, 564.1, 635.2, 699.7, 749.9, 790.0,
     & 827.9, 860.0, 882.7, 900.8, 915.4, 928.4, 938.7, 947.6, 955.5,
     & 961.5, 965.8, 970.6, 975.3, 978.1, 983.2, 988.0, 989.7, 991.7,
     & 994.3, 997.4, 998.9, 1000.6, 1001.8, 1003.2, 1004.2, 1005.6,
```

```
     & 1006.5, 1007.6, 1009.3, 1010.2, 1010.4, 1010.8, 1010.3, 1010.8,
     & 1011.5, 1012.0, 1013.4, 1014.4, 1015.3, 1015.3, 1016.5, 1016.2,
     & 1005.5, 987.5, 967.3, 947.2, 925.7, 904.7, 885.6, 866.5, 847.8,
     & 831.5, 816.0, 801.1, 787.1/
C t3 thermocouple 3
      data t3/ 297.5, 297.5, 297.5, 297.5, 297.6, 297.6, 297.5, 299.0,
     & 304.4, 318.6, 340.0, 369.4, 404.4, 443.2, 480.8, 529.3, 576.2,
     & 615.3, 650.2, 681.3, 707.6, 732.8, 756.9, 777.4, 796.0, 813.8,
     & 831.4, 848.7, 862.0, 874.2, 883.7, 894.8, 904.9, 910.1, 916.4,
     & 921.9, 926.7, 930.3, 933.7, 935.7, 937.9, 939.7, 941.5, 943.2,
     & 944.6, 947.0, 948.7, 948.6, 947.8, 947.6, 948.2, 949.0, 949.6,
     & 949.7, 950.8, 951.1, 952.3, 952.9, 952.8, 945.9, 932.6, 916.3,
     & 899.2, 880.4, 861.6, 844.2, 826.6, 809.2, 793.9, 779.4, 765.6,
     & 752.6/
C t4 thermocouple 4
      data t4/ 297.6, 297.6, 297.6, 297.7, 297.7, 297.7, 297.5,
     & 297.9, 299.3, 304.7, 315.6, 332.6, 351.0, 371.9, 399.9, 442.8,
     & 488.6, 527.0, 556.0, 578.8, 603.8, 628.7, 651.5, 671.0, 688.4,
     & 704.9, 718.4, 731.4, 743.4, 754.8, 765.5, 777.2, 789.1, 800.7,
     & 813.3, 825.6, 840.0, 851.9, 861.0, 867.7, 874.8, 879.6, 883.7,
     & 886.9, 889.2, 893.1, 895.2, 895.7, 896.1, 897.5, 898.7, 900.1,
     & 901.0, 901.2, 902.6, 903.4, 905.2, 906.2, 906.8, 901.0, 889.9,
     & 876.3, 861.8, 845.3, 828.8, 813.0, 797.0, 781.1, 767.2, 753.8,
     & 741.0, 729.0/
C t5 thermocouple 5
      data t5/ 297.8, 297.8, 297.8, 297.9, 297.8, 297.9, 297.9,
     & 299.6, 302.1, 306.8, 314.3, 325.1, 343.0, 356.3, 378.7, 416.0,
     & 471.9, 498.4, 517.2, 532.7, 551.4, 572.5, 594.2, 613.2, 630.2,
     & 646.3, 660.0, 672.5, 684.7, 695.1, 705.0, 714.5, 723.6, 732.1,
     & 739.9, 747.7, 755.5, 763.4, 770.1, 777.0, 784.6, 791.5, 798.7,
     & 806.0, 812.1, 821.0, 826.9, 831.0, 834.8, 838.6, 841.6, 844.8,
     & 847.5, 849.9, 851.8, 854.8, 856.9, 858.9, 860.1, 856.5, 847.9,
     & 837.9, 826.7, 813.1, 798.9, 785.5, 771.6, 757.8, 745.5, 733.4,
     & 721.5, 710.3/
C t6 thermocouple 6
      data t6/ 298.3, 298.3, 298.3, 298.3, 298.3, 298.3, 308.1,
     & 317.3, 326.6, 335.3, 345.3, 356.4, 370.7, 387.4, 399.2, 413.2,
     & 436.9, 462.7, 484.8, 504.6, 520.9, 535.2, 548.8, 564.0, 579.5,
     & 593.0, 604.8, 616.1, 626.9, 636.4, 645.3, 654.0, 661.3, 669.0,
     & 675.7, 682.5, 688.7, 694.7, 699.5, 703.4, 706.9, 710.6, 715.0,
     & 718.8, 722.4, 727.0, 731.1, 735.3, 739.1, 743.3, 747.6, 753.1,
     & 758.0, 762.6, 767.4, 771.3, 776.8, 781.9, 785.8, 785.7, 782.4,
     & 778.1, 771.1, 762.6, 753.3, 743.7, 732.9, 721.3, 710.6, 699.7,
     & 689.3, 678.8/
```

ss-5

```
C z distance from bottom plate TC to CUP TC's
      data z/ 0.0, 0.48, 1.11, 2.38, 3.65, 4.92, 6.83,16.51/
C ts time in s
      data ts/ 0.0, 29.8, 34.8, 39.8, 89.8, 99.8, 114.8, 129.8,
     & 139.8, 204.8, 299.8, 424.8, 599.8, 749.8, 1014.8, 1474.8,
     & 1999.8, 2419.8, 2839.8, 2929.8, 3039.8, 3199.8, 3414.8/
C t0 thermocouple 0 (bottom plate thermocouple)
      data t0/ 293.8, 293.8, 306.3, 355.7, 961.8, 1012.4, 1041.0,
     & 1048.6, 1047.9, 1029.1, 1024.4, 1023.1, 1023.8, 1023.9,
     & 1024.2, 1023.6, 1023.6, 1023.8, 1023.5, 919.4, 831.3,
```

```
     & 744.2, 665.6/
C t1 thermocouple 1
      data t1/ 300.0, 294.4, 294.5, 295.9, 534.9, 617.9, 682.8,
     & 735.2, 751.0, 816.9, 838.9, 854.4, 868.7, 879.8, 891.4,
     & 888.6, 900.8, 902.0, 894.9, 844.4, 774.3, 696.5, 628.3/
C t2 thermocouple 2
      data t2/ 300.0, 294.8, 294.8, 295.0, 424.3, 488.3, 548.4,
     & 598.9, 617.6, 705.4, 750.4, 789.9, 817.3, 834.2, 853.1,
     & 850.5, 864.5, 864.2, 851.2, 812.2, 748.4, 674.9, 610.5/
C t3 thermocouple 3
      data t3/ 300.0, 295.7, 295.7, 295.8, 323.7, 349.0, 407.8,
     & 440.1, 456.2, 556.5, 617.9, 668.6, 722.2, 754.0, 788.7,
     & 795.6, 809.4, 807.2, 787.4, 763.3, 708.9, 641.7, 583.8/
C t4 thermocouple 4
      data t4/ 300.0, 296.6, 296.6, 296.7, 311.7, 322.3, 356.7,
     & 385.8, 398.3, 496.0, 548.0, 607.5, 651.2, 674.9, 719.5,
     & 746.7, 758.8, 758.3, 737.4, 722.2, 677.1, 616.1, 563.2/
C t5 thermocouple 5
      data t5/ 300.0, 297.9, 298.0, 298.1, 311.3, 318.4, 344.5,
     & 358.2, 367.7, 465.0, 497.1, 567.2, 610.8, 622.9, 654.7,
     & 699.4, 712.5, 716.6, 695.9, 685.1, 647.9, 593.7, 544.3/
C t6 thermocouple 6
      data t6/ 300.0, 300.3, 300.5, 300.8, 307.5, 309.7, 314.8,
     & 323.6, 329.1, 376.4, 424.8, 471.0, 505.5, 517.1, 535.7,
     & 566.1, 585.6, 612.5, 604.9, 600.7, 577.9, 541.6, 499.9/
C t7 thermocouple 7 (Assumed temperature at the top of the cup)
      data t7/ 300., 300., 300., 300., 300., 300., 300., 300., 300.,
     & 300., 300., 300., 300., 300., 300., 300., 300., 300., 300.,
     & 300., 300., 300., 300./
```

Idal-8

```
C z distance from bottom plate TC to CUP TC's
      data z/ 0.0, 0.48, 1.11, 2.38, 3.65, 4.92, 6.83,16.51/
C ts time in s
      data ts/ 0.0 , 29.8, 59.8, 89.8, 99.8, 119.8, 129.8, 159.8,
     & 189.8, 214.8, 259.8, 274.8, 429.8, 559.8, 714.8, 1064.8,
     & 1169.8, 1269.8, 1409.8, 1549.8, 1694.8/
C t0 thermocouple 0 (bottom plate thermocouple)
      data t0/ 300.0, 295.8, 599.5, 969.6, 1013.3, 1041.5, 1045.7,
     & 1040.3, 1031.8, 1028.2, 1025.4, 1025.3, 1023.7, 1023.8, 1024.7,
     & 1023.8, 903.8, 828.4, 753.3, 696.4, 648.3/
C t1 thermocouple 1
      data t1/ 300.0, 296.2, 362.6, 595.0, 668.9, 766.1, 796.2, 847.3,
     & 867.0, 875.1, 882.7, 884.3, 896.9, 906.3, 908.7, 915.5, 849.1,
     & 785.7, 722.9, 669.5, 619.1/
C t2 thermocouple 2
      data t2/ 300.0, 296.7, 318.4, 445.9, 503.9, 601.0, 636.9, 715.7,
     & 759.4, 780.8, 800.6, 805.8, 832.1, 846.3, 850.0, 859.8, 810.3,
     & 754.5, 699.9, 649.2, 599.3/
C t3 thermocouple 3
      data t3/ 300.0, 297.3, 302.4, 334.9, 360.9, 425.3, 458.4, 543.9,
     & 595.3, 630.7, 682.4, 697.5, 764.8, 786.4, 793.4, 808.2, 770.7,
     & 720.7, 674.0, 626.1, 578.0/
C t4 thermocouple 4
      data t4/ 300.0, 297.8, 301.4, 318.2, 327.9, 364.9, 381.8, 452.9,
     & 502.1, 533.3, 578.9, 592.3, 695.6, 730.0, 744.7, 767.5, 739.6,
```

```
     & 694.4, 652.8, 606.8, 560.9/
C t5 thermocouple 5
      data t5/ 300.0, 298.5, 300.9, 314.7, 324.5, 345.7, 354.2, 407.8,
     & 451.1, 476.6, 509.0, 518.2, 610.0, 657.6, 685.4, 719.0, 698.3,
     & 659.0, 621.4, 577.7, 535.2/
C t6 thermocouple 6
      data t6/ 300.0, 299.5, 302.4, 309.3, 311.9, 320.3, 326.7, 344.6,
     & 367.1, 384.8, 413.0, 421.6, 483.8, 517.0, 542.3, 594.2, 597.1,
     & 574.2, 547.2, 512.4, 480.5/
C t7 thermocouple 7 (Assumed temperature at the top of the cup)
      data t7/ 300., 300., 300., 300., 300., 300., 300., 300., 300.,
     & 300., 300., 300., 300., 300., 300., 300., 300., 300., 300.,
     & 300., 300./
```

ldss-9

```
C z distance from bottom plate TC to CUP TC's
      data z/ 0.0, 0.48, 1.11, 2.38, 3.65, 4.92, 6.83,16.51/
C ts time in s
      data ts/ 0.0, 4.3, 54.2, 79.3, 109.3, 129.3, 139.3, 164.3, 234.3,
     & 274.3, 359.2, 499.2, 624.2, 804.3, 1074.3, 1344.3, 1474.2,
     & 1624.3, 1854.3, 2089.3/
C t0 thermocouple 0 (bottom plate thermocouple)
      data t0/ 300.0, 296.2, 296.2, 563.8, 941.5, 1029.5, 1039.6,
     & 1045.4, 1027.9, 1026.0, 1024.5, 1024.3, 1024.2, 1023.3,
     & 1024.0, 1023.9, 874.4, 768.6, 665.0, 589.1/
C t1 thermocouple 1
      data t1/ 300.0, 296.9, 296.9, 339.6, 542.5, 681.8, 727.0,
     & 796.9, 853.4, 864.2, 875.0, 885.7, 890.8, 894.8, 896.5,
     & 893.4, 806.4, 719.4, 621.2, 552.0/
C t2 thermocouple 2
      data t2/ 300.0, 297.4, 297.4, 314.5, 423.3, 538.0, 583.6,
     & 667.7, 771.6, 795.0, 816.7, 832.7, 839.6, 846.0, 847.1,
     & 842.6, 769.8, 691.7, 598.4, 533.5/
C t3 thermocouple 3
      data t3/ 300.0, 298.5, 298.5, 301.7, 328.4, 388.2, 421.0,
     & 493.9, 622.7, 675.8, 735.4, 767.6, 778.6, 789.6, 790.3,
     & 782.8, 724.2, 654.8, 568.7, 509.1/
C t4 thermocouple 4
      data t4/ 300.0, 299.3, 299.4, 301.4, 314.0, 336.3, 351.0,
     & 401.0, 515.5, 567.0, 637.2, 706.8, 728.4, 744.3, 746.4,
     & 736.1, 688.4, 624.3, 544.4, 489.4/
C t5 thermocouple 5
      data t5/ 300.0, 300.2, 300.3, 302.0, 311.8, 331.8, 343.6,
     & 366.5, 462.8, 501.7, 556.0, 623.5, 656.9, 683.5, 692.5,
     & 680.6, 645.6, 587.5, 514.7, 465.7/
C t6 thermocouple 6
      data t6/ 300.0, 301.4, 301.4, 304.7, 311.7, 318.1, 323.2,
     & 337.6, 386.9, 402., 456., 524., 557., 583., 593., 581.,
     & 571., 538., 465., 416./
C t7 thermocouple 7 (Assumed temperature at the top of the cup)
      data t7/ 300., 300., 300., 300., 300., 300., 300., 300., 300.,
     & 300., 300., 300., 300., 300., 300., 300., 300.,300.,300.,300./
```

600-amb-p4

```
C z distance from bottom plate TC to CUP TC's
      data z/ 0.0,2.06375,3.33375,5.23875,7.77875,16.66875,17.0,18.0/
```

```
C ts time in s
      data ts/0.0, 84.6, 109.6, 129.6, 149.6, 164.6, 234.6, 384.6,
     & 609.6, 834.6, 2014.6, 3384.6, 3514.6, 3669.6, 3869.6/
C t0 thermocouple 0 (bottom plate thermocouple)
       data t0/ 306.2, 306.7, 453.3, 669.4, 836.5, 871.8, 860.4,
     & 864.6, 865.3, 865.5, 865.0, 864.4, 768.5, 679.4, 607.8/
C t1 thermocouple 1
      data t1/ 312.1, 313.9, 318.5, 339.5, 379.6, 417.0, 532.1,
     & 586.7, 614.8, 632.8, 648.5, 647.2, 613.0, 553.4, 502.8/
C t2 thermocouple 2
      data t2/ 312.1, 313.5, 317.7, 331.1, 353.3, 373.1, 441.8,
     & 486.3, 511.4, 528.7, 568.0, 586.0, 561.0, 511.9, 468.7/
C t3 thermocouple 3
      data t3/ 312.1, 313.1, 316.8, 322.7, 327.0, 329.4, 351.5,
     & 386.0, 408.0, 424.5, 487.4, 524.8, 509.0, 470.3, 434.5/
C t4 thermocouple 4
      data t4/ 310.5, 311.2, 315.4, 321.0, 325.3, 326.6, 329.8,
     & 342.0, 352.9, 360.2, 392.3, 420.3, 418.7, 406.2, 389.3/
C t5 thermocouple 5
      data t5/ 307.0, 307.2, 308.2, 310.0, 311.9, 313.2, 316.1,
     & 319.2, 322.0, 324.3, 330.8, 332.6, 331.2, 329.4, 326.8/
C t6 thermocouple 6
      data t6/ 306., 306., 306., 306., 306., 306., 306., 306.,
     & 306., 306., 306., 306., 306., 306., 306./
C t7 thermocouple 7
      data t7/ 306., 306., 306., 306., 306., 306., 306., 306.,
     & 306., 306., 306., 306., 306., 306., 306./
```

600-1.54-p2

```
C z distance from bottom plate TC to CUP TC's
      data z/ 0.0,2.06375,3.33375,5.23875,7.77875,16.66875,17.0,18.0/
C ts time in s
      data ts/ 0., 49.7, 84.7, 114.6, 129.6, 234.6, 534.6, 780.7,
     & 1705.7, 2870.6, 3025.7, 3260.6/
C t0 thermocouple 0 (bottom plate thermocouple)
      data t0/ 310.3, 310.6, 590.2, 859.4, 892.9, 867.5, 865.8,
     & 866.1, 865.2, 865.3, 759.0, 634.4/
C t1 thermocouple 1
      data t1/ 319.0, 319.9, 347.1, 393.7, 416.5, 490.7, 544.1,
     & 576.7, 601.6, 610.3, 570.5, 502.4/
C t2 thermocouple 2
      data t2/ 318.3, 319.7, 377.6, 488.2, 532.7, 616.6, 656.0,
     & 669.4, 668.4, 675.1, 620.6, 539.5/
C t3 thermocouple 3
      data t3/ 318.0, 319.0, 339.7, 358.8, 363.2, 390.0, 423.7,
     & 445.4, 516.2, 547.0, 520.0, 465.6/
C t4 thermocouple 4
      data t4/ 315.9, 317.1, 338.3, 354.1, 355.0, 351.6, 362.6,
     & 372.0, 404.5, 454.4, 445.7, 416.5/
C t5 thermocouple 5
      data t5/ 310.8, 311.0, 317.6, 326.8, 329.4, 331.6, 329.7,
     & 331.4, 335.7, 341.6, 338.2, 333.1/
C t6 thermocouple 6
      data t6/ 310.,310.,310.,310.,310.,310.,310.,310.,310.,310.,
     & 310., 310./
C t7 thermocouple 7
```

```
      data t7/ 310.,310.,310.,310.,310.,310.,310.,310.,310.,
     & 310., 310./
```

600-3.58-p3

```
C z distance from bottom plate TC to CUP TC's
      data z/ 0.0,2.06375,3.33375,5.23875,7.77875,16.66875,17.0,18.0/
C ts time in s
      data ts/ 0., 79.8, 159.8, 204.8, 239.8, 319.8, 429.8, 534.8,
     & 614.8, 809.8, 1257.8, 1987.8, 2272.8/
C t0 thermocouple 0 (bottom plate thermocouple)
      data t0/ 330.6, 330.4, 967.0, 926.4, 888.5, 883.6, 880.2,
     & 879.0, 879.3, 878.1, 878.2, 874.7, 566.5/
C t1 thermocouple 1
      data t1/ 336.6, 337.8, 639.4, 685.9, 676.4, 676.0, 684.8,
     & 672.5, 681.1, 680.5, 685.9, 685.6, 544.1/
C t2 thermocouple 2
      data t2/ 333.4, 334.4, 476.7, 543.0, 567.8, 586.1, 607.1,
     & 606.0, 615.4, 617.4, 622.7, 622.1, 504.5/
C t3 thermocouple 3
      data t3/ 327.8, 328.4, 391.1, 403.4, 414.7, 439.4, 472.8,
     & 493.2, 508.6, 530.9, 555.9, 562.0, 469.0/
C t4 thermocouple 4
      data t4/ 323.7, 324.1, 378.8, 370.0, 365.1, 370.1, 381.5,
     & 389.7, 397.3, 411.7, 441.2, 469.6, 426.1/
C t5 thermocouple 5
      data t5/ 314.5, 314.7, 336.9, 338.8, 337.6, 336.5, 336.0,
     & 335.6, 335.6, 336.4, 339.8, 343.3, 334.6/
C t6 thermocouple 6
      data t6/ 330.,330.,330.,330.,330.,330.,330.,330.,330.,330.,
     & 330., 330, 330./
C t7 thermocouple 7
      data t7/ 330.,330.,330.,330.,330.,330.,330.,330.,330.,330.,
     & 330., 330., 330./
```

FORTRAN CODE for mean value analysis of experiment 750-2 programmed with help from Larry Schoof

```
      program burn
C23456789x123456789x123456789x123456789x123456789x123456789x123456789x1
C-----------------------------------------------------------------------
C
C This program calculates the mean and standard deviation of SF using
C mean value theory for the SANDmav00 runs.  The following twenty-five
C variables are used to propagate uncertainty:
C
C                rho0,Cp,emis,hrxn,s+1,E5,E6,E8,E9  <---initial runs
C                tinit,l0,e1,e2,e3,e4,e7,e10        <---later runs
C                e11,e12,e13,e14,e15,e16,esig,death <---later runs
C
C The initial runs were shown in the 1D burn sensitivity analysis to
C account for 99% of the variability in calculated burn velocity.
C It was not clear whether these variable still accounted for 99%
C of the uncertainty in the 2DAXI runs and the remaining variables
C where run to get a complete sensitivity analysis with all 25 vari-
ables.
```

```
C
C The derivative in this program are determined by perturbing the mean
C input parameter by 0.01 (1 percent).  A central difference derivative
C is calculated.
C-----------------------------------------------------------------------
C
C Parameter, include, and declaration statements
C-----------------------------------------------------------------------
C
      implicit none
C Parameter statements are replaced during compile
      integer MAXNUMELEM, MAXNUMTIME, MAXNUMFILES, nparam, MAXCLELEM
      parameter (MAXNUMELEM=6000, MAXNUMTIME=300, MAXNUMFILES=51)
      parameter (nparam=25)
      parameter (MAXCLELEM=99)
C n is the number of variables, nfiles is the number of exodus files
      include "exodusII.inc"
      integer i, j, k, n
      integer cpu_ws, io_ws, nfiles, ierr, ndim, numnp, nelem
      integer nelblk, numnps, numess, num_time_steps, numelb, numlnk
      integer numatr, id, id1, id2
      integer blockid, indexsf
      integer elemnum(MAXCLELEM)
      integer first, offset
      real dist(MAXCLELEM),xx(MAXNUMTIME),refmean,told,tnew
      real refp2sig,refm2sig
      real sf(MAXNUMELEM, MAXNUMTIME, MAXNUMFILES)
      real deriv(MAXNUMELEM, MAXNUMTIME, MAXNUMFILES)
      real sig(MAXNUMELEM, MAXNUMTIME)
      real sfp2sig(MAXNUMELEM, MAXNUMTIME)
      real sfm2sig(MAXNUMELEM, MAXNUMTIME)
      real gamma(MAXNUMELEM, MAXNUMTIME, MAXNUMFILES)
      real gamma2(MAXNUMELEM, MAXNUMTIME, MAXNUMFILES)
      real vers, fdum, fdstep, sum
      real time(MAXNUMTIME,MAXNUMFILES)
      real param(nparam),pstdev(nparam),pup(nparam),pdown(nparam)
      real x,x1,x2,y1,y2,up,down
      character*8 fn, filename
C MXSTLN declared in exodusII.inc as 32
C MXLNLN declared in exodusII.inc as 80
      character*(MXSTLN) var_names(28),namelb
      character*1 cdum
      character*(MXLNLN) title
C-----------------------------------------------------------------------
C DATA STATEMENTS
C-----------------------------------------------------------------------
C
      data cpu_ws,io_ws/0,0/
C blockid is the block identification number for reactive foam
C idexsf is the position of the SF element var. in the COYOTE input
deck
      data blockid,indexsf/ 30,2/
C nine variables: rho0,Cp,emis,hrxn,s+1,E5,E6,E8,E9
C eight more:     tinit, l0, e1, e2, e3, e4, e7, e10
C eight final:    e11, e12, e13, e14, e15, e16, esig, death
C 25 total variables 51 exodus files
      data param/ 0.364,1.,0.8,20.6,2.8,50000.,49500.,49300.,51600.,
```

```
C exout files: 2-3, 4-5, 6-7, 8-9, 10-11, 12-13, 14-15, 16-17, 18-19,
     &     300.0,0.78,50200.,50600.,49400.,50400.,50400.,49800.,
C exout files: 20-21, 22-23, 24-25, 26-27, 28-29, 30-31, 32-33, 34-35,
     &     50200.,50100.,50200.,51100.,49600.,49700.,3520.,0.036/
C exout files: 36-37, 38-39, 40-41, 42-43, 44-45, 46-47, 48-49, 50-51
      data pstdev/0.02,0.04,0.04,0.7,0.,149.,233.,104.,179.,
     &     3.0,0.01,247.,200.,111.,159.,79.,125.,
     &     132.,251.,130.,219.,165.,80.,17.,.007 /
      data fdstep/0.01/
      data first,offset/4589,346/
C     data refmean,refm2sig,refp2sig/0.5,0.95,0.05/
      data refmean,refm2sig,refp2sig/0.5,0.5,0.5/

C-----------------------------------------------------------------------
C
C CALCULATE DISTANCE (cm) EACH CENTERLINE ELEMENT IS FROM THE BOTTOM
C OF THE PLATE AND ASSIGN ELEMENT NUMBERS. (Here I assume each element
C is 1mm by 1mm.
C-----------------------------------------------------------------------
C

      dist(1) = 0.05
      elemnum(1) = first-offset
      do i = 1, maxclelem-1
         dist(i+1) = dist(i)+0.1
         elemnum(i+1) = elemnum(i)+1
      enddo

C-----------------------------------------------------------------------
C open files to write time 0.5 contour passes through element and the
C distance this element is from the bottom plate.
C-----------------------------------------------------------------------
C

      open(1,file='cl.mean',status='unknown',form='formatted')
      open(2,file='cl.p2sig',status='unknown',form='formatted')
      open(3,file='cl.m2sig',status='unknown',form='formatted')

C-----------------------------------------------------------------------
C nfiles is the number of exodus files needed for central difference
derivs
C-----------------------------------------------------------------------
C
      nfiles = 2*nparam+1
      if(nfiles.gt.maxnumfiles) STOP "nfile>maxnumfiles"
      do i = 1,nparam
         pup(i) = param(i)*(1.+fdstep)
         pdown(i) = param(i)*(1.-fdstep)
      enddo

C23456789x123456789x123456789x123456789x123456789x123456789x123456789x1
C Open exodus files and extract SF (solid fraction)
C filename is a function of i (e.g. if i=1, filename = "exout.01")
C first EXODUS file is mean result
C EXREAD and EXTIMS defined in exodusII.inc as 0 and 16, respectively
C23456789x123456789x123456789x123456789x123456789x123456789x123456789x1
```

```
      fn="exout."
      do i = 1,nfiles
        call fname(fn,6,i,filename)
        id = exopen (filename, EXREAD, cpu_ws, io_ws, vers, ierr)
        if (ierr.ne.0) STOP
        call ex-
gini(id,title,ndim,numnp,NELEM,nelblk,numnps,numess,ierr)
        if (ierr.ne.0) STOP
        call exinq (id, EXTIMS, num_time_steps, fdum, cdum, ierr)
        if (ierr.ne.0) STOP
        if (num_time_steps.gt.maxnumtime) STOP "num_t_steps>maxnumtime"
        call exgelb (id, BLOCKID, namelb, NUMELB, numlnk, numatr, ierr)
        if (ierr.ne.0) STOP
        do j = 1, num_time_steps
           call exgev (id,j,indexsf,blockid,numelb,sf(1,j,i),ierr)
           if (ierr.ne.0) STOP
        enddo
        call exgatm (id, time(1,i), ierr)
        if (ierr.ne.0) STOP
        call exclos(id,ierr)
        if (ierr.ne.0) STOP
      enddo

C23456789x123456789x123456789x123456789x123456789x123456789x123456789x1
C in the array sf:
C     first index is the element number
C     second index is the time step
C     third index is the file index
C sf(*,*,1) contains the mean SF
C sf(*,*,2) contains variable 1 perturbed up(1+eps, all other variables
at mean)
C sf(*,*,3) contains variable 1 perturbed down (1-eps, all other vari-
ables at mean)
C sf(*,*,4) contains variable 2 perturbed up (1+eps, all other vari-
ables at mean)
C sf(*,*,5) contains variable 2 perturbed down (1-eps, all other vari-
ables at mean)
C ...
C sf(*,*,20) contains variable 10 perturbed up (1+eps, all other vari-
ables at mean)
C sf(*,*,21) contains variable 10 perturbed down (1-eps, all other
variables at mean)
C
C  open exout.01 to read exodus parameters
C

      id1 = exopen ("exout.01", EXREAD, cpu_ws, io_ws, vers, ierr)
      if (ierr.ne.0) STOP

C
C  open 2dsen.e to and write exodus parameters from exout.01 and
C  define three new exodus variables: sfmean, sfp2sig, sfm2sig
C  EXCLOB defined in exodusII.inc as integer 1
C
      id2 = excre ("2dsen.e", EXCLOB, cpu_ws, io_ws, ierr)
      if (ierr.ne.0) STOP
      call excopy(id1,id2,ierr)
```

```
      if (ierr.ne.0) STOP
      call expvp (id2, "e", 28, ierr)
      if (ierr.ne.0) STOP
C nine variables: rho0,Cp,emis,hrxn,s+1,E5,E6,E8,E9
      var_names(1) = "SFMEAN"
      var_names(2) = "SFP2SIG"
      var_names(3) = "SFM2SIG"
      var_names(4) = "G2RHO"
      var_names(5) = "G2CP"
      var_names(6) = "G2emis"
      var_names(7) = "G2hrxn"
      var_names(8) = "G2sp1"
      var_names(9) = "G2E5"
      var_names(10) = "G2E6"
      var_names(11) = "G2E8"
      var_names(12) = "G2E9"
      var_names(13) = "G2T0"
      var_names(14) = "G2l0"
      var_names(15) = "G2E1"
      var_names(16) = "G2E2"
      var_names(17) = "G2E3"
      var_names(18) = "G2E4"
      var_names(19) = "G2E7"
      var_names(20) = "G2E10"
      var_names(21) = "G2E11"
      var_names(22) = "G2E12"
      var_names(23) = "G2E13"
      var_names(24) = "G2E14"
      var_names(25) = "G2E15"
      var_names(26) = "G2E16"
      var_names(27) = "G2ESIG"
      var_names(28) = "G2DEATH"

      call expvan (id2, "e", 28, var_names, ierr)
      if (ierr.ne.0) STOP

C23456789x123456789x123456789x123456789x123456789x123456789x123456789x1
2
C  Assume time and num_time_steps are not the same for every exodus
file.
C  Interplote using time from 1st exout file.  Calculate the deriva-
tive.
C

      do k = 1,nelem
         do j = 2,num_time_steps
            do i = 1,nparam
               x = time(j,1)
               x1 = time(j-1,2*i)
               x2 = time(j,2*i)
               y1 = sf(k,j-1,2*i)
               y2 = sf(k,j,2*i)
               up = y1+(y2-y1)*(x-x1)/(x2-x1)
               x1 = time(j-1,2*i+1)
               x2 = time(j,2*i+1)
               y1 = sf(k,j-1,2*i+1)
               y2 = sf(k,j,2*i+1)
```

```
               down = y1+(y2-y1)*(x-x1)/(x2-x1)
c              deriv(k,j,i) = (sf(k,j,2*i)-sf(k,j,2*i+1))/
c    &                        (pup(i)-pdown(i))
               deriv(k,j,i) = (up-down)/(pup(i)-pdown(i))
            enddo
         enddo
      enddo

C
C  calculate SIG, sfp2sig, and sfm2sig
C

      do k = 1,nelem
         do j = 1,num_time_steps
            sum = 0.
            do i = 1,nparam
               sum = sum+(pstdev(i)*deriv(k,j,i))**2
            enddo
            sig(k,j) = sqrt(sum)
            sfp2sig(k,j) = min(1.,sf(k,j,1)+2.*sig(k,j))
            sfm2sig(k,j) = max(0.,sf(k,j,1)-2.*sig(k,j))
          enddo
       enddo

C
C  calculate GAMMA and GAMMA**2, note the variables are only calculated
C  but only gamma2 is written to the exodus file.  However, to see
C  the value of gamma, you must create a new exodus variable.
C

      do k = 1,nelem
         do j = 1,num_time_steps
            do i = 1,nparam
                gamma(k,j,i) = pstdev(i)*deriv(k,j,i)/sig(k,j)
                gamma2(k,j,i) = max(0., gamma(k,j,i)*gamma(k,j,i))
            enddo
         enddo
      enddo

C
C Write element variables to the new exodus file
C

      do i=1,num_time_steps-1
         call exptim (id2, i, time(i,1), ierr)
         if (ierr.ne.0) STOP
         call expev (id2, i, 1, blockid, numelb, sf(1,i,1), ierr)
         if (ierr.ne.0) STOP
         call expev (id2, i, 2, blockid, numelb, sfp2sig(1,i), ierr)
         if (ierr.ne.0) STOP
         call expev (id2, i, 3, blockid, numelb, sfm2sig(1,i), ierr)
         if (ierr.ne.0) STOP
         call expev (id2, i, 4, blockid, numelb, gamma2(1,i,1), ierr)
         if (ierr.ne.0) STOP
         call expev (id2, i, 5, blockid, numelb, gamma2(1,i,2), ierr)
         if (ierr.ne.0) STOP
         call expev (id2, i, 6, blockid, numelb, gamma2(1,i,3), ierr)
```

```
         if (ierr.ne.0) STOP
         call expev (id2, i, 7, blockid, numelb, gamma2(1,i,4), ierr)
         if (ierr.ne.0) STOP
         call expev (id2, i, 8, blockid, numelb, gamma2(1,i,5), ierr)
         if (ierr.ne.0) STOP
         call expev (id2, i, 9, blockid, numelb, gamma2(1,i,6), ierr)
         if (ierr.ne.0) STOP
         call expev (id2, i, 10, blockid, numelb, gamma2(1,i,7), ierr)
         if (ierr.ne.0) STOP
         call expev (id2, i, 11, blockid, numelb, gamma2(1,i,8), ierr)
         if (ierr.ne.0) STOP
         call expev (id2, i, 12, blockid, numelb, gamma2(1,i,9), ierr)
         if (ierr.ne.0) STOP
         call expev (id2, i, 13, blockid, numelb, gamma2(1,i,10), ierr)
         if (ierr.ne.0) STOP
         call expev (id2, i, 14, blockid, numelb, gamma2(1,i,11), ierr)
         if (ierr.ne.0) STOP
         call expev (id2, i, 15, blockid, numelb, gamma2(1,i,12), ierr)
         if (ierr.ne.0) STOP
         call expev (id2, i, 16, blockid, numelb, gamma2(1,i,13), ierr)
         if (ierr.ne.0) STOP
         call expev (id2, i, 17, blockid, numelb, gamma2(1,i,14), ierr)
         if (ierr.ne.0) STOP
         call expev (id2, i, 18, blockid, numelb, gamma2(1,i,15), ierr)
         if (ierr.ne.0) STOP
         call expev (id2, i, 19, blockid, numelb, gamma2(1,i,16), ierr)
         if (ierr.ne.0) STOP
         call expev (id2, i, 20, blockid, numelb, gamma2(1,i,17), ierr)
         if (ierr.ne.0) STOP
         call expev (id2, i, 21, blockid, numelb, gamma2(1,i,18), ierr)
         if (ierr.ne.0) STOP
         call expev (id2, i, 22, blockid, numelb, gamma2(1,i,19), ierr)
         if (ierr.ne.0) STOP
         call expev (id2, i, 23, blockid, numelb, gamma2(1,i,20), ierr)
         if (ierr.ne.0) STOP
         call expev (id2, i, 24, blockid, numelb, gamma2(1,i,21), ierr)
         if (ierr.ne.0) STOP
         call expev (id2, i, 25, blockid, numelb, gamma2(1,i,22), ierr)
         if (ierr.ne.0) STOP
         call expev (id2, i, 26, blockid, numelb, gamma2(1,i,23), ierr)
         if (ierr.ne.0) STOP
         call expev (id2, i, 27, blockid, numelb, gamma2(1,i,24), ierr)
         if (ierr.ne.0) STOP
         call expev (id2, i, 28, blockid, numelb, gamma2(1,i,25), ierr)
         if (ierr.ne.0) STOP
      enddo

      call exclos (id1,ierr)
      if (ierr.ne.0) STOP
      call exclos (id2,ierr)
      if (ierr.ne.0) STOP

C-----------------------------------------------------------------------
C Write time 0.5 contour passes through centerline element for using
C sf(k,j,1), sfp2sig(k,j), and sfm2sig(k,j).  k here is the index for
C nelem and j is the index for num_time_steps.
C-----------------------------------------------------------------------
```

```
      told = -1.
      do 100, k = elemnum(1), elemnum(MAXCLELEM)
         do j=1,num_time_steps
            xx(j) = sf(k,j,1)
         enddo
         call locate(xx,num_time_steps,refmean,j)
         if((j.eq.0).or.(j.eq.maxclelem)) goto 100
         x = refmean
         x1 = sf(k,j,1)
         x2 = sf(k,j+1,1)
         y1 = time(j,1)
         y2 = time(j+1,1)
         tnew = y1+(x-x1)*(y2-y1)/(x2-x1)
         if(tnew.le.told) goto 101
         write(1,*) tnew/60., dist(k+1-elemnum(1))
         write(50,*) tnew/60., (gamma2(k,j,n),n=1,5)
         write(51,*) tnew/60., (gamma2(k,j,n),n=6,10)
         write(52,*) tnew/60., (gamma2(k,j,n),n=11,15)
         write(53,*) tnew/60., (gamma2(k,j,n),n=16,20)
         write(54,*) tnew/60., (gamma2(k,j,n),n=21,25)
C second index, 61, selects the 61 time step which is at 1800s or 30min
         write(60,*) dist(k+1-elemnum(1)), (gamma2(k,61,n),n=1,5)
         write(61,*) dist(k+1-elemnum(1)), (gamma2(k,61,n),n=6,10)
         write(62,*) dist(k+1-elemnum(1)), (gamma2(k,61,n),n=11,15)
         write(63,*) dist(k+1-elemnum(1)), (gamma2(k,61,n),n=16,20)
         write(64,*) dist(k+1-elemnum(1)), (gamma2(k,61,n),n=21,25)
         told = tnew
100   continue
101   told = -1.
      do 200, k = elemnum(1), elemnum(MAXCLELEM)
         do j=1,num_time_steps
            xx(j) = sfp2sig(k,j)
         enddo
         call locate(xx,num_time_steps,refp2sig,j)
         if((j.eq.0).or.(j.eq.maxclelem)) goto 200
         x = refp2sig
         x1 = sfp2sig(k,j)
         x2 = sfp2sig(k,j+1)
         y1 = time(j,1)
         y2 = time(j+1,1)
         tnew = y1+(x-x1)*(y2-y1)/(x2-x1)
C        if(tnew.le.told) goto 201
         write(2,*) tnew/60., dist(k+1-elemnum(1))
         told = tnew
200   continue
201   told = -1.
      do 300, k = elemnum(1), elemnum(MAXCLELEM)
         do j=1,num_time_steps
            xx(j) = sfm2sig(k,j)
         enddo
         call locate(xx,num_time_steps,refm2sig,j)
         if((j.eq.0).or.(j.eq.maxclelem)) goto 300
         x = refm2sig
         x1 = sfm2sig(k,j)
         x2 = sfm2sig(k,j+1)
         y1 = time(j,1)
         y2 = time(j+1,1)
```

```
         tnew = y1+(x-x1)*(y2-y1)/(x2-x1)
         if(tnew.le.told) goto 301
         write(3,*) tnew/60., dist(k+1-elemnum(1))
         told = tnew
300   continue
301   continue
      END

      SUBROUTINE FNAME(FN,LENGTH,N,NAME)
      CHARACTER FN*8,NAME*8
      CHARACTER*1 L1,L2
      INTEGER N,I1,I2,LENGTH
      CHARACTER DIGITS*10
      DIGITS='1234567890'
      I1=N/10
      L1 = DIGITS(I1:I1)
      I2=(N-I1*10)
      L2 = DIGITS(I2:I2)
      IF(I1.EQ.0) L1='0'
      IF(I2.EQ.0) L2='0'
      NAME=FN(1:LENGTH)//L1//L2
      return
      end

      SUBROUTINE LOCATE(XX,N,X,J)
C-----------------------------------------------------------------------
C Given xx(1:n), and given a value x, returns a value j such that
C x is between xx(j) and xx(j+1). xx(1:n) must be monotonic, either
C increasing or decreasing.  j=0 or j=n is returned to indicate that
C x is out of range.
C-----------------------------------------------------------------------
      IMPLICIT NONE
      INTEGER N,J,JL,JU,JM
      REAL XX(N),X
      JL=0
      JU=N+1
10    IF(JU-JL.GT.1)THEN
        JM=(JU+JL)/2
        IF((XX(N).GT.XX(1)).EQV.(X.GT.XX(JM)))THEN
          JL=JM
        ELSE
          JU=JM
        ENDIF
      GO TO 10
      ENDIF
      J=JL
      RETURN
      END
```

References

1. Hobbs, M.L., Erickson, K.L., and Chu, T.Y., "Modeling Decomposition of Unconfined Rigid Polyurethane Foam," Sandia National Laboratories report SAND99-2758, Albuquerque, NM (1999).

2. Hobbs, M.L., Erickson, K.L., and Chu, T.Y., "Modeling Decomposition of Unconfined Rigid Polyurethane Foam," *Polymer Degradation and Stability*, **69**(1), 47 (2000).

3. Jackson, L.P., Erickson, K.L., Castaneda, J.N., Borek, T.T., "Thermal Decomposition of Aged Rigid Polyurethane (RPU) Foam from the MC 3276," Sandia National Laboratories Report SAND2002-1132 (May 2002).

4. Erickson, K.L., Castaneda, J.N., Ulibarri, T.A., Derzon, D.K., Renlund, A.M., "Thermal Decomposition Chemistry of Rigid Polyurethane (RPU) Foams," Sandia National Laboratories Report SANDTBD, Albuquerque, NM (In Preparation-2002).

5. Erickson, K.L., Borek, T.T., Renlund, A.M., Ulibarri, T.A., Clayton, D., and Fletcher, T.H., "Thermal Decomposition Chemistry of a Rigid Polyurethane Foam," paper presented at the 222nd National Meeting and Exposition of the American Chemical Society (2001).

6. Gartling, D.K., Hogan, R.E., and Glass, M.W., "COYOTE – A Finite Element Computer Program for Nonlinear Heat Conduction Problems," Sandia National Laboratories Report SAND94-1173 (theory) and SAND94-1179 (user's manual), Albuquerque, NM (1998).

7. Bova, S.W., Glass, M.W., Dowding, K.J., Lover, R.R., and Cochran, R.J., "Calore: A Computational Heat Transfer Program: Volume 1: Theory Manual" and "Calore User Documentation Calore Version 1.1 User's Manual", Sandia National Laboratories Reports SANDTBD (Documents in Preparation, 2002).

8. Clayton, D., "Modeling Flow Effects During Polymer Decomposition Using Percolation Lattice Statistics," PhD Dissertation, Brigham Young University, Provo, UT (In progress-2002).

9. Solomon, P.R., Hamblen, D.G., Carangelo, R.M., Serio, M.A., and Deshpande, G.V., "General Model of Coal Devolatilization," *Energy & Fuels*, **2**, 405 (1989).

10. Grant, D.M., Pugmire, R.J., Fletcher, T.H., and Kerstein, A.R., "Chemical Model of Coal Devolatilization using Percolation Lattice Statistics," *Energy & Fuels*, **3**, 175 (1989).

11. Fletcher, T.H., Kerstein, A.R., Pugmire, R.J., and Grant, D.M., "Chemical Percolation Model for Devolatilization. 2. Temperature and Heating Rate Effects on Product Yields," *Energy & Fuels*, **4**, 54 (1990).

12. Fletcher, T.H., Kerstein, A.R., Pugmire, R.J., Solum, M.S., Grant, D.M., "Chemical Percolation Model for Devolatilization 3. Direct use of ^{13}C NMR data to Predict Effects of Coal Type," *Energy & Fuels*, **6**, 414 (1992).

13. Fischer, M.E. and Essam, J.W., “Some Cluster Size and Percolation Problems,” *Journal of Mathematical Physics*, **2**, 609 (1961).

14. Flory, P.J., *Principles of Polymer Chemistry*, Cornell University Press, Ithaca, New York (1953).

15. Hobbs, M.L., “HMX decomposition model to characterize thermal damage,” *Thermochimica Acta*, 384, 291 (2002).

16. Solum, M.S., Pugmire, R.J., Grant, D.M., “^{13}C solid-state NMR of Argonne Premium Coals,” *Energy & Fuels*, **3**, 187 (1989).

17. Shampine, L.F. and Watts, H.A., “DEPAC – Design of a User Oriented Package of ODE Solvers,” Sandia National Laboratories report SAND79-2374, Albuquerque, NM (1979).

18. Henley, E.J., and Seader, J.D., *Equilibrium-Stage Separation Operations in Chemical Engineering*, John Wiley & Sons, New York (1981).

19. Shampine, L.G., and Watts, H.A., “ZEROIN – a root-solving code,” Sandia National Laboratories Report SC-TM-70-631, Albuquerque, NM (1970).

20. Daubert, T.E., Danner, R.P., Subul, H.M., and Stebbins, C.C., *Physical and thermodynamic Properties of Pure compounds: Data compilation*, extant 1994 (core with 4 supplements), Taylor & Francis, Bristol, PA (1994).

21. Taylor, R.E., Groot, H., and Ferrier, J., “Thermophysical Properties of a Foam and Pyromark Paint,” Thermophysical Properties Research Laboratory Report TPRL 1833, Purdue University Research Park, West Lafayette, IN (1997).

22. Taylor, R.E., Groot, H., and Ferrier, J., “Thermophysical Properties of Two Foams A Report to Sandia national Laboratories,” Thermophysical Properties Research Laboratory Report TPRL 1964, Purdue University Research Park, West Lafayette, IN (1998).

23. Chu, T.Y., Hobbs, M.L., Erickson, K.L., Ulibarri, T.A., Renlund, A.M., Gill, W., Humphries, L.L., and Borek, T.T., “Fire-Induced Response in Foam Encapsulants,” in Proceedings SAMPE 1999-44th International SAMPE Symposium & Exhibition (1999).

24. Eldred, M.S., “Optimization Strategies for Complex Engineering Applications,” Sandia National Laboratories report SAND98-0340. Albuquerque, NM (1998).

25. Volltrauer, H.N. and Fontijn, A., "Low Temperature Pyrolysis Studies by Chemiluminescence Techniques. Real-Time Nitrocellulose and PBX 9404 Decomposition Studies", *Combust. Flame,* **41**, 313 (1981).

26. Beyer, W.H., *CRC Standard Mathematical Tables*, 26th Edition, CRC Press, Inc., Boca Raton, FL, 527 (1981).

27. Grønli, M., Antal, Jr. M.J., Várhegyi, G., “A Round-Robin Study of Cellulose Pyrolysis Kinetics by Thermogravimetry,” *Ind. Eng. Chem. Res.*, **38**, 2238 (1999).

28. Hobbs, M.L. and Romero, V.J., “Uncertainty analysis of decomposing polyurethane foam,” *Thermochimica Acta*, **384**, 393 (2002).

29. Robinson, D.G., “A Survey of Probabilistic Methods Used in Reliability, Risk and Uncertainty Analysis: Analytical Techniques,” Sandia National Laboratories Report SAND98-1189, Albuquerque, NM (1998).

30. McKay, M.D., Conover, W.J., Beckman, R.J., “A Comparison of Three Ways for Selecting Values of Input Variables in the Analysis of Output from a Computer Code,” *Technometrics*, **221**, 239 (1979).

31. Wyss, G.D. and Jorgensen, K.H., “A User’s Guide to LHS: Sandia’s Latin Hypercube Sampling Software,” Sandia National Laboratories Report SAND98-0210, Albuquerque, NM (1998).

32. Sethian, J.A., *Level Set Methods and Fast Marching Methods: Evolving Interfaces in Computational Geometry, Flud Mechanics, Computer Vision, and Material Science*, Cambridge University Press, Cambridge, UK (1999).

33. Hobbs, M.L. and Lemmon, G.H., “SPUF – Simple PolyUrethane Foam response model,” Sandia National Laboratories Report, Albuquerque, NM (In preparation, 2003).

Distribution

Brigham Young University (2)
Department of Chemical Engineering
Attn: Daniel Clayton
Dr. Thomas H. Fletcher
350 K Clyde Building
Provo, Utah 84602-4100

Easterling Statistical Consulting (1)
51 Avenida del Sol
Cedar Crest, NM 87008

Federal Aviation Administration (1)
Attn: Richard E. Lyon
Fire Safety Section, AAR-422
William J. Hughes Technical Center
Atlantic City International Airport, NJ 08405

New Mexico State University (1)
Department of Mechanical Engineering
Attn: Richard G. Hills
Las Cruces, New Mexico 88003

United States Department of Commerce
Attn: Kathryn M. Butler
Building and Fire Research Laboratory
National Institute of Standards and Technology
Gaithersburg, MD 20899

University of California, Berkeley (1)
Attn: Carlos Fernandez-Pello
Mechanical Engineering Department
6105a Etcheverry Hall
University of California
Berkeley, CA 94720

University of Utah (1)
Attn: Ronald Pugmire
Associate Vice President for Research
Professor of Chemical & Fuels Engineering
210 Park Building
Salt Lake City, UT 84112

University of Utah (1)
Attn: David M. Grant
Distinguished Professor of Chemistry
Henry Eyring Bldg
315 S 1400 East Rm 2020
Salt Lake City, UT 84112

University of Washington (1)
Dept of Mechanical Engineering
Attn: Ashley Emery
Box 352600
Seattle, WA 98195-2600

Sandia

1	MS0888	1811	R. L. Clough
1	MS0888	1811	E. M. Russick
1	MS0886	1822	R. P. Goehner
1	MS0886	1822	T. T. Borek
1	MS0481	2132	R. J. Harrison
1	MS0481	2132	D. R. Helmich
1	MS0481	2132	T. F. Hendrickson
1	MS0427	2134	R. A. Paulsen, Jr.
1	MS1452	2552	L. G. Minier
1	MS1454	2554	A. M. Renlund
1	MS0311	2616	M. J. Craig
1	MS1202	5932	T. A. Ulibarri
1	MS0748	6413	D. G. Robinson
1	MS9051	8351	A. R. Kerstein
1	MS9052	8361	R. Behrens, Jr.
1	MS9052	8361	S. B. Margolis
1	MS0841	9100	T. C. Bickel
1	MS0836	9100	M. R. Baer
1	MS1393	9100	T. Y. Chu (in Washington DC, Forrestal Building)
1	MS0826	9100	D. K. Gartling
1	MS0834	9112	M. R. Prairie
1	MS0834	9112	K. L. Erickson
1	MS0834	9112	S. M. Trujillo
1	MS0826	9113	S. N. Kempka
1	MS0834	9114	J. E. Johannes
1	MS0834	9114	T. A. Baer
1	MS0834	9114	P. L. Hopkins
1	MS0834	9114	A. M. Kraynik
1	MS0834	9114	P. R. Schunk
1	MS0834	9114	A. C. Sun
1	MS0836	9116	E. S. Hertel
1	MS0836	9116	B. L. Bainbridge
1	MS0836	9116	B. D. Boughton
1	MS0836	9116	J. F. Dempsey
1	MS0836	9116	D. D. Dobranich
1	MS0836	9116	R. C. Dykhuizen
1	MS0836	9116	N. D. Francis, Jr.
10	MS0836	9116	M. L. Hobbs
1	MS0836	9116	R. E. Hogan
1	MS0836	9116	C. Romero
1	MS0836	9116	R. G. Schmidt
1	MS0836	9117	R. O. Griffith
1	MS0836	9117	M. E. Larsen
1	MS0555	9122	M. S. Garrett
1	MS0555	9122	K. R. Thompson
1	MS0893	9123	M. K. Neilsen
1	MS0824	9130	J. L. Moya
1	MS0821	9132	L. A. Gritzo

1	MS0836	9132	W. Gill
1	MS1135	9132	J. T. Nakos
1	MS1135	9132	S. R. Tieszen
1	MS0828	9133	M. Pilch
1	MS0828	9133	B. F. Blackwell
1	MS0828	9133	K. J. Dowding
1	MS0828	9133	V. J. Romero
1	MS0828	9133	W.L. Oberkampf
1	MS0835	9140	J. M. McGlaun
1	MS0835	9141	E. A. Boucheron
1	MS0835	9141	S. W. Bova
1	MS0835	9141	M. W. Glass
1	MS0835	9141	R. R. Lober
1	MS0847	9211	M. S. Eldred
1	MS0819	9211	R. G. Trucano
1	MS0423	9732	J. A. Fernandez
1	MS0151	9750	A. C. Ratzel
1	MS0421	9800	W. Hermina
1	MS0139	9900	M. O. Vahle
1	MS0139	9905	S. E. Lott
1	MS0829	12323	B. M. Rutherford
1	MS0405	12333	T. R. Jones
1	MS0405	12333	L. A. Schoof
1	MS0405	12333	S. E. Camp

1	MS9018	8945-1	Central Technical Files, 8945-1
2	MS0899	9619	Technical Library